Nuclear envelope and nuclear response to mechanical deformation

Alice Williart

université
PARIS-SACLAY

Nuclear envelope and nuclear response to mechanical deformation

Enveloppe nucléaire et réponse du noyau aux déformations mécaniques

Thèse de doctorat de l'université Paris-Saclay

École doctorale n°577, Structure et Dynamique des Systèmes Vivants (SDSV)
Spécialité de doctorat : Biologie moléculaire et cellulaire
Graduate School : Life Sciences and Health, Référent : Faculté des Sciences d'Orsay

Thèse préparée dans **l'UMR144 Biologie Cellulaire et Cancer, Institut Curie, CNRS, Sorbonne Université (Paris)**
sous la direction de **Matthieu PIEL**, Directeur de Recherche
et la co-direction de **Nicolas MANEL**, Directeur de Recherche

Thèse soutenue à Paris-Saclay, le 9 octobre 2023 par

Alice WILLIART

Composition du Jury

Membres du jury avec voix délibérative

Martin LENZ Directeur de Recherche, Université Paris-Saclay / CNRS	Président
Nicolas BORGHI Directeur de Recherche, Université Paris Cité / CNRS	Rapporteur & Examinateur
Charlotte RIVIERE Maîtresse de conférences, HDR, Université Claude Bernard Lyon I	Rapporteure & Examinatrice
Maria-Elsa ALMONACID Chargée de Recherche, Collège de France / CNRS	Examinatrice

THÈSE DE DOCTORAT

NNT : 2023UPASL082

Remerciements

Cette thèse ne serait pas arrivée à son aboutissement sans l'aide précieuse de très nombreuses personnes.

Je tiens d'abord à remercier Matthieu et Nicolas, mes deux directeurs de thèse. Merci à Nicolas de m'avoir donné l'opportunité de faire cette thèse, même si le sujet s'est finalement éloigné de ce qui avait motivé la question initiale. Ta rigueur scientifique et ton immense connaissance de la littérature ont été très importantes dans la construction de ce projet. Merci à Matthieu de m'avoir acceptée dans son équipe, d'abord en stage, puis en thèse, et de m'avoir guidée pendant ces quatre années. J'ai beaucoup appris grâce à toi, à la fois scientifiquement et personnellement, et je tiens à te remercier de ta bienveillance durant cette période de la thèse qui peut être éprouvante.

Merci aux membres du jury, Martin Lenz, Nicolas Borghi, Charlotte Rivière, Maria Almonacid, et Nico Casartelli, pour le temps qu'ils ont consacré à ce travail. Les discussions pendant la soutenance ont été très enrichissants pour moi. Je remercie aussi chaleureusement mon comité de suivi, Antoine Coulon, Francesca Di Nunzio et Valérie Doye, pour leurs conseils et leur soutien lors de nos rendez-vous annuels.

Un grand merci à mes collaborateurs : Romain, qui a construit le versant physique de ce travail, et m'a (ré)expliqué les modèles, toujours avec patience et pédagogie, merci Damien de m'avoir évité de me battre avec le confineur dynamique et l'autofocus du spinning plus que nécessaire, thank you Michele for all the time you spent acquiring each single cell on the AFM. Sans vous, ce travail n'aurait pas pu aboutir.

Je remercie aussi Guilherme, grâce à qui j'ai appris écraser des cellules et à les regarder, et Xavier, le puits de science de biologie moléculaire et le mentor de mon tout premier stage.

Merci à l'équipe, vous avez été parfois la principale source de bonne humeur au labo quand les cellules ne coopéraient pas ! Merci Joseph, Anumita, Camille, Laura, Henri et Li, Pablo et Mathilde B. Merci Mathieu de tes conseils toujours sages, avant et après chaque présentation.

A Anvita, qui m'a montré tout ce qu'il fallait sur les lenti et le VIH, qui a été une mentor proche et chaleureuse, Zahraa, Larisa et Lucie, qui m'ont accueillie quand je suis arrivée, mes « grandes sœurs de thèse » merci de vos conseils, de votre soutien et de votre gentillesse !

A Kotryna et Theresa, je suis heureuse de vous compter parmi mes amies ! Merci de votre soutien et de votre écoute infaillible dans les moments de désespoir, des pauses thé et glaces, et des rires partagés.

Merci à mes amis, qui ont suivi de près ou de loin le drama de cette thèse : Angèle et tous nos brunchs de week-end, Mathilde F et tes encouragements, Laura et nos heures au téléphone, Aymeric sans qui aucune résolution de sport n'aurait tenu, Lise et nos sorties au musée, Juliette et nos dégustations de thé, Gwenaël, Malo et Pierre-Louis d'avoir été co-foyer avenue Jeanne d'Arc, Benoît, Camille, Théo, Marion, Alban, Julie. Ma vie est plus belle grâce à vous !

Merci à ma famille, qui a participé à me donner la curiosité du monde : mes grands-parents, qui ont le goût de la transmission, mes parents, qui m'ont soutenue dans mes choix d'études et ont toujours été compréhensifs même si mes problèmes de cellules, de virus et de microscopes ne leur parlaient pas beaucoup. Merci Adrien, mon frère, de m'écouter me plaindre, de me soutenir et me secouer en même temps.

Merci Jean de ton soutien et de ta confiance en moi, de toute ton aide durant la rédaction. Ce manuscrit n'aurait jamais été terminé sans toi.

TABLE OF CONTENTS

TABLE OF FIGURES

ABBREVIATIONS

5 meC	5 methylcytidine
53BP1	53 binding protein 1
ABD	Actin-Binding Domain
AI	artificial intelligence
ATM	ataxia-telangectasia mutated
ATR	ataxia-telangectasia related
BAF	Barrier-to-Autointegration
BFP	blue fluorescent protein
bp	base pair
C. elegans	*Caenorhabditis elegans*
CCT	Choline Phosphate Cytidyltransferase
Cdk	cyclin-dependent kinase
cGAS	cGMP-AMP synthase
CH	calponin homology domain
cPLA2	cytosolic Phospholipase A2
cryoEM	cryo electron microscopy
cryoET	cryo-electron tomography
CTCF	CCTC Binding Factor
CTDNEP1	C-terminal domain nuclear envelope phosphatase 1
DAG	diacylglycerol
DNA PK	DNA protein kinase
DNMT	DNA methyltransferases
DSB	double strand break
EBD	emerin-binding domain
EDMD	Emery-Dreifuss muscular dstrophy
EFC	elliptic Fourier coefficients
EMT	epithelial to mesenchymal transition
ER	endoplasmic reticulum
ESCRT	Endosomal Sorting Complex Required for Transport
FLIM	Fluorescence Lifetime Imaging Microscopy
FRAP	Fluorescence Recovery After Photobleaching
FRET	Förster Resonance Energy Transfer
GAP	GTPase Activating Protein
GEF	Guanosine Exchange Factor
HGPS	Hutchinson-Gilford progeria syndrome
HIV	Human Immunodeficiency Virus
HP	heterochromatin protein
HSV	Herpes Simplex Virus
HTLV	human T leukemia virus
ICMT	isoprenylcysteine carboxyl methyltransferase
Ig	immunoglobulin
INM	inner nuclear membrane
KASH	Klarsicht/Anc-1/Syne homology
KD	knock down
KO	knock out
LAD	lamina-associated domain
LAP	lamina-associated protein
LATS	large tumor suppressor
LBR	lamin B receptor
LEM	LAP2, Emerin, Man1
LINC	Linker of Nucleoskeleton and Cytoskeleton
LLPS	liquid-liquid phase separation
LPS	lipopolysaccharide
MLV	Mouse Leukemia Virus
MST	Mammalian STE20-like
MTOC	microtubule-organizing center
NE	nuclear envelope
NEBD	nuclear envelope breakdown
NES	Nuclear Export Signal
NHEJ	non-homologous end joining

NLS	Nuclear Localization Signal
NMR	nuclear magnetic resonance
NPC	nuclear pore complex
ONM	outer nuclear membrane
PA	phosphatidic acid
PC	phosphatidylcholine
PE	phosphatidylethanolamine
PI	phosphatidylinositol
PKC	protein kinase C
pLL	poly-l-Lysine
pLL-PEG	poly-L-Lysine-g-Polyethylene-glycol
PML	Promyelocytic Leukemia
PTM	post-translational modification
RCE	Ras converting enzyme
RNA Pol	RNA polymerase
ROCK	Rho-associated protein kinase
ROS	Reactive Oxygen Species
S. cerevisiae	*Saccharomyces cerevisisae*
S. pombe	*Schizosaccharomyces pombe*
SR	spectrin repeats
SUN	Sad1p and UNC-84 domain containing
TAD	topologically associated domain
TAN	transmembrane associated nuclear
TAZ	Transcriptional coactivator with PDZ motif
TEM	transendothelial migration
YAP	Yes-associated protein

INTRODUCTION

Phylogeny classically divides the tree of life into three branches: Bacteria, Archaea and Eukaryotes. While each branch has its own specificities and contains its own diversity, eukaryotic cells stand apart under the microscope for an organelle only they possess, the nucleus. Bacteria and Archaea also tend to have an internal organization that segregates their genome in a specific region of the cytoplasm. However, Eukaryotes have evolved a dedicated compartment that does not only regionalize, but also physically isolates, their genome from the rest of the cell. Despite this protective function, the nuclear envelope is a plastic exchange surface. Messenger RNA, proteins and ions transit through the nuclear pores, the nucleus is deformed when cells migrate in complex environments, and its existence can also be transient. In some species, including Mammals, cell division requires dissolution of the nuclear envelope and its reassembly at the beginning of the next cell cycle. The nucleus and its envelope emerge as highly dynamic entities, able to deform, reform and adapt to the environment. More and more studies emphasize the importance of mechanical cues from the environment in the behavior of the cell. While the plasma membrane, at the interface between the cell and its surroundings, was long considered as the key player in mechanosensing and mechanotransduction, the nucleus appears to have its role to play. As the largest and stiffest organelle in the cell, it has unique properties that can at the same time allow mechanosensitivity and make it susceptible to deformations. Due to the sensitive nature of its content, it is reasonable to expect that these deformations are being sensed but buffered. In this work, we try to understand how, in Mammalian cells, the nuclear envelope and lamina define the mechanical properties of the nucleus and its response to mechanical constrains, to modulate its contribution to cellular mechanosensing.

CHAPTER 1: THE NUCLEUS, A MULTILAYERED ORGANELLE

The nucleus is delimited by the nuclear envelope (NE), a double lipid bilayer composed of the inner and outer nuclear membrane (INM and ONM), joined at the nuclear pores, which are holes in the NE connecting the nucleoplasm and the cytoplasm (Figure 1). The ONM is continuous with the endoplasmic reticulum (ER), while the INM, continuous with the ONM, is separated from it by the nuclear pore complex (NPC) proteins. Both membranes delimitate the perinuclear space, typically of about 30 nm (Mellad *et al.*, 2011).

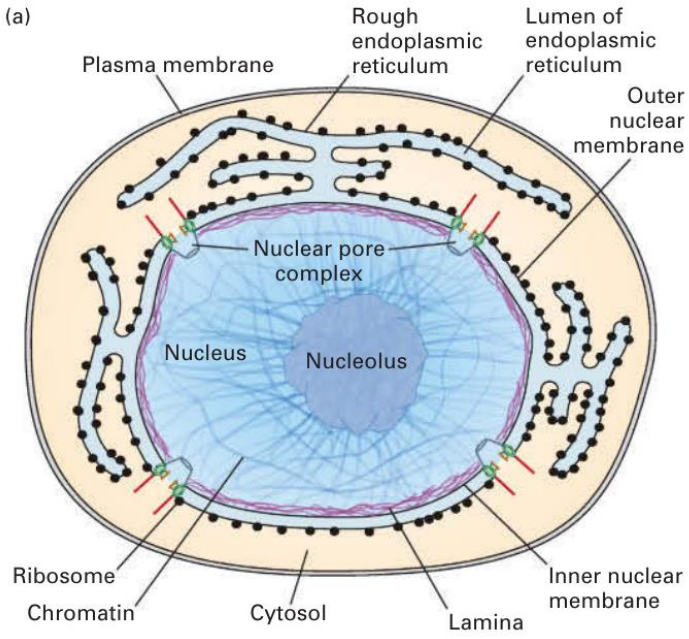

Figure 1: Ultrastructure of the nucleus
(Lodish et al., 2016)

In the first part of this introduction, we will go through the successive layers of the nuclear structure, starting from the outermost shell, the envelope, through the underlying lamina and to the chromatin. We will show that these components are in tight interaction with each other.

I. Outer and inner nuclear membranes

The nuclear membranes are designated together as the nuclear envelope and they define the border between nucleus and cytosol. They are also sometimes described as a specialized region of the ER. It has been established that Eukaryotes arose from the endosymbiosis of a Bacteria with an Archaea, but the origin of the nucleus itself is still unknown. Two models have been proposed to explain the emergence of the double-membrane nuclear envelope and of the ER (Baum and Baum, 2020). The outside-in model, which was predominant for a long time, proposes that the endomembrane network originates from an endosome-like intracellular compartments, that later gradually fused. Recently, an inside-out model was proposed, suggesting that the plasma membrane and intracellular membranes could emanate from large protrusion of the original Archaea. This model is compatible with recent discoveries made in Archaea (Baum and Baum, 2020) and proposes an interesting theory for the origin of nuclear pores.

In this first part, we will discuss how both nuclear membranes define two separate compartments.

A. Lipid composition of the nuclear membranes

The nuclear membranes are lipid bilayers whose precise composition remained unclear for a long time, due to the difficulty of isolating them without ER membrane contamination (Bahmanyar and Schlieker, 2020). In this chapter, we will discuss what distinguishes them from other cellular membranes, focusing on their lipid composition.

Mass spectrometry analysis has revealed that the ER membrane and the NE are composed of unsaturated glycerophospholipids, mainly phosphatidylcholine (PC) and phosphatidylethanolamine (PE), as well as the less abundant phosphatidylinositol (PI) (Jacquemyn *et al.*, 2017). A recent study of the NE composition with Nuclear Magnetic Resonance (NMR) showed that PC is by far the most abundant phospholipid in the NE, while cholesterol and sphingolipids levels are low compared to the plasma membrane (van Meer *et al.*, 2008; Bigay and Antonny, 2012; Dazzoni *et al.*, 2020). These elements paint the picture of flexible and fluid membranes, more so than the stiffer plasma membrane. Several studies have pointed to the role of lipid composition in the NE structure and barrier function. Enrichment in long-chain fatty acids of the sphingolipids family has been shown to improve the nuclear shape defects observed in aneuploid cells (Hwang *et al.*, 2019), and overexpression of Elo2, an enzyme promoting fatty acid chain elongation, rescues the phenotype of rupture-prone nuclei in yeast mutants deficient for certain INM proteins (Kinugasa *et al.*, 2019). The lipid composition of the NE can also be modulated by different enzymes. Lipins

are the key phosphatidic acid (PA) phosphatases catalyzing its dephosphorylation into diacylglycerol (DAG), the precursor of the main glycerophsopholipids of the membranes (Péterfy *et al.*, 2001). Lipin 1 in particular is a soluble protein shuttling between the cytoplasm and the nucleus depending on its phosphorylation state (Peterson *et al.*, 2011). It is a substrate for the C-terminal domain nuclear envelope phosphatase 1 (CTDNEP1), which has been shown to be enriched at the INM in *Caenorhabidtis elegans* (*C. elegans*) (Bahmanyar and Schlieker, 2020), as well as in mouse and fly cells (Jacquemyn *et al.*, 2021). The cytosolic phospholipase A2 (cPLA2) can be recruited to the NE and catalyze the synthesis of arachidonic acid (Enyedi *et al.*, 2016). Other INM proteins, such as Lamin B Receptor (LBR), are also involved in cholesterol metabolism (Tsai *et al.*, 2016). Far from being frozen in its composition, the NE lipid bilayer thus emerges as highly dynamic. Recent studies have shown that it can be a purveyor of lipid droplets (Romanauska and Köhler, 2018; Sołtysik *et al.*, 2021), non-conventional exosomes in activated neutrophils (Arya *et al.*, 2022) and can also produce long tubules extending into the nucleoplasm, coined nucleoplasmic reticulum (Malhas *et al.*, 2011; Drozdz *et al.*, 2017; Dazzoni *et al.*, 2020).

B. The nuclear pore complex, gateway between cytoplasm and nucleoplasm

Unlike the conventional plasma membrane, the nuclear envelope is pierced by numerous pores, which put the cytoplasm and nucleoplasm in direct continuity. The pores are regions of high membrane curvature where the ONM folds and gives way to the INM, structured by the nuclear pore complex, the largest protein complex present in the envelope. In this part, we go over the structure of this macromolecular complex and how it controls transport between nucleus and cytoplasm.

The NPC is a complex of about 34 different proteins organized by multimers of 8, 16, 32 or 64 units. It can reach a size of more than 100 MDa in vetebrates and is regularly distributed on the NE (Bley *et al.*, 2022). It follows an 8-fold symmetry around the axis of the pore as well as a pseudosymmetry across the NE (Beck and Hurt, 2017). The NPC is organized in three rings of transmembrane proteins: the inner ring pore ring, at the high curvature junction between INM and ONM, surrounded by the nuclear and the cytoplasmic rings on each side, which are in turn in interaction respectively with the nuclear basket and the cytoplasmic filaments (Figure 2A). The NPC represents a selective diffusion barrier between the nucleoplasm and the cytoplasm (Figure 2B). The inside of the channel, of a diameter of about 70 nm in *Schizosaccharomyces pombe* (*S. pombe*) (Zimmerli *et al.*, 2021), is filled with a meshwork of phenylalanine – glycine (FG) repeats from unstructured regions of the ring nucleoporins.

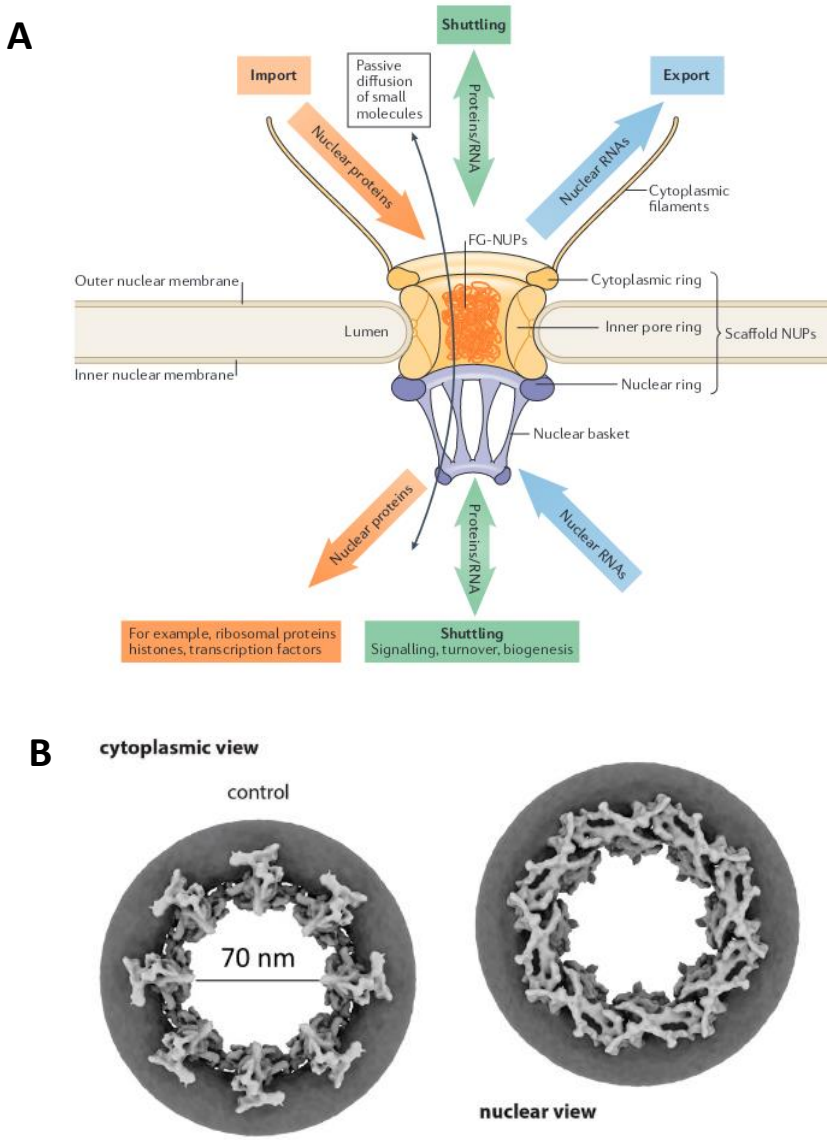

Figure 2: Overview of the nuclear pore complex

A. General architecture of the NPC (adapted from (Beck and Hurt, 2017))

B. Plasticity of NPC structure with diameters (adapted from (Zimmerli et al., 2021))

It allows molecules smaller than 40 - 60 kDa or 2.83 nm of Stokes radius to freely diffuse (Terry and Wente, 2009; Li *et al.*, 2016). Beyond this size, active transport requires the interaction of cargos with karyopherins, which can interact with and rearrange the FG repeats meshwork and shuttle between the cytoplasm and the nucleoplasm. The directionality of import and export is permitted by a small G protein, Ran, which is required for the crossing of the NPC. Its Guanosine Exchange Factors (GEF) and GTPase Activating

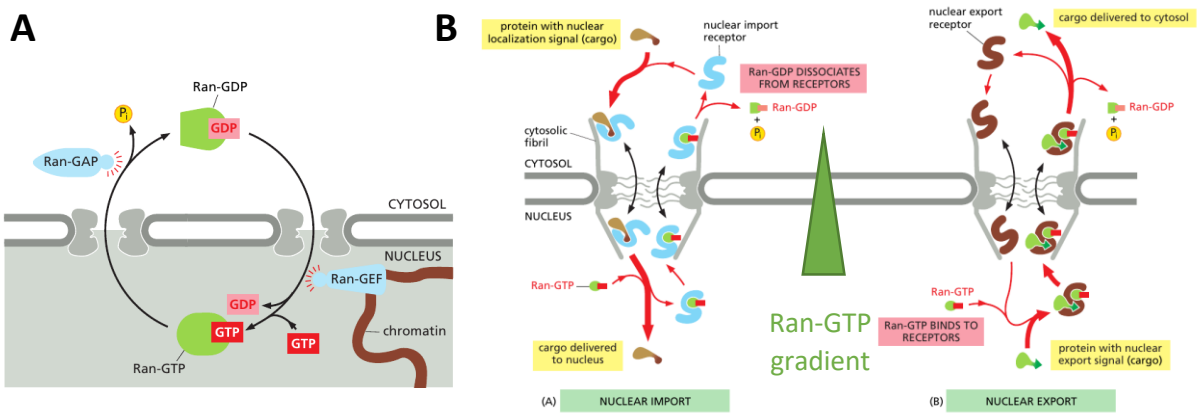

Figure 3: Principles of nucleo-cytoplasmic transport

A. Ran-GDP/GTP cycle B. Directionality of nuclear import and export (adapted from (Alberts et al., 2015))

Proteins (GAP) are exclusively found respectively on the nuclear and cytoplasmic side, resulting in a Ran-GDP/GTP gradient from the cytoplasm to the nucleus (Cautain *et al.*, 2015) (Figure 3A). Karyopherins involved in nuclear import, called importins, bind their cargo at low Ran-GTP/Ran-GDP levels, and dissociate from their cargo in high Ran-GTP conditions. Conversely, exportins, involved in nuclear export, bind to their cargo and Ran-GTP (Figure 3B). Active nuclear transport relies on the existence of a Nuclear Localization Signal (NLS) for import, and Nuclear Export Signal (NES) for export, recognized in cargos by importins or exportins. The directionality of the nucleo-cytoplasmic transport system is key in establishing a distinct protein content in the nucleoplasm. Importantly, a recent structural analysis of the NPC by cryo-electron microscopy (cryoEM) revealed its plasticity, as the pore can dilate or constrict depending on the environmental conditions (Zimmerli *et al.*, 2021).

C. Lipid and protein asymmetry between inner and outer nuclear membranes

Several studies have shown that despite their continuity, there is a distinct asymmetry in the proteome of the INM and the ONM (Schirmer and Gerace, 2005; Korfali *et al.*, 2012). Like most transmembrane proteins, INM integral proteins are synthesized in the ER and must therefore cross the NPC to reach the INM. Initially, it had been proposed that integral proteins with luminal domains smaller than the diffusion limit of the NPC could freely diffuse and would be retained in the nucleus through interaction with the underlying lamina or the chromatin, in the so-called diffusion-retention model (Katta *et al.*, 2014). This model explains how INM proteins such as LBR (Ellenberg *et al.*, 1997), Lamina-associated protein (LAP) 2 (Furukawa and Kondo, 1998) or emerin (Tsuchiya *et al.*, 2001) are selectively enriched in the nucleus.

However, there are INM proteins with luminal domains larger than 40 kDa, for which the NPC represents a lateral diffusion barrier. Moreover, energy depletion impairs the proper localisation of INM reporters (Ohba *et al.*, 2004), suggesting the existence of an active targeting. Indeed, several INM proteins contain a putative or classical NLS in their luminal domain, such as Sad1p and UNC-84 domain containing (SUN) 2 (Turgay *et al.*, 2010) or Heh1 and 2 in *Saccharomyces cerevisiae* (*S. cerevisiae*) (King *et al.*, 2006), and exploit a similar route as the soluble cargos.

Studies suggest that, just like they harbor distinct protein contents, INM and ONM differ in their lipid composition, as specific lipids mediate NPC assembly (Drin *et al.*, 2007) or viral production (Marschall *et al.*, 2011). These membranes are continuous at the level of the pores, raising the question of the origin of the difference in their composition. At first glance, lipid diffusion should not be strongly hindered by the NPC. This asymmetrical lipid distribution could have several origins. As discussed above, the activation of some enzymes involved in lipid metabolism, such as lipin, occurs specifically in the nucleoplasm, therefore restricting their activity to the INM. The Choline Phosphate Cytidyltransferase (CCT) α, a key enzyme in PC synthesis, is also restricted to the nucleus (Haider *et al.*, 2018). However, unless the production is continuous, the asymmetry should be averaged over time by lateral diffusion. The initial assumption was revisited, and it has been proposed that specific nucleoporins or the strong negative curvature at the level of the inner ring could restrict the diffusion of certain conic lipids (McMahon and Boucrot, 2015).

The nuclear envelope defines a polarized barrier between nucleus and cytoplasm. It harbors a distinct lipid and protein composition due to specific transport and synthesis mechanisms. The nuclear pores, which act as selective barrier between the two compartments, participate to the asymmetry between INM and ONM, and are key in establishing the distinct identity of the nucleus.

II. The perinuclear space, a compartment at the border between nucleus and cytosol

In this part, we focus on the space between both nuclear membranes, coined the perinuclear space. It is in continuity with the ER lumen.

A. The luminal space

Between the INM and ONM lies the perinuclear space. It is in continuity with the ER lumen and as such, is considered as a likely calcium reservoir (Jahed *et al.*, 2018), although it remains unclear whether ion channels or transporters are present at the INM or ONM. There have been reports of ion transporters on

the NE, such as an Na^+/K^+ ATPase in hepatocytes (Garner, 2002), calcium transporters in certain neuronal cells (Ledeen and Wu, 2007; Fedorenko and Marchenko, 2014), or in T and B cells (Franco-Obregón *et al.*, 2000). However, little is known about their precise characteristics and the role of the perinuclear space in calcium signaling is unclear.

It is believed that the distance between INM and ONM is largely maintained by the interactions between the components of the Linker of Nucleoskeleton and Cytoskeleton (LINC) complex (Crisp *et al.*, 2006).

B. The LINC complex, a spacer and linker in the perinuclear space

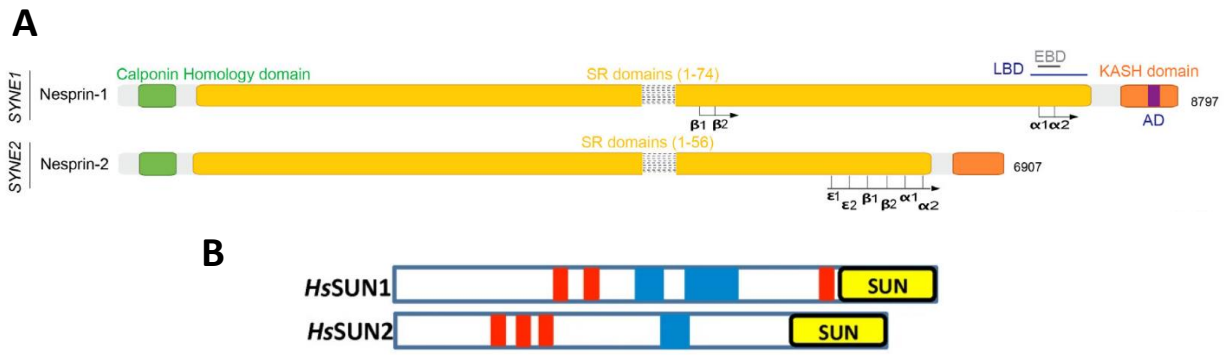

Figure 4: Structure of the main components of the LINC complex

A. Linear structure of the main nesprins proteins (Janin and Gache, 2018) B. Linear structure of SUN proteins (red: transmembrane domain, blue: coiled-coil domain) (Murphy et al., 2010)

The LINC complex is composed of two sets of proteins, on the INM and on the ONM, covalently bound in the perinuclear space by two disulfide bonds. Klarsicht/Anc-1/Syne homology (KASH) domain containing proteins, mainly nesprin 1, 2 and 3, reside in the ONM. They share a common organisation and a high homology, in particular nesprins 1 and 2. On their cytoplasmic side, nesprins are composed of a calponin homology domain (CH), also called Actin-Binding Domain (ABD) and spectrin repeats (SR), ending with a small emerin-binding domain (EBD) (Figure 4A). The ABD and SR domains mediate the nesprins' interaction with the cytoskeleton: actin filament through the ABD and microtubules through recruitment of microtubule-associated proteins. The full-length versions of nesprins 1 and 2, called giant nesprins, are the second and third largest proteins in Mammals, with sizes of 1 MDa and 800 kDa (Zhang, 2001). They are ubiquitously expressed in mammalian cells. Nesprin 3, also ubiquitously expressed, lacks the ABD and interacts instead with plectin, able to mediate interaction with vimentin and other cytoplasmic intermediate filaments (Wilhelmsen *et al.*, 2005). Smaller isoforms coming from alternative splicing of nesprins 1 and 2 display shorter SR domains and have a tissue-specific expression, with nesprin 1α2 and

nesprin 2α1 specifically expressed in heart and skeletal muscle tissues (Duong *et al.*, 2014). The KASH domain is the most conserved across all nesprins. It contains the transmembrane segment and the C-terminal part of the protein, in the perinuclear space. The KASH domain is covalently bound to the INM component of the LINC complex, the SUN proteins, and is essential to the cohesion of the LINC complex.

The SUN proteins are composed of the SUN domain, a coiled-coil region and a nucleoplasmic domain (Figure 4B). First identified in *C. elegans*, the most common isoforms at the NE in Mammals are SUN1 and SUN2 (Sosa *et al.*, 2012). The SUN proteins typically assemble in homo- and heterotrimers through their coiled-coil regions (Sosa *et al.*, 2012; Hieda, 2017) and interact with lamin A through their N-terminal nucleoplasmic domain in mammalian cells (Crisp *et al.*, 2006) or directly with chromosomes in yeasts, whose nuclei are devoid of lamins. Although SUN1 and 2 can partially compensate for each other, they have specific properties and functions. Interestingly, interaction with lamin A was found to be necessary for SUN2 localization at the NE, but not SUN1 (Crisp *et al.*, 2006), while SUN1 but not SUN2 is enriched at the NPC (Liu *et al.*, 2007).

Through its interaction with the cytoskeleton on one side through the nesprins, and the lamina on the other side through the SUN proteins (Figure 5), the LINC complex mechanically bridges the nucleoplasm, the cytoplasm and, beyond, the plasma membrane (Maniotis *et al.*, 1997). It is key to the nuclear morphology, as disruption of the LINC complex increases the width of the PNS (Crisp *et al.*, 2006), as well as to the mechanical force transmission from the environment outside the plasma membrane to the nuclear compartment. Of note, while most of the mechanical connection between the nucleus and the cytoskeleton goes through the LINC complex, NPC have also been found to mediate interaction with actin filaments.

Although the nucleus stands apart, its physical continuity with the ER and its mechanical association with the cytoskeleton in the cytoplasm underscore how integrated it is to the cell and to the mechanical cues imparted by the environment.

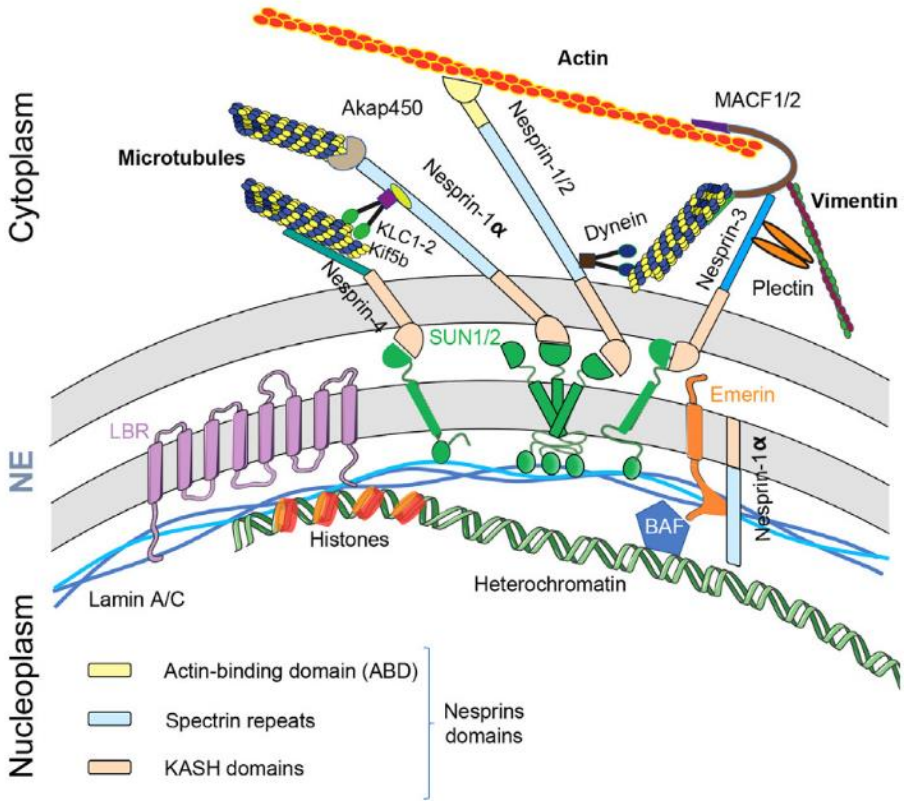

Figure 5: Overview of the LINC complex
(Janin and Gache, 2018)

III. The lamina, a meshwork underlying the envelope

In this part, we describe the structure and organization of the lamina, the meshwork below the inner nuclear membrane.

A. Structure of lamin filaments

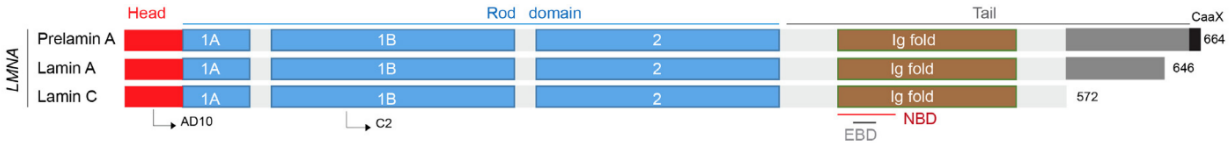

Figure 6: Structure of lamin A and C proteins
(Janin and Gache, 2018)

Like the actin cortex supporting the plasma membrane, the INM in Metazoans is lined on the nucleoplasmic side by the lamina, a meshwork composed mainly of intermediate filaments, the lamins, of a thickness of 14 nm (Turgay *et al.*, 2017). In mammalian cells, there are 2 types of lamins, A and B. The main B-type lamin-encoding genes are *LMNB1* and *LMNB2*, which give rise to lamin B1 and B2 (Höger *et*

al., 1990), while the main A-type lamin gene is *LMNA*, which can be alternatively spliced into lamin A or the shorter lamin C (Lin and Worman, 1993). They share a general organization composed of an N-terminal head, a central rod composed of 2 coiled-coil regions and a globular C-terminal tail containing an NLS, an immunoglobulin (Ig) fold and, for lamin A, B1 and B2, a CAAX (cysteine – (aliphatic amino-acid)² – any) motif at the C terminus, which is a site of multiple post-translational modifications (Parry *et al.*, 1986) (Figure 6). Lamin A, B1 and B2 are farnesylated on the cysteine by a farnesyltransferase, before cleavage of the AAX motif by the zinc metalloprotease ZMPSTE24 or the Ras-converting enzyme (RCE) 1 and carboxy-methylation on the now C-terminal cysteine by the isoprenylcysteine carboxyl methyltransferase (ICMT) (Rusiñol and Sinensky, 2006). Lamin A, at this stage called prelamin A, then undergoes a secondary cleavage by ZMPSTE24 between the Ig fold and the CAAX motif. At the end of the maturation process, only B-type lamins remain farnesylated and thus able to interact directly with the INM (Tenga and Medalia, 2020).

B. Organization of the lamin meshworks

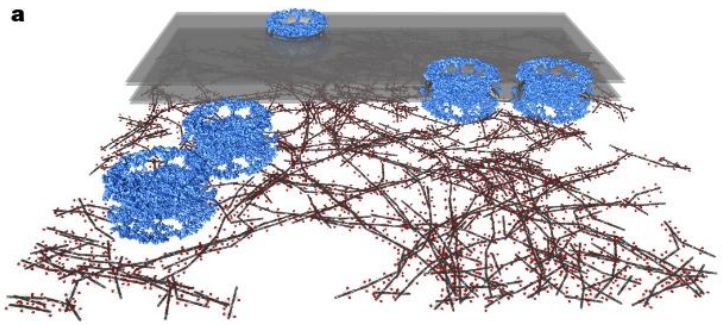

Figure 7: Reconstruction of the lamin meshwork
*(*Xenopus laevis *oocyte)*
Lamins (rod-domain in dark grey and immunoglobulin domain in red), NPCs (blue) and the inner and outer nuclear membrane (transparent grey), reconstruction after cryo-tomogram (Turgay et al., 2017)

How lamins organize into filaments and then a meshwork remained unclear for a long time because of the technical difficulty of structure determination. Recent advances in cryo-electron tomography (cryoET) have revealed that individual monomers assemble into dimers or tetramers via their coiled-coil regions and form head-to-tail interactions, constituting 3.5 nm thick filaments (Turgay *et al.*, 2017). The A- and B-type lamins organize in separate, concentric meshworks, with the farnesylated B-type lamins lining the INM and the A-type lamins underneath the B-type meshwork facing the nucleoplasm (Shimi *et al.*, 2008, 2015; Nmezi *et al.*, 2019). The lamin A meshwork appears to be less dense than its lamin B1 counterpart

and displays smaller pores and shorter edges (Shimi *et al.*, 2015). Fluorescence Recovery After Photobleaching (FRAP) experiments have shown that the turnover rate of the lamina is extremely low, as the fluorescence recovery is longer than 180 min (Moir *et al.*, 2000). As a comparison, the turnover of its plasma membrane counterpart, the actin cortex, is in the range of the minute (Fritzsche *et al.*, 2013). Unlike the cortex, the lamina is not endowed with contractility.

C. Lamin A and B expression levels

B-type lamins are ubiquitously expressed in mammalian cells (Höger *et al.*, 1990; Yang *et al.*, 2011) and are essential: the double knock-out (KO) *LMNB1*/*LMNB2* is embryonic lethal in mice (Yang *et al.*, 2011). On the contrary, A-type lamin expression varies depending on the cell type and the developmental stage. Lamin A/C expression is very low to non-existent in embryonic stem cells (Schatten *et al.*, 1985; Burke and Stewart, 2002), and it increases upon differentiation (Constantinescu *et al.*, 2006). Hematopoietic progenitors and certain immune cells such as neutrophils also express very low levels of A-type lamins (Röber *et al.*, 1990b). While the levels of A- and B-type lamins are stable in most cell types, immune cells are able to rapidly change the composition of their lamina: resting B cells express very low levels of lamin A/C but switch on its expression upon activation by the bacterial compound lipopolysaccharide (LPS) (Röber *et al.*, 1990a).

D. Lamina anchoring in the inner nuclear membrane

While the B-type lamins are anchored in the INM by their farnesylated tails, the association between INM and lamina is additionally ensured by a number of INM integral proteins. The aforementioned SUN proteins in the LINC complex are interacting with the lamin A meshwork, either directly or through small, alternatively spliced nesprins, such as nesprin 1 alpha 2 in skeletal muscles (Zhang, 2001; Mellad *et al.*, 2011). One large family of INM, lamina-interacting proteins is the LAP2, Emerin, Man1 (LEM) domain containing proteins. They are defined by their common 40 amino-acid domain interacting with the INM protein Barrier-to-Autointegration Factor (BAF), which directly binds DNA in a sequence-aspecific manner, and have been shown to interact directly with lamin B1 and B2 or lamin A/C (Barton *et al.*, 2015). As they interact with the lamins as well as BAF and histones, LEM domain proteins are bridging the INM, the lamina meshwork and the chromatin.

Of note, while there is no lamina in yeasts, similar functions are held by distant homologs of the LEM domain proteins, which are involved in membrane/DNA interactions (Gonzalez *et al.*, 2012). This likely indicates an ancestral function of DNA interactions with the nuclear envelope.

IV. The chromatin, a supramolecular complex of DNA and proteins

Inside the nucleus sits the genomic DNA of the cell, which contains most of its genetic information. In most Eukaryotes, DNA is organized in several long linear double-stranded polymers, the chromosomes. Each strand of DNA interacts with the other via base-pair weak interactions, described by Watson and Crick when the double helix structure of the DNA was resolved (Figure 8A). The DNA polymer is overall negatively charged because of the phosphate groups on its skeleton. The linear DNA in a human cell would be 2 m long and has to be compacted to fit in a nucleus which can, in a first approximation, be considered as a sphere of a diameter around 10 µm. The interaction of the DNA with multiple proteins, together forming the chromatin, participates to its 3D folding.

In this part, we briefly go over the linear DNA structure and detail its interactions with the proteins organizing its 3D structure.

A. Linear DNA and nucleosome organization

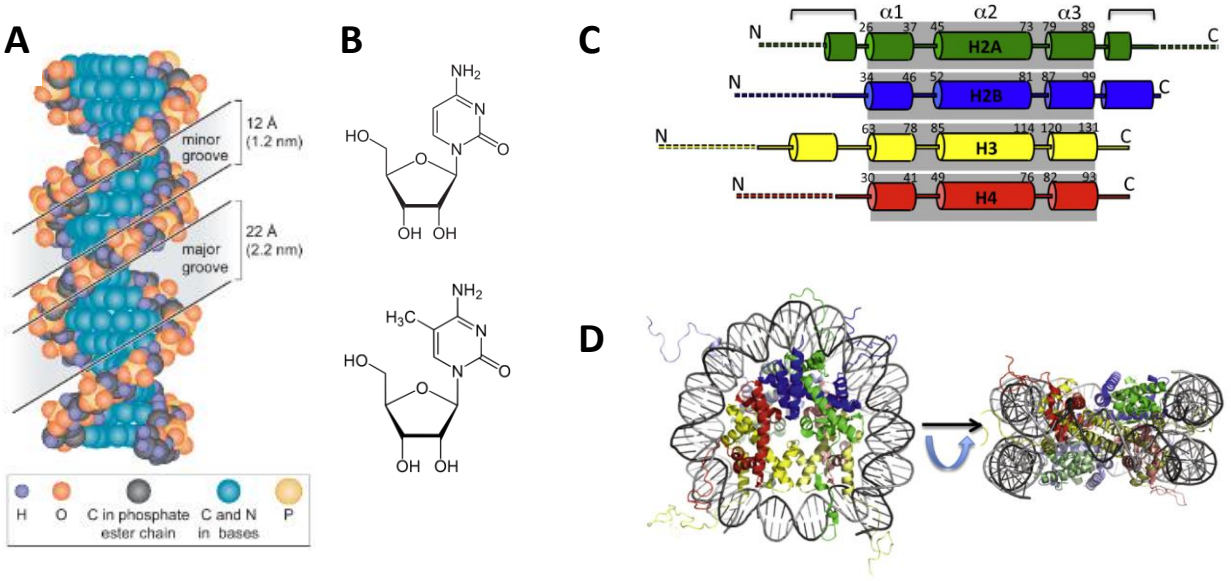

Figure 8: Structure of the basic unit of chromatin organization, the nucleosome
A. Linear DNA polymer (Watson et al., 2014) B. top: cytidine, bottom: 5-methylcytidine C. Structure of the core histones D. Top and lateral view of the nucleosome with the histone octamer and the wrapped DNA (Cutter and Hayes, 2015)

The linear DNA is wrapped around complexes called nucleosomes, organized as an octamer of histone proteins (Figure 8C). The canonical histones in the nucleosome are H2A, H2B, organised as a dimer, H3 and H4 in a tetramer (Figure 8D). This core nucleosome, of 5.5 nm height and 11 nm diameter (Richmond *et al.*, 1984) binds a 147-base pair (bp) long stretch of DNA. This constitutes a first level of compaction and reaches a 7-fold condensation. An additional histone called "linker histone", among which the more common is histone H1, can be bound to the octamer. It is thought to tighten the interaction between the DNA and the core nucleosome. Histone/DNA interactions are mediated by weak bonds between phosphates on the DNA and amides links or conserved lysin and arginin residues on the histone core (Luger *et al.*, 1997).

B. Covalent modifications of DNA and histones

The level of interaction between DNA and histones, as well as between nucleosomes, can be modulated by several covalent modifications of both DNA and proteins. The cytosin can be methylated on carbon 5 (5meC) (Figure 8B) by DNA methyltransferases (DNMT), either during DNA replication (maintenance DNMT1) or in the rest of the cell cycle (*de novo* DNMT3a and b) (Jones and Liang, 2009). DNA methylation has been shown to increase the binding affinity of DNA to histone tails (Li *et al.*, 2022). In turn, histones are the target of a wide variety of post-translational modifications (PTM). One of the key amino-acid targeted for PTM is lysin, which can be covalently altered on its free amin, but other amino-acids such as serin or arginin. Thus, PTM are usually referred to by the name of the targeted histone, the number of the modified amino-acid and the modification: H3K9me3 designates a trimethylation on the lysin 9 of histone 3. The most commonly described PTM are phosphorylation, simple, di- and tri-methylation and acetylation, although more and more modifications have been identified and proposed to modify chromatin structure (Millán-Zambrano *et al.*, 2022). Initially, histone modifications were thought to modify the nucleosomal structure, since addition of acetyl or methyl groups on the charged lysin residues would decrease the overall positive charge and the ability to interact with the negatively-charged DNA backbone. Certain histone PTM have been indeed identified in the core domains, at the interface with the DNA. However, the higher order of chromatin architecture and compaction does not emerge from tighter or looser DNA association to the nucleosome.

Several PTM are found in the tails, which are directed outwards and are crossing the DNA grooves (Luger *et al.*, 1997). Modifications in these domains participate to the supra-nucleosomal organisation of the chromatin by mediating nucleosome-nucleosome interactions or serving as platforms to assemble chromatin-remodeling complexes (Millán-Zambrano *et al.*, 2022).

Chromatin is classically divided between euchromatin, regions of locally looser, accessible and transcriptionally active DNA and heterochromatin, initially defined by its high electron density, where the DNA is more compacted, less open and usually transcriptionally silent. Each is associated to specific chromatin marks and histone PTM signature. Hallmarks of euchromatin include acetylated histones, which loosen the binding between DNA and histone, H3K36me3 and H3K4me3, which serve as a recruitment platform for transcription factors and RNA Polymerase (RNA Pol) II (Vermeulen *et al.*, 2007). On the other hand, two chromatin marks are considered as the hallmarks of heterochromatin. H3K9me3 is associated with constitutive heterochromatin, regions of the genome that are often gene-poor and remain highly condensed throughout the cell cycle and the life of the cell. H3K9me3 is recognized by Heterochromatin Protein (HP) 1 homologue-α, which in turn oligomerizes and assembles into a higher order complex. H3K27me3 is a hallmark of facultative heterochromatin, portions of the genome which contain genes and can be dynamically condensed or decondensed depending on environmental conditions.

C. 3D chromatin conformation

Chromatin organization had first been described to assemble into regular 30 nm fiber (Finch and Klug, 1976; Woodcock *et al.*, 1984). However, chromosome capture techniques, and one of its recent versions HiC, provided evidence for medium- and long-range interactions between distant regions of a chromosome and between chromosomes (Lieberman-Aiden *et al.*, 2009). This proposes an architecture with irregularly-distributed domains with local interactions, named Topologically-Associated Domains (TAD). Further works using similar techniques have shown that TADs can generally be delimited by loops anchored by CCTC Binding Factor (CTCF), a DNA-binding protein recognizing a consensus sequence present at insulators (Dehingia *et al.*, 2022).

The seminal work and other studies showed that long-range interactions are much more likely between DNA regions of similar compaction levels, *i.e.* that euchromatin and heterochromatin tend to interact more with themselves. In the case of constitutive heterochromatin, it has been proposed that HP1α drives its liquid-liquid phase separation (LLPS) from the rest of the nucleoplasm (Larson *et al.*, 2017; Wang *et al.*, 2019). The loci coding for the ribosomal genes also cluster together in membraneless organelles, the nucleoli, based on this principle (Lafontaine *et al.*, 2021).

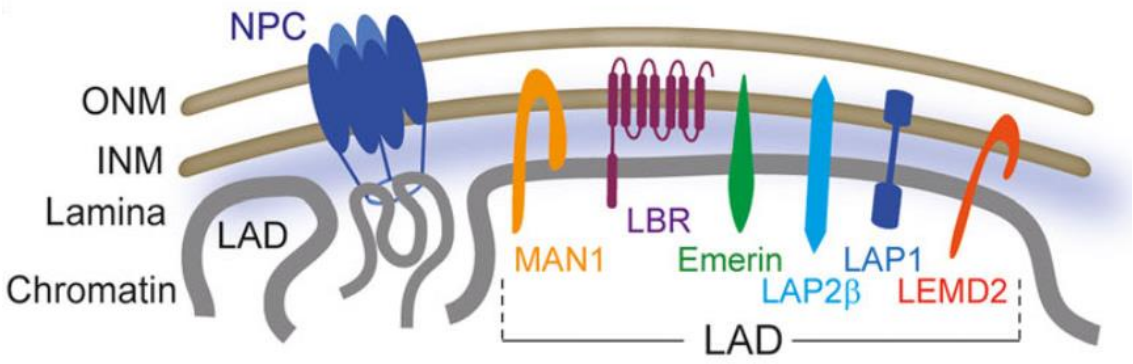

Figure 9: Anchoring of the lamina and the chromatin to the nuclear envelope
(Briand and Collas, 2020)

Additionally, the lamina and INM contribute to the organization of the chromatin in the nucleus. The chromatin is tethered to the lamina and the NE by protein/DNA interactions. Multiple INM proteins are described to interact with chromatin, among them the LEM domain proteins, LBR, and the SUN proteins, have been proposed as tethers (Figure 9). Studies have shown that LBR plays a key role in anchoring the chromatin to the NE (Solovei *et al.*, 2013; Amendola and Van Steensel, 2015; Herman *et al.*, 2021) and lamin A/C (Solovei *et al.*, 2013) and B1 (Chang *et al.*, 2022) have been found to be required for a proper anchoring in certain cell types. The chromatin regions in interaction with the lamina are called the Lamina-Associated Domains (LAD) and will be discussed in more details in the next chapter.

D. Non-histone proteins in the nucleoplasm

Of note, while the chromatin is the main component of the nucleoplasm, a number of soluble proteins are present in the nucleoplasm. The DNA machinery (DNA and RNA poylmerases, helicases, topoisomerases) as well as DNA damage repair factors, transcription factors, centromeric and telomeric proteins, are present as well, either in the soluble fraction or bound to the chromatin. There is also a pool of soluble lamin A/C, often found in association with LAP2α and interacting with euchromatin (Naetar *et al.*, 2017). A pool of nuclear actin has also been shown to be actively maintained (Dopie *et al.*, 2012) and while it remained unclear for a long time under which form actin was present in the nucleoplasm, there is evidence for nuclear actin filament assemble in certain conditions (Baarlink *et al.*, 2013; Plessner *et al.*, 2015). Nuclear G-actin has been found associated to multiple chromatin-remodeling complexes, in particular though its ATPase activity, and to all three human RNA polymerases (Percipalle, 2013). Nuclear actin filaments appear involved in several processes in mitosis or in DNA repair (Caridi *et al.*, 2018; Schrank

et al., 2018). In addition, several proteins are essential to LLPS-mediated formation of membraneless organelles, for instance Promyelocytic Leukemia (PML) in the PML nuclear bodies, and participate to the internal organization of the nucleoplasm.

All these elements paint the picture of a complex organelle, whose structure and architecture involve multiple layers and components, in tight interaction with one another.

CHAPTER 2: FUNCTIONS OF THE NUCLEAR ENVELOPE

The nuclear envelope and the underlying lamina set the nucleus apart from the cytoplasm. They constitute both a barrier and a scaffold, which protect the genome from alteration by the environment and organize its architecture. The first function is perhaps the most intuitive, as both NE and lamina puts the DNA behind additional layers from the cytoplasm and its many chemical reactions, and from the extracellular environment. In this chapter, we will focus on one example of the protective role of the nuclear envelope, and one example showing that the structural scaffold provided by the INM and the lamina have functional consequences for the cell.

I. The nuclear envelope and the lamina as a protective barrier

One of the primary functions attributed to the nucleus is the isolation and protection of the DNA from the cytoplasm and the environment. In this part, we will first give a few examples of detrimental contact of nuclear content with the cytoplasm, including pathogens, before focusing on how viruses who need access to the nucleoplasm for their replication cycle get around the NE barrier.

A. Risks of nucleoplasm/cytoplasm contacts

The cells are exposed to pathogens throughout their lives. Among them, certain viruses represent a particular risk for genome integrity. While most RNA viruses bring their own polymerases and complete their cycle in the cytosol, certain DNA viruses require access to host nuclear proteins to replicate. Retroviruses, which have a RNA genome, go through reverse transcription and require integration to produce new virions. In particular, integrative viruses are a threat to genome integrity and proper function. For instance, the Mouse Leukemia Virus (MLV) has been shown to preferentially integrate at enhancers and regulatory sites (LaFave *et al.*, 2014). This is associated with dysregulation of gene expression patterns and an increase in tumor frequencies in infected mice.

Additionally, the cytoplasm contains proteins detrimental to the host genome, such as nucleases like TREX1, or proteins whose contact with the genome could trigger unwanted pathways, such as DNA sensors like the cyclic GMP-AMP synthase (cGAS). It typically works as a DNA sensor in the cytoplasm, thus participating to antiviral surveillance. Uncontrolled mixing of cytoplasm and nucleoplasm has been shown

to cause TREX1-dependent DNA damage (Nader *et al.*, 2021), underlining the protective function of the intact NE. During mitosis, where the cyosol and the nuclear content come in contact, cGAS activity is inhibited by nucleosomes (Zierhut *et al.*, 2019), which provide an intrinsic protection from activation, and hyperphosphorylation by the Aurora kinase (Li *et al.*, 2021).

B. Viral breaching of the nuclear envelope barrier

Viruses with nuclear requirement have evolved different strategies to gain access to the nucleus.

As the nuclear import is a controlled process due to the selectivity of NPC, some viruses simply never cross the intact NE and require nuclear envelope breakdown (NEBD) in mitosis. It is the case of the Retrovirus Human T Leukemia Virus (HTLV) or of the Papillomavirus (Mettenleiter, 2016).

When the viruses enter an intact nucleus, the majority of them appears to proceed via interaction with the NPC, either directly or via hijacking of karyopherins. The capsid of Adenovirus is for instance directly binding Nup21' (Cassany *et al.*, 2015) The Herpes Simplex Virus (HSV) 1 relies on its essential protein VP1-2, which contains an NLS-like sequences (Abaitua *et al.*, 2012), to target the capsid to the NPC before injecting its DNA through the pore (Mettenleiter, 2016). A protein of the Epstein-Barr Virus (EBV) contains FG-repeats directly interfering with the FG-repeat nucleoporins, while other rely on NLS (Lee and Chen, 2021). In many cases, only the viral DNA is injected into the nucleus. For a long time, it was thought that it was also the case for the Human Immunodeficiency Virus (HIV), but the capsid has been shown to interact with the nucleoplasmic Nup153 (Di Nunzio *et al.*, 2013). Additionally, viral capsid has been detected in the nucleus and appears necessary to post-nuclear entry steps such as the integration into the genome (Peng *et al.*, 2014; Chin *et al.*, 2015; Chen *et al.*, 2016). The size of HIV pre-integration complex, composed of the reverse-transcribed DNA genome and associated proteins, already exceeds the diameter of the NPC (Bhargava *et al.*, 2018). The conical capsid is even larger with a height of 120 nm and a width of 60 nm but has been observed crossing intact NPC (Zila *et al.*, 2021). How such a large object manages to cross the NPC dense FG meshwork remains poorly understood.

In addition to requiring crossing the NE to enter the nucleus for replication purposes, several viruses assemble in the nucleoplasm and subsequently need to exit the nucleus in order to release new infectious particles (Mettenleiter, 2016). This is sometimes accomplished by triggering NEBD with a signalling cascade inducing lamina phosphorylation, like the Parvoviruses (Porwal *et al.*, 2013). This occurs likely via calcium efflux from the NE lumen triggering PKCδ and Cdk1/2 activation, which mimic mitosis entry. Herpesviruses form a Nuclear Egress Complex and remodels the INM protein distribution by increasing

the lateral diffusive mobility of LBR and emerin, as well as locally phosphorylating lamins (Hennig and O'Hare, 2015). Viral glycoproteins are sufficient to induce vesicle formation from the INM into the PNS (Klupp *et al.*), which then fuse with the ONM to exit into the cytoplasm.

Viruses have found multiple ways to get circumvent the protective function of the NE and its controlled nucleo-cytoplasmic transport. How the NE machinery is altered and repurposed by viruses shows that much about the cytoplasm/nucleus interface remains to be understood.

II. Functional consequences of nuclear architecture

So far, we have focused on the nuclear envelope and the lamina functions as barriers and structural components of the nucleus. However, studies have uncovered roles of INM proteins or the lamina meshwork in genome expression and maintenance. In this part, we will discuss how proximity to the NE may affect genome expression and maintenance.

A. Nuclear architecture and gene expression

The chromatin is associated to the lamina and the NE, through interaction with LBR (Solovei *et al.*, 2013; Amendola and Van Steensel, 2015; Herman *et al.*, 2021), laminB1 (Chang *et al.*, 2022) and lamin A (Solovei *et al.*, 2013). Systematic analysis of regions in interactions with the peripheral lamins has led to the definition the LADs. LADs are mainly heterochromatinic and are enriched in H3K9me2/3 and H3K27me2/3 marks (Figure B). Constitutive LADs are mostly composed of non-genic DNA but 5-10% of the LADS are estimated to encode genes (Van Steensel and Belmont, 2017). LADs are relatively homogeneous in terms of chromatin marks (Figure 12B).

A study showed that random insertions of a reporter in the genome were 5 to 6 times less expressed when the insertion was in a LAD (Akhtar *et al.*, 2013). This indicates that the geographical relation between peripheral chromatin and lamina is coupled with functional impacts on gene expression, and that LADs appear to be at least partly responsible for the generally low level of expression in the periphery. Based on the potential behaviors of promoters in LADs, it appears that, while not all promoters are susceptible to the peripheral localization-dependent inhibition, at least some are localization-sensitive (Figure 10A). LBR appears to play a key role in this phenomenon, in particular through its ability to recruit the heterochromatin-associated protein HP1 (Polioudaki *et al.*, 2001). On the contrary, the nuclear basket protein TPR is preventing LAD formation and heterochromatin accumulation at the NPC (Boumendil *et al.*, 2019), favoring active transcription in these regions. While the LADs are relatively conserved

throughout one cell cycle (Van Schaik *et al.*, 2020), they can be locally remodeled by active transcription (Brueckner *et al.*, 2020), underlining the link between architecture and expression. Additionally, lamin A/C loss upon activation in macrophages is required for the induction of the expression of pro-inflammatory cytokines (Mehl *et al.*, 2022). Although the mechanism is not fully understood, it provides evidence that lamina and proteins of the INM have functions beyond their structural role. These examples illustrate that proximity to the NE and DNA / lamina / NE interactions plays a part in gene expression control.

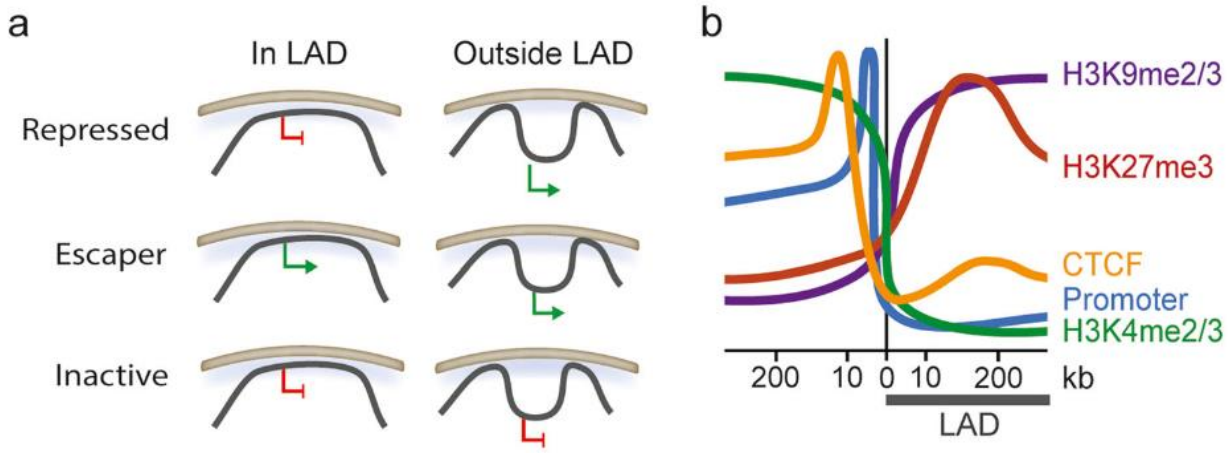

Figure 10: Promoter characteristics in Lamina-Associated Domains
A. Three different possible behaviors of promoters in LADs B. Epigenetic characteristics of chromatin in LADs (Briand and Collas, 2020)

B. Functions of nuclear envelope proteins and the lamina in DNA damage repair

Integral INM proteins have also been shown to play various roles in DNA-related processes. For instance, LBR binds H4K20me2 (Hirano *et al.*, 2012), a chromatin mark enriched at double strand break (DSB) sites (Paquin and Howlett, 2018). In yeast, DSB tend to cluster at the nuclear periphery, and interact with Mps3, a yeast SUN-domain protein or the nucleoporin Nup84 (Oza *et al.*, 2009). Their resolution is mediated by an error-prone repair mechanism called Break-Induced Repair (BIR), which is specifically hyperactivated when DSB are artificially targeted to the NPC (Chung *et al.*, 2015).

In mammalian cells, SUN1 SUN2 double KO MEF display a lack of Ataxia-Telangiectasia Mutated (ATM) phosphorylation, an early step of DNA repair. SUN1 and SUN2 were shown to interact with the DNA protein kinase (DNA-PK), an enzyme promoting the early steps of DNA repair by Non-Homologous End Joining (NHEJ) (Lei *et al.*, 2012). Progeria nuclei expressing prelamin A instead of the properly processed lamin A display delayed DNA damage response following UV irradiation (Liu *et al.*, 2005).

Therefore, multiple INM proteins as well as the lamina serve not only a tethering, structural function, but also actively participate to the regulation of DNA metabolism. This suggests that structural alteration of the NE can have functional consequences on the DNA machinery.

CHAPTER 3: DYNAMICS OF THE NUCLEUS AND ITS STRUCTURE

In the previous chapter, we showed that the nuclear envelope and the lamina are more than nuclear scaffolds and are modulating genome expression and maintenance. The nucleus is also more than a static organelle. In this chapter, we will discuss the dynamics of the nuclear architecture, focusing on the context of mitosis, and the plasticity of the nucleus' interactions with the rest of the cell, in the context of cell migration.

I. Dynamical remodeling of the nuclear envelope and lamina during mitosis

Unlike yeasts, which undergo "closed mitosis" with very local disruption of the NE, Metazoans go through cell division by a complete disassembly of the nucleus, which is termed an "open mitosis" (Figure 11). It is preceded by high condensation of the chromatin into mitotic chromosomes and nuclear envelope breakdown (NEBD). As the different nuclear components are heavily interconnected, this requires the disruption of multiple interactions. In this part, we will show how the different components disassemble and reassemble during cell division.

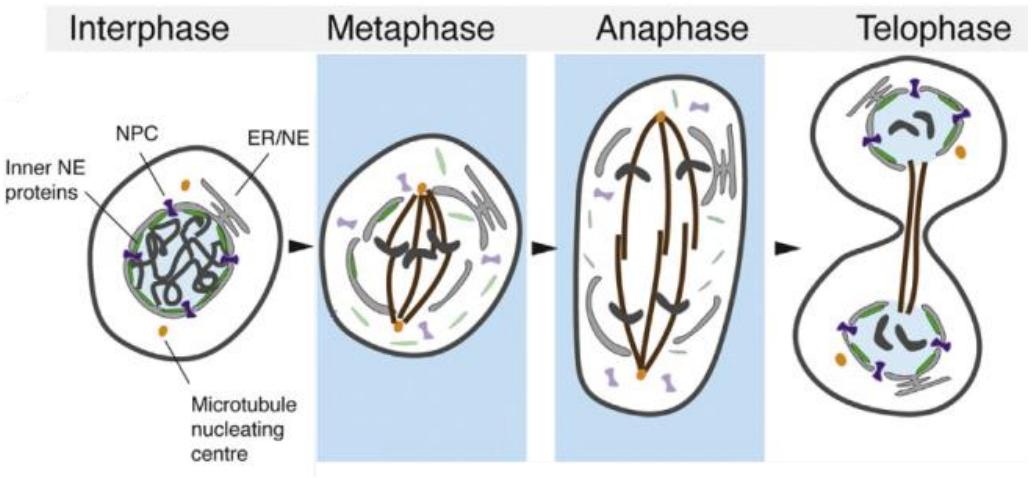

Figure 11: Nuclear envelope breakdown in open mitosis
Adapted from (Dey and Baum, 2021)

A. Sequence of disassembly and reassembly of the nucleus in open mitosis

The disassembly of the NE takes place in several steps, initiated by the activation of the G2-M associated complex Cyclin B - Cyclin-dependent kinase (Cdk) 1.

The chromatin starts to condense in prophase, prior to the NEBD. The initial event of NE disassembly consists in the disassembly of the NPC in a few minutes (Dultz and Ellenberg, 2010), which is triggered by nucleoporin phosphorylation by the Cyclin B - Cdk 1 (Glavy *et al.*, 2007). The lamin meshworks are also disassembled (Gerace and Blobel, 1980), following phosphorylation of lamin A and B by CdK1 (Peter *et al.*, 1990; Glavy *et al.*, 2007) and the Protein Kinase C (PKC) βII (Deacon *et al.*, 2002) disrupting the head-to-tail interactions between monomers (Jeong *et al.*, 2022). Interestingly, PKC βII is recruited at the NE specifically at the G2/M transition thanks to its elevated DAG levels (Deacon *et al.*, 2002) and its activity is required for NEBD and proceeding to mitosis. The NEBD itself requires stretching and tearing of the lamina by microtubules and dynein activity (Beaudouin *et al.*, 2002). The chromatin detaches from the NE and disentangling of the interactions between chromatin and NE is required for a proper chromosome segregation in mitosis (Champion *et al.*, 2019). Fragments of the NE disperse in the cytosol.

After the chromatid separation from the metaphase plate, daughter chromosomes are pulled towards the poles of the mitotic spindle during anaphase. The interphase nucleus starts assembling again in an order reminiscent of its disassembly. Pre-pore complexes bind to chromatin as soon as early anaphase (Dultz and Ellenberg, 2010) and NPC are fully reassembled after NE membrane reformation. Chromosomes are clustered together in anaphase by BAF, which, together with LAP2β and other INM, also mediates the attachment of the chromatin to the NE and recruits the membranes to the chromosomes (Samwer *et al.*, 2017). The membranes themselves are reformed on the chromatin from assembly of the NE/ER tubules (Lu *et al.*, 2011). Interestingly, while lamin B1 appears to stay attached to the membranes and is therefore brought back together with the NE reformation, lamin A/C is reimported in early G1. While the structure of the nucleus is fully reassembled in the daughter cells, some interactions are remodeled from one cycle to the next. In particular, LADs are completely disrupted during mitosis (Kind *et al.*, 2013) and how they reform during the next G1 compared to the previous cycle is not fully understood.

The nuclear structure thus appears to be very dynamic and at the same time relatively faithfully reformed even after complete disassembly.

B. Importance of mitosis in shaping the next interphase nucleus

Because of the numerous steps involved in both disassembly and reassembly of the nucleus, there are multiple possible errors, and a smooth completion of mitosis is required for an intact NE in the next cycle.

Mitotic errors can arise from multiple sources. Most of the reported cases originate from improper microtubule organization, whether it be centrosome amplification, which leads to multipolar spindles (Ganem *et al.*, 2009), or improper or too stable kinetochore-microtubules attachment (Bakhoum *et al.*, 2009). Both increase the probability of lagging chromosomes in anaphase, which can be damaged by the contractile furrow in cytokinesis, segregate to the wrong daughter cell, or form micronuclei (Levine and Holland, 2018). Micronuclei arise from NE assembly on a subset of chromosomes. They share a basic structure with the main nucleus, as they possess a nuclear envelope and underlying lamin filaments (Hatch *et al.*, 2013). However, they are characterized by a high instability and nearly always collapse, due to a discontinuous lamin B1 meshwork (Hatch *et al.*, 2013) or to dysregulated transport because of delayed NPC assembly (Krupina *et al.*, 2021). It has been suggested that the higher curvature may play a role in micronuclei fragility (Krupina *et al.*, 2021). Unlike the main nucleus, micronuclei ruptures fail to repair and ESCRT III appears to accelerate micronuclei breakdown rather than resealing their NE (Vietri *et al.*, 2020).

Additionally, failure to recruit it has been reported that exposure to Reactive Oxygen Species (ROS) during mitosis led to abnormal nuclear shapes due to mislocalization of BAF at mitosis exit (Ahn *et al.*, 2019). Bridging the lamina, the INM and the chromatin is a key role of BAF and the BAF A12T mutation, which causes the Nestor-Guillermo Progeria Syndrome, prevents its binding to lamin A/C, thus impairing proper NE rupture repair (Janssen *et al.*, 2022).

The complete disassembly and re-assembly of the nucleus in mitosis shows that the complex interactions between the different nuclear components can be completely rearranged. A smooth mitosis with functional interactions between chromatin and INM proteins is key in nuclear stability throughout cell cycles.

II. Plasticity of the nucleus' interaction with the cytoskeleton

A. Nuclear positioning at steady state and in migrating cells

Beyond its functions of DNA compartment, we have shown that the nucleus is strongly connected to the rest of the cell, be it the ER through the continuity with the ONM or the cytoskeleton via the LINC complex. These connections are highly dynamic and can be remodeled depending on the cell state. In particular, they are rearranged in migrating cells. Because the nucleus is the largest organelle in the cell, its positioning and movement during cell migration requires a rearrangement of its interaction with the cytoskeleton, in particular actomyosin.

At steady state, nuclear positioning is mainly controlled by LINC-microtubules interaction, although actin filaments also play a role (Starr, 2007). Certain subsets of LINC complexes appear to be predominantly involved. Nesprin 4 levels, which binds to kinesin 1, participate to the close position of the nucleus and the centrosome (Roux *et al.*, 2009). Microtubules and actin filaments are involved in nuclear position homeostasis by respectively moving the nucleus forward and rearward (Zhu *et al.*, 2017). Interestingly, SUN1 is required for forward re-centering, while SUN2 is necessary for rearward positioning correction.

Epithelial migration is associated with a repositioning of the nucleus in the cell. Migration initiation consists in a symmetry-breaking polarization and establishment of a contractile rear and an actin-rich lamellipodium at the front (Cramer, 2010) (Figure 12A). In this step, the nucleus is positioned at the rear of the cell, forming a leading edge – Golgi – centrosome – nucleus axis that is conserved throughout the migratory process (Vaidžiulytė *et al.*, 2022). Contrary to the initial assumption, the polarization step and the establishment of this axis are dependent on actomyosin contractility and microtubules appear to be dispensable in this step. The nucleus is pushed backwards by the retrograde actin flow, which in turn pulls on the microtubule organizing center (MTOC) (Gomes *et al.*, 2005).

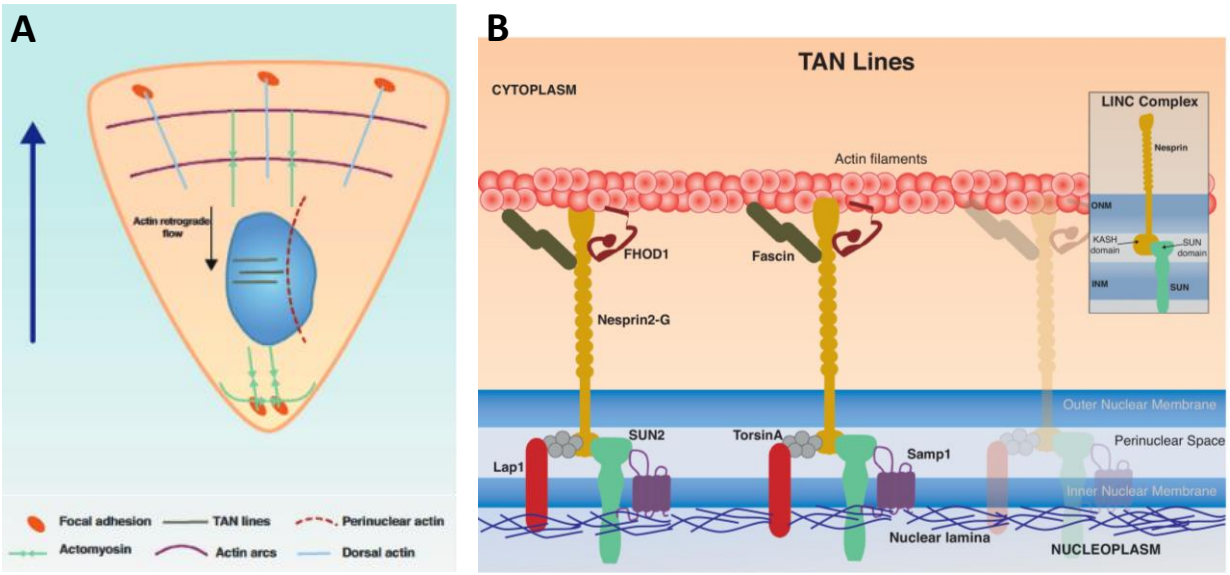

Figure 12: Reorganization of nucleus-cytoskeleton interaction in 2D migration

A. Overview of the cytoskeleton in a 2D migrating cell B. Specific nucleus/cytoskeleton interaction in mesenchymal migration (adapted from (Calero-Cuenca et al., 2018))

As the nucleus is the largest organelle in the cell, its displacement during migration requires force generation. Migration and nucleus positioning are tightly coupled by the Transmembrane Actin-associated Nuclear (TAN) lines (Figure 12B), which, through focal adhesions, actin filaments, nesprin-2 and SUN2 (Luxton *et al.*, 2010), link the environment, the protruding front, the actin flow and the nucleus. The existing data indicates that in 2D migration, the nucleus is strongly connected to the cytoskeleton and the plasma membrane, and it can be moved by actomyosin-generated forces.

B. Nuclear deformation upon cell migration in complex environments

The matter of nuclear positioning is challenged when cells migrate in more complex environments, such as the extracellular matrix of dense tissues. Studies have shown that some tissues, like myofibers, exhibit a matrix pore size as small as 3 µm (Weigelin *et al.*, 2012), which obviously require cell body deformation, but is also smaller than the diameter of most nuclei (5-10 µm in diameter). While the cytoplasm is relatively soft and deformable, the nucleus is 2-10 times stiffer than the rest of the cell (Davidson *et al.*, 2014). In such circumstances, the nucleus becomes a limiting factor to migration.

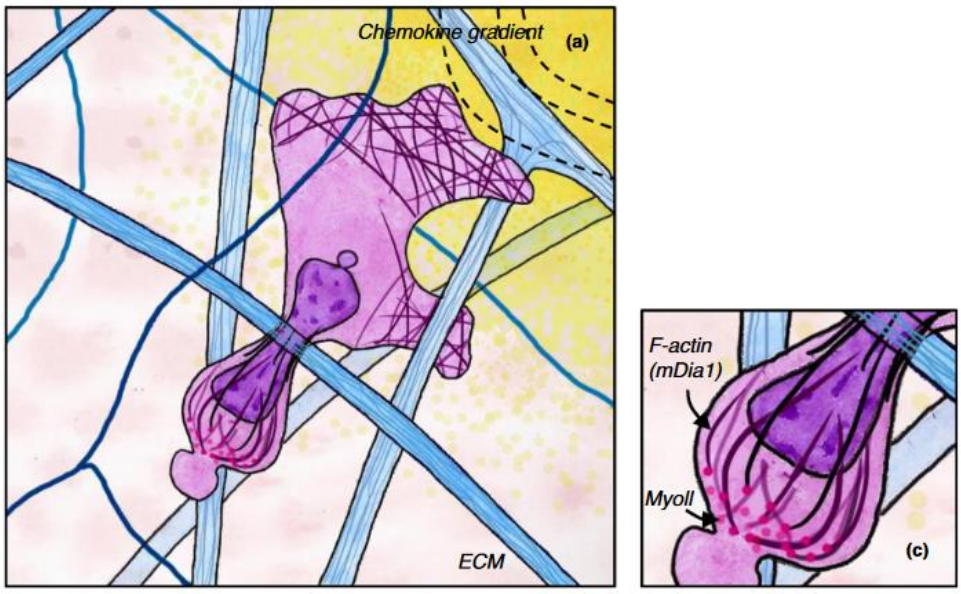

Figure 13: Nuclear deformation in 3D migration

Dendritic cell migration though a collagen extracellular matrix, zoom on actomyosin concentration at the cell rear (adapted from (Vargas et al., 2017))

Efficient migration in dense tissues can therefore employ two avenues: either degradation of the extracellular matrix to loosen the pores and remove the obstacles, for example with metalloproteases, or adapt the cell and nucleus body to the environmental constraints (Wolf *et al.*, 2013). When cells go through micrometric constrictions, and its deformation to cross the constriction is mediated by the assembly of an Arp2/3-mediated actin cap (Thiam *et al.*, 2016). Immune cells rely on a specific actomyosin organization (Vargas *et al.*, 2016; Barbier *et al.*, 2019) which enable a fast migration in dense environment without any degradation. Thus, immune cells are both able to deform their nuclei (Figure 13) and push them through constrictions by using the rear actomyosin-generated pushing force.

Immune cells tend to express low levels of lamin A/C (Röber *et al.*, 1990a, 1990b), and lower levels of lamin A/C make the nucleus more deformable and correlate with increased cancer cells' migratory capability (Bell *et al.*, 2022). This suggests that nuclear mechanical properties may play a role in this process. Consistently with this hypothesis, ectopic overexpression of lamin A/C in neutrophils strongly decreases their migration efficiency when crossing constrictions (Rowat *et al.*, 2013). This indicates that the mechanical properties of the nucleus can be tuned depending on the composition of the lamina and the NE and alter the response to deformation.

C. Nuclear probing of the environment

So far, we have mainly considered the nucleus as a limiting factor to overcome in the context of 3D migration. More and more studies have shown that it is likely to have an active role as well in confined environments. Taking advantage of the microfabricated microchannels mimicking pores of different sizes, a study has shown that cells tend to travel the path of least resistance and that the sampling of pore sizes is performed by the nucleus, which then modulates MTOC activity to orient the cell (Renkawitz *et al.*, 2019). The nucleus can also actively participate to the environment deformation. Immune cells in the circulation are able cross the endothelial barrier to exit the vessels and enter the tissues through a process called Transendothelial Migration (TEM). Activation of the endothelium by inflammatory signals and actin protrusions from the immune cells start to relax the tight junctions between endothelial cells to facilitate the TEM. However, the final steps of actomyosin remodeling in the endothelial cells are triggered by the insertion of the folds of the nuclei of neutrophils and T cells (Barzilai *et al.*, 2017).

These results show that in complex environments, the nucleus can be a hindrance to migration because of its stiffness and size. However, migrating cells can adapt their properties and their behavior by changing their nuclear composition and the level of forces generated by the cytoskeleton. Several studies are also hinting at active roles the nucleus can take in probing and sensing the environment.

CHAPTER 4: MECHANICS AND THE NUCLEUS

Cells can be challenged and deformed by the environment. Stiffening of the extracellular matrix in tumors induces a modification of integrin signaling and can lead to an increased invasive potential (Levental *et al.*, 2009). Migrating immune cells travel in complex environments and tend to follow the path of least resistance, sometimes trumping the chemoattractant gradient (Prentice-Mott *et al.*, 2013; Moreau *et al.*, 2019). This indicates that cells are able to mechanically sense their environment, a process called mechanosensing. As we showed in the previous chapter, the nucleus is mechanically connected to the rest of the cell through the LINC complex, and can be deformed by the environment as much as the cytoplasm. In this chapter, we will discuss both the role of the nucleus in mechanosensing and mechanotransduction, and how the nucleus' own mechanical properties can contribute to this ability.

I. Role of the nucleus in mechanosensing and mechanotransduction

In this part, we will present the mechanisms by which cells are able to sense the mechanical cues in their environment. From there, we will show that nuclei themselves contain mechanosensitive elements in their membranes and their lamina.

A. Evidence for a cellular mechanosensing

As the plasma membrane is the first interface through which the cells interact with the environment, this is where the ability to detect mechanical cues was first investigated. Focal adhesions are a complex macromolecular structure integrating mechanical cues from the extracellular matrix, while cell-cell junctions mediate the interactions with the neighbors. Additionally, mechanosensitive channels have been identified in the plasma membrane, such as Piezo1 (Wu *et al.*, 2017). Force sensing by the integrins and focal adhesions initiates signaling cascades involving small GTPases remodeling the cytoskeleton locally, but also activating cell-wide signaling, such as the MAP kinase pathway and can modulate cell fate on a large scale: apoptosis, migration, proliferation, … (Sun *et al.*, 2016). For instance, cells grown on stiff substrate tend to upregulate the expression of lamin A/C (Swift *et al.*, 2013).

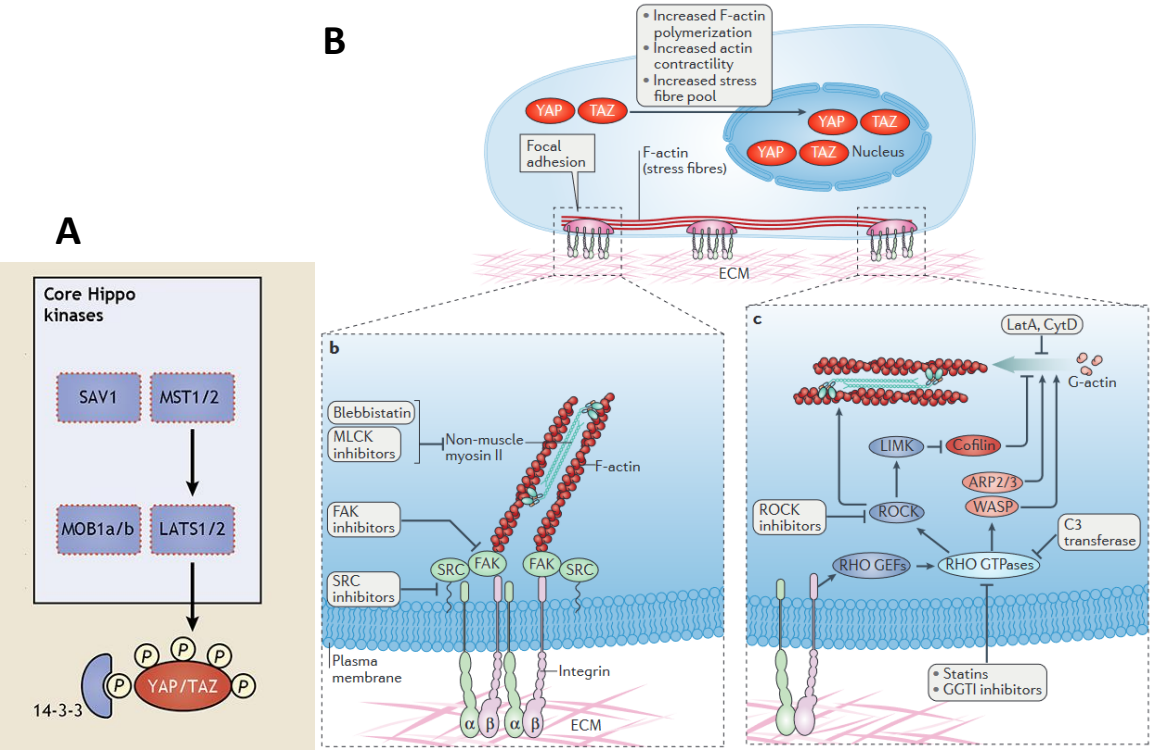

Figure 14: Mechanisms of YAP/TAZ activation

A. Hippo pathway activation (adapted from (Pocaterra et al., 2020)) B.a Mechanical activation b. Increase in actin stress fibers mediated by focal adhesions c. Increase in actin stress fibers mediated by integrins (Panciera et al., 2017)

The key transcription factors mediating the response to mechanical changes at the plasma membrane are Yes-associated protein (YAP) and Transcriptional coactivator with PDZ motif (TAZ), collectively denominated YAP/TAZ. This couple of transcription factors controls the expression of a large number of genes involved in cell growth and cell differentiation. When inactive, the YAP/TAZ complex is phosphorylated and sits in the cytoplasm, while its dephosphorylation induces its activation and nuclear translocation (Panciera *et al.*, 2017). YAP/TAZ was initially known as a target of the Hippo pathway, composed of the Mammalian STE20-like (MST) 1 and 2 kinases, which phosphorylate the Large Tumor Suppressor (LATS) 1 and 2 effector kinases (Figure 14A). In turn, they keep the YAP/TAZ complex in its phosphorylated, inactive state. The signals upstream the Hippo pathway remained poorly understood until YAP/TAZ was identified as a key mechanosensitive transcription factor.

The initial findings identified increased substrate stiffness or spreading area as a trigger for YAP/TAZ activation, independently of the classical Hippo kinases (Dupont *et al.*, 2011). LATS1/2 KD on soft substrates was not enough to force YAP/TAZ activation on soft substrates (Aragona *et al.*, 2013). These findings suggested the existence of a purely mechanical activation pathway (Figure 14B). However, studies

have found that LATS1/2 activity is controlled by F-actin (Wada *et al.*, 2011; Kim *et al.*, 2013), suggesting that mechanical activation of YAP/TAZ and the Hippo pathway may be intertwined. Additionally, Scribble, a polarity effector released from the plasma membrane in partial EMT, is for instance required for MST1 interaction with the LATS1/TAZ complex (Cordenonsi *et al.*, 2011).

The list of mechanical cues resulting in YAP/TAZ activation was later expanded to include increase in 3D matrix stiffness (Aragona *et al.*, 2013), shear stress (Nakajima *et al.*, 2017) and cell stretching (Benham-Pyle *et al.*, 2015). All these activation triggers require a functional actin cytoskeleton, underlining the importance of the mechanical cohesion of the cell.

B. Indications of nuclear mechanosensitivity

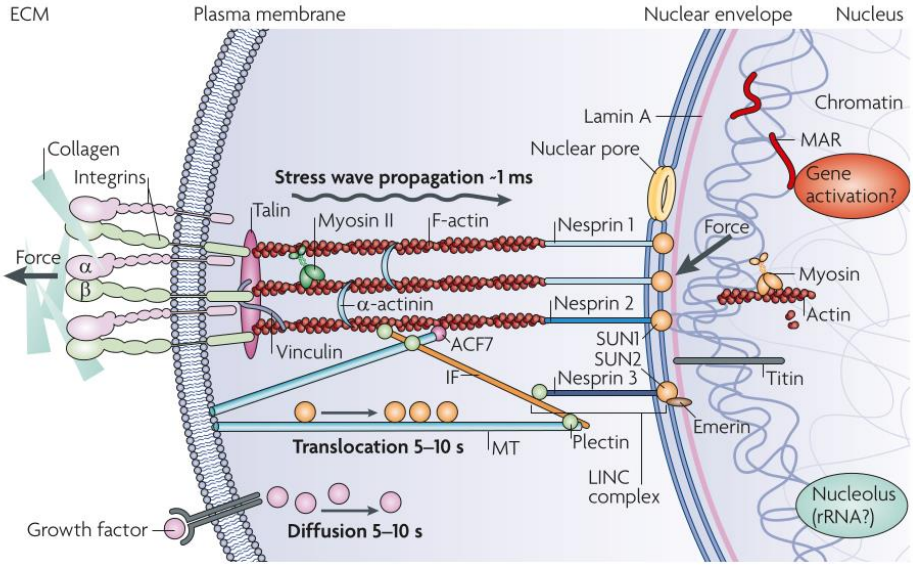

Figure 15: Relative speed of signal transmission from the plasma membrane to the nucleus
Estimation of speed transmission by mechanical, cargo-mediated or diffusive paths (Wang et al., 2009)

The plasma membrane, through focal adhesions, integrins and the actin cortex, is tightly connected to the actin cytoskeleton, and through the LINC complex, with the nucleus as well. It stands to reason that mechanical challenges to the plasma membrane could be directly transmitted to the nucleus and modeling has long suggested that this could be the fastest way of transducing a signal (Figure 17). Indeed, force changes in partial epithelial-to-mesenchymal transition (EMT) are transmitted by the actin cytoskeleton to the LINC complex and mediated by conformational changes in the nesprin head, as was shown by a Förster Resonance Energy Transfer (FRET) strain sensor (Déjardin *et al.*, 2020). Additionally, the nucleus by itself appears able to respond to forces. Pulling directly on nesprin-1 with magnetic

tweezers to mimic a pulling force by actin filaments induces a force-stiffening in isolated nuclei (Guilluy *et al.*, 2014). This behavior is independent on the chromatin condensation but requires a functional LINC complex, an intact lamina and the phosphorylation of emerin.

This suggests that mechanical constraints affecting the plasma membrane could be transduced to the nucleus. YAP/TAZ mechanosignaling was initially thought to involve only the plasma membrane and cytoplasmic sensors, but most of the mechanical cues inducing its activation are likely to be at least partially transmitted to the NE. Indeed, a study showed that YAP import was intrinsically mechanosensitive. While overexpression of LATS1/2 decreased the overall nuclear localization of YAP/TAZ, it remained sensitive to substrate stiffness: YAP was still partially translocating in the nucleus on stiff substrates. This suggested an intrinsically mechanosensitive import mechanism. The authors show a mechanically-induced increase in nuclear import, which can be explained by a NE stretch-dependent opening of the NPC (Elosegui-Artola *et al.*, 2017). This hypothesis is supported by the ability of the NPC to dilate and contract that was highlighted in nutrient starvation and osmotic shock in yeast (Zimmerli *et al.*, 2021).

It remained puzzling to understand how a larger NPC would result in a net import, as the intuitive assumption would be that transport in increased in both directions. This question led the same group to propose a more general framework for mechanosensitive protein import. For a given protein, a balance between its size and passive diffusion characteristics on the one hand, and the strength of its NLS on the other hand, defines whether the nuclear import can be mechanosensitive. A protein whose import is dominated by one or the other will not be sensitive to mechanically-induced NE opening, but the mechano-sensitive import emerges for intermediate sizes and NLS strengths (Andreu *et al.*, 2022).

These works indicate that not only the plasma membrane, but the NPC and the nuclear envelope, could be mechanosensory structures in the cell.

C. Mechanosensitivity of the nuclear envelope

Several pieces of evidence point to the nuclear envelope being able of mechanosensation. This was first identified in the zebra fish, where inflammation triggers cell and nuclear swelling. This is proposed to induce a stretching of the NE and activation of cPLA2, which catalyzes the synthesis of arachidonic acid from lipids in the NE (Enyedi *et al.*, 2016). This observation was confirmed in other systems, and cPLA2 was shown to be activated at a certain deformation threshold under uniaxial confinement, both in the zebra fish and in HeLa cells (Lomakin *et al.*, 2020; Venturini *et al.*, 2020). cPLA2 in turn activates the

actomyosin contractility as a response to confinement. This response occurs in a timescale of minutes after the deformation and does not require any transcription factor activity. What is particularly interesting is that cPLA2 activation and its downstream effect required confinement of the nucleus specifically: applying the same deformation to the cytoplasm did not have any effect (Lomakin *et al.*, 2020). cPLA2 activation upon confinement in dendritic cells has also been shown, in addition to its short-term effect, to induce genome-wide transcriptional changes (Alraies *et al.*, 2022). Similarly to cPLA2, Ataxia-Telangectasia Related (ATR) has been shown to be recruited at the NE upon its deformation (Kumar *et al.*, 2014). It is proposed to mediate a protective effect against nuclear damage in migration (Kidiyoor *et al.*, 2020)

These results confirm that the nuclear surface, envelope and/or lamina, is indeed mechanosensitive. One open question is whether these two signaling pathways interact with one another. cPLA2 activity appears to alter locally the NE lipid composition (Arya *et al.*, 2022). This raises the question whether its activity could be a prerequisite to the NPC opening and the mechanosensitive import of YAP/TAZ described in cells on stiff substrates.

D. Nuclear fragility and nuclear envelope ruptures

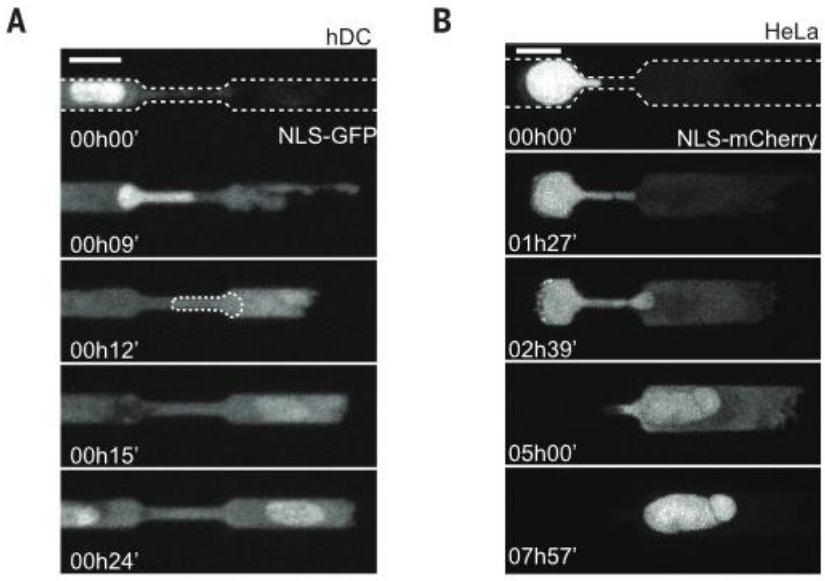

Figure 16: Nuclear envelope ruptures of cells migrating through constrictions
A. Human dendritic cell B. HeLa cell (constriction details: L=15 µm, h=2 µm) (Raab et al., 2016)

Nuclei are able to sense forces and can sustain a certain level of deformation. While a certain amount of force application triggers signaling pathways, too strong deformation can impair NE integrity and lead to NE ruptures, as is illustrated when cells are crossing narrow constrictions (Figure 16).

When dendritic cells or HeLa cells cross small constrictions in microchannels, the NE can detach from the lamina, form a bleb and rupture, exposing the nuclear content to the cytosol. The blebs themselves can contain chromatin, still bound to the bulk of the DNA but forming a herniation (Le Berre *et al.*, 2012; Denais *et al.*, 2016; Raab *et al.*, 2016). The NE rupture is repaired within minutes of the breach, with recruitment of BAF by the exposed DNA (Halfmann *et al.*, 2019) and resealing by Endosomal Sorting Complex Required for Transport (ESCRT) III. Interestingly, NE ruptures can also occur spontaneously at very low level and their frequency is increased in certain cancer cells (Vargas *et al.*, 2012), upon lamin B1 KD (Hatch *et al.*, 2013; Chen *et al.*, 2018), lamin A/C KD to a lower extent (Chen *et al.*, 2018), chromatin decompaction (Stephens *et al.*, 2018) or lipin regulator CTDNEP1 KD (Gunn *et al.*, 2023). Increased nuclear fragility is also observed in cells with laminopathy-associated mutations. Mutations in the *LMNA* gene associated with the Emery-Dreifuss muscular dystrophy (EDMD) induce deformed nuclei and increase the rate of NE ruptures (Earle *et al.*, 2020). Accumulation of progerin, the dominant negative truncated form of lamin A expressed in Hutchinson-Gilford progeria syndrome (HGPS) lacking the CAAX domain and which remains farnesylated, also exhibit increased fragility (De Vos *et al.*, 2011). Conversely, a vimentin cage protects nuclear integrity in migrating mouse embryonic fibroblasts (Patteson *et al.*, 2019), suggesting that the nucleus has an intrinsic fragility.

Sustained cycles of NE ruptures lead to DNA damages, either due to leakage of DNA repair factors (Irianto *et al.*, 2017; Xia *et al.*, 2018) or to DNA contact with cytosolic nucleases, such as TREX1 (Maciejowski *et al.*, 2015; Nader *et al.*, 2021). This can in turn induce senescence in non-transformed cells or promote a partial EMT (Nader *et al.*, 2021). Additionally, while NLS-GFP is quickly reimported into the nucleus following NE resealing (Hatch and Hetzer, 2015; Raab *et al.*, 2016), other proteins remain in the cytoplasm for a long period of time, such as the DNA repair factor 53 binding protein 1 (53BP1) in lamin A/C KD conditions (Xia *et al.*, 2018) or PML (De Vos *et al.*, 2011).

Interestingly, some blebs contain chromatin, called chromatin herniations, which could imply that the underlying lamina is breached as well. Failure of B-type lamin filaments has been observed in isolated *Xenopus laevis* oocyte nuclei under high forces, supporting the hypothesis that mechanical perturbations can indeed disrupt the meshwork (Sapra *et al.*, 2020). Nuclear blebs have been described before in lamin B1 depleted cells (Lammerding *et al.*, 2006), but the lamin A layer appeared intact under the NE (Shimi *et*

al., 2008). Few studies have investigated NE blebs in details and simultaneously analyzed the different lamins as well as the NE and DNA. While NE blebs seem to precede NE rupture in most cases, nuclei from *LMNA*$^{-/-}$, *LMNB1*$^{-/-}$, *LMNB2*$^{-/-}$ triple KO seem to rupture without forming NE blebs at all, while their single KO counterparts bleb and break (Chen *et al.*, 2018).

The origin of the blebs remains unclear. The fact that they are absent in triple KO nuclei suggests that a rigid shell underneath the NE, with anchoring of the membranes on an underlying structure, is required for the emergence of blebs. It has been proposed that the lamin filaments can sustain only a certain degree of curvature, and that bending exceeding their deformability leads to disruption of the meshwork (Pfeifer *et al.*, 2022). This frailty in the lamina could be the initial point of NE detachment and future chromatin herniation. Another study observed that NE blebs in HGPS nuclei occur more frequently at positions where the lamin meshwork is less dense (Funkhouser *et al.*, 2013). Recent, unpublished work has also shown that knocking down LBR led to increased NE blebs and proposes a link with LBR's function in cholesterol synthesis (Waterman lab, unpublished). Overall, NE blebs seem to occur when the lamina is more fragile, whether because of mutations or of mechanical deformation.

II. Mechanics of the nucleus and mechanosensitivity potential

Recent findings have established that the nucleus can act directly as a mechanosensor: cPLA2 has been proposed to insert in the INM upon osmotic shock (Enyedi *et al.*, 2016) or a threshold of mechanical deformation (Lomakin *et al.*, 2020; Venturini *et al.*, 2020). In this chapter, we will focus on understanding how the mechanical properties of the different nuclear components can play a role in nuclear mechanosensing. Additionally, while nuclear integrity in interphase is key to the proper compartmentation of the cell, the nucleus appears to be more fragile than it was initially envisaged. We will detail what are the potential candidates for mechanosensing at the nuclear level, from a molecular and from a physical point of view.

A. Contribution of the lamina

In this part, we will review the evidence indicating the major contribution of the lamina to nuclear mechanics. We will discuss the respective roles of lamin A/C and B in different contexts.

From a physical point of view, the lamina is considered as a thin, rigid, viscoelastic shell. Micropipette aspirations of cells at different stages of differentiation revealed that stem cells have softer nuclei that their differentiated counterparts and that the stiffness increases as the cells differentiate (Pajerowski *et*

al., 2007). This correlates with the lamin A/C expression level and the fact that lamin A/C KD in differentiated cells induced a rheology comparable to the stem cells (Pajerowski *et al.*, 2007). It corroborates previous reports that lamin A/C depletion decreases nuclear stiffness (Lammerding *et al.*, 2004).

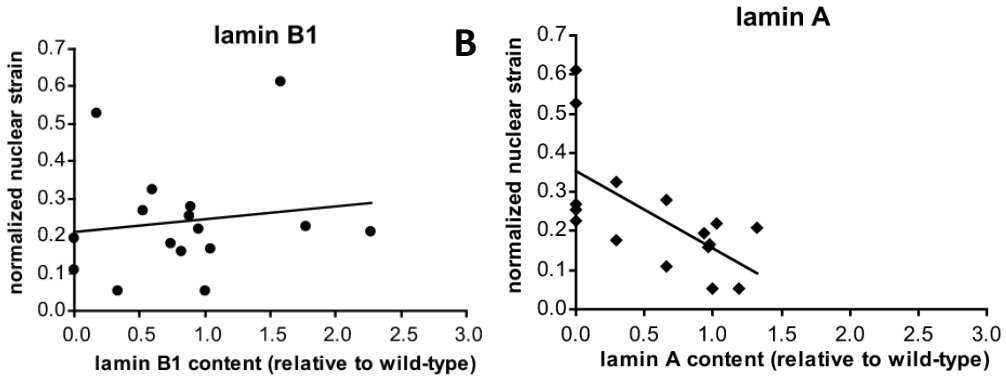

Figure 17: Differential contribution of B- and A-type lamins to nuclear stiffness
(Lammerding et al*., 2006)*
A. Normalized strain as function of the level of lamin B1 B. Normalized strain as function of the level of lamin A

Additionally, the nuclear strain response curves of biaxial deformation of the cells show that lamin A/C (Figure A), rather than lamin B1 or B2 (Figure B), is key in determining the overall mechanical properties of the nucleus (Lammerding *et al.*, 2006). Consistent with this finding, some mutations of lamin A/C observed in EDMD increase the deformation of the nucleus in micropipette aspiration experiments, revealing a decreased stiffness (Earle *et al.*, 2020). On the contrary, HGPS nuclei with progerin display stiffer nuclei (Booth *et al.*, 2015). Surprisingly, a recent study using fibroblasts from autosomal dominant leukodystrophy patients, in which lamin B1 is upregulated because of LMNB1 gene duplication, rigidity of the nucleus was found to be enhanced compared with wild-type cells, suggesting that under specific conditions B-type lamins can also contribute to nuclear stiffness (Ferrera *et al.*, 2014).

Not much is known on single-filament mechanics, as *in vitro* lamina assembly is technically challenging due to the multiple interaction partners. However, AFM probing of B-type lamins in *Xenopus laevis* oocyte nucleus shows that they display a stress-stiffening behavior and, as mentioned in the previous part, that the inter-filaments interactions can break under high forces (Sapra *et al.*, 2020). The recent development of a lamin A/C strain FRET sensor based on a couple of nanobodies directed against lamin A/C joined by a FRET pair gave new insights into the mechanics of the *in vivo* meshwork (Danielsson *et al.*, 2023). Hyperosmotic shock increases the FRET signal, indicating the expected decrease in tension. The lamina in

spread cells appears to be maintained under a steady-state level of tension, as evidenced by the higher FRET signal upon disruption of the LINC complex and inhibition of actomyosin contractility. Confinement of spread cells with a gel cushion decreases the FRET signal, indicating an increased strain in the meshwork.

Thus, lamin A/C appears to be the dominant component of the mechanical properties of the lamina, although lamin B1 may also contribute to stiffness. Evidence indicate that lamin A/C meshwork can be tensed, suggesting that it could be a component of nuclear mechanosensing.

B. Contribution of the chromatin

The chromatin itself must not be discounted as a mechanical player. From a physical point of view, the mechanical characteristics of the chromatin are still a matter of debate. The nucleoplasm itself is a crowded viscous fluid. Chromatin is understood as a complex viscoelastic material (De Vries *et al.*, 2007; Stephens *et al.*, 2017; Keizer *et al.*, 2022). An inherent difficulty to solving the question is the plasticity of the linear 10 nm chromatin fiber, which adopts different conformations depending on the salt concentration, rendering its *in vitro* study complex (Hansen *et al.*, 2021). Many reports account for a fluid-like behavior of the chromatin, assessed by FRAP experiments in *in vitro* reconstituted chromatin (Gibson *et al.*, 2019, 2023), by imaging of nucleosome dynamics (Nozaki *et al.*, 2017) or by direct manipulation of loci using magnetic particles (Keizer *et al.*, 2022). This last study is the only one preforming direct manipulation of the chromatin in live cells. It shows that a Rouse polymer model, *i.e.* a polymer with thermally-diffusing monomers in a viscous medium, connected by elastic bonds and without crosslinking, is enough to describe the behavior observed in response to the manipulation. On the other hand, there has been evidence for a solid-like behavior of local chromatin domains, by showing the absence of fluorescence recovery upon FRAP (Strickfaden *et al.*, 2020). The different results may be reconciled by understanding which length and time scales are being considered (Zidovska, 2020). One can imagine small, solid-like domains that can interact dynamically with one another and assemble into liquid-like compartments, as LLPS was shown to be important in intranuclear organization (Gibson *et al.*, 2019; Wang *et al.*, 2019; Lafontaine *et al.*, 2021; Al Jord *et al.*, 2022).

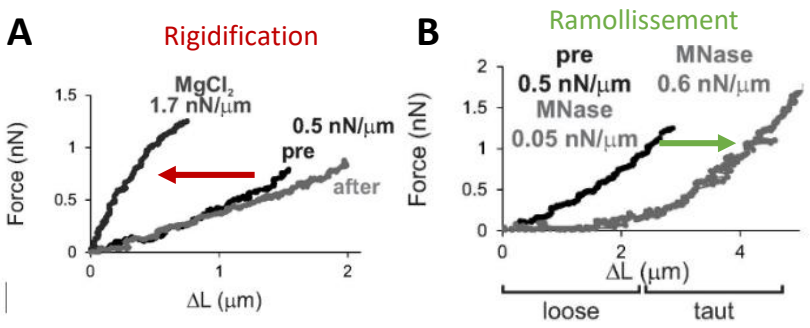

Figure 18: Chromatin contribution to nuclear mechanics
(Stephens *et al.*, 2017)
A. Augmentation de la condensation de la chromatine par traitement au $MgCl_2$ B. Réduction de la rigidité de la chromatine par digestion par micronucléase

While the chromatin is much softer than the lamina meshwork, the importance of its compaction state is not to be discounted.Increasing chromatin condensation is indeed enough to rescue the abnormal nuclear shapes and the number of blebs in lamin B1 deficient mouse embryonic fibroblasts HGPS patient cells (Stephens *et al.*, 2018).

C. Interplay between lamina and chromatin

Consistent with these results, lamina and chromatin appear to control nuclear mechanical properties on different scales. Digestion or decondensation of the chromatin decreases the nucleus spring constant when measured for small deformations, while depletion of lamin A/C but not lamin B1 leads to a smaller nucleus spring constant in large deformations. Conversely, lamin A/C overexpression appears to increase the nucleus spring constant in response to both small and large deformations (Stephens *et al.*, 2017). Lamina and chromatin are also coupled through LAD, and altering the chromatin state can in turn affect the lamina meshwork. Additionally, the drug treatments to alter chromatin compaction are incubated for over 24 hours, which could significantly alter overall protein levels.

Taking advantage of the *in situ* measure of the strain in the lamina with the FRET sensor, a study shows that chromatin decondensation, obtained here after 4 hours of drug treatment, is enough to induce an increase in the FRET signal, indicating a lower tension level (Danielsson *et al.*, 2023). Since increased condensation did not significantly alter the tension, we can hypothesize that the heterochromatin at the LADs is playing the role of force transmitter in this system. Additionally, untethering the chromatin from the INM in *S. pombe* softens nuclei (Schreiner *et al.*, 2015). While INM tethers to chromatin in yeast are

thought to play the functional role taken by the lamina in metazoan cells, this suggests that the INM – chromatin coupling may play a role in the mechanical properties of the nucleus as well.

D. Contribution of the nuclear membranes

Finally, the nuclear membranes themselves could be mechanosensitive, as is suggested by the activation of cPLA2 at the NE in hypo-osmotic shock and confinement (Enyedi *et al.*, 2016; Lomakin *et al.*, 2020; Venturini *et al.*, 2020). As the ONM is in continuity with the INM on one side and the ER on the other side, which constitute a nearly infinite membrane reservoir, it remains a matter of controversy whether the NE, INM or ONM, can be tensed at all. Lipids can laterally diffuse and the NPC have not been formally identified as a lateral diffusion barrier. However, as was discussed in Chapter 1, the asymmetrical lipid composition of INM and ONM suggests that it could be the case. Under the assumption that the NPC can indeed constitute a diffusion barrier for lipids from the ONM, the INM would not be in continuity with the ER from a diffusion point of view, and could be expected to have the ability to increase its tension. The nucleoplasmic reticulum and NE folds would be the only accessible membrane reservoirs under this assumption. Additionally, lateral lipid diffusion can also generate friction, which could in turn cause membrane tension. This could be particularly relevant at the level of the NPC.

Of note, vesicles are known to tolerate tensions of 1 – 10 mN/m before breaking (Evans *et al.*, 2003), which would be consistent with the fact that strong deformation triggers NE rupture (Denais *et al.*, 2016; Raab *et al.*, 2016; Nader *et al.*, 2021). A Fluorescence Lifetime Imaging Microscopy (FLIM) probe was developed to measure lipid packing and membrane tension, where the lifetime increases with membrane tension (Colom *et al.*, 2018). While it was initially developed for the plasma membrane, a 24 hour-long incubation time enabled the visualization of the NE and showed that after 30 min of continuous, cyclic stretching, the lifetime decreased, indicating of a lower NE tension (Nava *et al.*, 2020). While this appears counter-intuitive, as we would expect a higher tension upon stretching, the deformation is coupled to peripheral heterochromatin decondensation, which in turn affects NE tension. While the resolution is not sufficient to determine whether the tension increased in the INM, the ONM or both, it shows that the nuclear membranes are capable of mechano-adaptation and that the tension level can be modified. The probe toolbox has been expanded to target several organelles (Assies *et al.*, 2021) and future tools will hopefully be able to address this question. Additionally, the fact that the NE is folded in non-adherent conditions, opens up under confinement (Lomakin *et al.*, 2020; Venturini *et al.*, 2020) and can even break under strong confinement supports the tension hypothesis.

Finally, the INM is tightly linked to the underlying lamina meshwork and the chromatin, which may make it difficult to tease apart the respective contributions of the different layers. The coupling itself appears critical to the mechanical properties of the nucleus, as mouse embryonic fibroblasts devoid of emerin display lower mechanotransduction capabilities (Lammerding *et al.*, 2005).

It remains an open question which element gets tensed in the sandwiched multilayered NE is still unclear, depending on the extent and timescale of the deformation and whether tension in the lamina alters tension in the INM at all.

THESIS OBJECTIVES

As described in the introduction of this thesis, the nucleus has emerged in recent years as a key component of cellular mechanostransduction as well as an intrinsically mechanosensitive organelle. Deformation of the nucleus can activate different signaling pathways as response to the encountered mechanical stresses and, in extreme cases, to loss of nuclear integrity.

This project started initially from the role of SUN proteins in HIV infection. We hypothesized that mechanics could play a role in the nuclear steps of HIV replication cycle and sought to apply mechanical sresses during infection. The exploration of this question is presented in Appendix A, and, as part of a collaboration, gave rise to a publication (Bhargava *et al.*, 2021) presented in Appendix B.

Over the course of the investigation of this hypothesis, we realized little was known about the mechanical states of the nucleus and the nuclear envelope at different levels of deformation. In particular, we made the observation that in round cells, in absence of any mechanical stress, the nuclei displayed large folds that disappeared upon deformation. This prompted the main question presented in the Results: **How does the nuclear surface contribute to the nuclear mechanical properties upon deformation?**

In collaboration with Romain Rollin, a physicist, we aim to propose a physical model to explain the origin of the nuclear envelope folds and understand their implication for the evolution of nuclear envelope tension when the nucleus is deformed. Adapting the nested pump-and-leak model for nuclear volume (Rollin *et al.*, 2023), we test its predictions for the volume of the nucleus under mechanical constraints.

Over the course of my PhD, I additionally participated in the writing of two reviews, an article commentary and contributed to three research articles, detailed in the publication list in Appendix C.

MATERIAL AND METHODS

I. Cell culture

HeLa Kyoto cells with various markers were cultured in Dulbecco's Modified Eagle Medium enriched with Glutamax (DMEM/Glutamax, Life Technologies) supplemented with 10% v/v fetal bovine serum and 1% v/v penicillin-streptomycin (Gibco), called complete DMEM. RPE1 cells were cultured in DMEM/F12 (Life Technologies) supplemented with 10% v/v fetal bovine serum and 1% v/v penicillin-streptomycin. Both these cell lines were maintained at 37°C with 5% CO_2. MDA-MB-231 cells were cultured in Leibowitz-15 medium (L-15, Sigma Aldrich) supplemented with 2 mM glutamine (Gibco), 15% v/v horse bovine serum and 1% v/v penicillin-streptomycin. They were maintained at 37°C with 1% CO_2.

Cells are detached with Tryple Express (Gibco) prior to experiments.

II. Cloning

The lentivector plasmid pTRIP-SFFV-EGFP-LAP2b coding for the tagged nuclear envelope marker EGFP-LAP2b was obtained by cloning the LAP2b sequence from pN2-EGFP-LAP2b (Addgene) into pTRIP-SFFV-EGFP (from Nicolas Manel's lab). Both plasmids were digested with the restriction enzymes BsrgI (New England Biolabs) and KpnI (New England Biolabs) in CutSmart buffer following manufacturer recommendations. Fragments were migrated on a 1% agarose gel and purified, then ligated using the T4 DNA ligase kit.

III. Transduction for establishment of stable cell lines

Stable cell lines were established by transduction of lentiviral vectors. Lentiviral particles are produced in HEK293FT. HEK293FT are plated in DMEM at 0.8 M / well in a 6-well plate and transfected using the TransIT reagent (Mirrus) with 0.4 µg pCMV-VSVG, 1 µg psPax2 and 1.6 µg of the lentiviral vector of interest. The next day, the medium is changed to 3 mL of the medium of the target cells. The day after, is then added on target cells at the ratio of 2:1 v/v to cell medium, with protamine at a final concentration of 1 µg/mL. The medium is changed the next day.

IV. Lamin A/C knock down

The transfection follows an adapted version of the protocol described in (Sieprath *et al.*, 2015). Cells are plated at 0.45 M / well in a 6-well plate. They are transduced using the RNAiMAX reagent (Life Technologies) and non-targeting siRNA non-targeting (Horizon Discovery) or targeting *LMNA* (SMARTpool of 4 siRNA, Horizon Discovery), according to the manufacturer's specifications. The scheme includes two rounds of transfection separated by 48 hours, with a change of medium 24 hours after each transfection. The experiments are performed 48 or 72 hours after the second transfection.

V. Western blot

Protein levels were controlled by Western blot. Cells are harvested by trypsinization and counted to normalize future protein loading by cell number. Typically, 0.5 to 1 million cells were lysed. Cells are washed once in cold PBS and either frozen as dry pellets for later lysis, or directly lysed in RIPA lysis buffer with protease and phosphatase inhibitors. Lysates are then centrifuged at 11 000 g and the supernatant is transferred to a clean tube. It is then either frozen or used directly. Laemmli 2x is added and the lysates are run on commercial SDS-PAGE 4-12% gels (BioRad) at 90V for 15 min and 120V for 1-1.5 hr. Proteins are transferred on a nitrocellulose membrane using a semi-dry transfer protocol (Invitrogen). Membrane saturation is performed for 1 hr with PBS + Tween 0.1% + 4% BSA. Washes are done with PBS + Tween 0.1%. All antibodies are diluted in PBS + Tween 0.1% + 4% BSA. Primary antibodies are typically used at 1:200 dilutions and are incubated overnight at 4°C. Secondary antibodies are coupled to the Horseradish Peroxydase. They are typically diluted at 1:1000 or 1:5000 (GAPDH) and are incubated for 1 hr at room temperature. Membranes are revealed using the SuperSignal West PicoPLUS reagents (Invitrogen) following manufacturer's recommendations.

VI. Drugs treatments

When cells are treated with drugs, they are pre-incubated with for 20 min prior to the experiment. Latrunculin A (Sigma) is resuspended in DMSO and used at 2 µM unless specified otherwise. Y27632 is resuspended in water and used at 10 µM unless specified otherwise. Nocodazole is resuspended in DMSO and used at 10 µM unless specified otherwise.

VII. Confinement devices

A. Static 6-well plate confiner

The 6-well confiner is a device that was previously described in (Le Berre *et al.*, 2014) and is presented in Figure 19A. Using a glass-bottom 6-well plate (MatTek), it allows to confine cells at a defined height in each well. It relies on a biocompatible polymer, polydimethylsilane (PDMS), that can be prepared to obtain different stiffness depending on the ratio between the polymer (RTV, A) and the reticulating agent (RTV, B). The device consists of pistons attached to the plate's lid, at the edge of which we position coverslips with a microfabricated PDMS layer with micropillars of controlled height (Figure 17A).

The pistons are cast in soft PDMS (ratio 37.5:1 w/w) in metallic mold and cured overnight at 65°C. They are deformable and will absorb the excess of force when the user puts the lid on the plate. The 12 mm diameter glass #1 coverslips (VWR) are coated with a microfabricated layer of rigid PDMS (ratio 5:1 w/w). These micropillars are rigid enough to be resistant to deformation even during the confinement and enable to control the confinement height (Figure 17B). The PDMS is poured on a SU8 wafer obtained by photolithography with the array of micropillars of the desired height. It is cured for 20 min at 95°C.

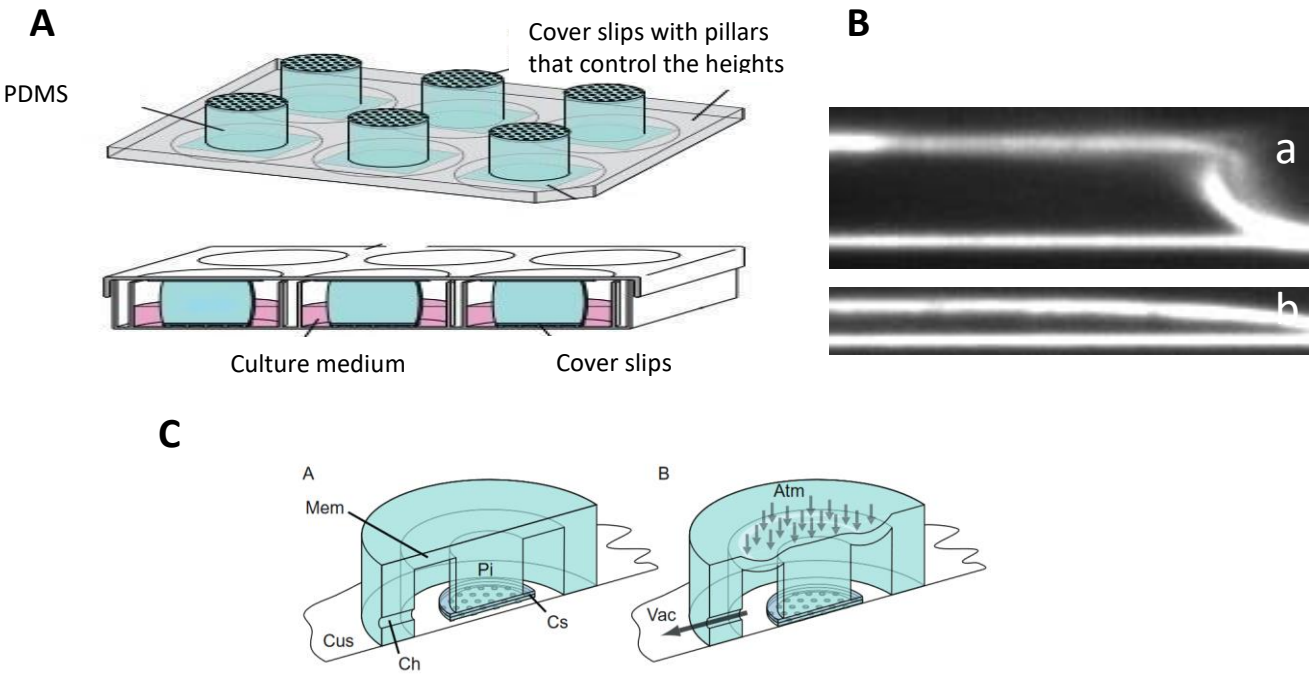

Figure 19: PDMS-based microfabricated confinement devices

A. 6-well plate static confinement device (top: lid, bottom: confinement on the plate) B. Orthogonal view of the confinement chamber (a. 10 µm, b 3 µm)C. Dynamic confinement device (Mem: membrane, Cus: culture substrate, Ch: connection hole, Pi: piston, Cs: coverslip, Vac: vacuum, Atm: atmospheric pressure) (A: non confined, B: lowered, confinement)

The PDMS surface on the coverslip and the glass bottom of the plate can then be treated to alter their properties. The PDMS is plasma-activated using a plasma cleaner system and incubated with poly-L-Lysine-g-Polyethylene-glycol (pLL-PEG, SuSoS) at 0.1 mg/mL in HEPES at pH 7.4 for 1 hour to prevent cells from adhering. Coverslips are then incubated for at least 1 hour in the medium used for an experiment in the absence of drug treatment and at least 4 hours with drug treatment to equilibrate medium and PDMs. As most experiments were conducted for short durations, the glass bottom of the plate was left untreated, as the experiment time was shorter than spreading time. In the case of the fast-spreading RPE1 cells, the glass bottom was plasma-activated and incubated with poly-L-Lysine (pLL) at 1 mg/mL in HEPES at pH 7.4 for 1 hour to prevent cells from attaching and spreading.

B. Dynamic confiner

The dynamic confiner device is also described in (Le Berre *et al.*, 2014). It enables following the same cells prior to and during confinement, as well as after its release, in a glass-bottom 35 mm dish (Fluorodish). The device is based on a device molded in rigid PDMS (ratio 10:1) to which a coverslip similar to what has been described for the static confiner can be affixed. Upon connection of the device to a pump, the negative pressure will lower the roof of the device and thus bring down the micropillars to the glass bottom dish, imposing the desired confinement height (Figure 19C).

In this system, cells need to be attached to the dish to prevent them from being chased when the micropillars are lowered. The glass bottom is therefore treated with pLL at 1 mg/mL in HEPES at pH 7.4 to enable cell attachment without spreading.

Dynamic confiner experiments were performed by Damien Cuvelier and the analysis by myself.

VIII. Micropatterns

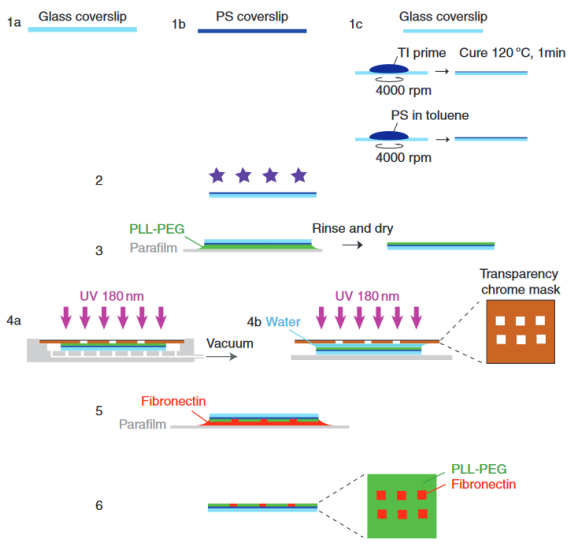

Figure 20: Micropatterning protocol

1a: starting glass coverslip, 2: plasma-activation, 3: pLL-PEG coating, 4b: UV irradiation on water layer, 5: fibronectin coating, 6: micropatterned coverslip

Micropatterns were prepared on glass coverslips following the protocol described in (Azioune *et al.*, 2010), following the protocol for glass coverslips in figure 20. Glass coverslips were mounted on bottom-less 35 mm dishes.

Cells were plated at 0.5 M/mL and let spread overnight. Imaging was performed the next day on a Leica DMI8 microscope, equipped with CSU-X1 Yokogawa spinning disk module. The acquisition was realized with a 40x oil objective (N.A. 1.30) and collected by the Hamamatsu Orca flash 4.0 camera.

Micropatterns experiments were realized by Henri Popard and analyzed by myself.

IX. Atomic Force Microscopy (AFM)

The 35 mm glass-bottom dishes were mounted in a dish heater (JPK Instruments) and kept at 37 °C under an inverted light microscope (Axio Observer.Z1; Zeiss) equipped with a confocal microscope unit (LSM 700; Zeiss) and the atomic force microscope (AFM) head (CellHesion 200; JPK Instruments). Custom-made, wedge cantilevers enable to confine and probe an entire cell, as describe in (Fischer-Friedrich *et al.*, 2014) (Figure 21).

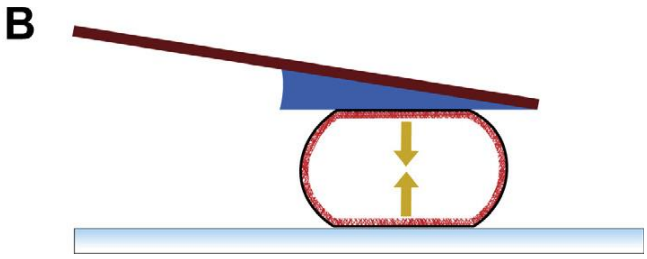

Figure 21: Wedge cantilever
(Fischer-Friedrich *et al.*, 2014)

These focused ion beam (FIB)-sculpted, flat silicon microcantilevers were processed and calibrated as described in (Cattin *et al.*, 2015). The microcantilevers were fixed on a standard JPK glass block and mounted in the AFM head. They were calibrated each time they were being mounted. The confinements were typically done by programming preset target heights and the cantilever was lowered at a speed of 0.5 µm/s. Images are acquired with a 60x water objective.

For the stepwise confinement with target heights 20, 12, 8, 6, 5, 4 and 3 µm, images were acquired after relaxation of the force signal. Z stacks were acquired at 20 and 12 µm and the middle plane was acquired for the other heights.

AFM experiments were performed by Michele Nava (ETH Zürich) and analyzed by myself and Romain Rollin.

X. Volume calculation

Images are acquired on a Leica DMI8 microscope, equipped with CSU-X1 Yokogawa spinning disk module. The acquisition was realized with a 63x oil objective (N.A. 1.40) and collected by the Hamamatsu Orca flash 4.0 camera.

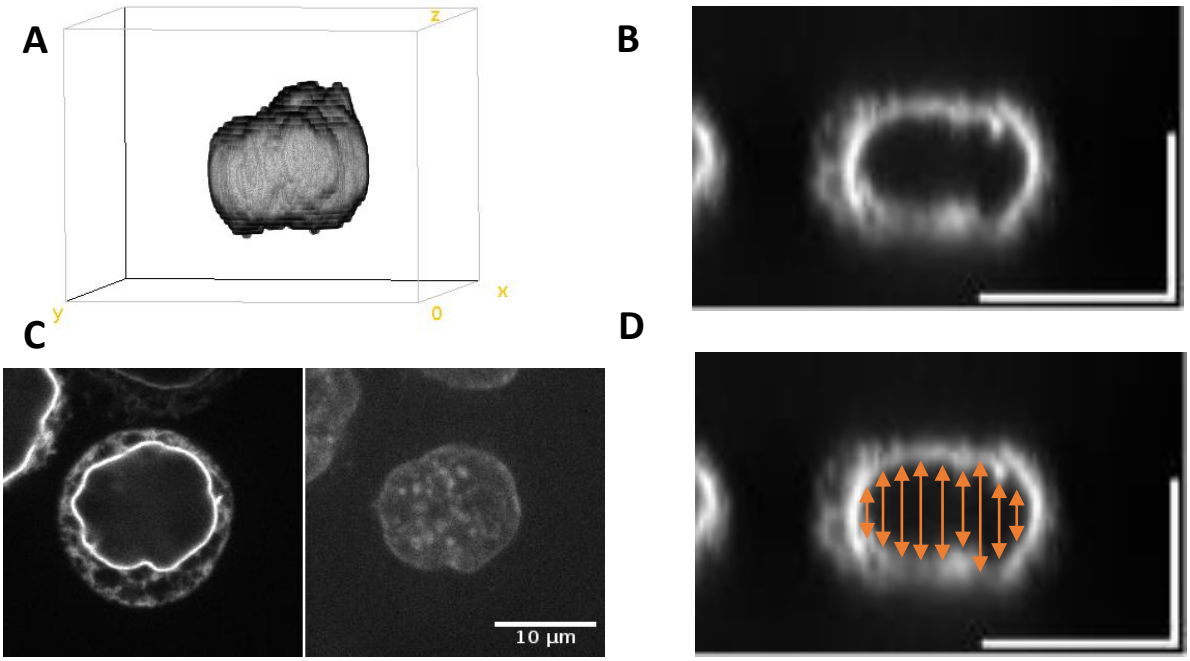

Figure 22: Image analysis for volume calculation

Confinement height: 8 µm A. 3D view of the nucleus (based on Hoechst staining) B. Orthogonal view of EGFP-LAP2b labeling (scale bar: 10 µm) C. Middle plane view of the nucleus (left: EGFP-LAP2b, right: Hoechst) D. Average height calculation

The method used to calculate the volume of the nucleus requires nuclear envelope and chromatin staining in confocal microscopy. Z stacks of both chromatin and nuclear envelope are acquired with a Z step of 0.4 µm or lower. For the cell lines considered in this work, a nucleus confined at 8 µm or below is flattened from its resting approximately spherical shape to a large cylinder (Figure 22A and B). We take advantage of this shape to estimate the volume by multiplying the projected area of the nucleus in the middle plane by the average height of the nucleus. The projected area is obtained by classical thresholding on the Hoechst signal in the middle plane (Figure 22C). The average height is obtained from a resliced orthogonal view of the nuclear envelope labeling. A homemade python script detects the position of the nuclear envelope and measures the distance between top and bottom 2 pixels by 2 pixels. It uses the derivative of the pixel intensity to position intensity peaks. An average value is thus computed for the cell (Figure 22D). It allows to take into account the curvature and the potential shape irregularities of the nuclear envelope. The confinement height is obtained by a similar method, on a portion where the top and bottom NE are parallel.

XI. Nuclear envelope fluctuations

Movies of one plane every 250 ms are acquired with a 200 ms exposure at 3-5% laser power on a Leica DMI8 microscope, equipped with CSU-X1 Yokogawa spinning disk module. The acquisition was realized with a 63x oil objective (N.A. 1.40) and collected by the Hamamatsu Orca flash 4.0 camera. The images are corrected for bleaching using the Fiji plugin Bleach Correction with the Single Ratio method. Single cells are then individualized and registered with the Fiji plugin MultiStackReg (Thevenaz *et al.*, 1998), with the Rigid Body method that corrects for both translation and rotation. On each individual cell, 4 lines were drawn across the nuclear envelope and resliced over time to obtain kymographs of the nuclear envelop at these positions. The NE position at each timepoint is determined by fitting a parabola on an 8-pixel stretch centered on the maximal intensity and taking the abscissa of the parabola peak. The amplitude of fluctuations is calculated as the difference between the 9th and 1st deciles (Figure 23)

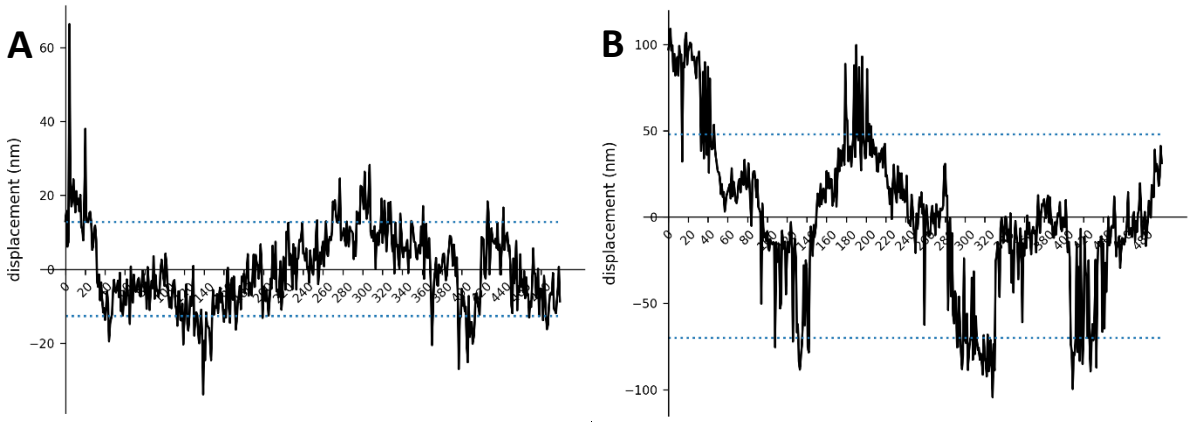

Figure 23: Examples of nuclear envelope trajectories

XII. Image analysis

A. Nuclear shape

All the measures and calculations detailed below are determined from binary images obtained from manually-controlled threshold on the NE labeling.

B. Elliptic Fourier Coefficients ratio

Initially, we started by using the classical shape descriptors provided by Fiji, such as circularity, solidity and roundness. However, the dynamic range of these measures is quite narrow and did not fully translate into numbers the shape changes we observe. Pr. Tanmay Lele and his student kindly provided the MATLAB

script used in (Tamashunas *et al.*, 2020), that implements the calculation of the Elliptic Fourier Coefficients (EFC) first described in (Lammerding *et al.*, 2006), and that we adapted. Briefly, the method relies on fitting successive Fourier ellipses to approximate the shape of the object. The EFC ratio is defined as a ratio of the contribution of the first harmonic compared to all the others:

$$EFCratio = \frac{major\ axis_1 + minor\ axis_1}{\sum_{i=2}^{N}(major\ axis_i + minor\ axis_i)}$$

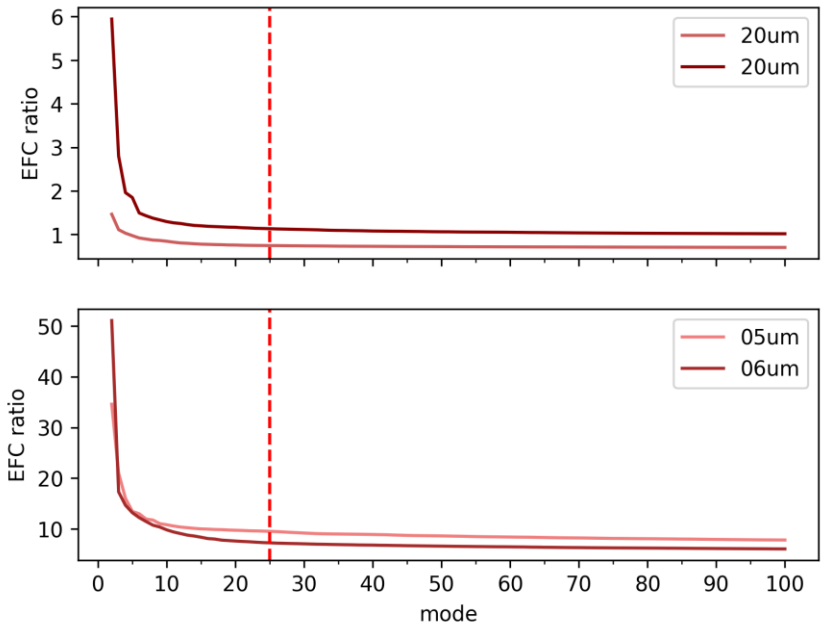

Figure 24: Choice of number of harmonics for EFC ratio calculation
Red line: N=25

An arbitrary number of harmonics N, typically the smallest that enables a good Fourier fit to the shapes, is chosen (N=25 in (Lammerding *et al.*, 2006) and N=15 in (Tamashunas *et al.*, 2020). In order to define the number of harmonics to use, we manually compared the fit quality for several values of N. For very round nuclei, a few harmonics are enough to approximate the shape (Figure 24), while the more folded nuclei required more. 15 harmonics as used in Tamashunas *et al*. were insufficient in our case, while 25 harmonics appeared to fit the shapes relatively well. We used a more systematic approach to define unique value of N by plotting the EFC ratio against a range of values for N for the same test nuclei. We found that the EFC ratio reaches a stable value very quickly for very folded nuclei, even when the fits is not yet good, while it seems to keep decreasing slightly if we keep increasing N for very round nuclei. We settled for N=25, as it was a good compromise between the fitting quality and the stability of the measure.

C. Curvature and distance from convex hull

Curvature and distance from convex hull are calculated using a custom Python script. The contour is obtained from binary images thanks to the contour detection function of the Python OpenCV library. From the regularly spaced contour, we calculate the Menger curvature for each point, using and adapting the library developed in (Marciniak *et al.*, 2021). The Menger curvature is calculated by fitting a circle going through 3 points: the central point and one on each side, at a distance that is adjusted depending on the pixel size. We then plot it against the curvilinear abscissa, raw or normalized to 100 for comparison with other cells.

In order to assess the depths of the folds on the contour, we determine the distance of each point on the contour to the convex hull of the nucleus mask. The convex hull and distances are obtained using the Convex Hull and Distance Map functions in Fiji. Further processing and plotting are done by a homemade Python script. For now, the distance to the edge is calculated as a number of pixels. A future analysis pipeline would refine this to give a more precise measure of the distance.

RESULTS

CHAPTER 1: CHARACTERISTICS OF NUCLEAR ENVELOPE FOLDS

Observations in a variety of contexts have shown that far from the smooth, ovoid shape that nuclei adopt in 2D culture *in vitro*, nuclei *in vivo* can exhibit irregular shapes with highly folded NE. In this chapter, we are detailing *in vivo* and *in vitro* contexts where NE folds have been observed, from embryonic development to spreading and mechanical deformation.

I. Nuclear envelope folds *in vivo* in mouse embryos

During early mouse embryonic development, the fertilized egg divides and form first a sphere of proliferating cells. As part of the developmental process, some cells start to actively pump fluid into the interstitial space, which leads to the formation of a fluid-filled cavity called the blastocoel. On one side, it is delimited by a single layer of cells, while on the other, an internal mass of cells is developing. Cells exhibit very different shapes depending on their position relative to the blastocoel. Cells on the embryo surface are thin and have a large area, whereas cells inside the embryonic mass are more compact and rounded. Staining of lamin A/C and lamin B1 (Figure 25A) reveals that these different cell shapes are paralleled by differences in nuclear shape.

The nuclei at the surface are smooth and flat (Figure 25B.d), in a shape reminiscent of what nuclei of adherent cells cultured in dishes can look like. On the contrary, nuclei in the mass of the embryo display wrinkled nuclei with large NE folds. This is readily apparent on the 3D projection (Figure 25A) and can be seen as well on single slices. Nuclei can exhibit wide folds (Figure 25B.a, b and c, green arrows) or deep inwards invaginations (Figure 25B.a and b, yellow arrows). Qualitatively, nuclear shapes correlate with cellular shapes, which themselves are a consequence of their topological and mechanical environment.

These images provide evidence that NE shapes in tissues are highly diverse. They can be visualized in certain 2D slices but actually occur in 3D. While 3D segmentation of nuclei based on DAPI staining has greatly improved over the past few years, a good 3D, and even 2D, detection of folds can be challenging. Irregular shapes such as the invaginations are not easily recognized by current Artificial Intelligence (AI) based software. We are currently working on 3D NE segmentation methods to capture the folds in an automated manner and be able to quantify the shape variability.

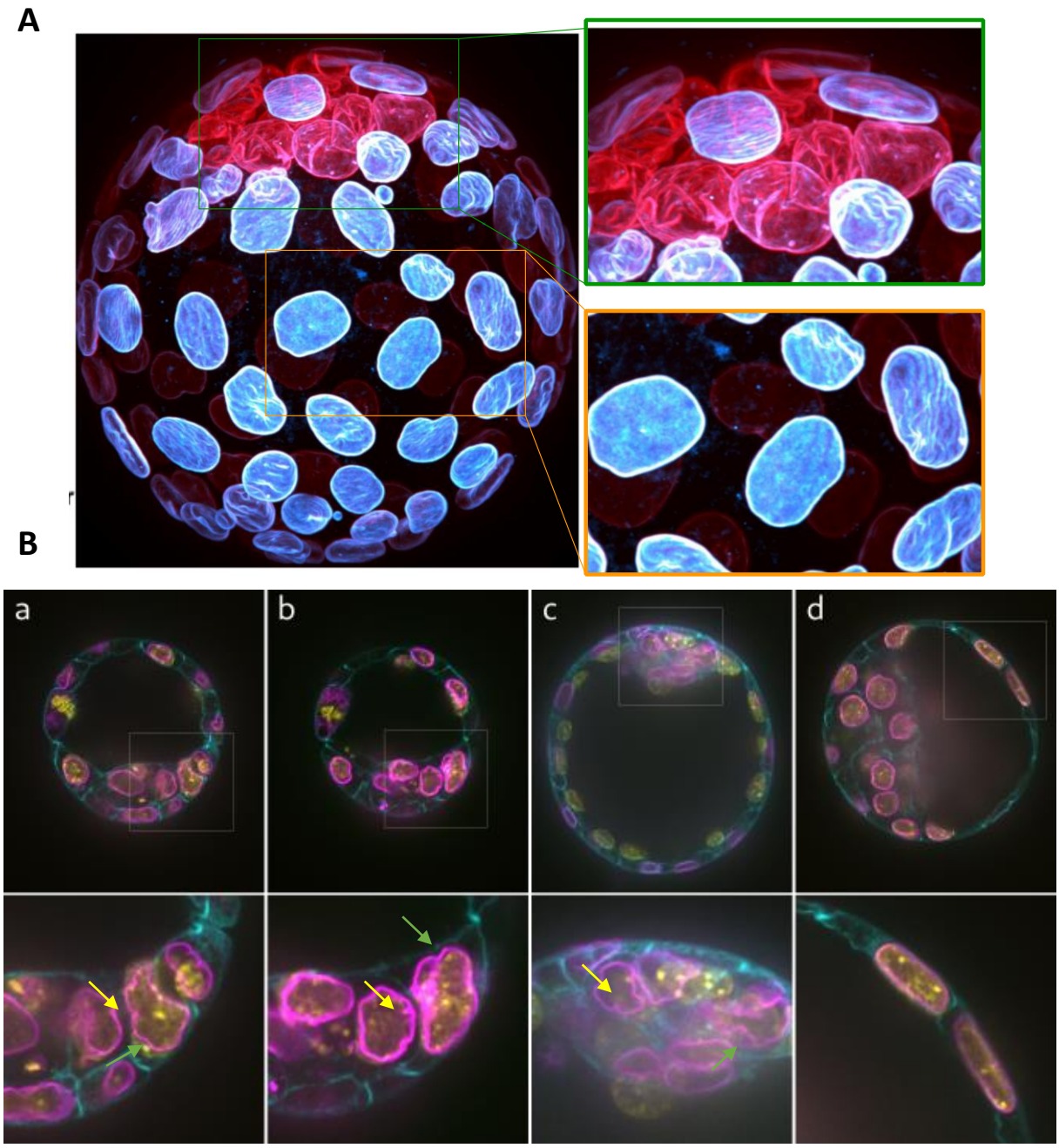

Figure 25: Heterogeneity of cellular and nuclear shape in mouse embryo
Courtesy of Jean-Léon Maître (Institut Curie)
A. 3D reconstruction of a mouse embryo (blue: lamin A/C, red: lamin B1)
B. Slices of mouse embryo (a and b: 2 planes from embryo1, c: embryo2, d: embryo3) (yellow: DAPI, cyan: phalloidin, magenta: lamin B1)

II. Nuclear envelope folds *in vitro* by modulating the spreading area

We hypothesized that the state of the nucleus is associated to the overall shape of the cell. We wanted to reproduce *in vitro* the differences between the large, flat cells of the embryo surface, and the more ovoid cells of the interior. We decided to modulate the cell spreading area with micropatterns of diameters of 30, 20 and 10 µm (Figure 26A).

On micropatterns of 30 µm diameter, the nuclei are relatively flat and smooth. Decreasing the spreading area is associated with higher nuclei and increases the appearance of large invaginations

We explored several quantifications of shape irregularity. The EFC ratio (defined in Material and Methods, XII.B.) is calculated using a manual thresholding of the NE labeling, in order to capture the shape as precisely as possible. A low EFC ratio value indicates an irregular shape, where the weight of the first mode of the elliptic Fourier decomposition is low compared to later modes (Tamashunas *et al.*, 2020). On the contrary, a high EFC ratio indicates that the first mode accounts for a large part of the shape (Figure 26B). The values at 10 µm and 20 µm diameters are very similar and while there is a trend towards a higher EFC ratio value for cells on 30 µm patterns, the difference is not significant (Figure 26C). This metric, which captures well the overall change in nuclear shape compared to a sphere, is thus not able to detect well nuclear envelop folds.

Using the same NE-based contour detection, we then introduced two metrics to study the folds themselves, still based on 2D slices – we have not yet developed methods for 3D analysis of the nuclear shape (a first difficulty being to reconstruct the nuclear envelop in 3D with a good detection of the folds). We measured on each point of the contour the Menger curvature (defined in Material and Methods XII.C), which varies between -1 and 1 pixel^{-1}, with negative values for concavity and positive values for convexity (Figure 26D). and the distance of the contour to its convex hull (Figure 26E).

Figure 26: Increasing the spreading area correlates with an opening of the folds

N=1, n=66, 63, 13 for 10, 20 and 30 µm, statistical test: Kruskal-Wallis (: p-value<0.05, **: <0.005, non-significant if nothing is specified)*

A. Representative images of cells on patterns of different diameters B. EFC ratio values on binary masks C. EFC ratio by pattern diameter (median + SD) (Kruskal-Wallis test: all ns) D. Contour color-coded for Menger curvature value E. Contour color-coded for distance to convex hull (pixels) F. Distribution of curvature (all contours are pooled by pattern diameter), orange shade: range of values considered as highly curved NE G. Proportion of highly curved NE by pattern diameter H. Distribution of distance to convex hull (all contours are pooled by pattern diameter), orange shade: range of values considered as deep NE I. Proportion of deep NE by pattern diameter (Kruskal-Wallis test: all ns)

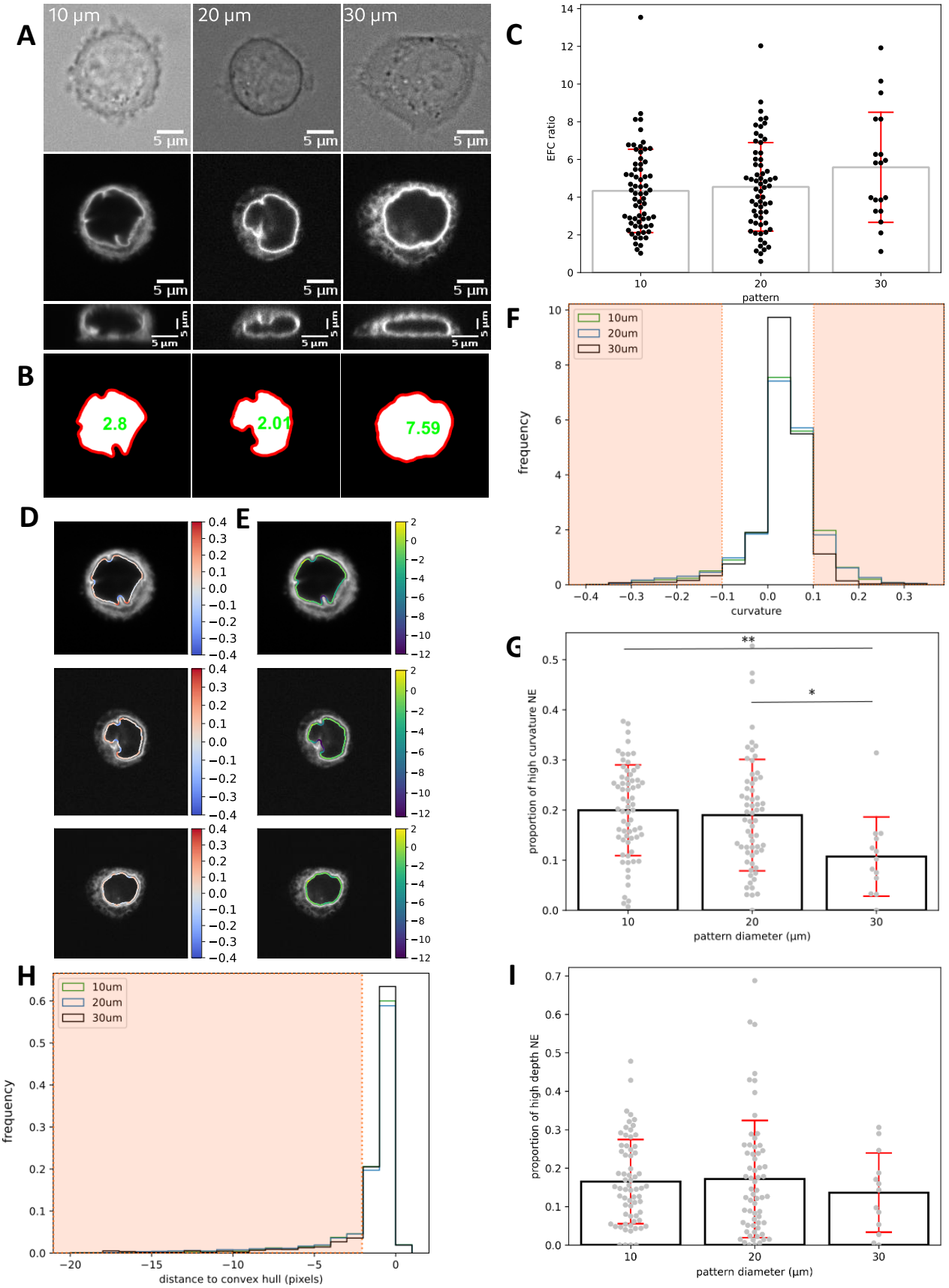
A
10 µm
20 µm
30 µm
5 µm
B
2.8
2.01
7.59
C
EFC ratio
pattern
10
20
30
D
E
F
10um
20um
30um
frequency
curvature
G
proportion of high curvature NE
pattern diameter (µm)
**
*
H
10um
20um
30um
frequency
distance to convex hull (pixels)
I
proportion of high depth NE
pattern diameter (µm)

The average value of the curvature on the whole contour varies very little, and it is more informative to look at the overall distribution. All distributions display a high peak of curvature values between 0 and 0.05, which correspond to the majority of smooth regions on the contour. The distribution is asymmetrical, with a long tail towards negative values, which correspond to the deeper regions of the folds, and a shorter, higher tail towards positive values, which correspond to the borders of the folds (Figure 26D and F).

Because the majority of the contour falls into curvature values close to 0, we sought to define a measure focusing on values associated with folds. We calculate a NE curvature score by taking the proportion of the contour with curvature values below -0.1 or above 0.1 (Figure 26F, highlighted regions). The proportion of highly-curved NE is about 20% on 10 and 20 µm micropatterns but falls at 10% on 30 µm patterns, indicating a loss of folds when spreading area is increased (Figure 26G).

We calculate a similar score on the distance to the convex hull. The majority of the NE is smooth, *i.e.* completely convex, with distance to the hull close to 0. On the contrary, inwards folds correspond to negative values, with the lowest values corresponding to the folds' deeper regions. We defined the distance score as the proportion of points with a distance value lower than -2 pixels (Figure 26H, highlighted region). The distance score slightly decreases between 10 and 20 µm patterns on the one hand and 30 µm patterns on the other hand (Figure 26I). However, the difference is modest and non-significant.

These different measurements evaluate different aspects of the contour shape, and all of them give the trend of increased shape irregularity (EFC ratio increase) and NE folding (decrease proportion of highly curved and deep NE) in more rounded cells. Taken together, they suggest that less spreading area induces more folding of the NE, similar to what can be observed in rounded cells *in vivo*. There are several limitations to the experiment so far. The first is purely technical. Cells on the largest patterns are not using the full available spreading area and are thus not as flat as cells of the trophectoderm in mouse embryos. The second limitation arises from the measures we are using. We are calculating different folding scores based on the contour detection in the middle plane of the nucleus, but the folds occur in three dimensions.

Since cell flattening due to spreading was limited, we decided to experimentally impose the degree of flattening with external confining forces.

III. Opening of the nuclear envelope folds by mechanical confinement

As the invaginations open up upon spreading, we sought to characterize how the NE folds behave when cells are prevented from spreading but subjected to external mechanical compression.

Using a static 6-well plate confiner (Le Berre *et al.*, 2014), we can study the shape of the nucleus at the population level at different heights of confinement (Figure 27). As the nuclear diameter of HeLa cells is around 10 µm, confinement at 20 and 10 µm does not mechanically alter the NE. In order to precisely describe the level of deformation that confinement is applying on the nuclei, we measured for each confinement height the maximal height of the nucleus. It is in general slightly lower than the imposed confinement height. Nuclei of non-spread cells at 20 µm (non-confined control) display deep invaginations, visible in the 2D sections as well as on orthogonal views. The maximal Z projection of the NE labeling shows the wrinkles in the Z axis. These characteristics are mostly conserved at 10 µm confinement, which, depending on the nuclear size, does not always induce a significant deformation of the nucleus. Upon further confinement, the deep inwards folds open up and are replaced by undulations of the NE (Figure 27 – 8 µm). When the confinement reaches 5 µm, the NE is completely smooth (Figure 27 – 5 µm). 3D reconstruction of the nuclei based on the DNA staining shows how the irregular spherical shape flattens into a smooth pancake-like shape. Of note, the resolution of the microscopy here does not allow for a visualization of smaller-scale, sub-micrometric folds.

Interestingly, while the Hoechst staining (chromatin) gives some indication of the NE shape, it is not enough to recapitulate it. In particular, the smaller invaginations which are clearly visible with EGFP-LAP2b at 20 µm are not at all observable on the chromatin staining. This underlines the importance of using a NE marker, here an INM protein, and shows the limits of looking at chromatin only to evaluate nuclear shape.

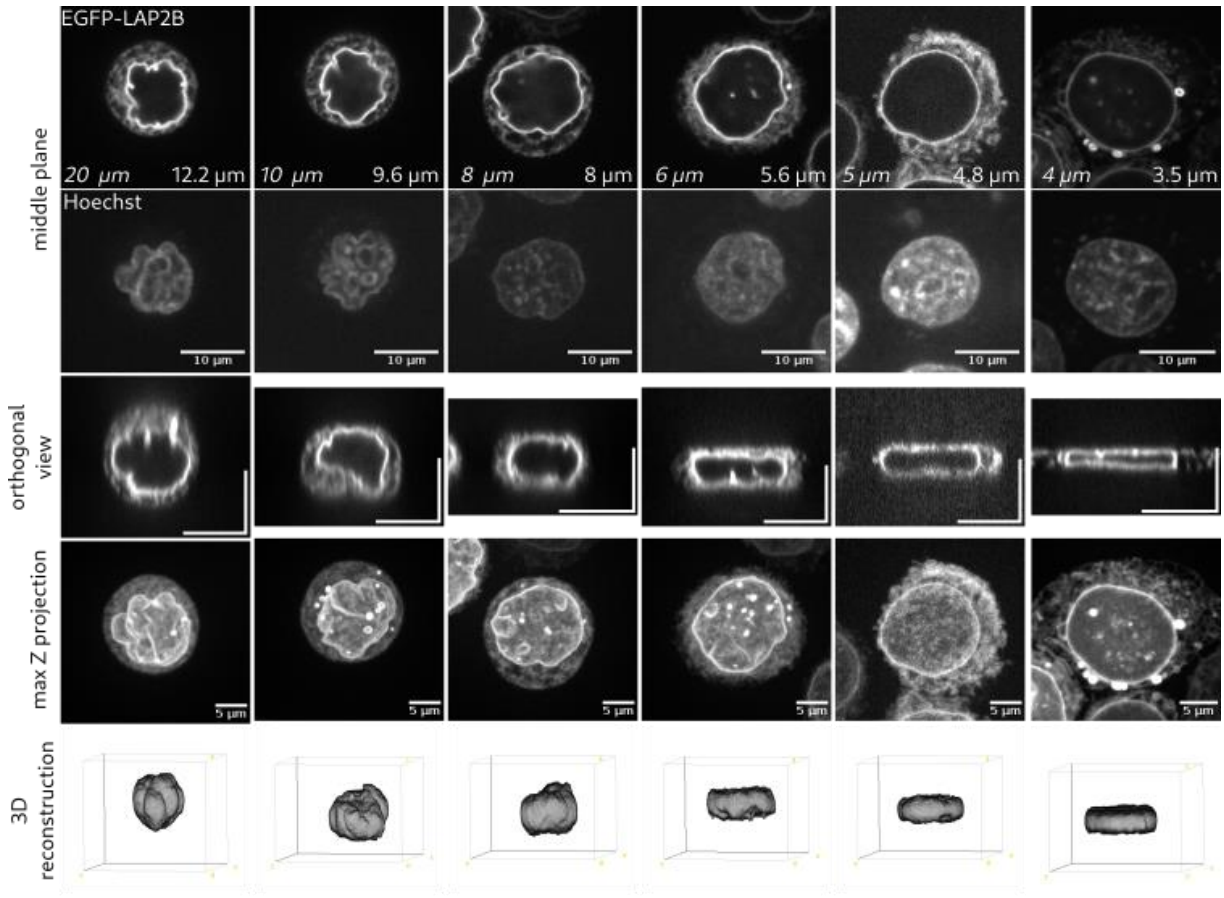

Figure 27: Representative nuclei at different confinement heights

Italics: confinement height, straight: maximal nuclear height as measured on the orthogonal views. The 3D reconstruction is done using the Hoechst staining.

The EFC ratio starts at low values in non-confined conditions, consistent with non-smooth, irregular shapes, and increases progressively upon confinement, indicating the increased smoothness of the nuclei (Figure 28A and B). It reaches its maximum at 4 µm. Certain nuclei at low heights start having nuclear blebs and DNA herniations, which explains why the EFC ratio can be low even at high confinement.

To evaluate curvature, the cells were classified by nuclear height, binning them by 2 µm bins for convenience and clarity of display. At high heights, the curvature distribution is wide (Figure 28C, yellow curve) with values ranging from -0.4 to 0.4, indicating curved regions in the NE. These correspond to the folds, with the negative values associated to the valley of the fold and the positive values to its borders, as is shown on the color-coded contour representations (Figure 28C). Upon confinement increase, *i.e.* height decrease, the distribution narrows around 0, which corresponds to smooth shapes. The tails of the distributions are reduced, consistent with disappearance of the folds (Figure 28E). This is quantified by the curvature score, showing that the proportion of highly curved NE decreases from around 20% at high heights to nearly 0 below nuclear heights of 4 µm (Figure 28F).

We next assessed the distance of the contour to the convex hull. Representative images with color coded contour are shown in Figure 28D. At high heights, the distribution of distance displays a long tail towards negative values. Upon confinement increase, the proportion of values close to 0 increases, indicating smooth contours (Figure 28G). This is quantified by the distance score, which shows that the proportion of deep NE decreases from approximately 30 % in non-confined conditions to 10% when the nuclear heights is lowered to 3 µm (Figure 28H).

Figure 28: Characterization of NE folds opening by curvature and distance measurements

A. EFC ratio of representative images B. EFC ratio on the population (red: mean + standard deviation on 6 bins of equal width) (N=3, n=218) C. Curvature along the contour of representative images at decreasing confinement heights D. Distance to convex hull (in pixels) along the contour of representative images at decreasing confinement heights E. Distribution of curvature at different nuclear heights (binning by 2 µm) (N=3, n=285) F. Distribution of curvature at different nuclear heights (binning by 2 µm) (N=3, n=285)

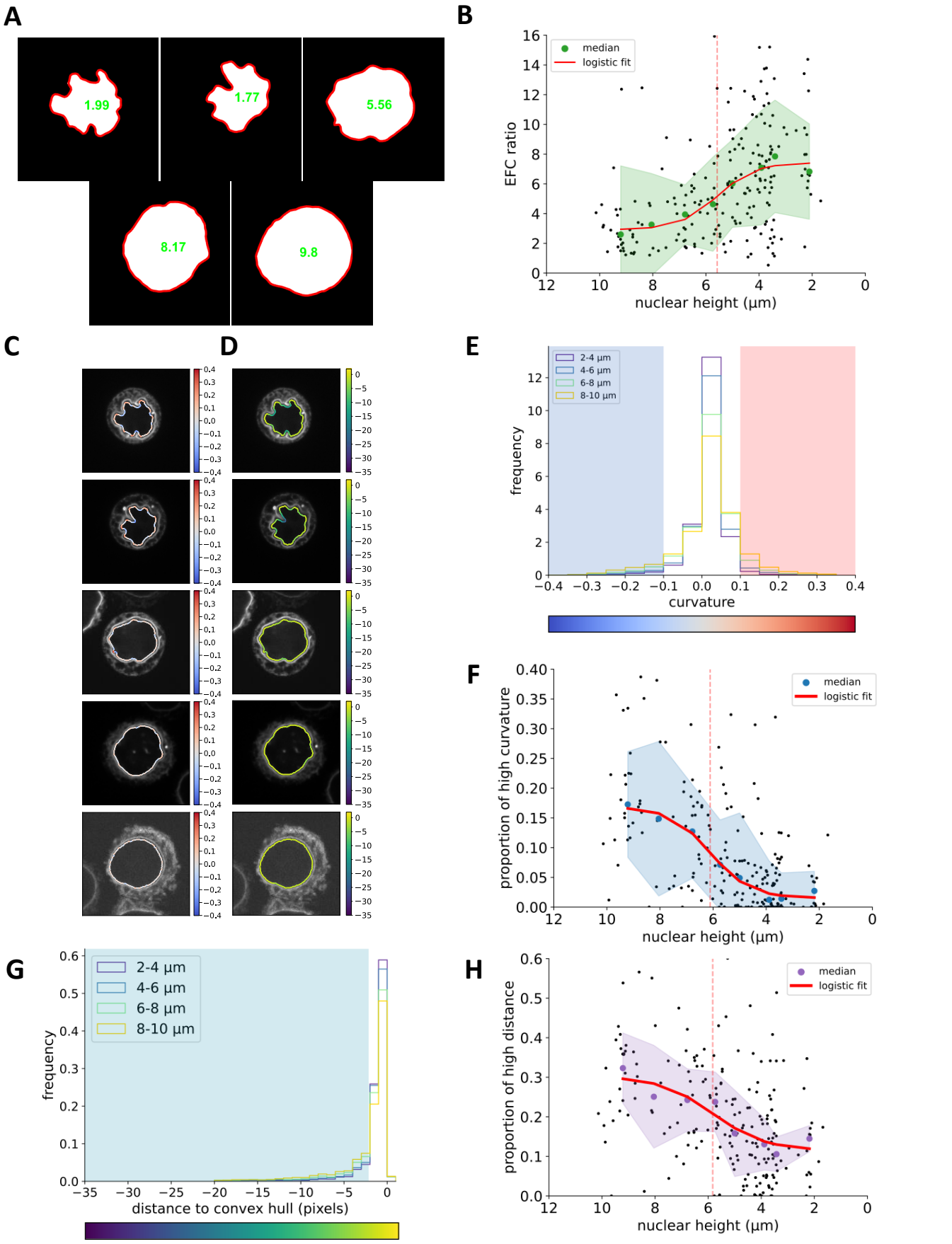
A
1.99
1.77
5.56
8.17
9.8
B
median
logistic fit
EFC ratio
nuclear height (μm)
C
D
E
2-4 μm
4-6 μm
6-8 μm
8-10 μm
frequency
curvature
F
median
logistic fit
proportion of high curvature
nuclear height (μm)
G
2-4 μm
4-6 μm
6-8 μm
8-10 μm
frequency
distance to convex hull (pixels)
H
median
logistic fit
proportion of high distance
nuclear height (μm)

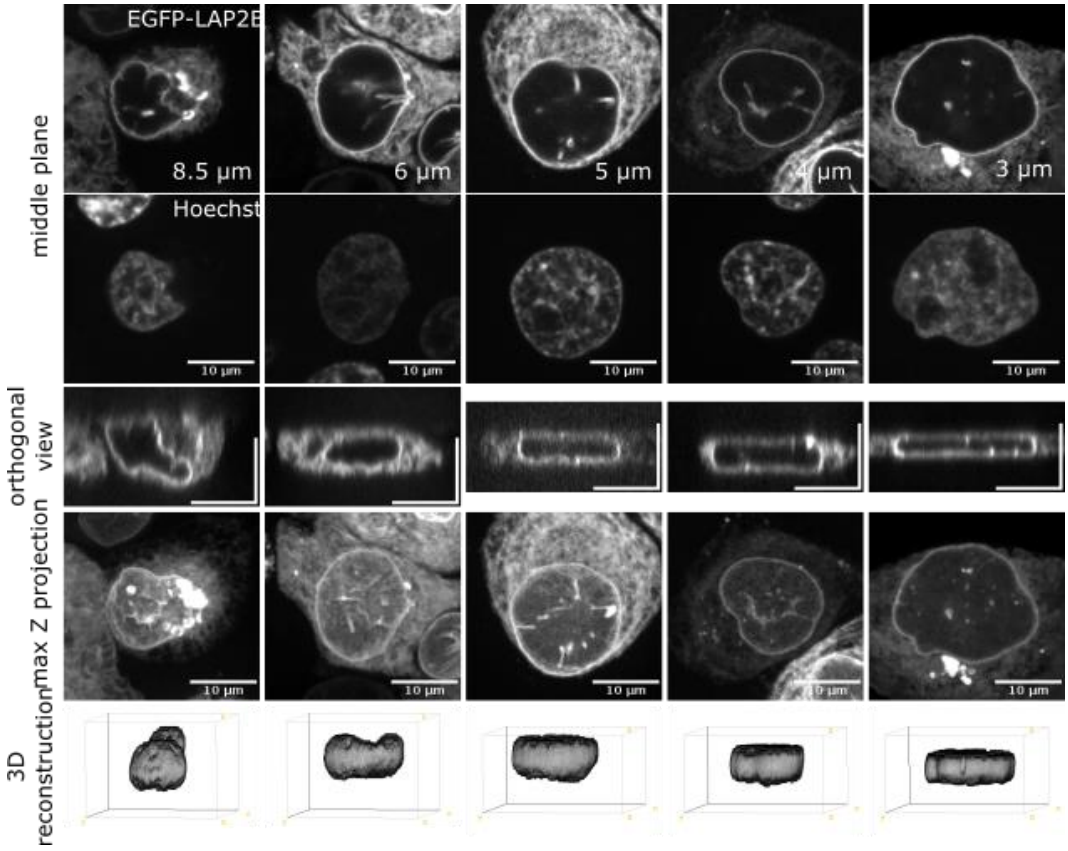

Figure 29: NE unfolding by mechanical confinement in MDA-MB-231

We make the same qualitative observations in MDA-MB-231 cells. 3D NE folds are opened and flattened by 2D confinement, as can be seen in Figure 29.

Taken together, the measurements of shape irregularity coincide to provide numbers for the qualitative observation of NE unfolding upon confinement. The folds observed on non-adhesive cells here are more numerous and of a larger amplitude than the ones observed on 10 µm patterns, while the fully flattened cells show no fold at all. These results show that in non-spread, non-mechanically constrained states, nuclei display large NE folds which are not always associated with invaginations of the chromatin. These folds can be opened by externally imposed cell flattening. As applying deformation induces their opening, we wondered what would happen upon confinement release.

IV. Reversibility of folds opening upon confinement

As the NE unfolds upon external mechanical constraints, we wondered whether the folds would reform if the constraint was released. If they did not, it would mean that the NE is irreversibly deformed and follows a plastic deformation. On the contrary, if they did, it would indicate that the NE behavior has an elastic component. Based on the literature, this second hypothesis is what we expected to observe (Dahl, 2004; Lammerding *et al.*, 2006). An open question remained whether the folds would reform exactly as they were prior to deformation.

By using the dynamic confiner system, we confined non-spread HeLa cells at 8 µm, a height sufficient to lose most of the invaginations, and then released the confinement. Before lowering the pillars, the nuclei are displaying the folds presented above with deep invaginations (Figure 30A, pre-confinement). Upon confinement, the NE opens up and smoothens, as is expected (Figure 30A, confined). Once the confinement is released, the NE wrinkles immediately (Figure 30A, 0s). Over time after confinement release, the shape of the wrinkles quickly changes. In 10 s, some wrinkles deepen, reforming invaginations, while most others rather smoothen to form flatter regions. Interestingly, on this representative movie and on others, deep invaginations reform at new regions, different from the pre-confinement invaginations. When the confinement was not sufficient, deep invaginations that have not been fully opened could reform upon deconfinement (Figure 30B, green arrow).

The comparison of NE behavior before, during and after confinement can be quantified using the same parameters as described above. The quantifications are performed on the middle plane of the Z stack acquired prior to confinement for the pre-confinement stage and on the single frames acquired during or after confinement. Confinement is associated with an increase in nuclear projected area (Figure 30C) as the nucleus deforms. The nuclear area decreases upon confinement release, thus enabling to define confined and post-confined time periods. Using thresholding methods to assess the overall NE shape over time, we show that, as expected from Chapter 1.3, we can calculate the same parameters, as described previously. As expected, the EFC ratio increases upon confinement, as the nuclei become smooth when the folds are opening (Figure 30D). It decreases again when confinement is released. Both curvature and distance scores decrease upon confinement, and increase again after confinement is released (Figure 30E). Because the thresholding was done in a semi-automated manner, the measures are relatively noisy. A more precise contour analysis will be presented in Chapter 2. In order to compare macroscopically the different confinement stages, we average the values during or after confinement.

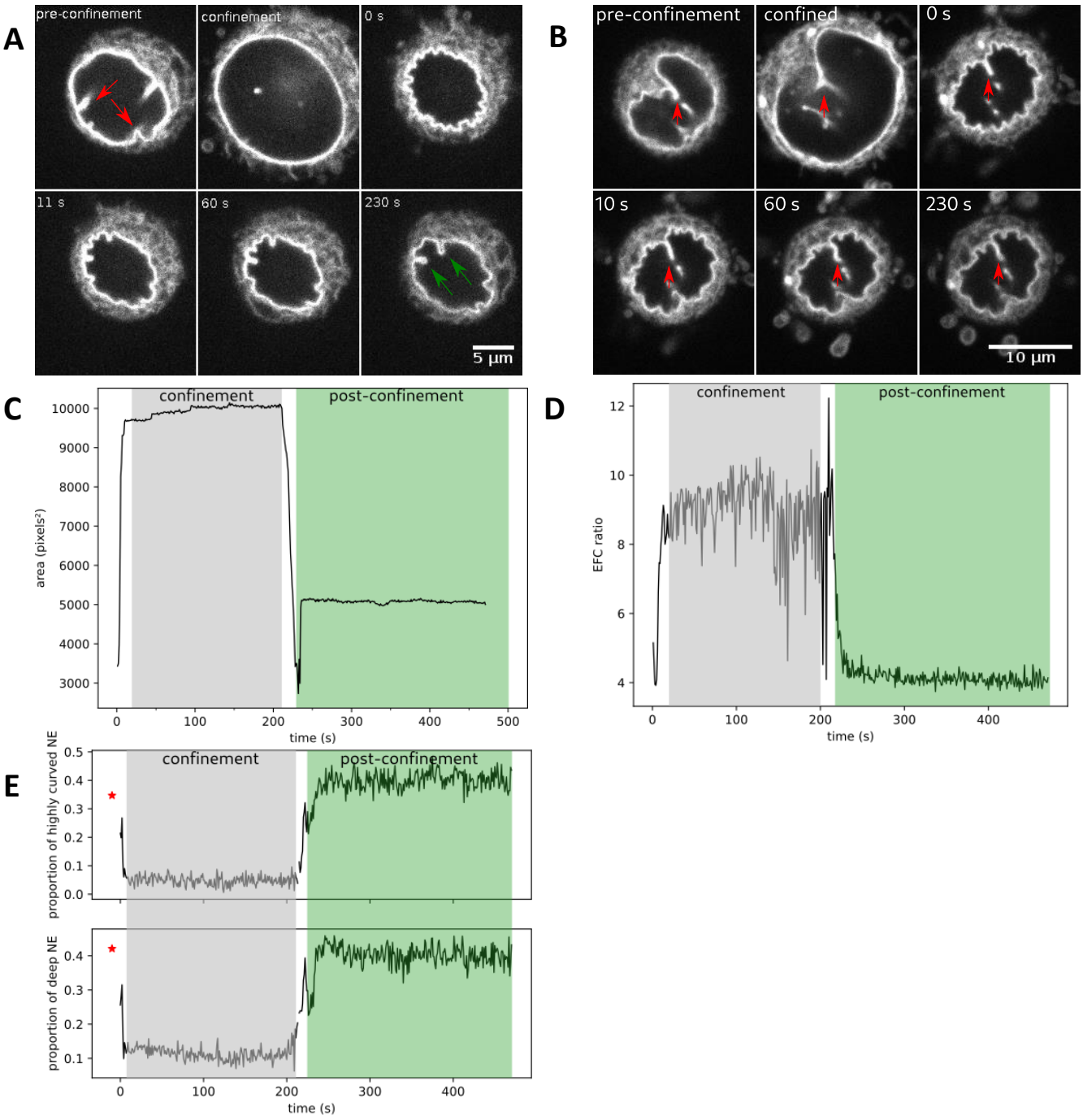

Figure 30: Unfolding and refolding of the NE by confinement and after confinement release

Confinement at 8 µm for approx. 2-3 min, N=2, n=16, NE labeling: EGFP-LAP2b

A. Images of one representative fully unfolded nucleus before, during and after confinement

B. Images of one representative fully unfolded nucleus before, during and after confinement

C. Representative curve of nuclear projected area over time D. Representative curve of EFC ratio over time E. Representative curves of curvature and distance scores over time (red star: pre-confinement value)

We normalized the EFC ratio to the highest expected value, which is during confinement. As expected, we observe in all cells a lower EFC ratio before and after confinement, confirming that folds are present before and after mechanical deformation (Figure 31A). Interestingly, although the difference is not statically significant, the EFC ratio post-deconfinement is lower than its pre-confinement counterpart.

The distribution of curvature narrows as expected upon confinement, as the NE becomes smooth. The distribution is more spread in pre- and post-confinement states, with values effectively ranging from -0.3 to 0.3 (Figure 31B). Interestingly, the central post-confinement peak is much lower than its pre-confinement counterpart. The curvature score, calculated on the cumulated distributions of all contours over time, shows that pre-confinement nuclei have in average 18% of highly-curved NE. This number drops to 8% upon confinement and rises again to 42% after confinement release (Figure 31C).

The distributions of distance to the convex hull show similar results. The distribution concentrates close to 0 as expected upon confinement. It is spread towards negative values in the pre- and post-confinement states, consistent with NE folding (Figure 31D). The percentage of deep NE starts in average at 28%, decreases to 15% upon confinement and increases to 42% after confinement release (Figure 31E).

NE unfolding upon mechanical confinement is a reversible process, although when NE folds are fully opened, they do not reform in the same position. Interestingly, although the difference is non-significant, the post-confinement state is characterized by a lower EFC ratio and slightly higher proportions of highly curved and deep NE than the pre-confinement shape. Consistently with the representative images, this suggests that after confinement release, NE folds reform at a higher frequency and shallower than in the initial state and that NE shapes are on average more irregular when the confinement is lifted, before smoothening again as large invaginations reform.

Figure 31: NE folds reformation after confinement release

N=2, n=16, statistical test: Kruskal-Wallis (: p-value<0.05, **: <0.005, etc, non-significant if nothing is specified)*

A. EFC ratio before, during and after confinement – black lines: single cells, red line: mean + SD B. Distribution of curvature (cumulated distribution of all cells, by confinement stage)

C. Curvature score (single cells, by confinement stage) D. Distribution of distance to convex hull (cumulated distribution of all cells, by confinement stage)

E. Distance score (single cells, by confinement stage)

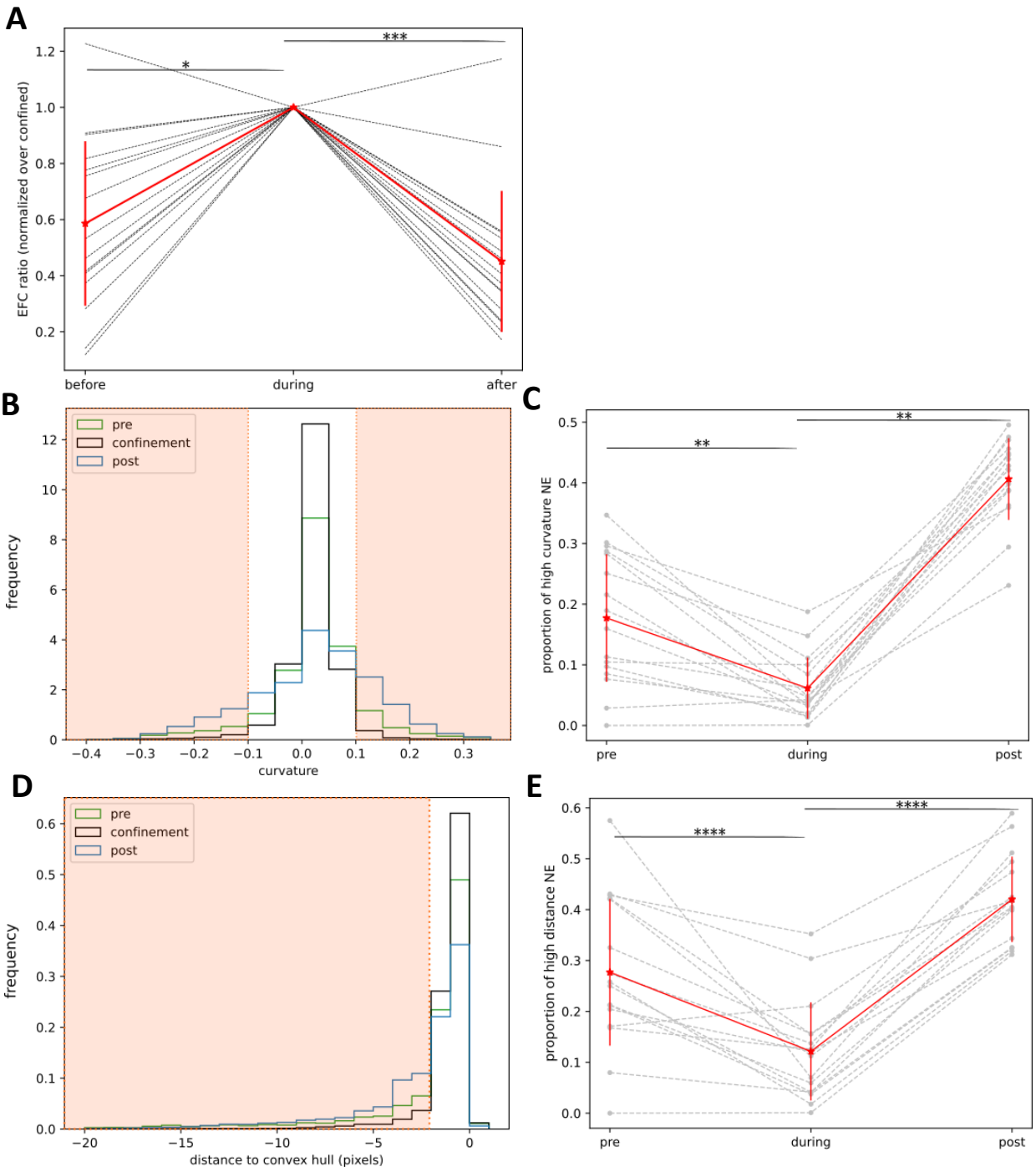
A
EFC ratio (normalized over confined)
before
during
after
*
***
B
pre
confinement
post
frequency
curvature
C
proportion of high curvature NE
**
**
pre
during
post
D
pre
confinement
post
frequency
distance to convex hull (pixels)
E
proportion of high distance NE
****
****
pre
during
post

Taken together, these results suggest that NE folds are a common feature of rounded nuclei, that can be observed *in vivo* and reduced by flattening in vivo as well as with different methods *in vitro*, such as altering spreading area or mechanical confinement of the cells. Mechanical constraints, whether internal from cell spreading, or externally applied, as uniaxial 2D confinement, appear to be key in their dynamics. The reversibility of the unfolding due to flattening, suggested us to consider fold formation as driven by elastic processes. The fact that folds reform in different locations than their pre-confinement positions oriented us towards the hypothesis of mechanical instability rather than an intrinsic heterogeneity in the lamina or the chromatin anchoring (Lionetti *et al.*, 2020).

CHAPTER 2: A MODEL TO EXPLAIN THE PHYSICAL ORIGIN OF THE ENVELOPE FOLDS

The dynamic observations of the unfolding – reformation of the folds upon confinement and de-confinement, served as basis to Romain Rollin, then PhD student in the Physics and Chemistry department at Institut Curie (UMR168) under the supervision of Jean-François Joanny and Pierre Sens, to propose a mechanical model to explain their origin.

I. Qualitative explanation of the model

The model considers a simplified nucleus with the lamina as a thin stiff elastic layer, enclosing the chromatin as a soft elastic substrate. It is inspired by the model described in (Brau *et al.*, 2011). The parameters of both layers are estimated based on the literature, as detailed in the following table (modified from table 2.2 in Romain's PhD manuscript).

Parameter	**Value**	**Reference**
Lamina stretching modulus (K)	25 mN/m	(Dahl, 2004)
Lamina thickness (e)	14 nm	(Turgay *et al.*, 2017)
Lamina Young modulus (E_L = K/e)	2.10^6 Pa	
Chromatin Young modulus (E_C)	10^3-10^4 Pa	(Hampoelz and Lecuit, 2011; Nava *et al.*, 2020)
Chromatin Poisson ration (v_C)	0.4-0.5	

Table 1 Parameters of the thin shell model

The lamina is characterized by its bending modulus $B = K.h^3$

As presented in the introduction, the chromatin and the lamina are connected through multiple protein-protein interactions, mediated among others by LBR, LEM-domain proteins and SUN proteins. Therefore, the model makes the simplified but reasonable assumption of a perfect attachment between chromatin and lamina. The central hypothesis of the model is the existence of a resting length mismatch between the chromatin and the lamina, with the assumption that the resting length of the lamina L_L is larger than the resting length of the chromatin L_C, *i.e.* that there is an excess of NE compared to the surface of the chromatin. This hypothesis will be discussed in further details in the Discussion section of this manuscript.

In order to resolve the resting length discrepancy, the system can display two limiting regimes: either the lamina is compressed and/or the chromatin is extended (Figure 32a), or both chromatin and lamina bend to accommodate the mechanical frustration, in a purely bent state without any tension/compression (Figure 32b). If we now define $\delta = \frac{L_L - L_C}{L_L}$ as the ratio of excess resting length of the lamina compared to the chromatin, the resolution of the model free energy states shows that the bent state becomes more favorable for δ as small as 1% (δ_1^*). For details on the resolution of the model, we refer the reader to(Rollin, 2021).

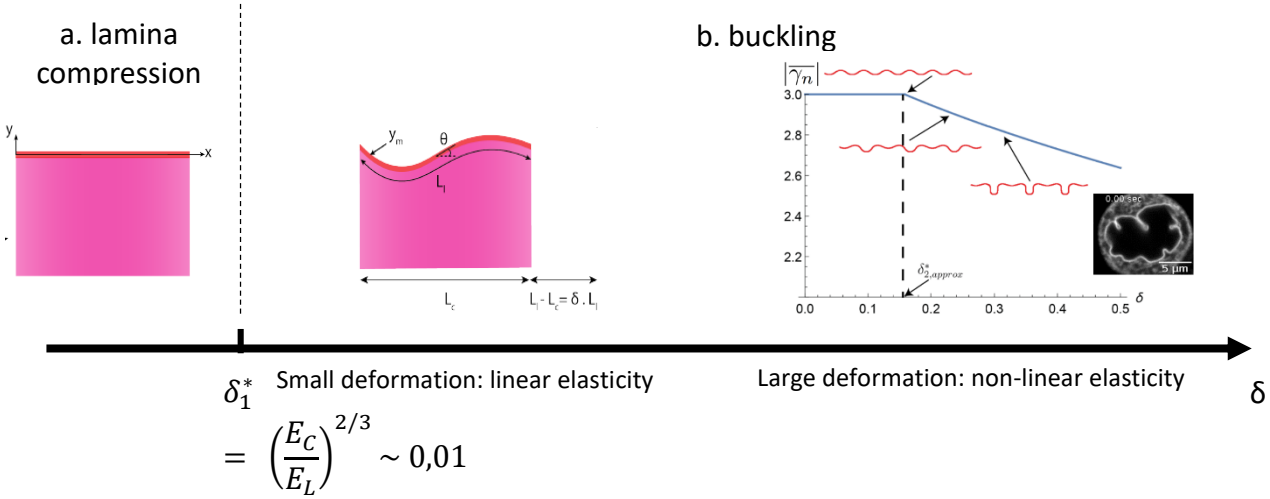

Figure 32: Modelling of the nucleus in the thin shell model and limiting cases to resolve resting length discrepancy

A 1% surface mismatch between NE and chromatin is sufficiently low that it is highly likely to be reached in cells. This simple model is therefore in line with the observation that nuclei are not smooth in many different contexts. However, the sinusoidal, symmetric and interface-wide wrinkles do not match the observations of the focalized, inward invaginations. Moreover, precisely because of the low value of δ_1^*, δ in cells is likely to be far superior to this 1%. This makes the simple linear model insufficient to represent the deformation, as large strains are susceptible of generating non-linearities. Following again closely the approach developed in (Brau *et al.*, 2011), the model is modified to incorporate a geometrical non-linearity, which translates into a term to the power of two. A second threshold δ_2^* for symmetry breaking emerges from it such that $\delta_2^* \approx \left(0.105 \frac{E_c^{eff}}{E_c^{eff\prime}}\right)^2$,with $E_c^{eff} = \frac{2E_c(1-\nu_c)}{(1+\nu_c)(3-4\nu_c)^2}$ and $E_c^{eff\prime} = \frac{E_c}{2} - \frac{(1-2\nu_c)(13-16\nu_c)}{(1+\nu_c)(3-4\nu_c)^2}$. For mathematical and calculation details, we again refer the reader to the chapter 2.3 of (Rollin, 2021). Unlike the threshold for buckling δ_1^* that was dependent on parameters of

both lamina and chromatin, this threshold for symmetry breaking is exclusively dependent on parameters of the chromatin and displays a stronger dependence on its Poisson ratio. This result was not completely expected and it can be puzzling to see no effect at all of the properties of the thin shell.

Predictions of NE profiles can be made from the non-linear theory, for different values of δ at a given ν_c (Poisson ratio of the chromatin), here ν_c = 0.4 (Figure 33). For $\delta > \delta_2^*$, we now have symmetry-breaking invaginations that, for large values of δ, leads to the tear drop-shaped inward folds that we observe experimentally on the nuclear envelope.

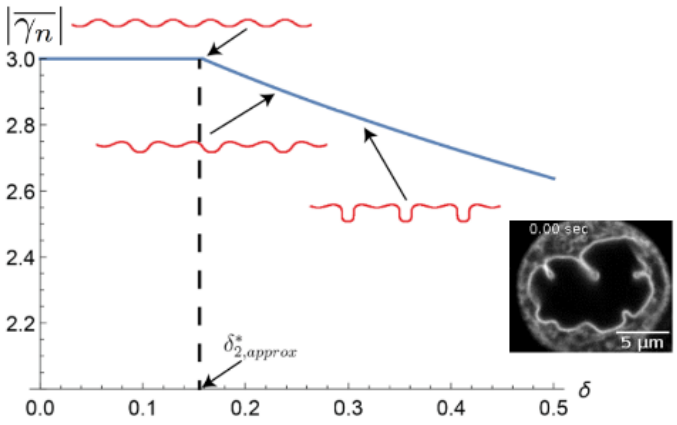

Figure 33: Predicted NE profile as a function of the resting length mismatch between lamina and chromatin

Of note, in this simple description of the nucleus, the assumption of a purely elastic chromatin induces a periodicity of invaginations that is not observed in cells. Further refinement of the model by taking into account the viscous component of the chromatin would be required. Such considerations have been taken into account for macroscopic folds of a polyester film over water (Pocivavsek *et al.*, 2008), which display folds with shapes very similar to what we observe in HeLa nuclei (Figure 34). Interestingly, the symmetry-breaking is not intrinsically predicted in that model and the authors propose gravity as a reason why it is always observed experimentally. While this is not likely to be applicable in our system, a symmetry-breaking factor could be the differences between the nucleoplasmic and cytoplasmic media, or the intrinsic curvature of the nucleus, which gives different boundary conditions than a flat surface. Additionally, how to account for the non-periodic distribution of the invaginations remains to be explored.

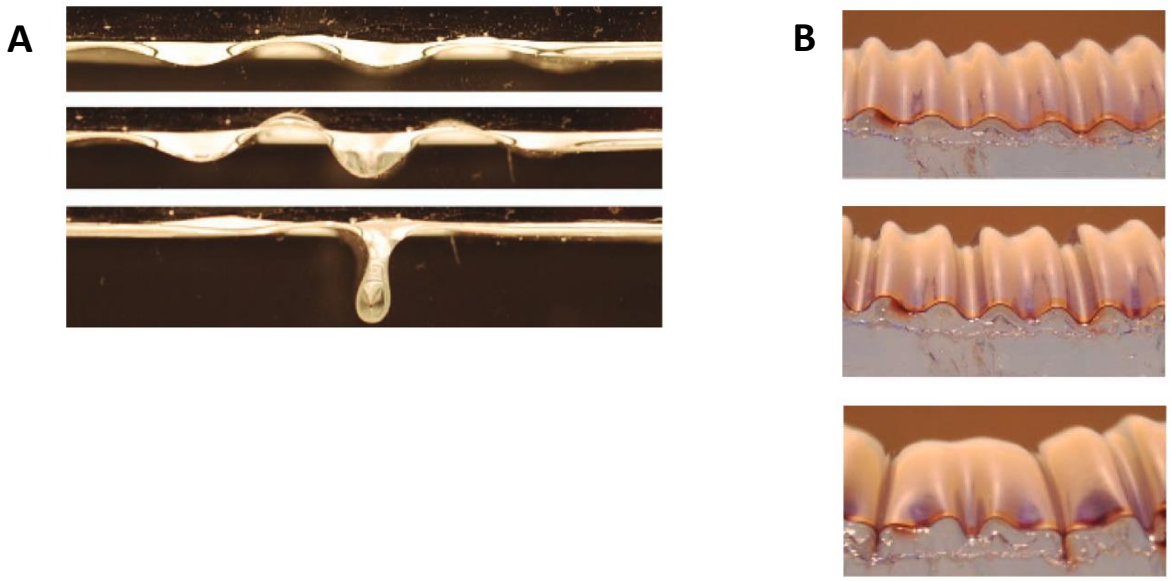

Figure 34: Formation of folds in a polyester film

(Pocivavsek et al., 2008)

A. Folds formation in a polyester film on water under increasing compression forces

B. Folds formation in a polyester film on a gel under increasing compression forces

II. Experimental validation of model predictions

From this model, there are predictions that we can test experimentally. Lowering δ in a given nucleus should open the folds, while increasing it incrementally should induce their re-formation by travelling along the shapes predicted in Figure 33. One way of modulating δ experimentally is to artificially change L_L by 2D confinement. As the chromatin is a soft material, we assume that its new resting length will be increased under compression, thus lowering δ. Conversely, de-confining the cell should restore L_L to its natural resting value, bringing back δ again to its pre-confinement value. As was shown in Chapter 1, confining the cells indeed opens up the folds. In the 2D confinement system, the timescales of compression are too fast to be able to follow changes of shape in a stepwise manner. However, it is possible to follow the recovery after de-confinement. The theory does not include any dynamics. However, we can make the assumption that progressive deformation of the nucleus corresponds to a succession of fast equilibrium points corresponding to increases in δ at a timescale we can follow. The model predicts that immediately after confinement release, the NE should buckle as described for $\delta_1^* < \delta < \delta_2^*$, and that over time, the folds should focalize and grow in a restricted number of points, thus decreasing the frequency of apparent folds and increasing their depth. Simultaneously, the regions between folds should flatten.

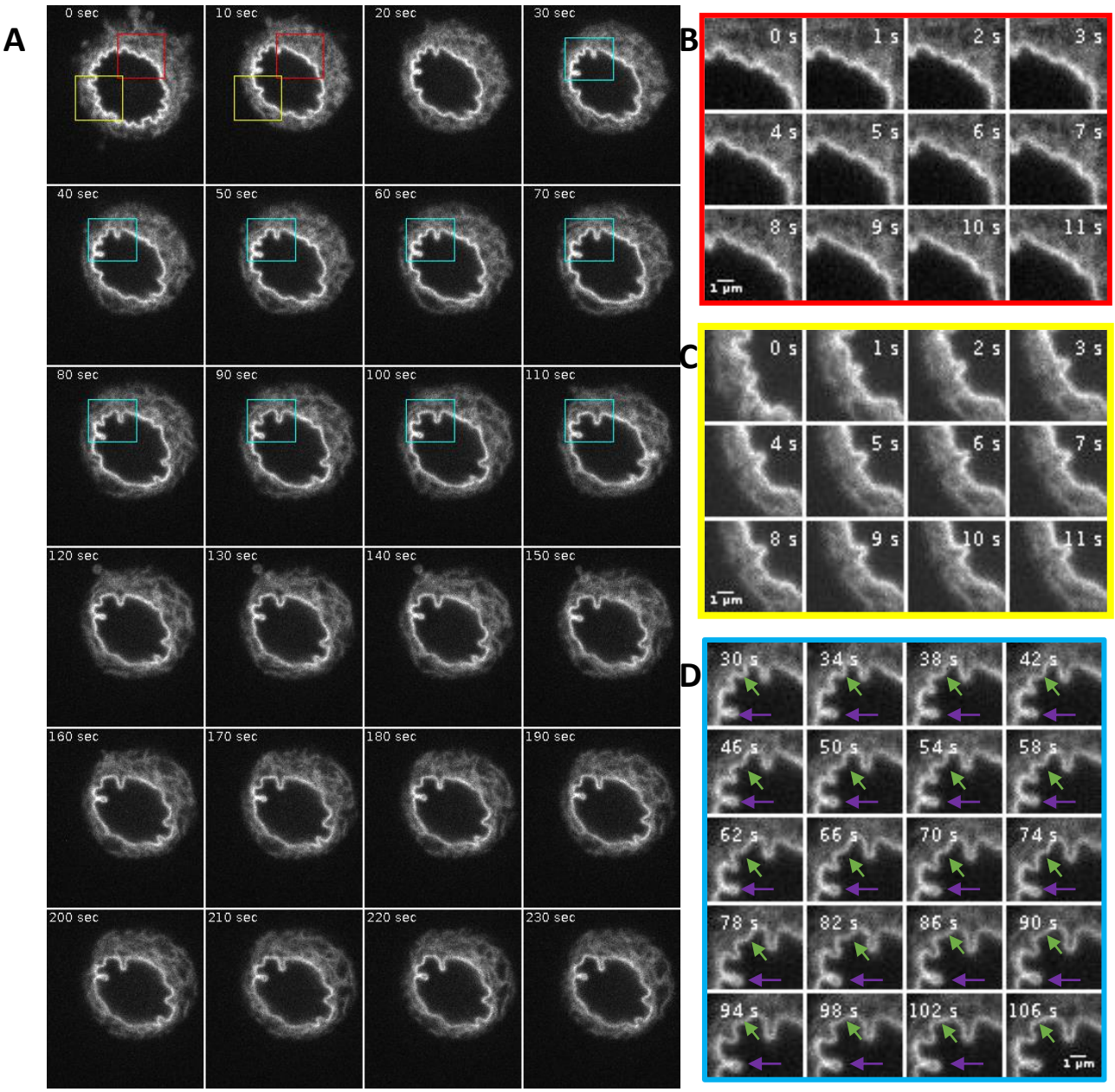

Figure 35: Acquisition of NE folds after confinement release: a representative example

Confinement at 8 µm

A. Nucleus over time starting after full release of the confinement B., C. and D. zoom on different regions of the NE illustrating flattening and fold deepening

We show in Figure 35 a representative movie of the NE shape following the release of an 8 µm confinement. Of note, confinement at 8 µm is sufficient to open most of the pre-confinement invaginations (Figures 28 and 35). Inset B shows the deepening of a single invagination winning over the multiple sinusoidal folds. Inset C shows the dampening and flattening of the sinusoidal over time. There is a first, rapid process (approximately 10 sec), where the sinusoidal folds disappear, while the flattening and the deepening of other folds continues on a longer timescale, on the scale of the minute.

In order to be able to trace the evolution of the fold frequency, we measured curvature along the perimeter of the nucleus as a function of the normalized curvilinear abscissa immediately after de-confinement (t = 0 s) and after several durations (t = 11s, 60s, 230s). Additionally, we traced the convex hull of the nucleus mask as a referent point for the edge of the nucleus. From there, we can map the nucleus perimeter to its distance from the edge of the hull and follow the evolution of the folds' depth. We proceeded to a detailed quantification on one representative cell, but a similar behavior is observed in the 18 cells that were observed.

As predicted by the model, at t = 0 s, which corresponds to a value of δ lowered by the just-released confinement, the NE displays sinusoidal folds at high frequency, as is observed by the repeated changes in curvature sign (Figure 36A, top left panel). This is underlined by the wide distribution (Figure 36B, violet curve), mostly centered around the average curvature. They are numerous and of modest depth, as is shown on Figure 36C.

As soon as 10 s post confinement release, the frequency of curvature sign changes has decreased (Figure 36A, top right panel) and the curvature distribution has narrowed (Figure 36B, blue curve). The frequency of curvature values close to 0 increases, which is consistent with a flattening at several regions of the NE (Figure 36A and C). This correlates with the increased frequency of points at small distances from the convex hull (Figure 36D).

Figure 36: Quantification of curvature and distance to convex hull to characterize the folds
A. Curvature along the contour for each timepoint, B. Curvature distribution (dotted line: average curvature) C. Distance to convex hull along the contour for each timepoint, D. Distance to convex hull distribution (dotted line: average distance) E. Proportion of highly curved NE over time (red star: pre-confinement value) F. Proportion of high distance NE over time (red star: pre-confinement value)

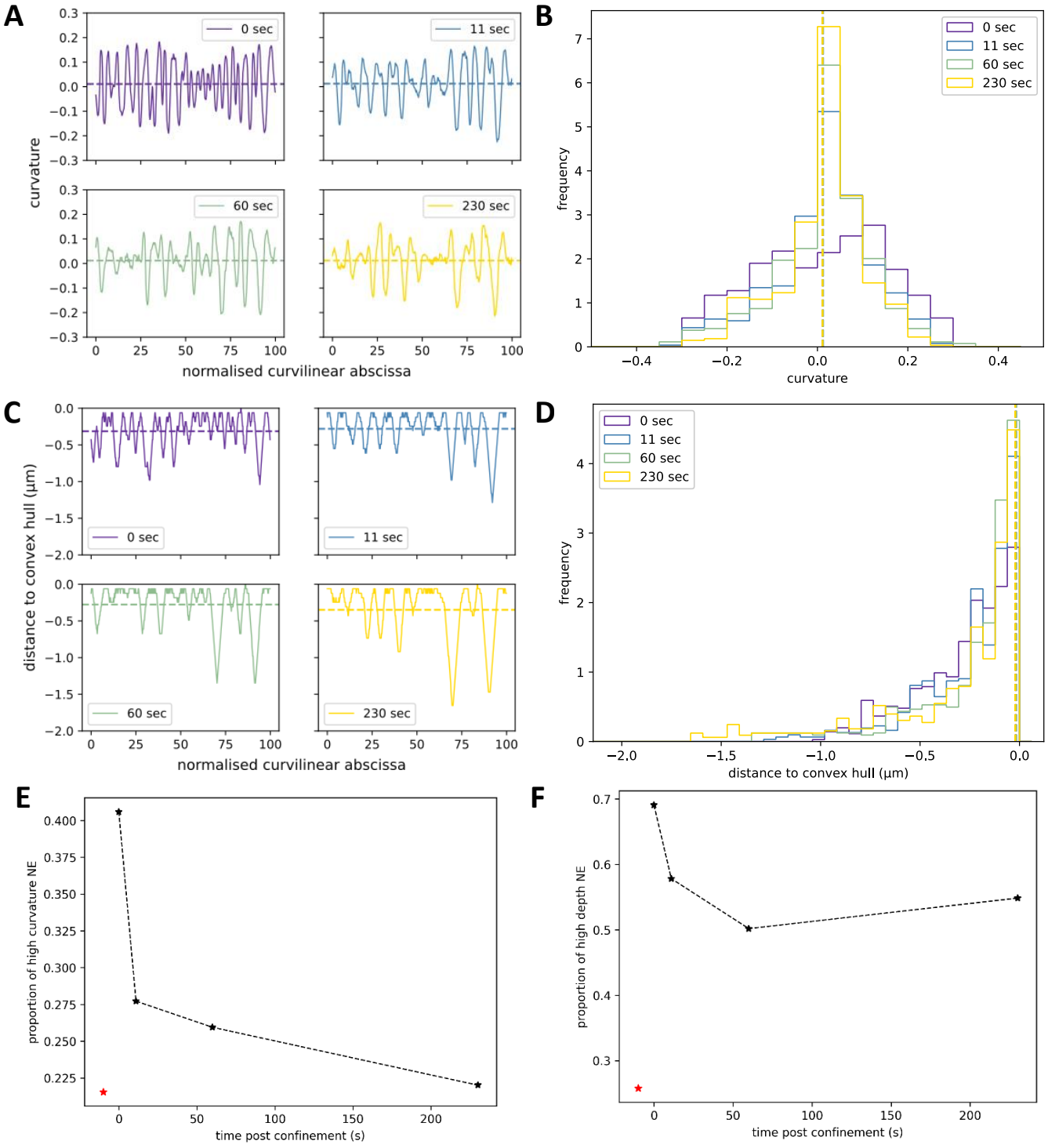
A
0 sec
11 sec
60 sec
230 sec
curvature
normalised curvilinear abscissa
B
0 sec
11 sec
60 sec
230 sec
frequency
curvature
C
0 sec
11 sec
60 sec
230 sec
distance to convex hull (µm)
normalised curvilinear abscissa
D
0 sec
11 sec
60 sec
230 sec
frequency
distance to convex hull (µm)
E
proportion of high curvature NE
time post confinement (s)
F
proportion of high depth NE
time post confinement (s)

The local deepening and consolidation of the folds continues at longer time points, as shown with the negative peaks of distance to the convex hull (Fig 36C). Flattening of the NE in other regions is quantified by the increased frequencies of small depths and curvature close to 0.

The flattening of the NE can be quantified by the curvature score, which decreases over time (Figure 36E). The distance score shows the deepening of certain folds after the resorption of others by the initial decrease followed by a slight increase (Figure 36F). Overall, the progressive fold focalization and deepening fits with the predicted shape at different values of δ.

III. Role of the lamina in nuclear envelope folds' dynamics

From the model calculation, the rigidity of the lamina is expected to alter the value of δ_1^*, *i.e.* the threshold for the switch from pure compression to pure bending, but the calculation does not predict a role for δ_2^*, where the symmetry-breaking occurs. As a first approximation of lamina rigidity alteration, we knocked down lamin A/C, expecting to decrease lamina stiffness. Of note, LMNA KD nuclei in non-spread conditions and before confinement display irregular shapes but inwards folds similar to control (Figure 37B).

While we have yet to perform a detailed shape analysis on these movies, we can qualitatively observe a sharp difference in the refolding after confinement release. si Non-Targeting (siNT) exhibit a behavior very comparable to WT control, with sinusoidal folds flattening in certain areas and deepening in others (Figure 37B). However, siLMNA nuclei go from smooth under confinement to angular folds upon confinement release, without displaying the small sinusoidal folds initially observed in control. Moreover, the shape stabilizes after 10 s, whereas control nuclei are dynamic until at least 90 s after confinement release (Figure 37B, C and D).

These results, which need to be confirmed by quantification on all the cells, indicate that changes in the lamina drastically affect the dynamics of NE deformation. Due to our protocol, the KD is transient but the cells have already been partially knocked-down for a few days when the experiment is performed. Therefore, we cannot exclude that we may be altering the state of the chromatin and its properties as well as the lamina. Further controls would be required to assess this point, for example controlling for key hetero- and euchromatin marks such as H3K9me3, H3K27me3 or H3K9ac, or mechanical probing of the chromatin itself.

While positioning these results with regards to the mechanical model remains challenging, they underline the importance of lamin A/C in NE dynamical responses to deformation.

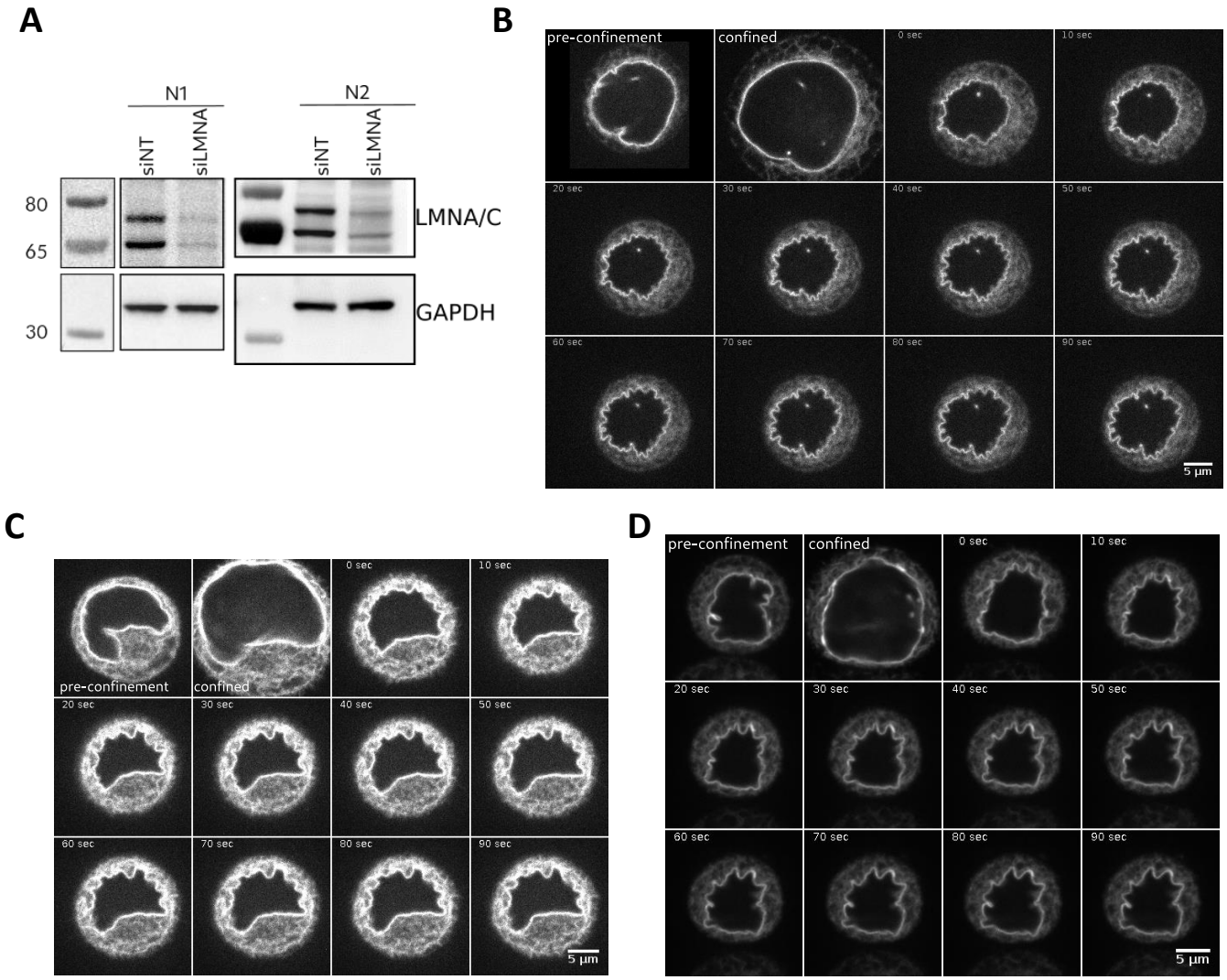

Figure 37: Pre- and post-confinement behavior of the NE in LMNA KD cells

Confinement at 6 µm, labeling: EGFP-LAP2b (N=2, n=13)

A. KD efficiency control by Western Blot (N=2 experiments) B. Representative movie of control si Non-Targeting cells

C. and D. Representative movies of si LMNA cells

Here, we propose a purely mechanical model that can explain the folds we observe in various contexts *in vivo* and *in vitro*, based on a resting length mismatch between the stiff, thin layer of the lamina and the soft bulk of the chromatin. A simple linear model predicts that a surface mismatch of 1% between lamina and chromatin is enough to generate buckling of the NE and irregular nuclear shapes. The addition of a geometric non-linearity introduces the symmetry-breaking, deep invaginations observed in the cells. Using dynamic confinement followed by confinement release, we tested the predictions of the model for different levels of length mismatch by following the folds' reformation after de-confinement. We showed that after confinement release, the NE forms folds again, starting with regular, sinusoidal folds consistent with the predictions of moderate δ values. Over time, their number decreases and they deepen, while the regions between folds flatten, which correlates with the shape prediction of higher δ. This process requires the presence of lamin A/C. Additional experiments are required to assess its dependency to the cytoskeleton. In particular, microtubules have been proposed for other types of folds (Biedzinski *et al.*, 2020). Preliminary results suggest that they do not play a major role for the type of folds we are observing here and will be discussed in the Discussion part of this manuscript.

CHAPTER 3: THE NUCLEAR TENSION DISPLAYS TWO REGIMES OF RESPONSE TO DEFORMATION

One key corollary of the mechanical instability model is that as long as the length mismatch is above the buckling threshold, the tension in the lamina remains low. On the contrary, once the length mismatch goes below this threshold, the tension in the lamina should increase abruptly, thus defining a threshold deformation for NE tension increase. The existence predicts that as long as there are folds, the NE should be able to deform without getting tensed.

I. Approximation of the nuclear envelope tensile state by measure of fluctuations

In order to test this prediction, we measured NE fluctuations at different confinement heights. From kymographs on different points on the NE, we extracted the position of the NE over time and measured the amplitude of the fluctuations around the average NE position. Of note, these fluctuations are strongly decreased upon treatment by the Rho kinase (ROCK) inhibitor Y27632, which inhibits contractility. This indicates that they are an active process and likely originate from dynamic pulling on the NE by the actin cytoskeleton. We interpret the NE fluctuations as a read out of the tension in the envelope and its ability to deform. We reason than a tensed NE will resist pulling much more strongly than if it is loose.

For visualization purposes, the NE contour of representative cells at different heights was plotted with a color code for time. At 20 µm confinement, the position varies distinctly over time, indicating that the NE is highly dynamic. Of note, the invaginations are fluctuating as well but remain otherwise unaffected. At 8 µm confinement, some regions of the NE are still fluctuating but it is much less apparent (Figure 38A). When the nuclear height reaches 5 µm, the NE is completely smooth and static, as is shown by the superposition of the contours at the different timepoints. This is shown by the quantification, as the fluctuations remain constant from 10 to 7 µm confinement heights at 150 nm, and decrease below 6 µm. A lower plateau at 100 nm is reached and the fluctuations are not decreasing further (Figure 38B). Interestingly, when comparing the increase in the EFC ratio, *i.e.* the smoothening of the NE, with the decrease in the fluctuations, we observe that the NE reaches a mostly smooth shape while still fluctuating. This suggests that even in the absence of large-scale invaginations, there are still smaller-scale folds, which are not detectable at the resolution we are imaging, that enable the NE to have some degree of freedom.

Additionally, previous work from the lab shows in absence of lamin A/C, the fluctuations are not decreasing at all upon confinement (Lomakin *et al.*, 2020).

Similar results are observed in MDA-MB-231 cells. The amplitude of fluctuations is stable around 150 nm until the nuclear height reaches 6 µm and then decreases to 100 nm (Figure 38C).

While the differences on the images are very readily apparent, they are much less clear on the quantification. In particular, fluctuations between non-confined control and 8 µm have already decreased, the average amplitude values are very similar. Moreover, the NE appears fully static at 5µm and below, whereas the measure gives a high background. We hypothesize that the measure could be dominated by noise in the method for NE position detection.

As imperfect as the measure is, this suggests that, following the model prediction, the NE can deform while still fluctuating, until the nuclear height reaches a threshold height around 6 µm. Below this height, the fluctuations stop and the NE becomes tensed. However, we wanted to study the NE tension in a more quantitative manner.

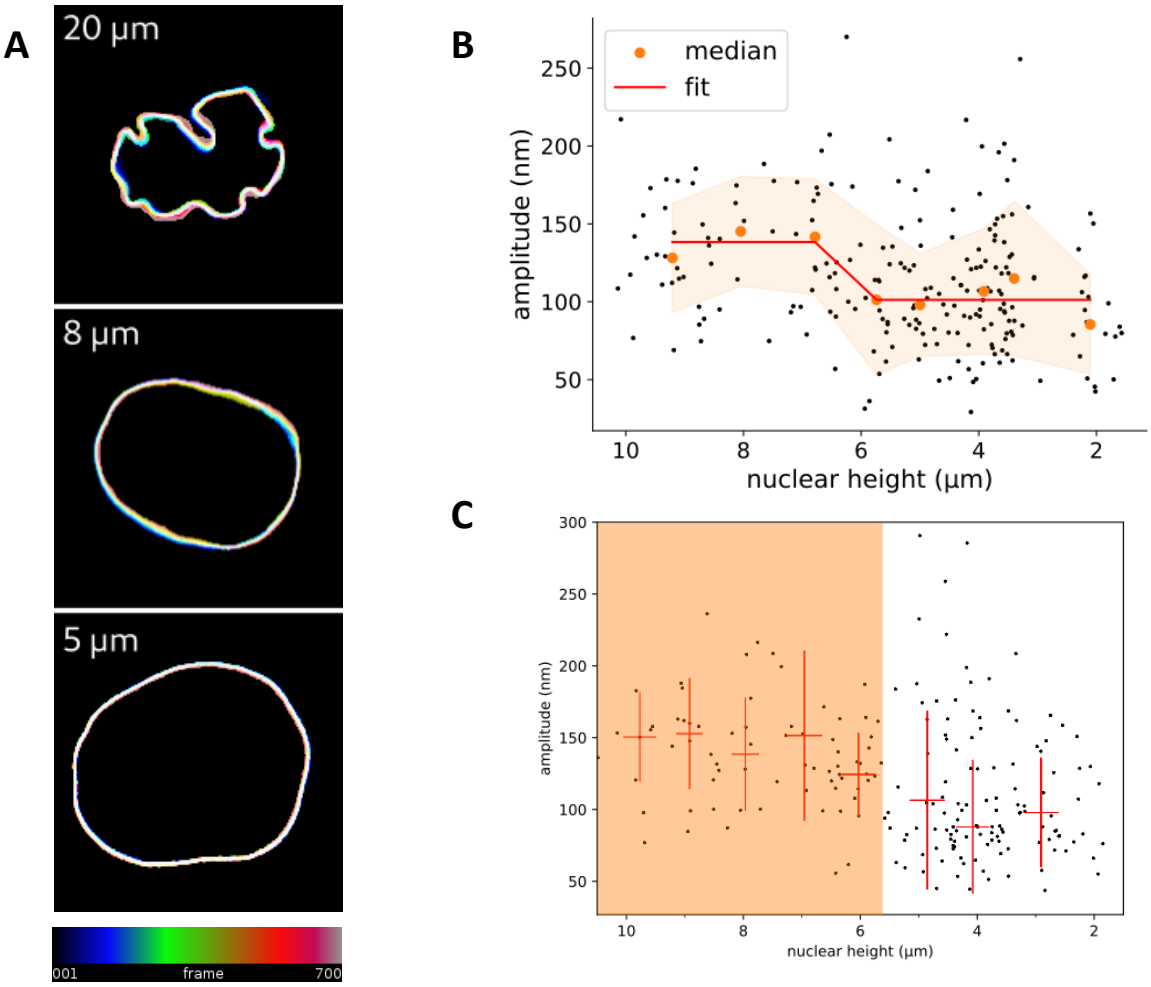

Figure 38: NE fluctuations decrease below a deformation threshold

A. Representation of EGFP-LAP2b over time, following the temporal color code, at different confinement heights B. Quantification of NE fluctuations amplitude in HeLa cells under confinement (orange: mean +SD of evenly spaced bins in height) C. Quantification of NE fluctuations amplitude in MDA-MB-231 cells under confinement (red: mean +SD of evenly spaced bins in height)

II. Quantitative measure of forces in confined cells

After obtaining a first hint of nuclear deformation without tension, we aimed to directly and quantitatively measure forces applied on the cell when the nucleus is deformed. In order to obtain quantitative force measurement, we took advantage of the wedged cantilever AFM developed by the lab of Daniel Müller, that we previously used to assess the cell contractile response to confinement (Lomakin *et al.*, 2020). The flat and wide cantilever enables deformation of a whole cell rather than a local indentation, in a simple 2D confined geometry, with a control on the height and speed of deformation, and the force given by the AFM. We performed a stepwise confinement of single cells, starting from 20 or 25 µm (non-confined control) before going down to 12, 8, 6, 5, 4 and 3 µm, with a waiting time of at least 3 min at each height to leave time for relaxation.

Similarly to what we observed at the population level and with the dynamic confiner, NE folds open up upon stepwise confinement (Figure 39A). AFM provides a time-resolved force curve enabling to follow the force exerted by the cell on the cantilever in real time. We can separate the force response during each compression in four steps: the ramp, with the response to the lowering of the cantilever, the peak, the relaxation and the steady state (Figure 39B). Our analysis so far has mainly focused on the peak and the steady state after relaxation, which we consider as the new nuclear state after each compression. The short-term dynamics in the ramp and the decay are currently under investigation, as they require further theoretical developments.

Figure 39: Overview of AFM output

A. Representative images of one cell under successive confinement steps (NE labeling: EGFP-LAP2b) B. Force curves of two representative cells treated with DMSO (control) or latrunculin A at 2 µM C. 3D reconstruction based on Hoechst staining D. Comparison of theoretical and measured resting heights (dashed line: x=y) E. Nucleus deformation ratio as a function of height (whole population, n=88 cells) F. Nucleus deformation rate as a function of height, average by condition (approx.. 12 cells per condition)

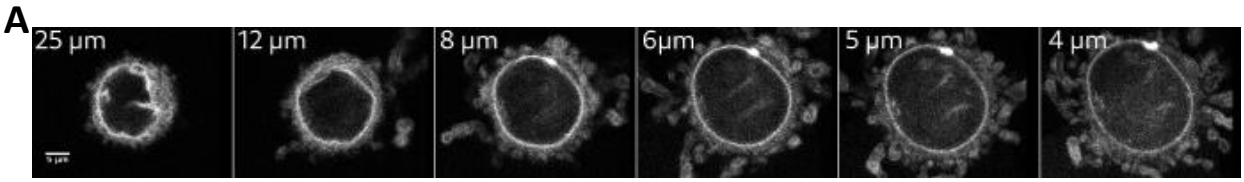
A
25 µm
12 µm
8 µm
6µm
5 µm
4 µm

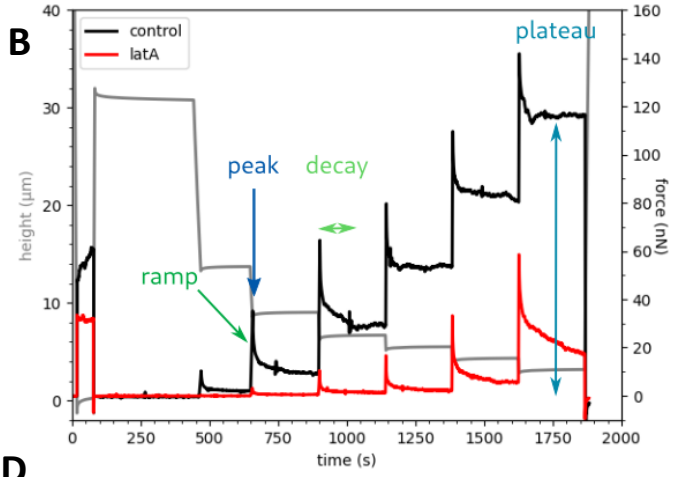
B
control
latA
plateau
peak
decay
ramp
height (µm)
force (nN)
time (s)

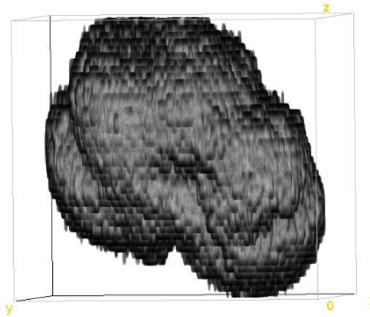
C

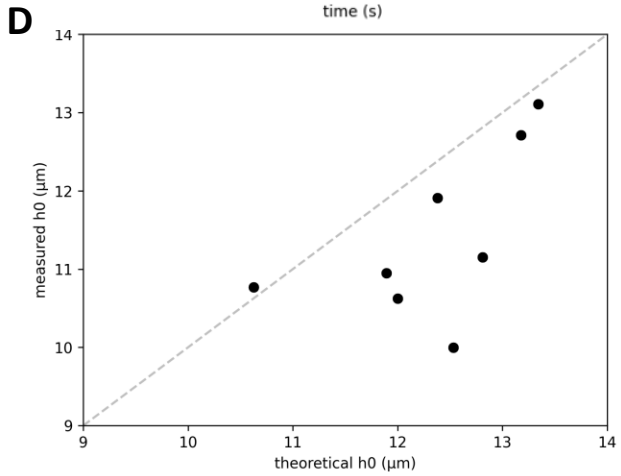
D
measured h0 (µm)
theoretical h0 (µm)

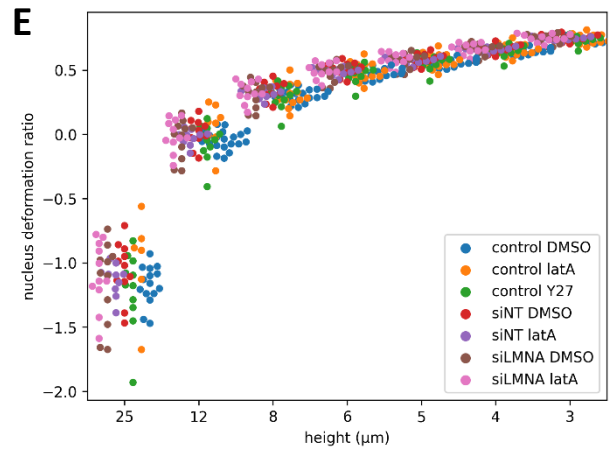
E
nucleus deformation ratio
height (µm)
control DMSO
control latA
control Y27
siNT DMSO
siNT latA
siLMNA DMSO
siLMNA latA

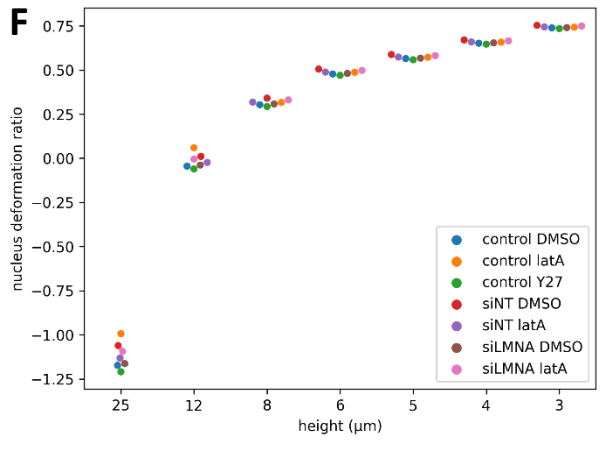
F
nucleus deformation ratio
height (µm)
control DMSO
control latA
control Y27
siNT DMSO
siNT latA
siLMNA DMSO
siLMNA latA

Using the images acquired at 25 µm, we can measure a resting height h_0 for each nucleus and convert the height into a deformation ratio. We approximate h_0 as the diameter of the nucleus in the middle plane, which assumes a spheroid shape, where the two larger dimensions are equivalent, even with shape irregularities. This is not an unreasonable assumption based on 3D reconstruction (Figure 39C). Additionally, h_0 can be estimated by the shape equations described in (Rollin, 2021). The theoretical h0 is consistently slightly higher than the measured value (Figure 39D) but the difference between the two measures is relatively small (7% error margin).

We used the theoretical h_0 for the following analyses to each height h into a deformation ratio $r = 1 - \frac{h}{h_0}$. The nucleus deformation ratio shows the heterogeneity of the cell population in terms of the nuclear size, as some nuclei are already deformed at 12 µm. All the observed conditions are similarly heterogeneous (Figure 39E) and the average values do not appear to differ significantly between conditions (Figure 39F).

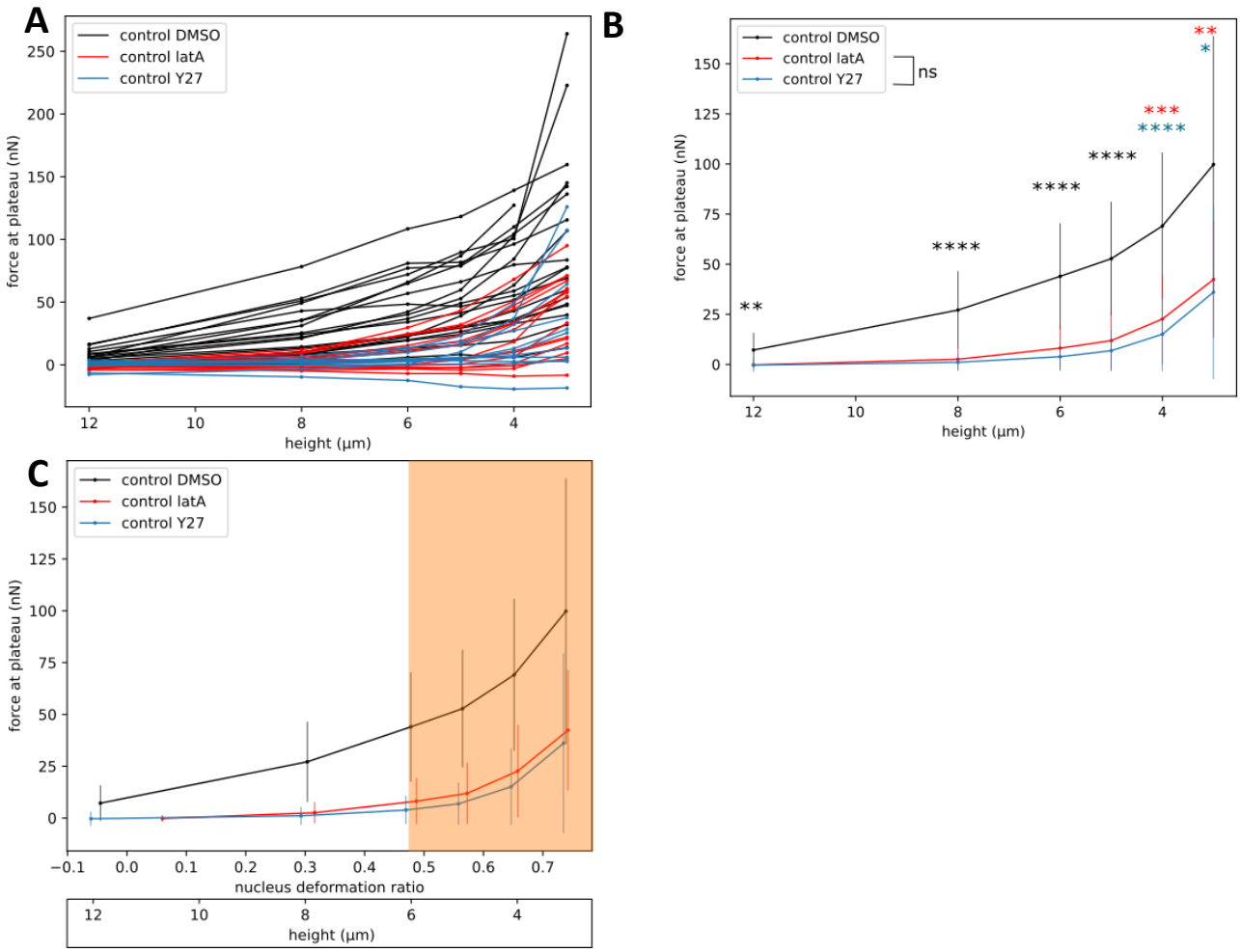

Figure 40: The nucleus becomes tense past a threshold of deformation

DMSO and latrunculin A: N=3, n=20 (DMSO) / 14 (latA), Y27632: N=2, n=11

Forces are normalized by the force at 25 µm

A. Force at peak for single cells as a function of height B. Force at plateau (median + SD) as a function of the nucleus deformation rate (statistical test: mixed-effects model on single cell values (: p-value<0.05, **: p-value<0.005, etc), black star: DMSO vs latA and Y27, red star: DMSO vs latA, blue star: DMSO vs Y27632) C. Force at plateau (median + SD) as a function of the nucleus deformation rate*

From the force trajectories, we can compute force/height curves, as shown in Figure 40A. Plotting the force responses as a function of height or nuclear deformation ratio shows that both representations are very similar (Figure 40B and C). For easier comparison with previous experiments, we will represent the deformation as a function of the height. In this part, we focus the analysis on the force at plateau (after relaxation), which represents the new steady state of the cell.

In control conditions, the force at the peak and at steady state increase as soon as the confinement reaches 12 µm height, and keep increasing steadily as the height decreases and reaches a value of a few hundred pN in average at 3 µm (Figure 40B and C, black curves). In cells treated with latrunculin A, we observe much lower forces compared to the control, both at peaks and at steady state, which is consistent with the fact that the stiffest element of the cell, the actin cortex has been removed. Strikingly, there is no increase of the force at 8 µm and a very small increase at 6 µm, but the force starts to increase below 6 µm, reaching about 25% of the control force at 3 µm height (Figure 40B and C, red curves). As the latrunculin A treatment fully depolymerizes the cortex, we sought to probe cells with an intact cortex but devoid of contractility. We use the Rho kinase inhibitor Y27632, which inhibits the contractility with only minor alterations of the cortical actin network. This treatment yields results very similar to latrunculin A. This indicates that the bulk of the cellular force response comes from the actin cortex tension due to actomyosin contractility (Figure 40B and C, blue curves). Indeed, we know from the literature that the cell cortex is the main contributor to the mechanical properties of the cell. Previous results from the lab have shown that confining the nucleus activates acto-myosin contractility (Lomakin *et al.*, 2020), which is consistent with the force increase observed in control conditions upon nuclear deformation.

As the residual force is visible in absence of contractility and actin cortex, it has to arise from internal cell components. As the nucleus is the stiffest organelle of the cell, we hypothesize that it might be the source of the residual force. We know from confinement experiments that the nuclei are strongly deformed already from 8 µm onwards and most large invaginations are lost at that height, but our analysis of NE fluctuations shows that it sharply diminishes below 7-6 µm, which is also the threshold identified to trigger the nuclear ruler pathway in Lomakin et al. The quantitative measurement of the force shows that the force in LatA treated cells increases below 6 µm, which corresponds to a nuclear deformation ratio of around 55%. We hypothesize that the force increase observed below 6 µm could be due to the increase in NE tension. This suggest a model of deformation of the nucleus with two distinct ranges. A first range would occur without NE tension until a threshold of about 6 µm, which is matching the height at which

NE fluctuations stop. Below this height, the nucleus starts exerting forces upon deformation, which we interpret as an increase in NE tension.

III. Origin of the tension in the nucleus

Among the different nuclear components, the most likely to contribute to the mechanical response we observe for confinement at low height is the lamina, and, based on prior literature (Lammerding *et al.*, 2006; Stephens *et al.*, 2017), most likely lamin A/C. In order to test this hypothesis, we performed the same AFM experiment with stepwise confinement on HeLa cells treated with a control non-targeting siRNA (siNT) or a siRNA against lamin A/C (siLMNA). If lamin A/C is indeed the main contributor to the force response when we abolish the cortical contribution, we expect to see a loss of this response in lamin A/C KD cells.

Using two rounds of siRNA transfection induces a good depletion of lamin A/C (Figure 41A). Unfortunately, the siNT appears to already affect the mechanics of the actin-depleted cell (Figure 41B and C, latA). Indeed, the increase in the force response at steady state upon decreasing the height is very slightly (and non-significantly) smaller for the siNT than the non-treated control, both in DMSO and latrunculin A (Figure 41B). This indicates that the steady-state after relaxation is associated with less force generation (Figure 41C, grey and orange curves). These experiments could be repeated with alternatives methods of siRNA transfection, such as electroporation, or be transposed in *LMNA*$^{-/-}$ cells, to obtain a cleaner control. However, comparison of the lamin A/C KD condition to its matching siNT control is already informative about its contribution to mechanical deformation.

In presence of a functional cortex, the forces generated at the plateau in response to deformation are slightly lower but not significantly in the KD cells (Figure 41D and E, black curves). In latrunculin A treated cells, the residual force at plateau is nearly abolished (Figure 41D and E, red curves). The difference with the siNT latA condition is nearly significant and the statistics could likely be improved by adding more cells.

This goes in the direction of our hypothesis that the residual force stems from the nucleus, and indicates that lamin A/C is the main contributor to nuclear tension.

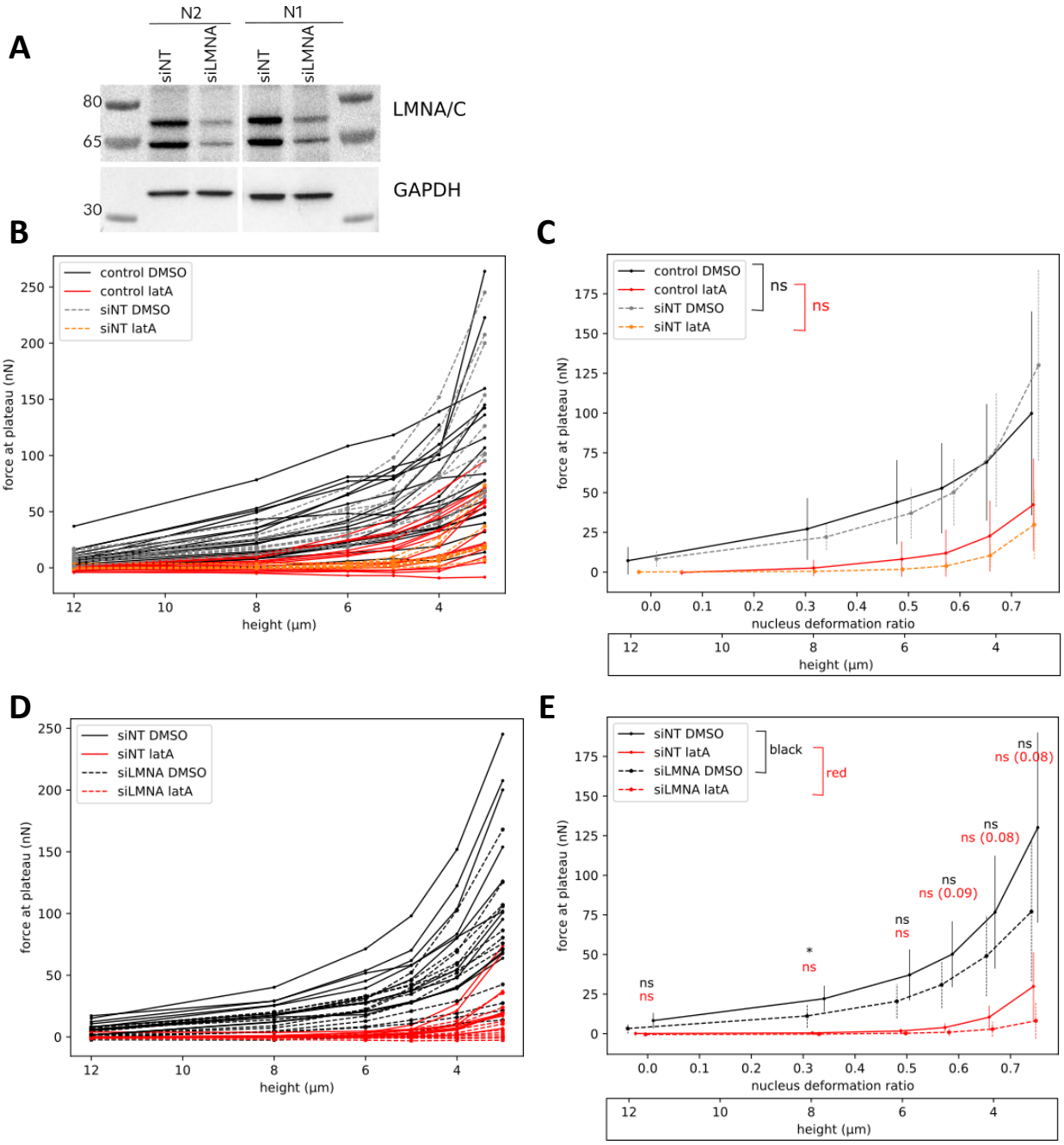

Figure 41: The lamin A/C is a key contributor to the generation of nuclear tension

N=2, n= 11 (siNT DMSO) / 10 (siNT latA) / 12 (siLMNA DMSO) / 11 (siLMNA latA)

Forces are given as a function of the cantilever height.

A. Western blot controlling KD efficiency B. Comparison of force at plateau for siNT and non-treated control for single cells as a function of height (mixed effects model) C. Comparison of force at plateau for siNT and non-treated control as a function of the nucleus deformation rate, with corresponding heights (median + SD) D. Force at plateau in LMNA KD conditions for single cells as a function of height E. Force at plateau LMNA KD conditions (median + SD) (2-way ANOVA)

We can estimate the contribution of lamin A/C to the nuclear force by comparing the forces in siLMNA latrunculin A and siNT latrunculin A conditions. At heights where the residual force exists in the siNT latrunculin A condition, *i.e.*, below 6 µm, we estimate that lamin A/C contributes to approximately 80% of the nuclear force response. (Figure 42, black histogram). Additionally, we estimate the total contribution of lamin A/C over the entire deformation to equal 84% (Figure 42, red dashed line).

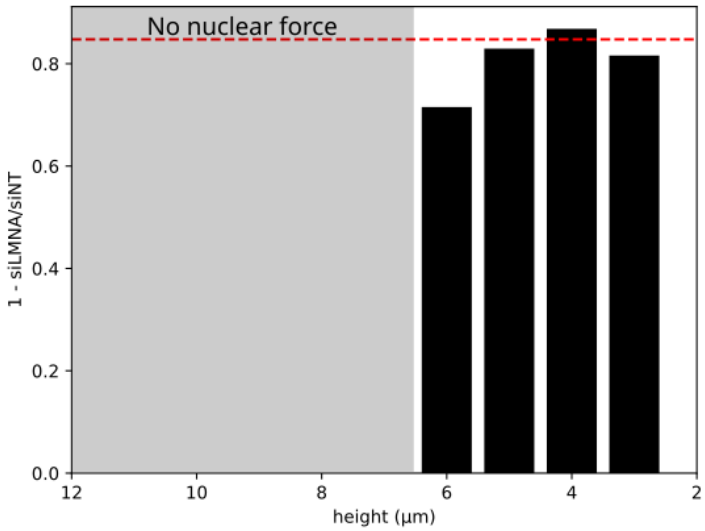

Figure 42: Lamin A/C contributes to the majority of the nuclear force upon deformation

Height-by-height lamin A/C contribution to nuclear force $\left(1 - {F(siLMNA\ latA)}/{F(siNT\ latA)}\right)$ *(grey area: no nuclear force in DMSO)*

Red line: Overall lamin A/C contribution to nuclear force response $\left(1 - {\int F(siLMNA\ latA)}/{\int F(siNT\ latA)}\right)$

As mentioned in chapter 2, lamin A/C KD is known to alter the chromatin architecture. Since large deformations rely on lamina mechanics rather than chromatin (Stephens *et al.*, 2017), we expect that it should play a minor role. Nevertheless, controlling the chromatin state in lamin A/C KD cells is required. To confirm that the chromatin contribution is negligible in our settings, we can alter the overall compaction level and forcing chromatin condensation, for example with methylstat, a demethylase inhibitor, or forcing chromatin decondensation, for example with the deacetylase inhibitor trichostatin A. However, this method is not entirely orthogonal to lamin A/C knock-down, as altering the chromatin condensation state could, in turn, affect the lamina itself.

Taken together, the experimental results support a model of nuclear envelope with a response to deformation with a sharp transition from a non-tensed to a tensed state. We show that nuclei, which are in a folded state with a fluctuating NE in rounded cells, display two regimes of response to deformation. The first regime, until approximately 50% of their initial diameter, enables deformation at low force, which we interpret as deformation without envelope tension. The second regime, below this deformation threshold which, in HeLa cells, corresponds to approximately 6 µm, associates deformation with increase in nuclear tension, mainly borne by lamin A/C.

CHAPTER 4: CONSEQUENCES OF THE TWO REGIMES OF NUCLEAR ENVELOPE TENSION ON THE PHYSIOLOGY OF THE NUCLEUS

Previous work from the lab showed that fast changes in cell shape, because they result in an increase in cell plasma membrane tension, by affecting the ion fluxes, can modulate cell volume transiently (Venkova *et al.*, 2022), a process called mechano-osmotic coupling. Although the nuclear envelop has a totally different mechanics and regulation of fluxes of osmolytes, changing its tension could also affect the volume of the nucleus, as also suggested by a recent work from collaborators (Pennacchio *et al.*, 2022). A recent theoretical work extended the classical Pump-Leak model to the case of the volume of the nucleus, termed nested Pump-Leak (Rollin *et al.*, 2023) and served as a basis for the work presented below.

I. Prediction from the nested Pump-Leak model: the two regimes of nuclear envelop tension also lead to two regimes of nuclear volume changes upon deformation

The nested Pump-Leak model can be extended to introduce the additional constraint of the tension in the lamina (Rollin *et al.*, 2023). We assume that at the timescale we are considering (minutes), ions and metabolites are equilibrated through the NPCs. Therefore, the osmotic pressure in a compartment depends only on the amount of proteins. We can express the osmotic pressure difference at the NE, with the cytoplasm as reference, as $\Delta\Pi = \frac{N_N}{V_N} - \frac{N_C}{V_C}$, with N_N and N_C the respective amounts of proteins in the nucleus and the cytoplasm, and V_N and V_C their respective volumes. If we now compute the hydrostatic pressure difference, we can express it after doing the balance of forces at the NE and we obtain $\Delta P = 2\gamma$ C, with γ the NE tension and C its curvature. Because we consider the steady state, we have $\Delta P = \Delta\Pi$.

Therefore, at very low-tension level in the NE, γ is close to or equal to 0, leading to $\Delta P = \Delta\Pi \approx 0$. In these conditions, the nuclear volume then is predicted to simply depend on the protein content of the cell and the cytoplasmic volume: $V_N = \frac{N_N}{N_C} V_C$. However, when the tension starts to increase, $\Delta P > 0$ and this simple relationship is not conserved. In that case, the intranuclear pressure increases, which leads to water efflux and volume decrease.

Therefore, the model predicts that as long as the NE tension is close to 0, the volume should not change. Conversely, increased NE tension would induce an increase in intranuclear pressure and thus a nuclear volume decrease.

II. Experimental validation of model prediction

In order to test this prediction, we first took advantage of the combined height precision and imaging of the AFM. We calculated the volume using the shape equations defined in (Rollin, 2021) on the cells treated with latrunculin A.

As predicted by the theory, the nuclear volume is approximately constant, or slightly increasing, until the cantilever height reaches 6 µm (Figure 43A), which corresponds to a nucleus deformation ratio of about 60% (Figure 43B). Below this height, which, based on results shown in Chapter 3.2, correspond to the height where the nucleus becomes tensed, the nuclear volume decreases. At 3 µm, it has lost up to 30% of its initial volume. Volume loss starts when the force applied on the nucleus exceeds 5 nN (Figure 43C).

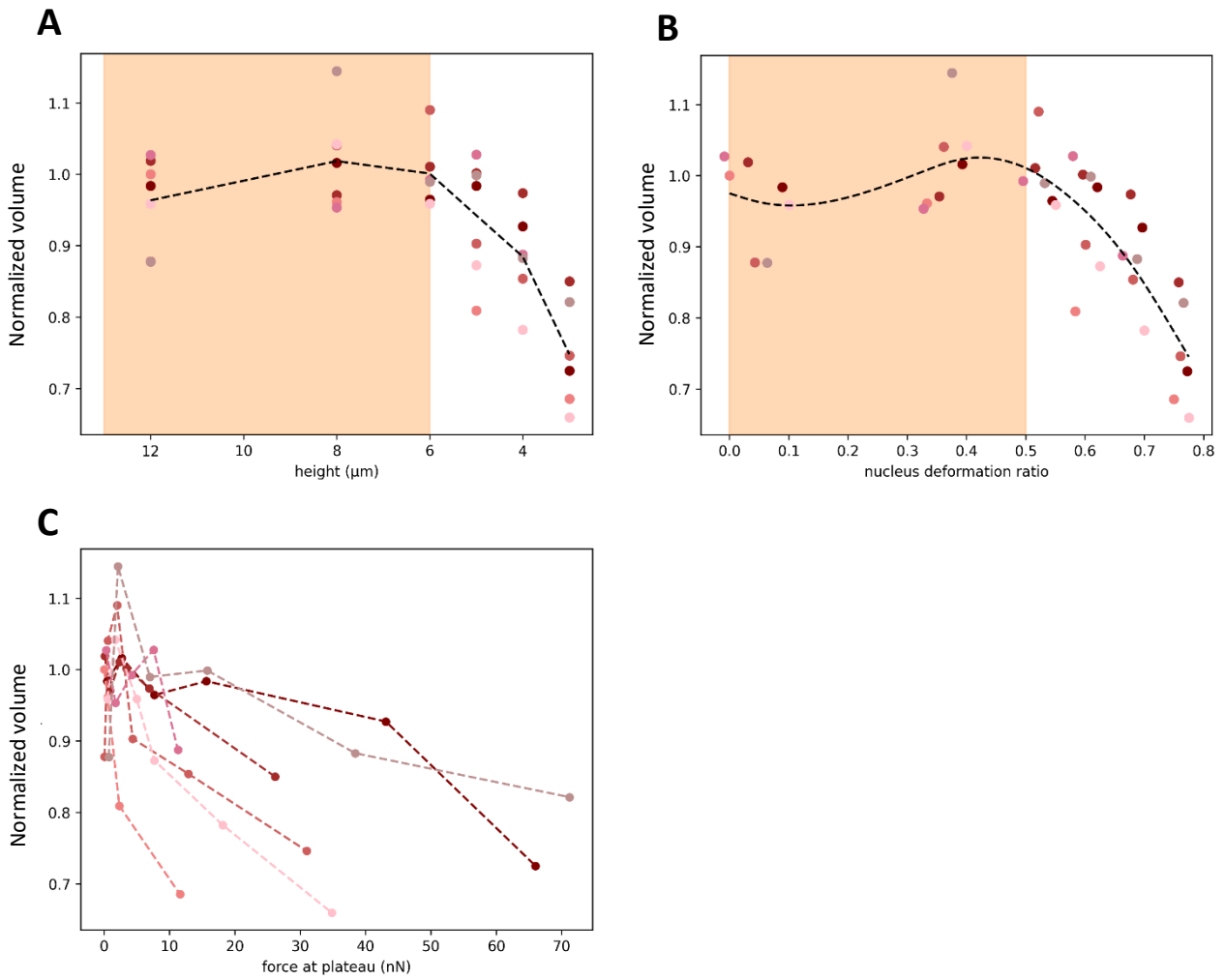

Figure 43: Two-regime volume response under AFM deformation

N=2, n=6, volume normalized to 25 µm value

A. Normalized volume as a function of cantilever height (black: average values) B. Normalized volume as a function of nucleus deformation ratio (black: smooth fit) C. Normalized volume as a function of the force at plateau

As these measurements are done only on a few cells, we moved to the static confiner in control conditions to confirm this finding on a larger cell population. Thanks to the AFM experiments, we know whether the NE is tensed or loose at the different nuclear heights. As described in the methods, we make the geometrical assumption of a cylinder for nuclei, so that the volume can be obtained by multiplying the projected area by the average height of the nucleus. We observe that for a range of deformation from non-confined to 5 µm, the nuclear volume is barely altered, remaining approximately at 750 μm^3 (Figure 44A). Below this threshold, the nuclear volume is decreasing sharply and reaches 450 μm^3 at 3 µm nuclear height. Of note, the volume dispersion is very large. As we are looking at an entire population, there is a diversity of cell cycle stages which may increase the variability. S/G2 cells are markedly less folded than their G1 counterparts (Lomakin *et al.*, 2020).

As indicated by the results with the AFM, the nuclear volume two-regime response is observed in latrunculin A-treated cells, showing that this behavior is largely independent on the actin cytoskeleton. Using the static confiner, we perform the same experiment at the population level. Overall, the behavior of the latrunculin A treated cells is very similar to the control. The resting volume at the plateau is slightly higher than the DMSO control but it remains constant at 700 μm^3 until 5 µm nuclear height before decreasing to slightly less than 600 μm^3 at 3 µm nuclear height (Figure 44B).

Additionally, while we are lacking force measurements in MDA-MB-231 cells, we observe a similar trend. Nuclear volume remains constant at 600 μm^3 until 5 µm, before decreasing to 500 μm^3 (Figure 44C). The volume loss is less dramatic than in HeLa cells and could be explained by lower nuclear forces.

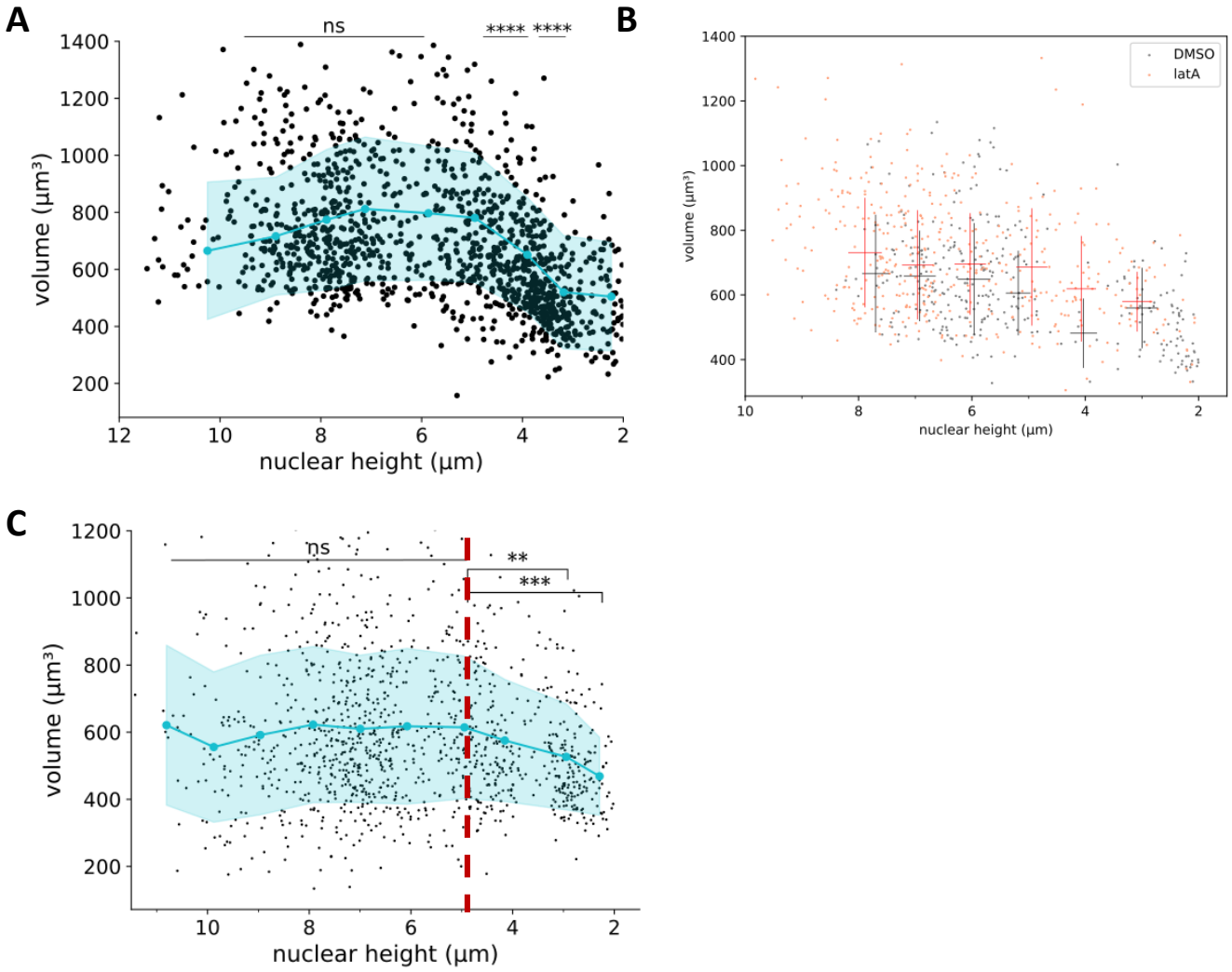

Figure 44: Volume response to deformation at the population level

Kruskal-Wallis test, plotted median + SD

A. HeLa nuclear volume as a function of nuclear height (N=6, n=1234) (1 µm bins) B. HeLa nuclear volume as a function of nuclear height, treated with DMSO or latrunculin A (N=3, n=749)

C. MDA-MB-231 nuclear volume as a function of nuclear height (1 µm bins)

The predictions of the model are qualitatively validated: there is a range of deformation, until 5 to 6 µm in HeLa, where the nucleus deforms without volume loss, in an actin-independent fashion. Because of the noise present in the data at the population and the dependency of the theory on the initial nuclear height, we tested the model quantitatively on the results from the AFM-based confinement. We considered the cells treated with latrunculin A, as the model does not take into account the cytoskeletal forces.

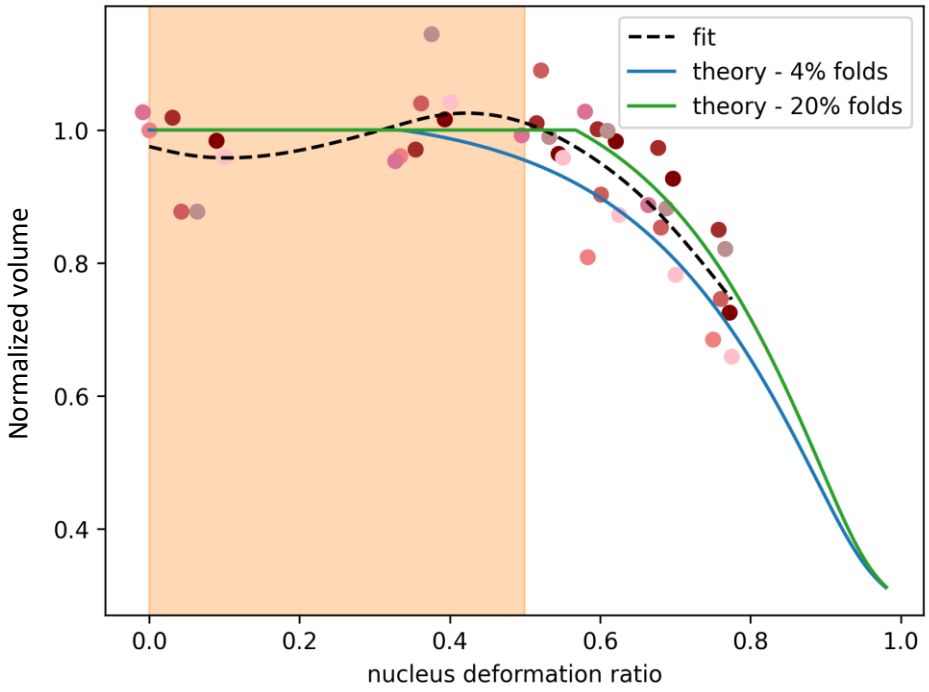

Figure 45: Comparison between model predictions and experimental data
Mean squared error: 4%: 0.1076, 20%: 0.1074

Both models are fitting the data adequately and have similar levels of mean squared error. We will be testing different proportions of folds to fit the experimental data best. Refinement of the model to include cytoskeletal could also be informative.

Taken together, these findings show that there are two regimes of volume response to nuclear deformation. The first one occurs without volume loss, while below a threshold of approximatively 5 µm, the nucleus starts losing volume. This behavior is conserved between HeLa and MDA-MB-231 cells. Based on the AFM experiments, we show that the two regimes of volume response match the two regimes of NE tension: while the NE tension remains low, there is no volume loss, and when it starts to increase, the volume starts to decrease. The threshold for both NE tension and volume loss is situated at 5 µm. There is a qualitative agreement with the theoretical predictions estimations of both 4% and 20%, which at the moment does not take into account any cytoskeletal forces. These results would indicate that while the threshold separating the two regimes does not depend on the actin cytoskeleton (meaning that the percentage of folds in the NE does not depend on actin), actin filaments could play a role in the strength of the volume decrease below the threshold, potentially by participating in modulating the NE tension upon confinement.

Of note, while we distinguish here the model predictions for different hypotheses of NE surface excesses, the experimental data is very noisy and this cannot be used to actually estimate the amount of folds. More experiments with high resolution imaging would be required to estimate the amount of reservoir in the different conditions.

III. Role of the lamina in the volume response

A logical prediction from the model is that perturbation preventing NE tensing would prevent the volume loss, and, conversely, that increasing the NE tension would facilitate a volume decrease. In order to test this prediction, we perform a lamin A/C KD following the same protocol to prevent NE tension increase.

The behavior of the siNT condition is slightly different than the fully non-treated control, as the nuclear volume decreases already between 7 and 6 µm from 800 μm^3 to 700 μm^3, and it decreases slightly below 4.5 µm, reaching 600 μm^3 at 3 µm (Figure 46A). The volume at plateau of the siLMNA is slightly higher than the siNT control (900 μm^3 vs 800 μm^3) and seems to decrease slightly less as well, reaching 700 μm^3 at 3 µm (Figure 46B).

We chose to separate the data by the position of the nuclear height compared to 4.5 µm. Nuclear force measurements in Chapter 3. II. indicated a steep increase below 5 µm confinement height, for which 4.5 µm is the lowest measured nuclear height. Plotting the values in this manner shows again that the resting volume of lamin A/C KD cells is slightly higher than control (Figure 46C), and indicates a trend of smaller volume decrease, although it is not significant (Figure 46D).

Because of the noise in the data, we are currently analyzing the results from the confinement performed by AFM.

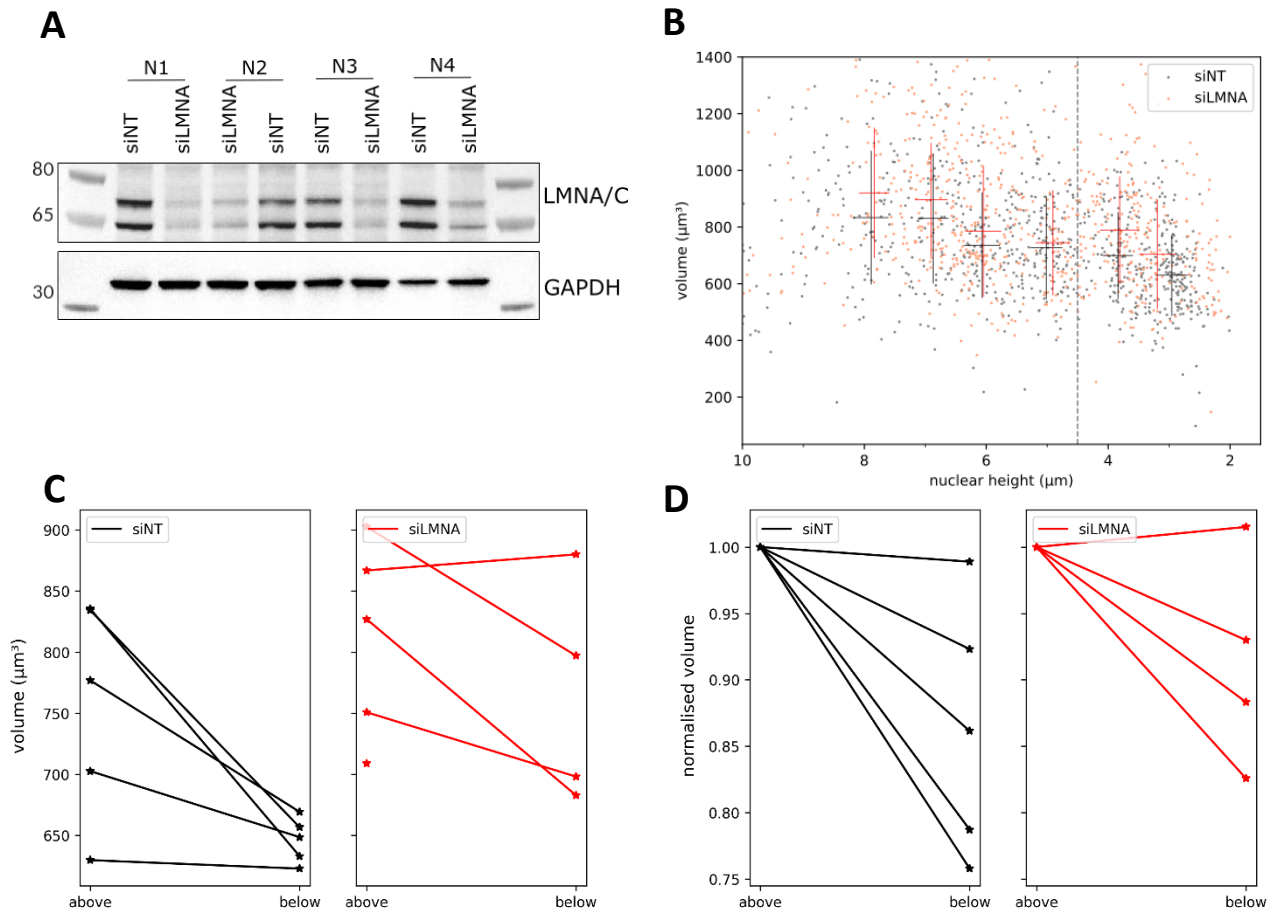

Figure 46: Lamin A/C KD effect on the nuclear volume response

A. Western blot to validate KD efficiency B. Nuclear volume as a function of nuclear height in siNT and si LMNA conditions (N=5, n=759 (siNT) / 630 (siLMNA)) (median + SD, vertical line at 4.5 µm) C. Nuclear volume by separating by nuclear height position compared to 4.5 µm (median by experiment) (Friedman test: ns) D. Normalized nuclear volume above and below 4.5 µm (median by experiment, normalized by value above 4.5 µm) (Friedman test: ns)

DISCUSSION

I. Summary of the main findings

In this work, we have shown that nuclei, far from being only smooth spherical objects, can assume a large variety of shapes. *In vivo*, while the nuclear envelope is smooth and oval in cells on the flat layer at the surface of the embryo, the nuclei in the inner mass can display deep, inward folds. This can be reproduced *in vitro* by modulating the cells' spreading area, which led us to hypothesize that mechanical constraints could lead to opening of the NE folds. Indeed, 2D uniaxial mechanical confinement induces gradual NE folds opening. We used different metrics to measure the degree of folding, such as the EFC ratio, which had been proposed in (Lammerding *et al.*, 2006), the fraction of highly curved NE and the fraction of deep NE far from the convex hull. The NE unfolding is reversible, as releasing the confinement leads to formation of new folds. Interestingly, when folds were completely opened, they reformed in places different from their pre-confinement position. This suggested us that they might originate from a dynamic instability, leading to random formation points, rather than to specific chromatin anchoring points (Lionetti *et al.*, 2020)

We proposed a model describing the chromatin as a soft elastic gel on which sits a thin rigid elastic layer, representing the lamina. The stiffness mismatch between the soft and the rigid layers, combined with the hypothesis of a surface mismatch of at least 1%, is predicted to induce NE buckling, and, for larger surface mismatches, symmetry-breaking, focalized inward folds. In order to test this model, we studied the short-term dynamics of NE re-folding after confinement release as a proxy to alter the surface mismatch between NE and chromatin. We observed that immediately after confinement release, NE folds were numerous, regular and sinusoidal. Some progressively focus and deepen, while most others flatten. These different stages qualitatively correspond to shape predictions for different degrees of surface mismatch, supporting the principle of the model. Most of this dynamic is lost upon lamin A/C knock-down.

One key feature of such a model is that as long as there is some level of folding in the NE, there is virtually no tension. It predicts therefore a range of nuclear deformation without increase of tension as long as the NE has some reservoirs it can draw from. Once it is completely unfolded, the NE should become tense. We tested this prediction with two different methods. We first showed that the nucleus deforms while the NE is still fluctuating, until a height of 6 µm. Further deformation lead to a smooth, seemingly static nuclear envelope. We confirmed this finding by quantitatively measuring forces exerted by single cells in response to mechanical confinement with AFM. We showed that in control conditions, cells exert no forces until the nucleus starts being deformed, and the forces then gradually increase with the

deformation. In absence of the actomyosin cortex, or when contractility is inhibited, most of the force response disappears. A residual force is observed starting from 6 µm and increasing as the confinement becomes stronger. The nucleus is the stiffest organelle in the cell and the threshold of apparition is reminiscent of the height at which the NE stops to fluctuate. We proposed that the residual force we saw in absence of cortex and myosin activity was originating from the nucleus. We validated this hypothesis by showing that 80% of the residual force disappears in absence of lamin A/C. Taken together these results confirm the model prediction: in HeLa cells, the nucleus is able to deform without tensing until a confinement height of 6 µm. Below this height, it becomes tense and most of the tension is supported by the lamin A/C.

The nested pump-and-leak model proposes an explanation for nuclear volume at steady-state, and also predicts its behavior when adding tension in the nucleus/cytoplasm interface: the existence of a regime of deformation without NE tension lead to the prediction of a deformation without volume loss. While there is no tension in the NE, the nuclear volume is entirely determined by the osmotic balance between the cytoplasm and the nucleus. However, when the NE is tensed, an additional mechanical component contributes to the force balance at the nuclear envelope and leads to increased intra-nuclear pressure, which would be resolved by increased intra-nuclear osmotic pressure, *i.e.* volume loss. We confirmed this prediction both on single cells and on the population level.

With this work, we propose a mechanical model for the NE folds observed in cells subjected to low mechanical stresses. Its two major implications are a two regime response of the nucleus to mechanical confinement, first in terms of nuclear tension, and as a consequence, of nuclear volume. For a range of deformation, corresponding, in HeLa cells, to confinement heights greater than 6 µm, the nucleus is able to deform without increasing its tension and without altering its volume. When confinement reaches below 6 µm or lower, the nucleus becomes tensed and starts losing volume. We thus propose the nuclear surface as a key factor in the ability of the nucleus to deform without altering its tensile state and sustain constraints.

II. Technical limitations

A. Nuclear envelope detection

One of the recurrent drawbacks we faced lied in the precise detection of nuclear envelope folds. Because shapes can be very irregular already in 2D, automated methods are not always accurate and tend to smooth the contours. As they are precisely what we want to measure, we could not rely on such methods and often had to semi-manually define the NE contours. While this can be done for snapshots, it becomes impossible to do it for movies. Collaborators are currently trying to train AI-based algorithms to precisely detect the shape in 2D and, hopefully, in 3D.

B. Lamin A/C knock-down

One of the important predictions of the model is that if the nuclear tension is not increasing, the nuclear volume should not decrease. We initially tried stable cell lines with shRNA, that gave a very good depletion level without altering lamin B1 and lamin B2 levels, but that was lost after a freezing-thawing cycle. Moreover, the results in AFM were very surprising, as the force response of LMNA sh cells treated with latrunculin A was higher than the LacZ sh cells.

Unfortunately, the results observed at the whole-population level are very variable, perhaps owing to cell-cycle stage differences. We are currently analyzing the AFM-based images to calculate the volume trajectories at the single-cell level using the shape equations from (Rollin, 2021), where we expect a smaller volume loss compared to control.

III. Load-bearing capability of the nuclear envelope

A. Challenges of nuclear envelope fluctuations quantification

In our experiments, we did not test whether the tension in the lipid bilayers themselves increased. As discussed in the Chapter 3.1 of the results, we assessed NE tension indirectly by measuring NE fluctuations. While the movies are giving very obvious differences between non-confined cells, cells confined at 8 µm and cells confined at 5 µm and below, our current quantification is not capturing the information we have. The chief reason is the difficulty to detect the NE precisely enough that a few pixel displacements are detected. Algorithms developed by (Almonacid *et al.*, 2019) give quantifications over the entire contour with a very good dynamic range but rely on full intra-nuclear staining, such as NLS-GFP or Hoechst, rather than NE labelling, and do not solve the issue of NE detection. Once we have a better

detection method, we hope to be able to give a better quantification on the movies we already have acquired, but the measure would still be indirect.

B. Methods to assess nuclear envelope tension

AFM measurements provide a very quantitative measure of nuclear forces but, as the results in Chapter 3.3 showed that they are mostly born by lamin A/C, but the question remains whether this is accompanied by an increase of tension in the membranes themselves. There are only few methods to investigate this question. A FRET sensor in the nesprin head was built to measure the force exerted by the actin cytoskeleton on the NE through the LINC complex (Déjardin *et al.*, 2020). In absence of force, the two moieties of the FRET pair are in close enough proximity to obtain FRET, while in the presence of a pulling force, they grow apart and the FRET signal decreases. We observed in preliminary experiments in 3T3 with dynamic confinement that upon confinement at 3 µm, the FRET signal decreases, indicating that confining induces a pulling force by the actin on the nucleus. This is reversible, as releasing the confinement restores the initial level of FRET signal, and abolished in presence of latrunculin A. However, this measures the tension in the nesprin and not in the lipid bilayers.

A Fluorescence Lifetime Imaging Microscopy (FLIM) probe was developed a few years ago (Colom *et al.*, 2018), called Flipper, that inserts into membranes and whose fluorescence lifetime depends on the packing and the geometry of lipid-lipid interactions. It was proposed as a lipid tension sensor by showing that the lifetime increased upon hypoosmotic shock. Initially developed for the plasma membrane, an ER probe was recently released. We had some technical difficulties finding the correct staining parameters to have an acceptable NE staining, as well as the imaging parameters. Additionally, the hydrophobic probe binds PDMS and cannot be combined with the static confiner, which means that only short term experiments with the dynamic confiner are possible. We are currently working with the lab of Aurélien Roux to develop a probe that could be targeted specifically to the NE.

Because of the continuity of the ER with the ONM, it is unlikely that the ONM could ever lack reservoir and be stretched to the point of tension. However, as discussed in the introduction, the INM could be sufficiently isolated from the ONM by the NPC to reach this point. We hypothesize that when the lamina is tensing at confinement heights of 5 µm and less, the INM becomes tense as well. We propose that this is the basis for the confinement-dependent cPLA2 activation reported by the literature (Lomakin *et al.*, 2020; Venturini *et al.*, 2020), as well as the mechanosensitive nuclear import described for YAP/TAZ and other transcription factors (Elosegui-Artola *et al.*, 2017; Andreu *et al.*, 2022).

IV. Dynamics of force and volume response at different timescales

In this thesis, I have focused on the nuclear responses at a timescale of minutes: 3-4 min in the force and volume responses by AFM and approximately 30 min for the volume response at the population level. However, different parameters are likely to come into play depending on the timescale that is considered. At a timescale of seconds, physical parameters such as nuclear poroelasticity and the fluxes of water are likely to be prevalent. At the intermediate timescale of minutes, which was considered in this thesis, we assume constant protein content, because even if the import rate is immediately altered, time is required for it to significantly impact the amount of proteins, and the main players are the force and nuclear tension. This is not likely to hold true at longer timescales of hours, in which the protein content itself can change due to changes in import/export.

A. Force response dynamics upon confinement

As we mentioned in Chapter 3.2 of the results, the AFM experiments yield a large amount of information. The analysis so far has focused on the plateau as the new steady-state of the cell, but the whole curve contains more information that we have only started to exploit. In particular, the force curves during the lowering of the cantilever and during relaxation can provide physical parameters for the short timescale dynamic response.

The force during the ramp, normalized to the force at peak, is exponential for height transitions until 6 µm height (Figure 47A), which is consistent with a model of deformation without any volume loss. This fits with the longer-term response we showed in Chapter 4.II. of the Results, based on the shape equations proposed in (Rollin, 2021). However, when the cantilever is lowered to heights lower than 5 µm, the ramp curve becomes linear, which is not possible to explain if we do not suppose that the nuclear volume decreases during the deformation. Interestingly, this transition occurs at the same threshold as the apparition of nuclear tension and volume loss, suggesting that the short term response can be indicative of the threshold between the two regimes of deformation. We wonder whether we observe this very fast volume loss because the deformation imposed by the cantilever is comparatively slow (0.5 µm/s). We are currently repeating the experiments with faster cantilever lowering to see if the volume loss during deformation is lost when the deformation speed increases.

The relaxation curves also depend on the height. Until 6 µm height, the relaxation times are similar when comparing the forces normalized to the value at peak. The relaxation time at 5 µm and 4 µm increases

slightly compared to the previous heights, while the normalized relaxation curve at 3 µm indicates that the relaxation is not complete in the acquisition time (Figure 47B). Interestingly, the threshold of nuclear tension appears again in the relaxation time. We are currently repeating the experiments with a longer acquisition time to confirm our estimation of the force at plateau is correct.

These quantifications have been realized on only one cell so far and must be repeated. Nevertheless, this confirms with different measures that the nuclear tension increases at 5 µm, while the mechanical properties of the nucleus remain constant until this height is reached. The two-regime tension response appears confirmed with these additional quantifications.

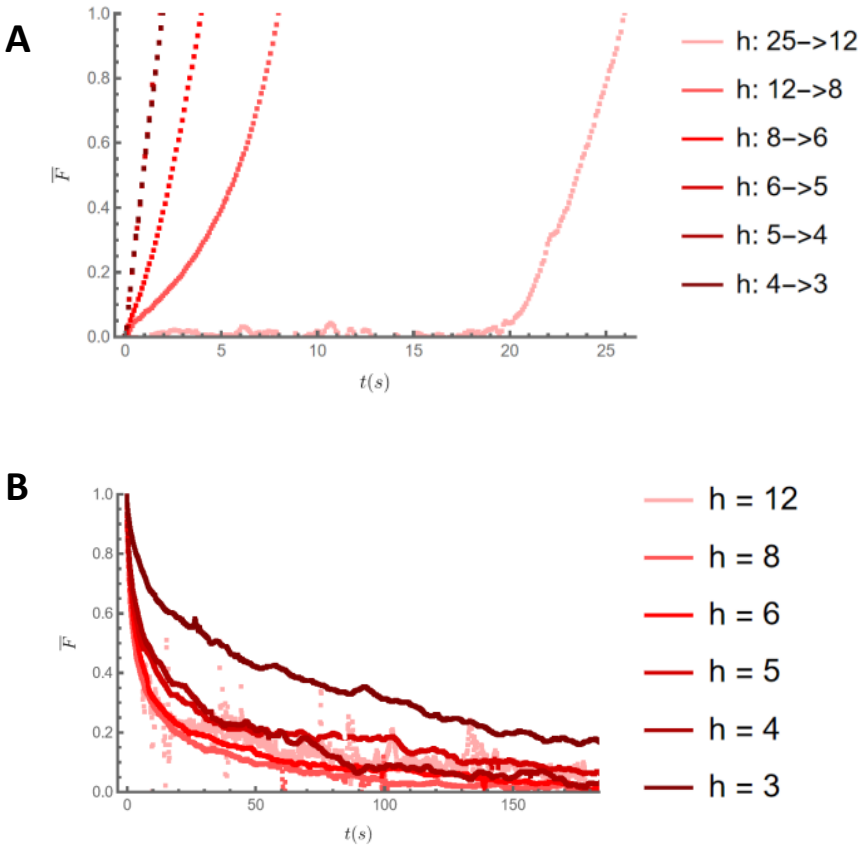

Figure 47: Short term dynamics of nuclear force in response to AFM deformation

Curves of one cell

A. Normalized force as a function of time during the cantilever lowering (normalized by the force at peak)

B. Normalized force as a function of time during relaxation at each height (normalized by the force at peak)

B. Long term volume measurement

All the volume measurements have been performed shortly after confinement and at only one timepoint, using the geometrical assumption of a cylinder. This method has two limits: the first is that it does not work for unconfined cells, where the cylindrical approximation is too far, and the second is the amount of light required for each acquisition. The 3D illumination is damaging enough to the cell that long-term imaging is not advised.

A method was recently published that enables measurement of both cytoplasmic and nuclear volume on an epifluorescence microscope (Pennacchio *et al.*, 2022), by an adaptation of the fluorescence exclusion method (FXM) used to measure cellular volume (Cadart *et al.*, 2018). Briefly, it relies on the classical FXM with Dextran in the culture medium for the cell volume, and homogeneous cytoplasmic labelling to extract the nuclear volume. Unlike 3D-based methods, it does not require intensive illumination, it is very well-suited to long-term imaging and reduces the risk of photobleaching and phototoxicity. With this technique, we could have a long-term acquisition and assess long-term dynamics of nuclear volume changes. It is for instance unknown whether the nucleus recovers from volume loss in the high deformation regime.

Additionally, this method has the advantage of providing the simultaneous measure of cytoplasmic volume. The cell loses volume as soon as it is confined (Venkova *et al.*, 2022), before the nuclear volume is affected, but little is known about cellular volume under high confinement. These insights could be particularly interesting to confront to the nested pump-and-leak model (Rollin *et al.*, 2023).

V. Role of the cytoskeleton in NE folds dynamics and nuclear volume response

As the nucleus is mechanically linked to the rest of the cell via the LINC complex, the cytoskeleton could play a role in changes in the NE shape that we observe upon confinement release. In particular, microtubules have been found to be required to alter NE shape in the context of early hematopoiesis (Biedzinski *et al.*, 2020). Interestingly, microtubules in this case are only required for the establishment of the folds, but not their maintenance. Moreover, unpublished from collaborators indicates that microtubules are responsible for nuclear morphology aberrations in polyploid cells (Gemble, unpublished).

We tested the NE folds reformation after confining and releasing the cells in presence of nocodazole to assess the contribution of microtubules to the phenotype. Of note, we are so far lacking the DMSO control. Nuclei display less folds in absence of microtubules than the non-treated control at steady state but NE folds do form after confinement release. They are first sinusoidal but soon seem to flatten everywhere (Figure 48A and B). This hints that microtubules might not be required for NE folds formation in our system.

Nocodazole treatment is known to activate contractility as a side effect of releasing the RhoA GEF H1 (Chang *et al.*, 2008). At the dose we used, cells display plasma membrane blebs, indicative of increased myosin activity (Figure 48C). This could explain why the folds are less present in the nocodazole-treated condition, as contractile actin fibers are able to deform the nucleus (Kanellos *et al.*, 2015; Takaki *et al.*, 2017). Additional conditions, either with lower doses of nocodazole or combined with a contractility inhibitor, such as blebbistatin or Y27632, are required to conclude on this question.

Additionally, cytoskeletal forces have been found to be involved in nuclear volume control, by modulating nuclear import (Pennacchio *et al.*, 2022). We have shown that latrunculin A treatment does not alter significantly the two-regime tension and volume response, and contractility does not affect the two-regime of tension. However, microtubules and intermediate filaments cannot be fully discounted yet. For instance, vimentin in MEFs has been shown to protect the nucleus in confined environment (Patteson *et al.*, 2019) and could for instance buffer the deformation.

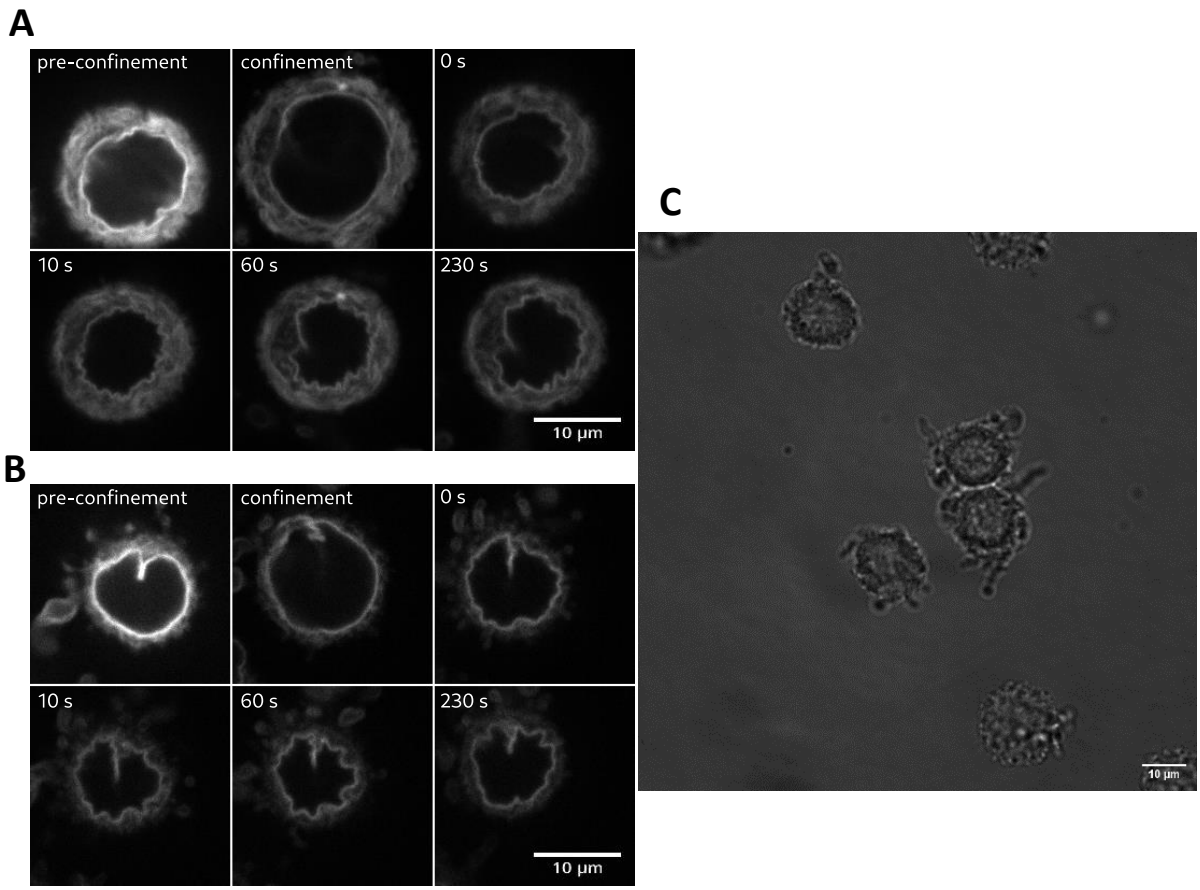

Figure 48: NE folds opening and reformation under confinement upon treatment with nocodazole
Cells were treated with nocodazole at 10 µM for 15 min before acquisition.
A. and B. Representative movies of nocodazole-treated cells before, during and after confinement
C. Brightfield image of nocodazole-treated cell

VI. Origin of the nuclear envelope excess surface

The central hypothesis of the model of the mechanical instability is that the NE has a surface excess compared to the chromatin. We hypothesize that the excess of membrane could come from the NE assembly at the end of mitosis, before chromosome decondensation, and would provide membrane forming the invaginations in G1. As discussed in the introduction, INM proteins like BAF and LAP2b are recruited early in telophase (Figure 49A), and the envelope assembles from ER cisternae on the still-condensed chromosomes (Lu *et al.*, 2011) (Figure 49B).

The sphere is the shape with the lowest surface to volume ratio. Since the NE assembles on an irregular, cylindrical group of chromosomes, it has an excess of surface compared to the equivalent approximate sphere the nucleus assumes when interphase cells. We propose that the geometry of NE assembly drives an excess of surface of the envelope compared to the underlying chromatin bulk, which in turn determines how large the range of "safe" deformation could be.

The main difficulty to test this hypothesis lies in the precision of 3D NE detection required to calculate the total membrane surface and monitor the nuclear volume. It could be argued that the nucleus grows upon chromosome decondensation in early G1 and that there is no excess of NE surface when the chromatin is in its interphase condensation level. In order to determine this, we need to be able to calculate the surface-to-volume ratio at the end of telophase and at the beginning of G1. Additionally, we can alter the geometry of the metaphase plate by having cells undergo mitosis under confinement, forcing it into a shape inducing less surface area excess.

If this hypothesis is validated, it could mean that the amount of available membrane deposited in late telophase determines the maximal surface area the nuclear envelope can reach. It could be a cue for mechanosensing during deformation but also for growth. As the nucleus grows in volume during the cell cycle (Pennacchio *et al.*, 2022), the nuclear envelope should unfold at least partially. A study has shown that nuclear flattening at the G1-S transition is required for cell cycle progression by inducing the activation of transcription factors AP1 and TEAD (Aureille *et al.*, 2019). This phenomenon is actomyosin-dependent but can be reproduced by confinement in absence of contractility, and the nuclear recruitment of the transcription factors is lost upon lamin A/C KD. We could imagine a model where growth and cytoskeletal forces lead to nuclear tensing, which in turn would affect transcription factors import and trigger cell cycle progression. This could be envisioned as a measure by the cell of the amount the nucleus has grown.

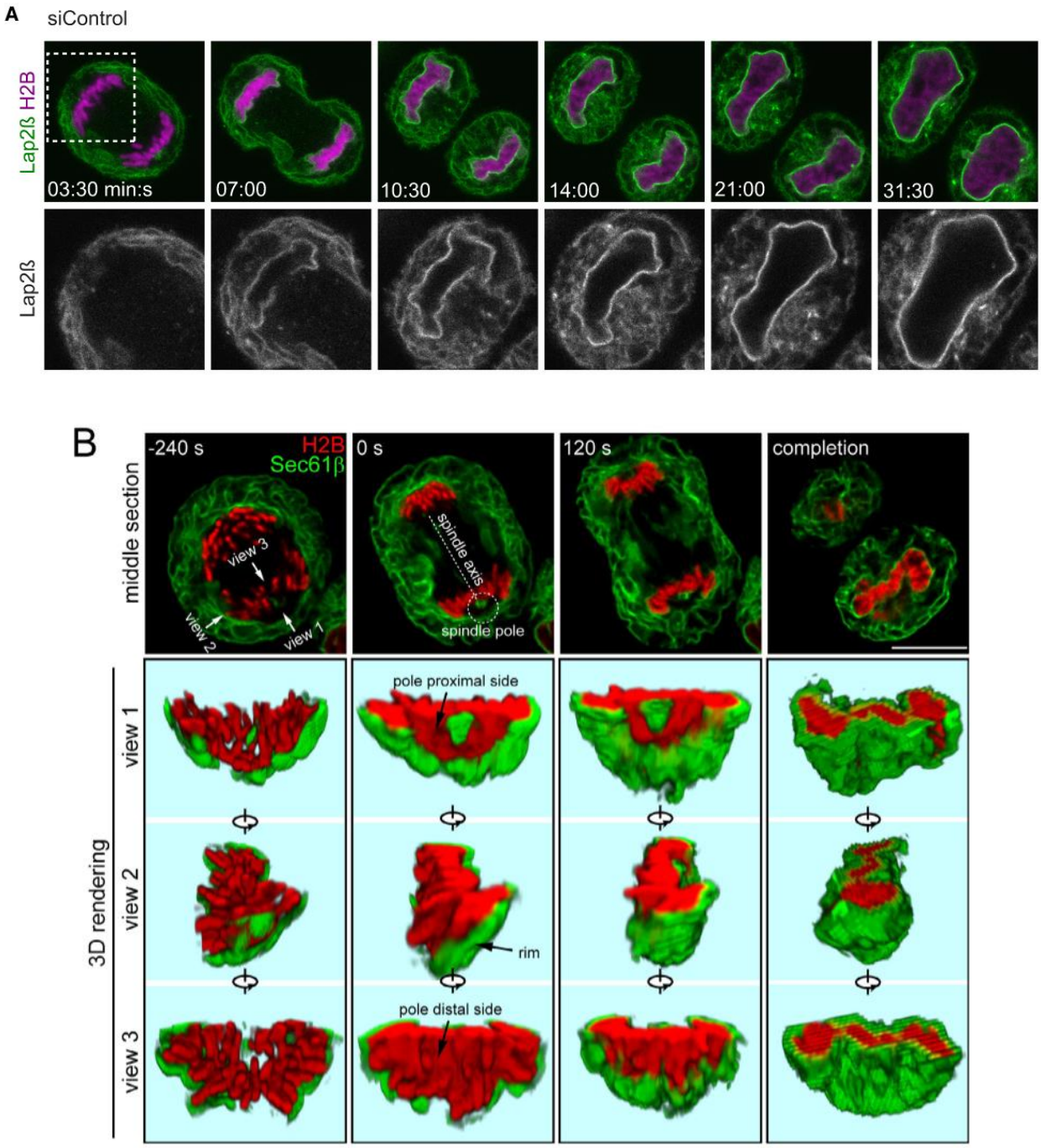

Figure 49: NE assembly after mitosis

A. NE assembly at the end of mitosis in HeLa cells (Samwer et al., 2017) B. 3D reconstruction of NE assembly at the end of and after mitosis in HeLa cells (Lu et al., 2011)

VII. Physiological consequences of the two-regime response to deformation

The nucleus is a tightly regulated compartment, where the respective concentrations of the different components participate to their proper structure and function. We propose that the regime of deformation without nuclear tension and volume loss represents a “safe” regime, enabling the nucleus to accommodate changes in the mechanical constraints in the environment. Of note, a previous study had reported a nuclear volume loss of up to 60% in micropipette aspiration experiments (Rowat *et al.*, 2006). However, the geometry in this type of experiment is very different from 2D confinement and might explain the difference.

Various nuclear processes require tight control of concentrations, which all increase upon volume loss. Liquid-liquid phase separation exists for certain ranges of concentration, and certain proteins on the edge of phase-separating could reach the critical concentration upon strong deformation. The machinery involved in DNA metabolism may also be altered, as well as the chromatin organization. There is evidence that confinement induces DNA damage replication fork stalling in MDA-MB-231 cells confined at 5 µm (Shah *et al.*, 2021).

Nuclei can sustain a wide range of mechanical constraints but they can also rupture when they migrate through narrow microchannels (Denais *et al.*, 2016; Raab *et al.*, 2016) or are strongly deformed in certain solid tumors (Nader *et al.*, 2021). In these situations, rupture events are preceded by NE blebs (Figure 50A). In HeLa cells, 30% of the nuclei display cGAS foci, indicative of NE ruptures, at 4 µm, and 70% exhibit signs of rupture at 3 µm (Figure 50B). We propose that nuclear volume loss might increase the intra-nuclear pressure to a point that the lamina and the envelope cannot sustain, thus leading to NE blebs and, eventually, ruptures.

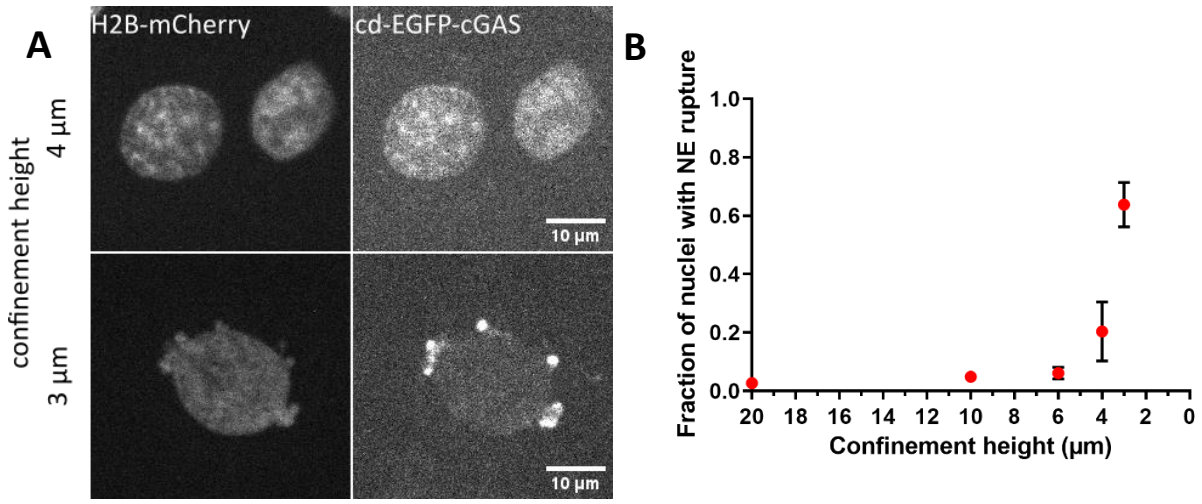

Figure 50: Nuclear envelope rupture under confinement

A. Representative images of intact (top row) and ruptured (bottom row) nuclei (cd-EGFP-cGAS: catalytically dead EGFP-cGAS) B. Quantification of fraction of ruptured nuclei depending on confinement height (N=3, n=315)

VIII. Concluding remarks

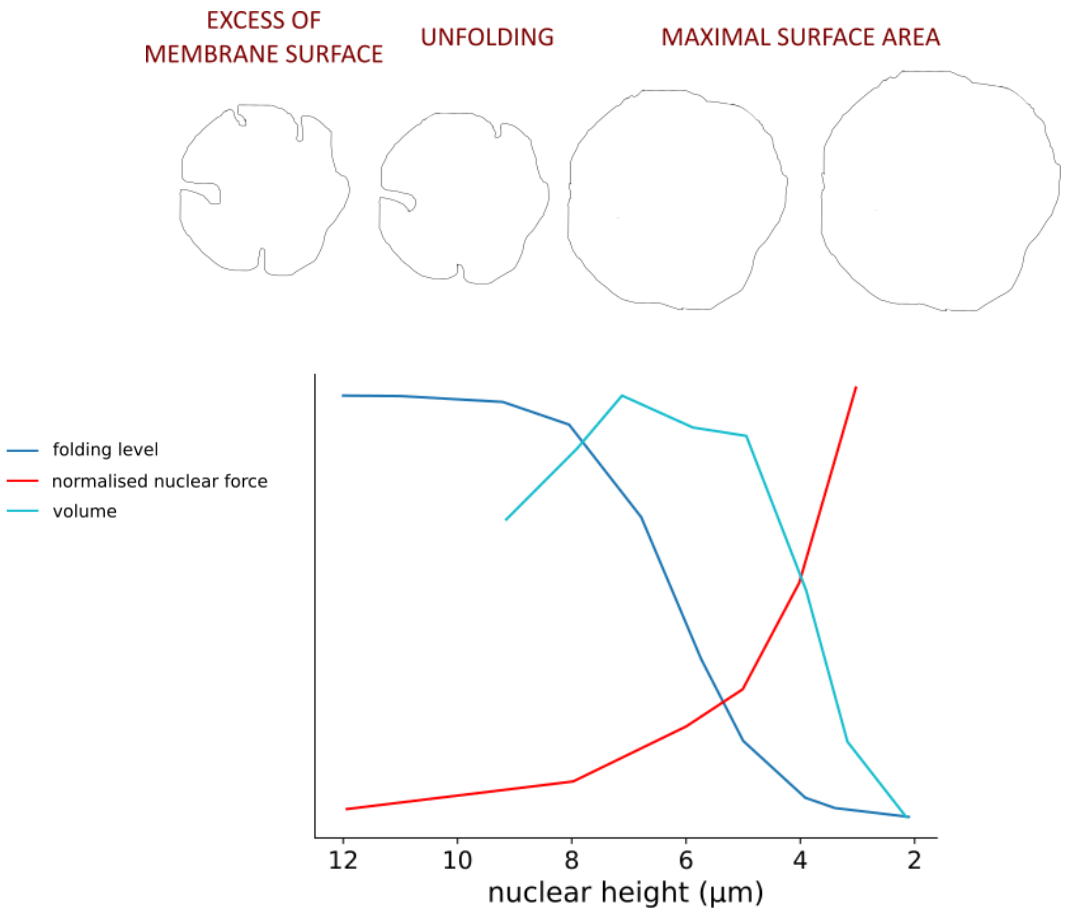

Figure 51: Working model of the nuclear response to deformation

In this work, we have examined how the nuclear envelope can alter its shape in response to deformation. We have shown that nuclear envelope folds are naturally present when nuclei are not subjected to any forces, and that mechanical constraints can open them. Nuclear envelope invaginations reform after confinement release in a dynamical fashion, which supports a model explaining their origin by a mechanical instability. We hypothesize that the instability arises from a surface mismatch between the lamina and the chromatin, taking its root at the nuclear envelope assembly in telophase. The existence of folds implies that the nuclear envelope holds no tension in resting, non-adhering conditions, and the model predicts that, as long the nuclear envelope has folds, deformation can occur without nuclear tension. We confirm this prediction and show that the nucleus deforms in two regimes, first without generating any tension, then, below a deformation threshold, by building tension in the lamin A/C meshwork. An adaptation of the nested pump-and-leak model (Rollin *et al.*, 2023) predicts that as long as

the tension at the nuclear envelope is low, the nucleus should keep a constant volume. This prediction is confirmed in two deformation settings and we show that the two-regime volume response is largely independent of the actin cytoskeleton.

We propose that this two-regime response enables the nucleus to adapt to a range of mechanical constraints without altering its properties. Nuclear tension is a signal detected by the cell (Lomakin *et al.*, 2020; Venturini *et al.*, 2020) and triggers a variety of signaling pathways (Elosegui-Artola *et al.*, 2017; Alraies *et al.*, 2022). We propose that the nuclear volume loss resulting from nuclear tension increases intra-nuclear pressure, eventually causing nuclear envelope ruptures.

APPENDIX A: HIV infection and mechanical constraints

INTRODUCTION

The Human Immunodeficiency Virus (HIV) comprises two viral species, HIV-1 and HIV-2. It is a human lentivirus, belonging to the family *Retroviridae*, subfamily Orthoretrovirinae. Its diploid ssRNA viral genome is rapidly reverse-transcribed into DNA by the viral reverse transcriptase. A nucleoprotein complex containing the newly synthesized viral DNA, known as the pre-integration complex, is then translocated into the cell nucleus, where the viral integrase mediates successful integration of the viral DNA into the host genome (Bhargava *et al.*, 2018).

Unlike HTLV, which requires NEBD and mitosis, HIV is able to cross the intact NE in interphase (Bhargava *et al.*, 2018). While it was long thought that only the pre-integration complex entered the nucleus, intact capsids have been shown to cross the NPC (Zila *et al.*, 2021) and have been observed inside the nucleoplasm (Peng *et al.*, 2014; Chin *et al.*, 2015). This indicates both the high plasticity of the NPC and the efficiency of the virus in hijacking host transport routes. The importance of the NE crossing in HIV cycle is highlighted by the interactions of the capsid with NPC components, such as Nup153 (Di Nunzio *et al.*, 2013).

Independent works have shown that INM proteins SUN1 and, to a lesser extent SUN2, play a role in HIV infection. Both overexpression and knock-down of SUN1 strongly decreases infection levels (Lahaye *et al.*, 2016; Schaller *et al.*, 2017; Luo *et al.*, 2018; Bhargava *et al.*, 2021), and similar effects are observed for SUN2 (Donahue *et al.*, 2016, 2017; Lahaye *et al.*, 2016). Because SUN proteins are key in mechanical properties of the nucleus, and since the nuclear shape is strongly altered when SUN2 is overexpressed (Donahue *et al.*, 2016; Lahaye *et al.*, 2016), we made the hypothesis that mechanical constraints might affect the nuclear steps of HIV cycle. This axis was the initial direction of my PhD project.

MATERIAL AND METHODS

I. Virus and viral particles preparation

VSVG-pseudotyped lentiviral particles containing pTRIP-SFFV-tagBFP-2A were prepared as described in Material and Methods – Transduction. Viral particles are produced in HEK293FT by transfection of 2.6 µg of viral genome (HIV-GFP Vpr+ Vif+ Vpu+ Env- Nef-) and 0.4 µg of pVSVG, using the TransIT reagent.

II. Cell lines

Transfection experiments were performed on HeLa Kyoto stably overexpressing H2B-mCherry and a catalytically dead version of EGFP-cGAS. Infection experiments with HIV-GFP were performed on HeLa Kyoto without any labeling.

III. Infection and transfection under confinement

Cells are plated in T75 flasks and were transfected with pTRIP-SFFV-tagBFP-2A or infected with HIV-GFP in presence of protamine at 1 µg/mL at a final v/v dilution of 1/5 the next day. The virus is washed 3.5 hours after infection and cells are confined at different heights on 6-well glass bottom dishes for 14 hours, following the protocol described in Material and Methods – Confinement – Static confiner. The time window was chosen to cover the nuclear entry and integration steps in HeLa cells (Dharan *et al.*, 2020). For coating the glass with poly-L-Lysin-g-PEG, the plates are plasma-activated and incubated with pLL-PEG in HEPES at 0.5 µg/mL for 1 hour. The confinement is lifted and cells are recovered the next day. They are plated and cultured for 48 hours. Infection levels are then analyzed by flow cytometry.

IV. Infection on different spreading surfaces

Glass-bottom 6-well plates were plasma-activated and incubated with HEPES 10 mM pH 7.4, fibronectin at 1 µg/mL or poly-L-Lysin at 0.5 mg/mL resuspended in HEPES for 1 hour at room temperature. Cells seeded at 0.5 M/well and let overnight. Cells were transfected with pTRIP-SFFV-tagBFP-2A or infected with HIV-GFP in presence of protamine at 1 µg/mL at a final v/v dilution of 1/5 the next day. Cells on fibronectin were additionally treated with DMSO or Y27632 at 5 µM for the duration of the experiment. The medium was washed after 48 hours, cells were fixed in PFA 1% in PBS and analyzed by flow cytometry.

RESULTS

I. Transfection efficiency is not affected by spreading conditions

As a first approximation of changes in mechanical constraints, we plated cells n different spreading substrates: plain glass and glass coated with fibronectin, two conditions where the cells can easily spread, glass coated with fibronectin and treatment with the contractility inhibitor Y27632, which releases the forces exerted by actomyosin, and glass coated with pLL, where cells can adhere but not spread.

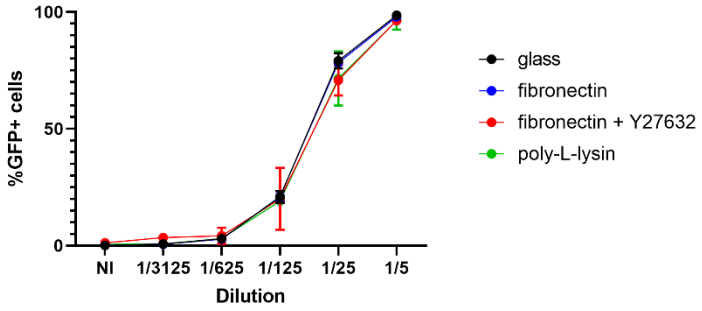

Figure 52: Infection with HIV-GFP is not affected by plating on different substrates
Statistical test: 2-way ANOVA – no effect of coating

We do not observe any difference between conditions at any dilution (Figure 52). However, since the transfection occurs in the different spreading conditions on cells that are already spread, it is not possible to disentangle potentially contradictory effects on particle entry and cytoplasmic or nuclear stages.

II. Transfection efficiency decreases with confinement

In order to have more controlled deformations, we moved to a static confiner system to impose different heights to the cell. We first started to use a lentivral vector with a pTRIP-SFFV-tag-BFP-2A genome that recapitulates entry and import of the actual virus, without accessory proteins. We infected the cells and wait for 3 hours until the particles were inside the cells before confining them at various heights. In order to focus on the nuclear steps of the cycle, we took advantage of the timeline described in (Dharan *et al.*, 2020) for HeLa cells and defined a time window between 3 and 17 hours post infection.

We performed the experiment first using a simplified model system consisting of a lentiviral particle expressing the BFP. Due to experiment-to-experiment variability, we obtain different infection levels in the control, non-confined 20 µm confinement height condition (Figure 53A). Regardless of the percentage, infection levels are similar from 20 µm to 10 µm confinement height, and decrease steadily as confinement height becomes smaller. In average, the infection efficiency drops to 65% at 3 µm confinement height (Figure 53B).

We initially had the hypothesis that NE rupture might favor viral entry to the nucleus. Using cGAS foci as a reporter of loss of NE integrity, we estimated the percentage of ruptured nuclei at the different confinement heights (Figure 53C). There is nearly no rupture until 4 µm confinement height, where the percentage of ruptured nuclei reaches about 70 to 80%, both in non-transfected and transfected cells. (Figure 53D). This first shows that transfection does not affect the proportion of NE ruptures in the cells. We can conclude that NE rupture does not increase infection level.

Because we initially performed the experiments on non-coated glass dishes, we realized that cells could still spread. Spreading represents a mechanical constraint for the cell by and on itself, and typical spread cell nuclei are about 6 µm high. In order to circumvent this, we treated the glass-bottom dishes with pLL-PEG to prevent cell adhesion and spreading. The infection efficiency decreased slightly between 20 and 10 µm confinement height, increased to its non-confined value at 8 µm and decreased again below 6 µm (Figure 53E). The relative decrease appeared smaller than on glass, as the infection level drops to 80% at 3 µm on average.

Taken together, these results suggest that increased confinement of the nucleus decreases transfection efficiency. NE ruptures do not improve transfection efficiency, suggesting that access to the nucleus is not the limiting factor to transfection efficiency in confined cells.

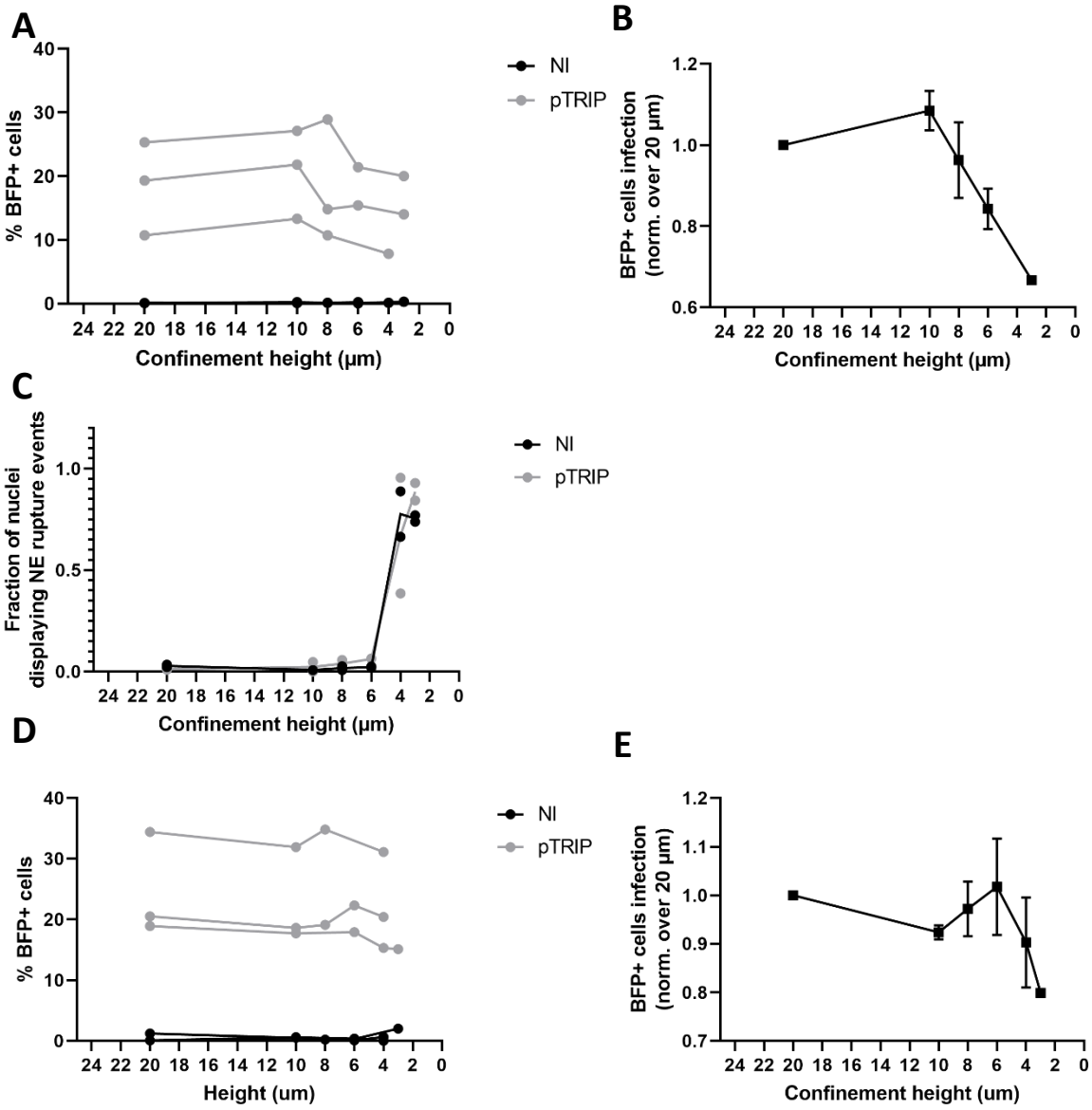

Figure 53: Efficiency of lentiviral vector transfection decreases upon confinement and is not rescued by nuclear envelope rupture

A. Percentage of BFP positive cells 48 hours post-confinement release (confinement on non-coated glass) B. Normalized proportion of BFP positive cells (normalized over level at 20 µm) C. Proportion of ruptured nuclei depending on the confinement height D. Percentage of BFP positive cells 48 hours post-confinement release (confinement on pLL-PEG coated glass) E. Normalized proportion of BFP positive cells (normalized over level at 20 µm)

III. Confinement does not appear to affect HIV infection

Assessment of the infection levels by flow cytometry gives a readout of the endpoint of the viral cycle and of the sum of all its steps: reverse transcription, nuclear entry, integration and expression. Lentiviral particles containing pTRIP plasmids as genomic content are assumed to recapitulate native viral behavior for the first three steps. However, the pTRIP vector contains a SFFV promoter, which can be active as soon as it is in the nucleus. Unlike HIV, they do not depend on integration to be expressed. In order to confirm our findings, we performed the combined infection and confinement using pseudotyped HIV-GFP, which requires integration to be expressed.

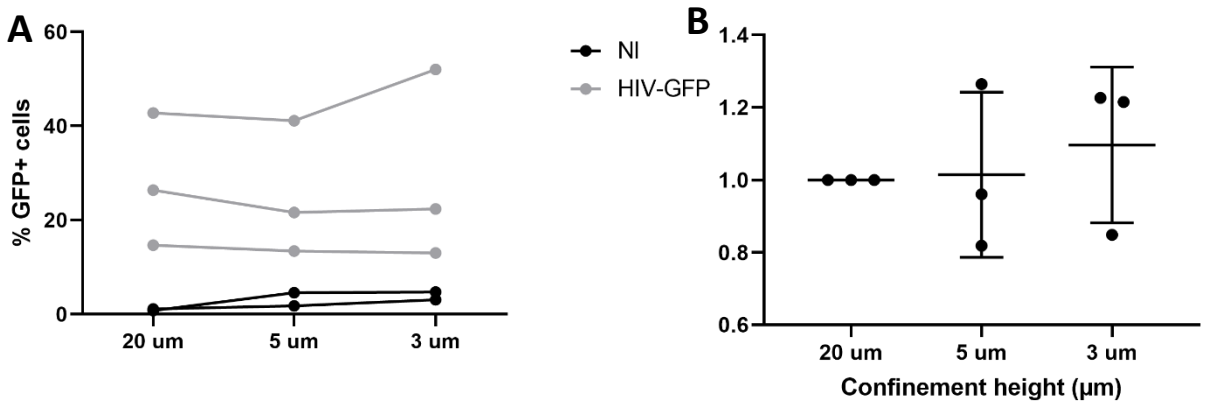

Figure 54: Confinement at different heights does not affect HIV-GFP infection
A. Percentage of GFP+ cells B. Proportion of GFP+ cells normalized over percentage at 20 µM
Statistical test: 2-way ANOVA – no effect of confinement height

We tested two confinement heights to deform with or without altering NE integrity. At 5 µm, the nucleus is strongly deformed but without NE ruptures, while 70% of the nuclei are ruptured at 3 µm (Figure 50).

Neither of the confinement heights affect the infection efficiency (Figure 54), indicating that neither deformation nor NE rupture impact HIV infection efficiency.

Taken all together, these results suggest that altering the mechanical state of the NE does not significantly affect infection efficiency. While proteins involved in mechanical pathways are playing important roles in HIV infection, their effect is not likely to go through mechanical constraints. Interestingly, and perhaps counterintuitively, deforming the NE to the point of forcing NE rupture does not facilitate infection. We hypothesize that efficient integration or expression could require an intact nucleus.

DISCUSSION

In this work, we have shown that transfection with a lentiviral efficiency decreases upon mechanical constraint by confinement at heights lower 10 µm. However, unlike our initial hypothesis, mechanical constraints do not appear to alter the efficiency of HIV infection.

By using fluorescence as the read out of transfection and infection, we are looking at the endpoint of the viral cycle. qPCR for the different viral species (late RT for the total viral amount, 2-LTR for nuclear entry and integrated for successfully integrated viruses) would be the way to test whether intermediate steps are affected by confinement, even if these effects could cancel each other out. However, the static confiner has a low cell yield. It is a tool best suited to test multiple conditions by imaging or a few conditions by molecular biology. Therefore, recovering enough material to perform qPCR is very challenging. As there was no overall effect on the efficiency, we did not pursue this route. It is also the reason why we tested only virus dose under confinement.

One consequence of our finding is that losing the nucleo-cytoplasmic compartmentation when the NE ruptures at strong confinement does not improve infection efficiency. This is counterintuitive, as one would expect removing the NE barrier would favor viral nuclear entry and thus infection efficiency. We hypothesize that proper interactions with the NPC might be required for a "licensing" of the virus. Viral capsids have been observed in the nucleus (Chen *et al.*, 2016), and are known to interact with the nucleoplasmic side of the pores (Di Nunzio *et al.*, 2013). We can imagine that steps such as capsid disassembly could require interactions with nuclear pores and that viruses entering the nucleus by an alternative route might not be integration-efficient. The state of the chromatin, potentially altered in ruptured nuclei, could be important for the ability of the virus to integrate in the host genome.

APPENDIX B: Major contribution to a publication

As part of the effort to understand how the NE might affect HIV infection, I collaborated with Anvita Bhargava on her project to understand how SUN1 and SUN2 overexpression inhibits the virus. This gave rise to a research article where I am second author.

In this paper, Bhargava *et al.* show that HIV infection is more efficient in a context of DNA damage, which is known to be associated with elevated chromatin mobility (Caridi *et al.*, 2018), a phenomenon shown to be linked with lamins and SUN proteins (Oza *et al.*, 2009). Increasing chromatin dynamics, by inducing DNA damage or depleting lamin A/C, increases the infection efficiency, while decreasing it with elevated SUN1 and SUN2 levels, is associated with lower virus titers. The inhibitory effect of SUN1 and SUN2 can be partially rescued by uncoupling the LINC complex.

My contribution consisted in the image analysis of nuclear rotation and chromatin mobility.

Cell Reports

Article

Inhibition of HIV infection by structural proteins of the inner nuclear membrane is associated with reduced chromatin dynamics

Graphical abstract

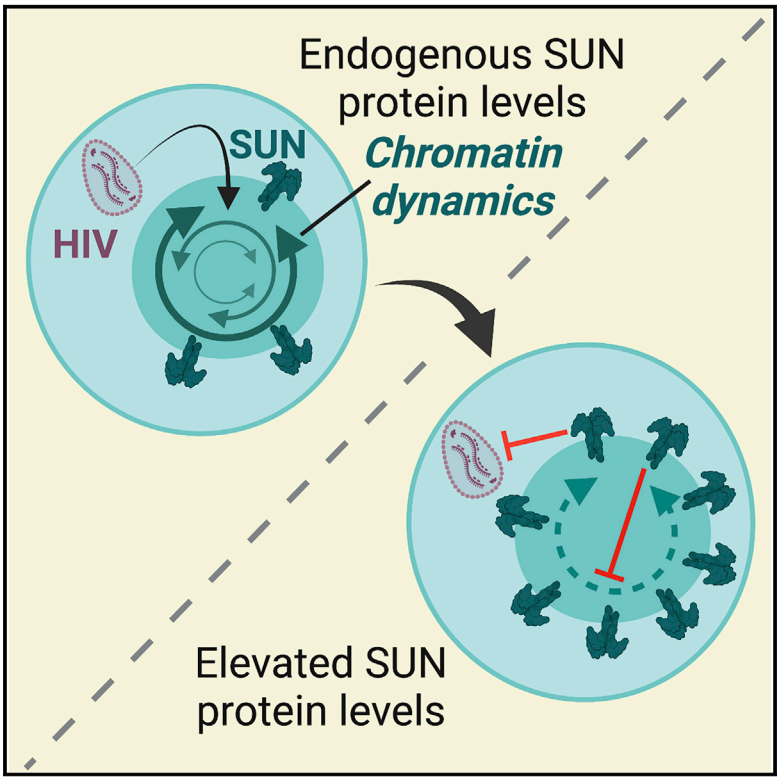

Highlights

- SUN1 and SUN2 show strain-specific antiviral activities against HIV-1 and HIV-2
- The DNA damage response is implicated in the antiviral effect of SUN proteins on HIV-1
- SUN proteins inhibit nuclear rotation and chromatin movements

Authors

Anvita Bhargava, Alice Williart, Mathieu Maurin, ..., Matthieu Piel, Xavier Lahaye, Nicolas Manel

Correspondence

nicolas.manel@curie.fr

In brief

Elevated levels of nuclear envelope proteins SUN1 and SUN2 inhibit HIV infection through an unresolved mechanism. Here, Bhargava et al. show that SUN proteins inhibit nuclear rotation and chromatin movements, indicating a role for chromatin dynamics and the DNA damage response in the control of HIV infection.

Bhargava et al., 2021, Cell Reports *36*, 109763
September 28, 2021
https://doi.org/10.1016/j.celrep.2021.109763

CellPress

Cell Reports

CellPress
OPEN ACCESS

Article

Inhibition of HIV infection by structural proteins of the inner nuclear membrane is associated with reduced chromatin dynamics

Anvita Bhargava,[1] Alice Williart,[2] Mathieu Maurin,[1] Patricia M. Davidson,[3,5] Mabel Jouve,[4] Matthieu Piel,[2] Xavier Lahaye,[1,6] and Nicolas Manel[1,6,7,*]

[1]Institut Curie, PSL Research University, INSERM U932, Paris, France
[2]Institut Curie, PSL Research University, CNRS UMR144, Paris, France
[3]Laboratoire Physico-Chimie Curie, Institut Curie, CNRS UMR168, Sorbonne Université, PSL Research University, Paris, France
[4]Institut Curie, UMR3215, Paris, France
[5]Present address: 4Dcell, Montreuil, France
[6]These authors contributed equally
[7]Lead contact
*Correspondence: nicolas.manel@curie.fr
https://doi.org/10.1016/j.celrep.2021.109763

SUMMARY

The human immunodeficiency virus (HIV) enters the nucleus to establish infection, but the role of nuclear envelope proteins in this process is incompletely understood. Inner nuclear transmembrane proteins SUN1 and SUN2 connect nuclear lamins to the cytoskeleton and participate in the DNA damage response (DDR). Increased levels of SUN1 or SUN2 potently restrict HIV infection through an unresolved mechanism. Here, we find that the antiviral activities of SUN1 and SUN2 are distinct. HIV-1 and HIV-2 are preferentially inhibited by SUN1 and SUN2, respectively. We identify DNA damage inducers that stimulate HIV-1 infection and show that SUN1, but not SUN2, neutralizes this effect. Finally, we show that chromatin movements and nuclear rotations are associated with the effects of SUN proteins and Lamin A/C on infection. These results reveal an emerging role of chromatin dynamics and the DDR in the control of HIV infection by structural components of the nuclear envelope.

INTRODUCTION

Successful infection of cells by the human immunodeficiency virus (HIV) requires an active transport of the virus through the physical barrier of the nuclear envelope. Nuclear entry of HIV is coordinated with the completion of reverse transcription and selection of integration sites (Dharan et al., 2020; Schaller et al., 2011). The capsid (CA) protein of HIV engages multiple interactions with nuclear pore complex (NPC) components and associated proteins such as cyclophilin A (CypA) to achieve this coordination (Yamashita and Engelman, 2017).

In the nuclear envelope, in addition to NPC proteins, SUN proteins located at the inner nuclear membrane impact HIV infection (Bhargava et al., 2018). SUN1 and SUN2 are integral proteins of the inner nuclear envelope of somatic cells. They play essential roles in the maintenance of genomic stability and the resolution of DNA damage (Lawrence et al., 2016; Lei et al., 2012). SUN proteins possess a lamin-binding domain at their N terminus located in the nucleoplasm. Lamins are intermediate filament proteins that assemble the nuclear lamina, a dense meshwork contributing to mechanical protection, organization of chromatin domains, and recruitment of DNA repair factors (Burke and Stewart, 2013; Gonzalo, 2014). At their C terminus, SUN proteins interact with the KASH domains of nesprins in the perinuclear space. Nesprins are large integral proteins of the outer nuclear membrane (Burke and Stewart, 2013). Nesprins have multiple interactions with cytoskeletal proteins, enabling a dynamic anchoring of the nucleus within the cells.

SUN2 was first identified as an antiviral factor against HIV-1 in the context of a cDNA screen (Schoggins et al., 2011). Subsequent studies confirmed and extended the antiviral viral effect of SUN1 and SUN2 overexpression on HIV-1 and HIV-2 infection (Donahue et al., 2016; Lahaye et al., 2016; Luo et al., 2018; Schaller et al., 2017). SUN1 and SUN2 overexpression limits the level of HIV-1 nuclear import (Donahue et al., 2016; Luo et al., 2018; Schaller et al., 2017), leading to reduced viral integration. Furthermore, nanotubes of HIV-1 capsid and nucleocapsid proteins produced *in vitro* pull down SUN1 and SUN2 proteins from cell lysates, suggesting that SUN proteins and the viral capsid protein may interact directly or indirectly during infection (Schaller et al., 2017).

The role of endogenous SUN2 in HIV-1 infection has been examined, but a consensus has not been reached (Donahue et al., 2017; Lahaye et al., 2016; Schaller et al., 2017; Sun et al., 2018). Three studies concurred with a requirement for SUN2 in HIV-1 infection in primary CD4$^+$ T cells, in

monocyte-derived dendritic cells, and in THP-1 cells, although the strength of this requirement varies between cell type (Donahue et al., 2017; Lahaye et al., 2016; Schaller et al., 2017). A fourth study obtained contradicting results and proposed that endogenous SUN2 instead limits HIV infection at the level of viral promoter expression (Sun et al., 2018). We initially proposed that HIV infection requires an optimal level of SUN2 protein, and that both depletion and overexpression impair infection, not necessarily through the same mechanism (Lahaye et al., 2016). This notion fits well with the structural role of the LINC complex in nuclear architecture. Of note, endogenous SUN2 level varies with the extent of T cell activation (Sun et al., 2018). It is thus conceivable that variable experimental conditions between studies, particularly using sensitive primary immune cells, could account for the variable effects of endogenous SUN2 on HIV infection. SUN2 is also implicated in the effects of cyclophilin A on HIV-1 infection. In HeLa cells, SUN2 overexpression abrogates the sensitivity of the HIV-1 capsid mutant N74D to cyclophilin A inhibition (Lahaye et al., 2016). In primary $CD4^+$ T cells and murine bone marrow-derived dendritic cells, endogenous SUN2 is required for the cyclophilin A-dependent steps of HIV infection (Lahaye et al., 2016). Another study, however, did not observe this effect in primary $CD4^+$ T cells (Donahue et al., 2017). These differences may reflect the use of different readouts for quantifying the impact of cyclophilin A inhibition on infection.

Our understanding of the antiviral effect of SUN1 is less advanced. In HEK293A cells, the antiviral effect of SUN1 overexpression requires the interaction of cyclophilin A with HIV-1 capsid protein (Luo et al., 2018). In THP-1 cells, endogenous SUN1 is not required for HIV-1 infection (Schaller et al., 2017).

The strong antiviral effect of SUN protein overexpression on HIV infection exploits one or several points of weakness in the viral replication cycle. The cellular mechanisms by which elevated levels of SUN expression block HIV infection are not known. Intriguingly, SUN2 overexpression is associated with alteration of nuclear envelope shape, suggesting that SUN might interfere with HIV infection through a perturbation of the integrity of the nucleus (Donahue et al., 2016; Lahaye et al., 2016). However, it has not been possible so far to explain how SUN proteins are perturbing cellular and nuclear physiology to impact HIV.

RESULTS

SUN1 and SUN2 proteins demonstrate HIV-strain-specific antiviral effects

To gain insights in SUN1- and SUN2-mediated antiviral effects on the early steps of HIV infection, we first performed a comparative assessment of the antiviral effect of SUN1 and SUN2 on HIV infection in primary cells. To this end, we overexpressed SUN1 and SUN2 in primary monocyte-derived macrophages (MDMs) using lentiviral vectors (Figure 1A). In order to focus on the early phase of infection, cells were infected using single-round HIV-1 and HIV-2 encoding GFP in the place of the Nef gene. SUN1 and SUN2 induced an antiviral effect on HIV-1 and HIV-2 (Figure 1B). Unexpectedly, SUN1 and SUN2 did not show an identical antiviral effect on the two strains. The calculation of the ratio of inhibition by SUN1 over SUN2 revealed that HIV-1 was preferentially inhibited by SUN1, while HIV-2 was preferentially inhibited by SUN2 (Figure 1B). In MDMs, HIV-1 infection is sensitive to inhibition by cyclosporin A (CsA) (Saini and Potash, 2006), and we previously showed that SUN2 overexpression blocks the effect of CsA on infection in other cell types (Lahaye et al., 2016). Here, SUN1 and SUN2 also blocked the effect of CsA on HIV-1 infection in MDMs (Figure 1B). Although not the primary focus of this study, this strengthens the notion that the SUN1 and SUN2 antiviral effects implicate a CsA-sensitive step of HIV infection. We next analyzed the progression of HIV-1 and HIV-2 infection in the context of SUN protein expression using quantitative real-time PCR on viral DNA species, using reverse transcriptase inhibitors as controls (Figure S1A). SUN1 and SUN2 overexpression had no significant impact on the total amount of HIV-1 DNA, but they reduced the levels of 2-long terminal repeat (LTR) circles, which are a hallmark of viral entry into the nucleus, and of integrated viral DNA (Figure 1C). The reduction of HIV-1 integrated DNA was more significant for SUN1 than SUN2, while it was the opposite for HIV-2. These experiments indicate that SUN1 and SUN2 impact the nuclear steps of HIV infection but have strain-specific antiviral effects.

We similarly overexpressed SUN1 and SUN2 in HeLa cells (Figure 2A). SUN1 overexpression had a greater inhibitory effect on HIV-1 infection than on SUN2 overexpression, whereas in HIV-2 infection, SUN2 overexpression had a greater effect than SUN1, recapitulating the results obtained in MDMs (Figures 2B and 2C). In HeLa cells, wild-type (WT) HIV-1 is not sensitive to CsA, but HIV-1 capsid N74D is, similar to HIV-1 WT in MDMs (De Iaco and Luban, 2014). We thus used this mutant to address the relationship between the antiviral effect of SUN and CsA sensitivity. Both SUN1 and SUN2 abolished CsA sensitivity of HIV-1 capsid N74D in HeLa cells (Figures 2D and 2E). We next measured the levels of HIV-1 DNA species. SUN1 and SUN2 reduced the levels of integrated HIV-1 DNA, and this effect was more pronounced for SUN1 (Figure S1B). We also observed a small but significant inhibition of total viral DNA levels by SUN1 and of 2-LTR circles by SUN2. We compared the antiviral effects of SUN1 and SUN2 on different HIV-1 strains. The antiviral effect of SUN1 was more important than that of SUN2 for all HIV-1 lab strains (NL4-3, Lai, JR-CSF, and YU-2) and transmitter/founder strains (THRO, CH058, and CH077) tested. In contrast, the antiviral effect of SUN2 was more important than that of SUN1 for two HIV-2 strains tested (ROD9 and JK71312As) (Figure 2F). Of note, HIV-1 Lai and JR-CSF were resistant to SUN2, while JK7312As was resistant to SUN1. We thus focused on HeLa cells for additional experiments aimed at characterizing the strain-specific inhibition of SUN1 and SUN2.

Strain-specific antiviral activity maps to the nucleoplasmic domain of SUN proteins

Cell-cell communication factors of innate immunity, such as interferons and cyclic guanosine monophosphate-adenosine monophosphate (cGAMP), can contribute to antiviral effects on top of cell-intrinsic restriction factors. Using a co-culture of SUN1/2-expressing cells and control cells expressing a fluorescent marker (TagRFP657), we found that the strain-specific effect of SUN1 and SUN2 on HIV-1 and HIV-2 infection is entirely cell-intrinsic in HeLa cells (Figure 3A). To determine whether SUN1 and SUN2 induced an antiviral state at the cell-intrinsic

CellPress
OPEN ACCESS

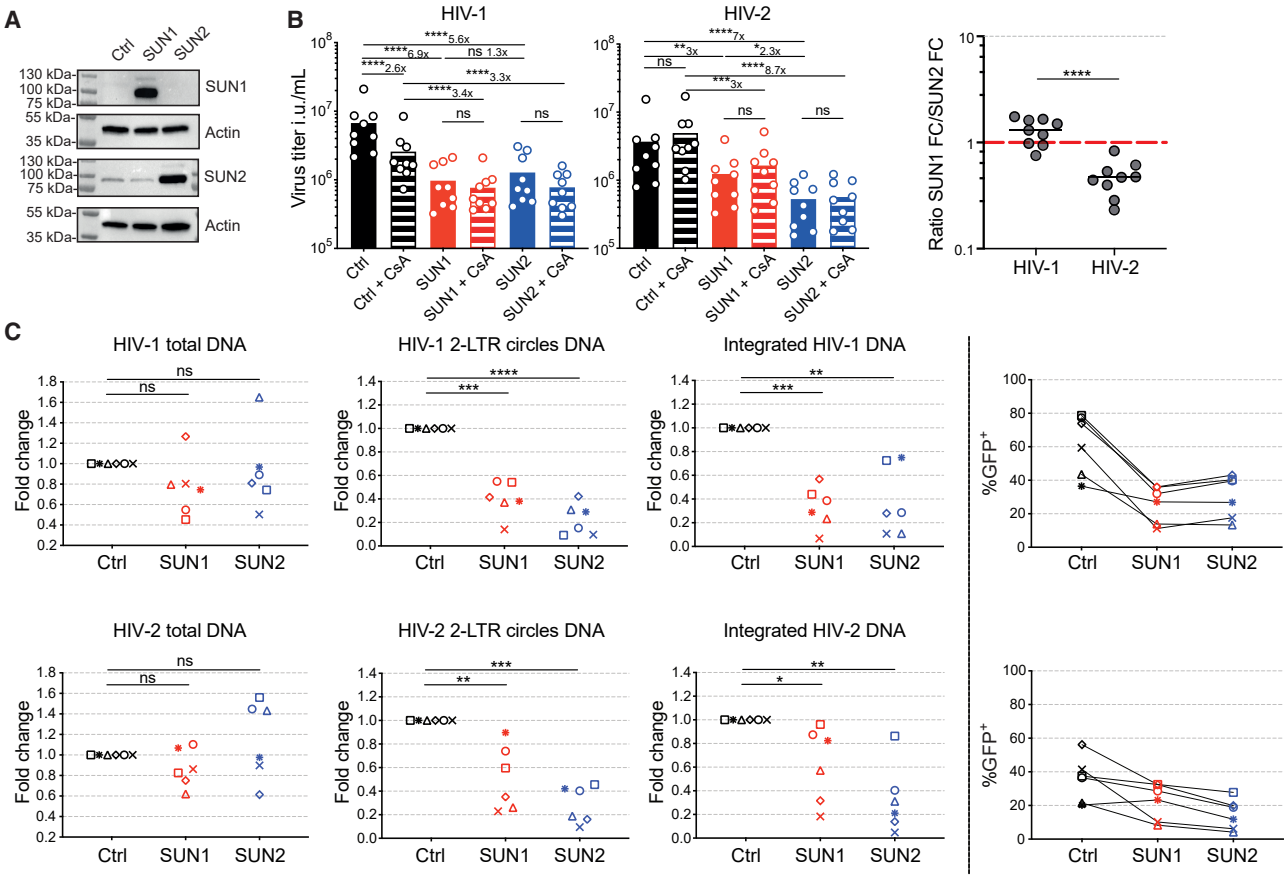

Figure 1. Distinct antiviral activities of SUN1 and SUN2 against HIV-1 and HIV-2 in primary macrophages

(A) Detection of SUN1, SUN2, and actin in MDMs transduced with mTagBFP-2A control, SUN1, or SUN2 lentivectors (representative of n = 3).

(B) (Left) Viral titers as infectious units (IU) per mL based on percentages of GFP$^+$ MDMs 48 h after infection with serial dilutions of HIV-1 or HIV-2 encoding GFP in Nef and pseudotyped with vesicular stomatitis virus glycoprotein G (VSV-G), with or without 2 μM CsA (n = 9 donors, paired repeated measures (RM) one-way ANOVA on log-transformed titers with a Sidak's post-test, line at mean). (Right) Ratios of titer fold change (FC) control over SUN1 (SUN1 FC) or control over SUN2 (SUN2 FC) (paired t test, line at mean).

(C) (Left) Detection of HIV-1 total DNA, 2-LTR circles DNA, and integrated DNA by quantitative real-time PCR at 24 h after infection with HIV-1 or HIV-2 (dilution factor, 0.17) of MDMs transduced with mTagBFP (blue fluorescent protein)-2A control, SUN1, or SUN2 lentivectors. (Right) Infection levels for each donor (n = 6 donors, quantitative real-time PCR data are represented as donor-matched fold change compared to control; one-sample t test).

Ctrl, control. *p < 0.05, **p < 0.01, ***p < 0.001, ****p < 0.0001; ns, not significant. See also Figure S1.

level through expression of other antiviral genes, we performed a transcriptomic analysis of SUN1 and SUN2 overexpressing cells. Strikingly, we could not detect any differentially expressed genes in this dataset, aside from SUN1 and SUN2 themselves (Figure S1C). Next, we generated chimeras between SUN1 and SUN2 to map the strain-specific antiviral effect (Figures 3B and 3C). We found that the N-terminal nucleoplasmic domains of SUN1 and SUN2 confer strain specificity (Figures 3D and 3E). These results establish that SUN1 and SUN2 exert a cell-intrinsic HIV-strain-specific antiviral effect on HIV infection that maps to the nucleoplasmic domain of SUN proteins.

Interplay between SUN proteins, HIV infection, and the DNA damage response

As a next step, we attempted to characterize the cellular processes affected by elevated levels of SUN proteins. SUN1 and SUN2 are required to limit the accumulation of DNA damage in cells (Lei et al., 2012). Since HIV infection is a DNA-damaging event, we considered the possible interplay between SUN proteins, HIV infection, and the DNA damage response. We examined the level of γH2AX, an early marker of the DNA damage response. At baseline, we did not detect any change of γH2AX levels upon SUN1 or SUN2 expression (Figures 4A and 4B). To induce DNA damage, we selected etoposide, a topo-isomerase II inhibitor. Interestingly, SUN1 overexpression but not SUN2 significantly limited the levels of induced γH2AX after etoposide treatment (Figures 4A and 4B). To explore the potential link between DNA damage and infection, we infected HeLa cells in the presence of etoposide for the first 4 h of the experiment. However, etoposide gradually induces apoptosis of treated cells (Rello-Varona et al., 2006), which hampered our ability to detect viable cells to measure infection after 48 h. To circumvent this,

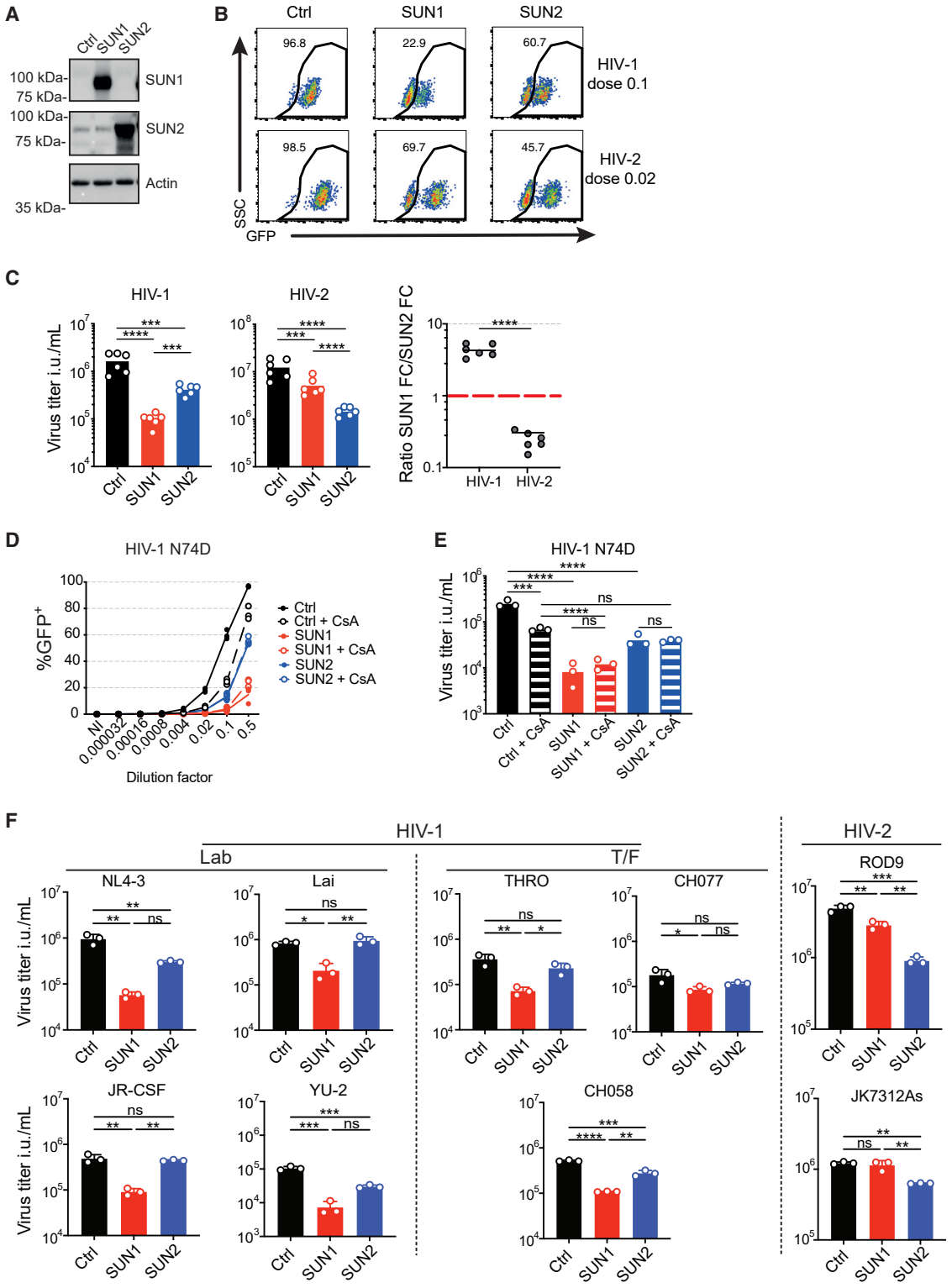

Figure 2. Distinct antiviral activities of SUN1 and SUN2 against multiple HIV-1 and HIV-2 strains in HeLa cells

(A) Detection of SUN1, SUN2, and actin in HeLa cells transduced with mTagBFP-2A control, SUN1, or SUN2 lentivectors.

(B) GFP expression in BFP$^+$ HeLa cells transduced with mTagBFP-2A control, SUN1, or SUN2 lentivectors, 48 h after infection with indicated dilutions of HIV-1 and HIV-2 (representative data from one experiment at the indicated dose of virus).

(legend continued on next page)

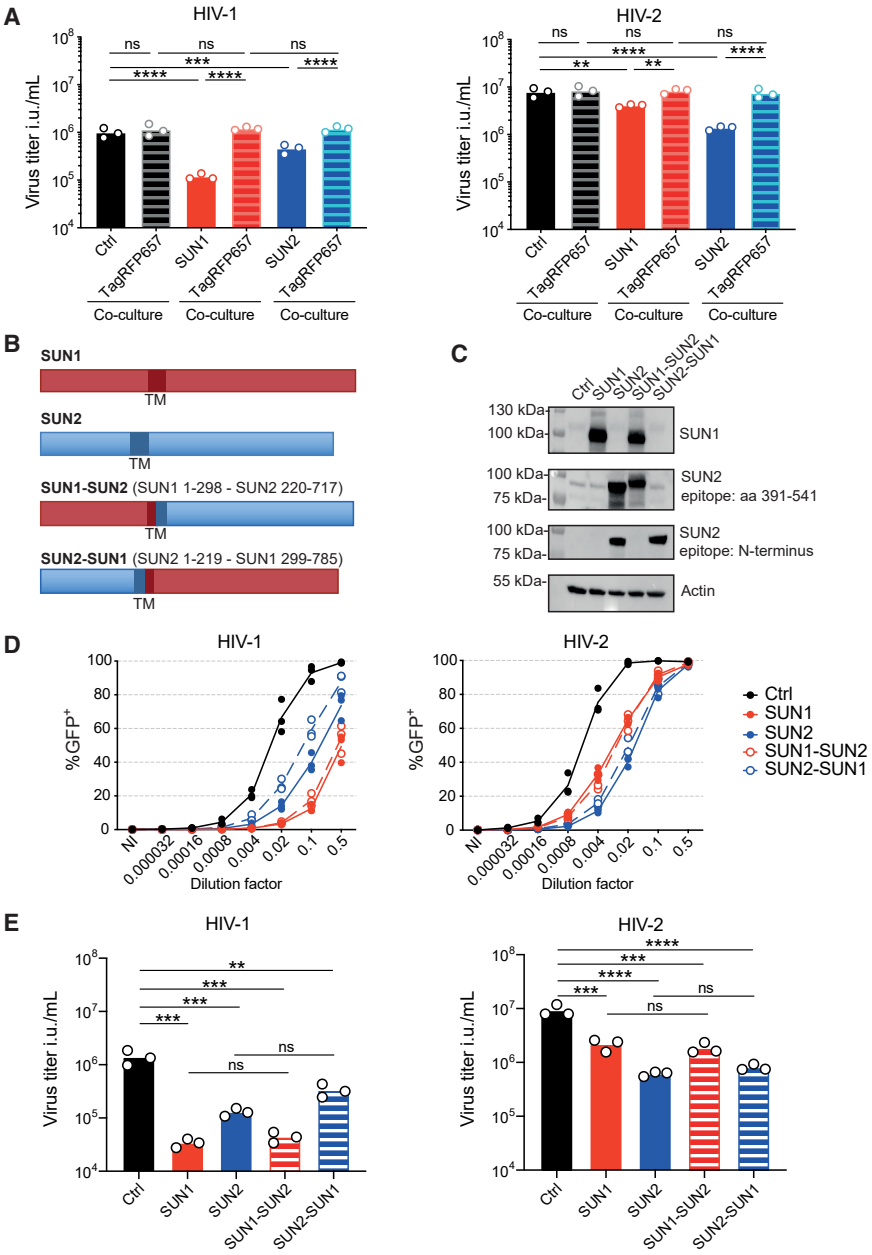

Figure 3. Mapping of the strain-specific antiviral activity of SUN proteins

(A) mTagBFP-2A Ctrl, mTagBFP-2A-SUN1, and mTagBFP-2A-SUN2 expressing HeLa cells were co-cultured at a 1:1 ratio with HeLa cells expressing TagRFP657-2A and infected with serial dilutions of HIV-1 and HIV-2. Titers were calculated based on the percentage of GFP$^+$ cells in 48-h post-infection dilutions within the indicated populations (n = 3 independent experiments, paired RM one-way ANOVA on log-transformed titers with Sidak's post-test, line at mean).

(B) Schematic representation of chimeric proteins between full-length SUN1 (red) and SUN2 (blue). Amino acid residues retained in hybrid proteins are indicated within brackets.

(C) Detection of SUN1, SUN2, and actin in HeLa cells transduced with the indicated mTagBFP-2A lentivectors. Two antibodies targeting SUN2 that recognize different epitopes within the protein were used.

(D) Percentage of GFP$^+$ in BFP$^+$ HeLa cells transduced with the indicated mTagBFP-2A lentivectors, 48 h after infection with serial dilutions of HIV-1 or HIV-2 (n = 3 independent experiments).

(E) Viral titers based on percentages of GFP$^+$ cells shown in (D) (n = 3, paired RM one-way ANOVA with Sidak's post-test, line at mean).

**p < 0.01, ***p < 0.001, ****p < 0.0001; ns, not significant. See also Figure S1.

we cultured cells in the presence of the caspase inhibitor Q-VD-Oph and lower doses of etoposide. Q-VD-Oph did not prevent γH2AX induction by etoposide treatment (Figure 4C). Etoposide treatment increased HIV-1 infection by 2-fold on average (Figure 4D). HIV-2 infection was also increased but significantly at only one dose of etoposide tested, with a smaller fold change. Next, we combined SUN expression with etoposide to determine the epistatic relationship between DNA damage induction and SUN expression on the level of HIV infection. Here, we used a higher MOI to observe the antiviral effect of SUN proteins. The increase induced by etoposide treatment on control cells was consistently observed across experiments. Interestingly, SUN1 abrogated the proviral effect of etoposide treatment and, in sharp contrast, etoposide treatment rescued cells from the antiviral effect of SUN2 (Figures 4E and 4F). We next explored the effects of bleomycin, which induces direct double-stranded DNA breaks akin to etoposide. Bleomycin induced upregulation of γH2AX (Figure S2A). SUN1 slightly reduced this

(C) (Left) Viral titers based on percentages of GFP$^+$ cells after infection with serial dilutions of the indicated viruses (n = 6, paired RM one-way ANOVA on log-transformed titers, with Tukey's post-test, line at mean). (Right) ratios of titer FC control over SUN1 (SUN1 FC) or control over SUN2 (SUN2 FC) (paired t test, line at mean).

(D) Percentage of GFP$^+$ in BFP$^+$ HeLa cells transduced with mTagBFP-2A control, SUN1, or SUN2 lentivectors, 48 h after infection with serial dilutions of HIV-1 or HIV-1 capsid N74D, with or without treatment with 2 μM of CsA (n = 3 independent experiments).

(E) Viral titers as in (D) (n = 3, paired RM one-way ANOVA on log-transformed titers with Sidak's post-test, line at mean).

(F) Viral titers based on percentages of GFP$^+$ or p24$^+$ cells after infection with serial dilutions of indicated HIV-1 and HIV-2 viral strains (n = 3, paired RM one-way ANOVA with Sidak's post-test, line at mean + SD).

*p < 0.05, **p < 0.01, ***p < 0.001, ****p < 0.0001; ns, not significant. See also Figure S1.

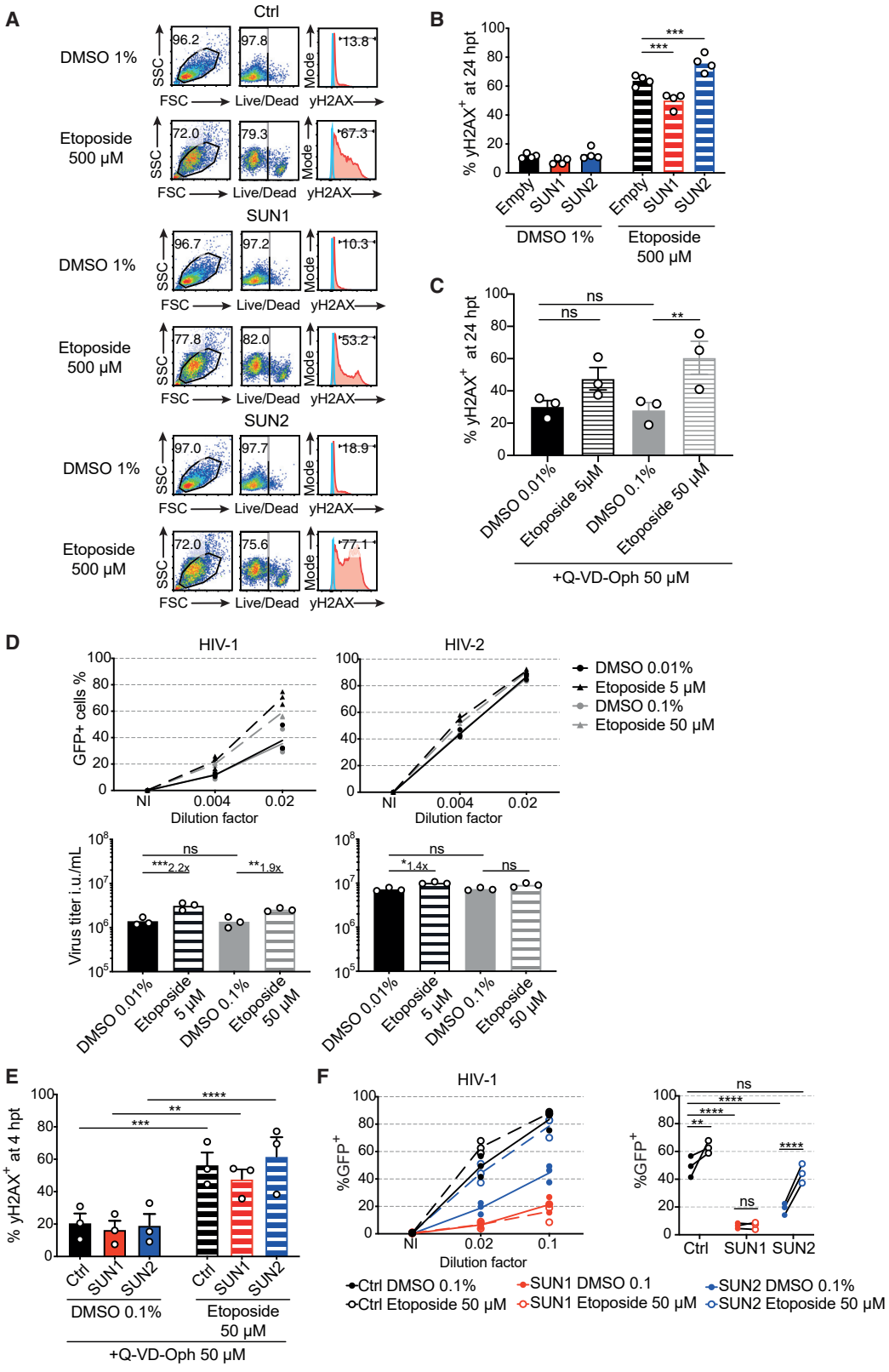

(legend on next page)

induction in all experiments, while SUN2 had no impact. Similar to etoposide, HIV-1 infection was increased by bleomycin treatment (Figure S2B). This pro-viral effect of bleomycin was lost upon SUN1 expression, while it was consistently maintained with SUN2. Next, we tested hydroxyurea and UV treatments, which cause DNA damage rather through DNA replication stress. Both treatments induced upregulation of γH2AX (Figure S2C). However, they did not have an effect on the rate of HIV-1 infection (Figure S2D), indicating that HIV infection is modulated by only a subset of DNA damaging agents. Overall, these results show that SUN1 overexpression, which restricts HIV-1 infection more than SUN2, operates downstream of DNA damage induction, while SUN2 overexpression impacts infection upstream of DNA damage induction.

DNA damage induction by ATR inhibition and role of HIV-1 Vpr

Next, we looked for a different approach to induce DNA damage that would be functionally linked to the nuclear envelope. ATR is a DNA damage sensor that functions as a checkpoint at the nuclear envelope in response to mechanical stress (Kumar et al., 2014). ATR inhibition heightens DNA damage in cells (Foote et al., 2018). Furthermore, in HIV-1, expression of the accessory protein Vpr causes DNA damage and activates ATR (Roshal et al., 2003), although the relevance of this effect in the context of virion-packaged Vpr is unknown. Considering the significance of ATR at the nuclear envelope and its relationship with Vpr, we asked whether DNA damage induction by ATR inhibition, SUN, and Vpr are functionally related. We inhibited ATR using AZD6738, a next-generation inhibitor with improved specificity (Foote et al., 2018). As expected, ATR inhibition increased the levels of γH2AX in HeLa cells (Figure S3A). We next infected HeLa cells with p24-normalized and sucrose cushion purified stocks of the HIV-1 single-round virus and its HIV-1 Vpr-deficient (Vpr^-) counterpart. ATR inhibition increased Vpr-positive HIV-1 infection in HeLa cells by 2-fold, similar to etoposide treatment (Figure S3B, left panel). Concomitant SUN protein overexpression inhibited HIV-1 infection and reduced the magnitude of the proviral effect of ATR inhibition. Unexpectedly, the titer of the p24-normalized HIV-1 Vpr^- was slightly higher than the HIV-1 WT counterpart in HeLa cells, and HIV-1 Vpr^- was insensitive to ATR inhibition (Figure S3B, right panel). However, HIV-1 Vpr^- remained sensitive to the antiviral effect of SUN protein expression. In sum, these data implicate the kinase ATR in limiting HIV infection of HeLa cells. Intriguingly, the data also revealed that sensitivity to ATR inhibition is a HIV-1 Vpr phenotype in single-round infection of HeLa cells.

Endogenous Lamin A/C limits HIV-1 infection in HeLa cells

We sought to further explore the relationship between infection, DNA damage, and structure of the nuclear envelope. Electron microscopy analysis revealed that both SUN1 and SUN2 overexpression induced deep invaginations of the nuclear envelope, which appeared more pronounced with SUN2 (Figure 5A). This raised the possibility that alteration of the shape of the nucleus could be responsible for the antiviral effect. We searched for an orthogonal approach to perturb the nuclear envelope structure and the DNA damage response. Lamin A/C expression is required to maintain a regular nuclear shape (Lammerding et al., 2004) and to protect from DNA damage (Singh et al., 2013). We used short hairpin RNA (shRNA) to reduce expression of Lamin A/C (Figure 5B). Similar to SUN protein overexpression, knockdown of Lamin A/C compromised the regularity of the nuclear envelope shape (Figure 5C). To quantify this effect, we measured the shape descriptor "solidity" of the nucleus: solidity values close to 1 indicate smoothly convex nuclei while lower values correspond to deformed, lobulated nuclei, presenting concave invaginations. Overexpression of SUN proteins and silencing of Lamin A/C increased nuclear envelope deformation, and this effect was less pronounced in cells overexpressing SUN1 compared to SUN2 (Figure 5D). The endogenous levels of Lamin A/C and SUN proteins were not reciprocally affected by SUN overexpression or Lamin A/C silencing. (Figure 5B). After infection, Lamin A/C knockdown unexpectedly increased HIV-1 infection levels by 1.6-fold, while HIV-2 infection was not affected (Figure 5E). Lamin A/C thus limits HIV-1 infection in HeLa cells. Given the opposing effects of SUN overexpression and Lamin A/C knockdown on HIV-1 infection, we examined whether the antiviral effect of SUN proteins requires endogenous lamins. We knocked down Lamin A/C, Lamin B1, and Lamin B2 and co-expressed SUN proteins (Figure 5F). Viable Lamin B1-depleted HeLa cells could not be maintained in culture. Lamin A/C depletion enhanced HIV-1 infection as above, and Lamin B2 depletion had no effect (Figure 5G). SUN proteins maintained their antiviral effect

Figure 4. Interplay between HIV-1 infection, SUN proteins, and the DNA damage response

(A) Viability and γH2AX intracellular staining in HeLa cells transduced with mTagBFP-2A control, SUN1, or SUN2 lentivector, 24 h after treatment with 500 μM etoposide or 1% DMSO as control (representative experiment from n = 3).

(B) Quantification of $γH2AX^+$ HeLa cells treated as in (A) (n = 4, paired RM one-way ANOVA with Sidak's post-test, line at mean).

(C) Quantification of $γH2AX^+$ HeLa cells 24 h after a 4-h treatment with 5 or 50 μM etoposide or corresponding DMSO control. 50 μM Q-VD-Oph was present throughout the experiment (n = 3, paired RM one-way ANOVA with Sidak's post-test, line at mean ± SEM).

(D) (Top) Percentage of GFP^+ HeLa cells 48 h after infection with two dilutions of HIV-1 (plasmid HIVGFP env^-nef^-) or HIV-2. Cells were treated and infected simultaneously, and the drugs and the virus were washed out at 4 h post-treatment/infection. 50 μM Q-VD-Oph was maintained throughout the experiment. (Bottom) Viral titers based on percentages of GFP^+ cells (n = 3, paired RM one-way ANOVA with Sidak's post-test, line at mean).

(E) Quantification of $γH2AX^+$ HeLa cells transduced with mTagBFP-2A control, SUN1, or SUN2 lentivectors, 4 h after treatment with 50 μM etoposide or corresponding DMSO control (n = 3, paired RM one-way ANOVA with Sidak's post-test, line at mean ± SEM).

(F) (Left) Percentage of GFP^+ cells in BFP^+ HeLa cells expressing control, SUN1, or SUN2 lentivectors and treated as in (E), 48 h after infection with purified HIV-1 (plasmid HIVGFP env^-nef^-). Right, GFP^+ percentages at viral dilution 0.02 (n = 3, experimental pairs are indicated; RM ANOVA two-way test, uncorrected Fisher's least significant difference [LSD] test). 50 μM Q-VD-Oph was maintained throughout the experiment.

hpt, hours post-treatment. *p < 0.05, **p < 0.01, ***p < 0.001, ****p < 0.0001; ns, not significant. See also Figures S2 and S3.

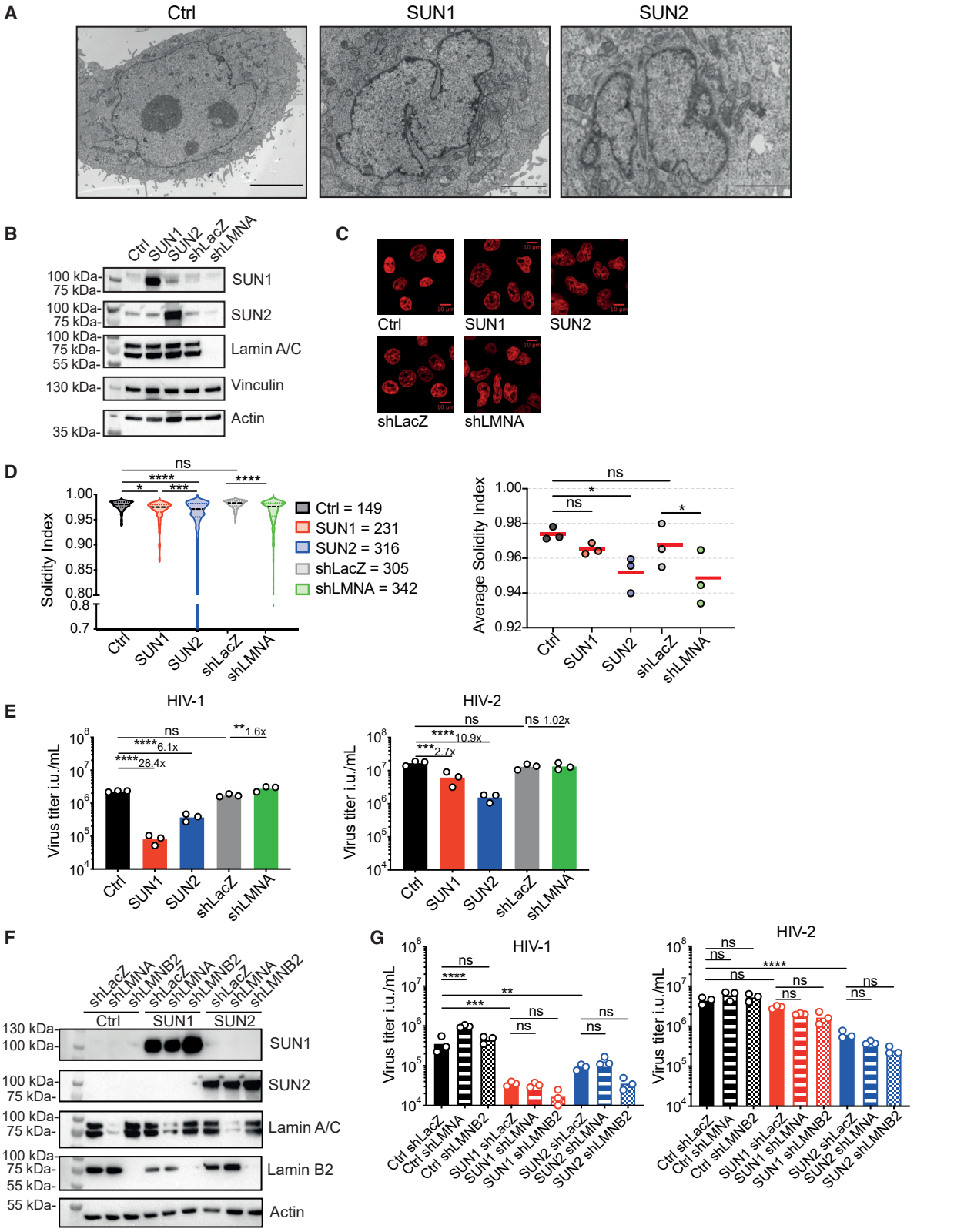

(legend on next page)

irrespective of the level of Lamin A/C and Lamin B2. This shows that the effect of elevated levels of SUN proteins is dominant on the effect of Lamin A/C depletion on HIV-1 infection. Furthermore, these results indicate that the increase in nuclear envelope shape irregularities does not explain how Lamin A/C depletion and SUN protein overexpression affect HIV infection.

Next, we examined the level of γH2AX after etoposide treatment and Lamin A/C depletion. Treatment with a high dose of etoposide (500 μM) for 24 h induced an increase of γH2AX level in WT HeLa cells, while a lower dose (50 μM) had no impact at this time point (Figure S4). In the absence of Lamin A/C, HeLa cells became hypersensitive to etoposide treatment (Figure S4). Thus, the increase in HIV-1 infection observed after Lamin A/C depletion correlates with an increased sensitivity to DNA damage. Altogether, these results establish a functional correlation between the effect of SUN protein and endogenous Lamin A/C on HIV-1 infection and the cellular response to DNA damage induced by an exogenous compound.

Elevated SUN proteins do not alter NPC density, passive import, or cell stiffness

We next sought to identify the mechanisms that delineate the effects of elevated SUN proteins and endogenous Lamin A/C depletion on infection. We characterized biophysical and structural parameters in SUN-expressing cells. HIV-1 enters the nucleus through NPCs. We labeled NPCs using a marker of Nup153 on tangential confocal microscopy sections of the nuclear envelope (Figure S5A). Overexpression of SUN proteins did not alter NPC density at the nuclear envelope (Figure S5B). To determine whether the NPC functionality was impaired by SUN protein overexpression, we measured passive diffusion through the NPC using a fluorescence recovery after photobleaching (FRAP) assay on ubiquitous GFP. SUN proteins had no impact on the rate of recovery of nuclear GFP (Figure S5C; Video S1). Lamin A/C depletion reduces stiffness of the nuclear envelope, resulting in a more deformable nucleus (Lammerding et al., 2004). To determine whether the expression of SUN proteins induced the opposite to match the effects on infection, we measured the viscoelastic properties of the nuclei using a microfluidic micropipette assay (Davidson et al., 2019). While we confirmed that Lamin A/C-depleted cells are more deformable, expression of SUN proteins had no impact on nuclear deformability (Figure S5D).

HIV-1 infection requires movement of the chromatin

Next, we turned our attention to the endogenous state of chromatin. We performed live imaging of cells with a DNA stain after SUN overexpression or Lamin A/C depletion. We observed that SUN1 and SUN2 overexpression appeared to lock the nucleus in place, while nuclei of Lamin A/C-depleted cells appeared highly dynamic (Figure 6A; Video S2). We first asked whether the extent of chromatin movement inside the nuclei was altered. We isolated videos of single nuclei and performed a registration step to normalize x-y positions and angle, therefore suppressing general nuclei displacement and rotation. We next measured chromatin movement in the registered nuclei by performing a particle image velocimetry (PIV) analysis. Strikingly, SUN1 and SUN2 overexpression reduced the displacement of chromatin over time and this effect was more pronounced with SUN1, while Lamin A/C depletion had the converse effect (Figures 6B and 6C). HeLa cells also exhibit seemingly random rotation of their nuclei at various speeds and frequencies. Using the same dataset, we measured the rotation of the whole nucleus relative to the cytoplasm. We corrected the translational displacement of nuclei by registration and measured the angle of rotation over time using a custom-made analysis script (Video S3). SUN1 and SUN2 reduced the average speed of nuclear rotation (Figures 6D and 6E) and the fraction of time spent rotating above a threshold of 1° (Figures S6A and S6B). The rotation of Lamin A/C-depleted nuclei was visibly higher than that of controls but could not be reliably quantified due to the high levels of chromatin displacement that hampered the ability to set reference points.

If SUN proteins inhibit HIV infection by limiting chromatin movements, increasing rotation would be expected to overcome the viral restriction. SUN proteins form the LINC complex with nesprins at the nuclear envelope by interaction with their KASH domain within the perinuclear space. Expression of the isolated KASH domain (spectrin repeat-KASH, SR-KASH) functions as a dominant negative by disrupting the SUN-nesprin interaction and displacing nesprins from the nuclear envelope (Starr et al., 2003). We co-expressed SR-KASH with SUN proteins (Figure 7A; Video S4). Strikingly, SR-KASH increased the rotation speed of chromatin in control and SUN-overexpressing cells (Figures 7B

Figure 5. SUN proteins inhibit HIV infection at the nuclear envelope independently of endogenous lamins

(A) Representative electron micrograph showing nuclei in control, SUN1, and SUN2 overexpressing HeLa cells (scale bars, 10, 2, and 5 μm, respectively).

(B) Detection of SUN1, SUN2, Lamin A/C, and actin in HeLa cells transduced with mTagBFP-2A control, SUN1, or SUN2 lentivectors, negative control LacZ (shLacZ), or Lamin A/C (shLMNA) targeting shRNA-encoding lentivectors.

(C) Nuclei of HeLa cells lines as in (B) visualized on fixed cells using SiR-DNA dye. Images show signal from an individual, central confocal plane. Scale bars, 10 μm.

(D) Solidity index of nuclei as in (C). (Left) Data from one representative experiment out of three. Legend indicates total number of nuclei analyzed per cell line. Unpaired one-way ANOVA with Sidak's post-test, line at median. (Right) Average solidity index across three independent experiments (paired one-way ANOVA with Sidak's post-test, line at mean).

(E) Viral titers based on percentages of GFP^+ HeLa cells lines from (B) after infection with serial dilutions of HIV-1 and HIV-2 (n = 3, paired RM one-way ANOVA with Sidak's post-test, line at mean).

(F) Detection of SUN1, SUN2, Lamin A/C, Lamin B2, and actin in HeLa cells co-transduced with mTagBFP-2A control, SUN1, or SUN2 lentivectors and with LacZ, Lamin A/C, or Lamin B2 (shLMNB2) targeting shRNA-encoding lentivectors.

(G) Viral titers based on percentages of GFP^+ HeLa cells as shown in (F) after infection with serial dilutions of HIV-1 and HIV-2 (n = 3, paired RM one-way ANOVA with Sidak's post-test, line at mean).

*p < 0.05, **p < 0.01, ***p < 0.001, ****p < 0.0001; ns, not significant. See also Figures S4 and S5 and Video 1.

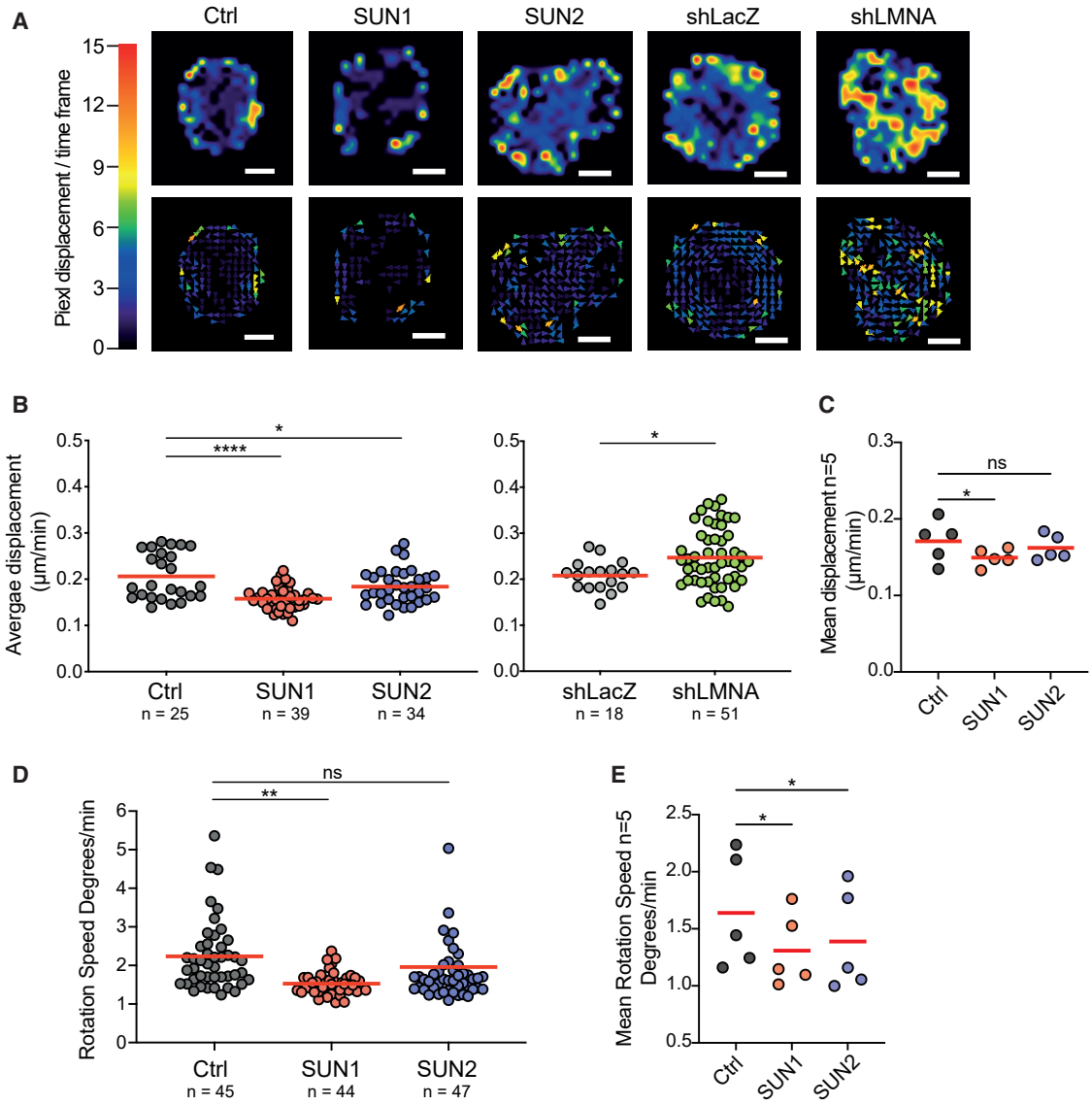

Figure 6. SUN protein overexpression and endogenous Lamin A/C limit movements of the chromatin

(A) Particle image velocimetry (PIV) of DNA within nuclei of HeLa cells transduced with mTagBFP-2A control, SUN1, or SUN2 lentivectors, negative control LacZ, or Lamin A/C targeting shRNA-encoding lentivectors. PIV is shown for individual representative nuclei of each cell line; top panels show overall flow, and bottom panels show individual vectorial displacements between two consecutive frames corresponding to 2 min of imaging. Scale bars, 5 μm. Reference color scale for pixel displacement per time frame is shown on left.

(B) Quantification of DNA displacement as μm/min from images as in (A). Results are shown for one experiment from n = 2. (Left) Unpaired one-way ANOVA with Sidak's post-test, line at mean. (Right) Unpaired Student's t test, line at mean.

(C) Average chromatin displacement within nuclei of HeLa cells transduced with mTagBFP-2A control, SUN1, or SUN2 lentivectors (n = 5 independent experiments, paired one-way ANOVA with Dunnett's post-test, line at mean).

(D) Quantification of nuclear rotation speed as degrees/min in HeLa cells transduced with mTagBFP-2A control, SUN1, or SUN2 lentivectors and imaged as in (A). Results are shown for one experiment from n = 5. Unpaired one-way ANOVA with Sidak's post-test, line at mean.

(E) Average nuclear rotation speed within nuclei of HeLa cells as in (D) (n = 5 independent experiments, paired one-way ANOVA with Holm-Sidak's post-test, line at mean).

*p < 0.05, **p < 0.01, ****p < 0.0001; ns, not significant. See also Figure S6 and Videos S2 and S3.

and 7C) and significantly increased the fraction of time that SUN1-overexpressing cells spent rotating (Figures S6C and S6D). In contrast, SR-KASH had no significant effect on the shape of the nuclei (Figure S6E). Upon HIV-1 infection, SR-KASH partially reverts the antiviral effects of SUN1 and SUN2 (Figure 7D). Overall, these results indicate that the impact of SUN and Lamin A/C proteins on HIV-1 infection is associated with the movement of chromatin within the cells.

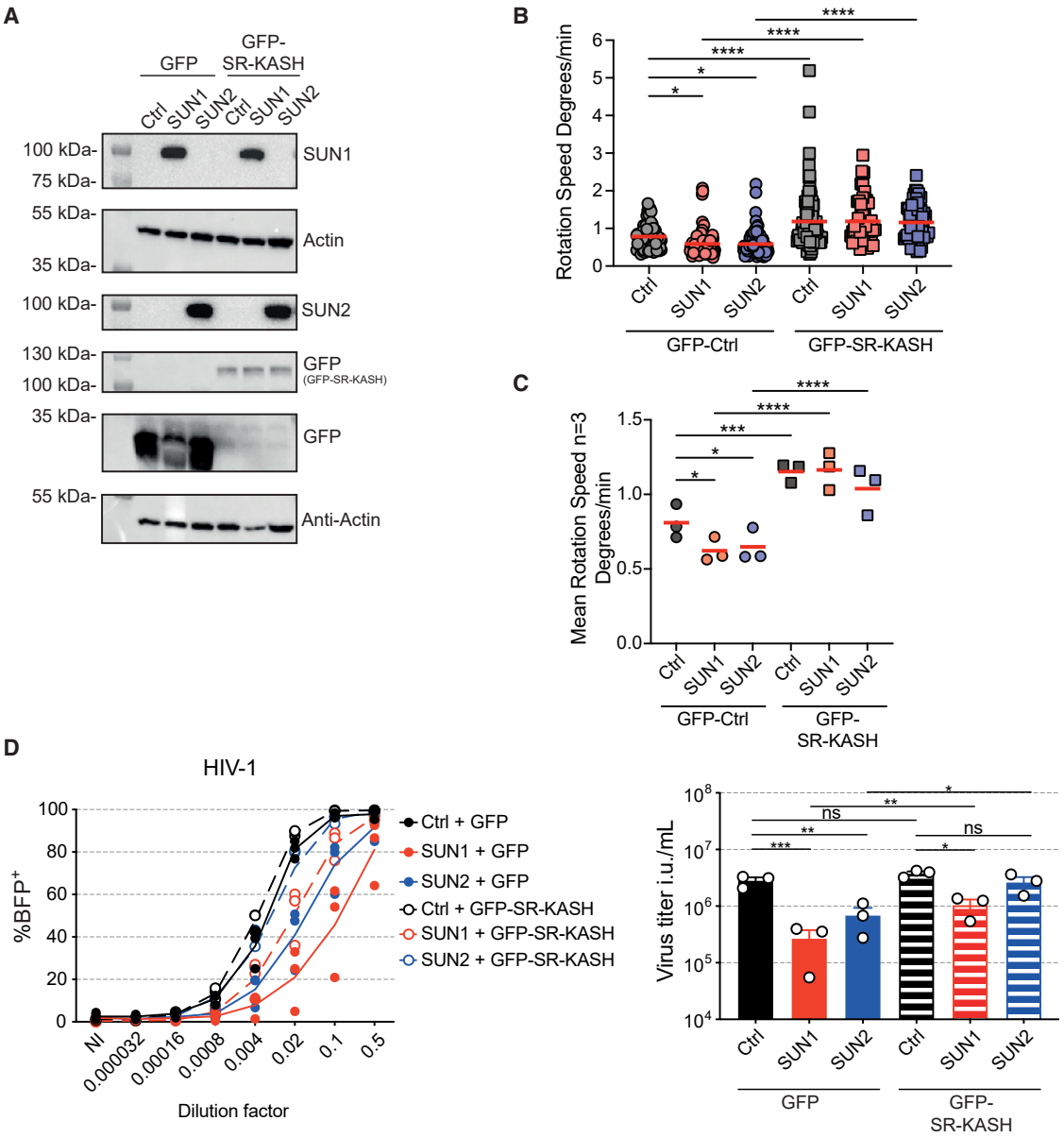

Figure 7. Increased rotations of chromatin limit the SUN-mediated antiviral state

(A) Detection of SUN1, SUN2, GFP, and actin in HeLa cells transduced with TagRFP657-expressing control, SUN1, or SUN2 lentivectors, combined with control GFP or SR-KASH DN fused to GFP-expressing lentivectors. The same lysates were loaded onto two separate membranes; the housekeeping control is shown for both.

(B) Quantification of nuclear rotation speed as degrees/min in HeLa cell lines as in (A), based on images taken every 6 min. Results are shown for one experiment from n = 3. Unpaired one-way ANOVA with Sidak's post-test, line at mean.

(C) Average rotation speed of nuclei as in (B) (n = 3 independent experiments, paired one-way ANOVA with Sidak's post-test, line at mean).

(D) (Left) Percentage of BFP^+ within $tagRFP657^+$ HeLa cells 48 h after infection with serial dilutions of HIV-1 encoding BFP in the place of Nef, pseudotyped with VSV-G. (Right) Viral titers based on percentages of BFP^+ cells (n = 3, paired RM one-way ANOVA on log-transformed titers, with Sidak's post-test, line at mean ± SEM).

*p < 0.05, **p < 0.01, ***p < 0.001, ****p < 0.0001; ns, not significant. See also Figure S6 and Video S4.

DISCUSSION

Our findings reveal that SUN1 and SUN2, although paralogs, have distinct effects on HIV infection. SUN1 overexpression is more efficient at inhibiting HIV-1 than is SUN2. Meanwhile, SUN2 overexpression shows a marked antiviral activity against HIV-2. An analysis of the viral step impacted by these two proteins also reveals differences: SUN1 inhibits more significantly

HIV-1-integrated DNA than does SUN2, while it is the converse for HIV-2. The strain-specific antiviral effects of SUN1 and SUN2 were conserved across all viral clones tested. We also reveal that SUN1 and SUN2 differ in their response to DNA damage and its impact on HIV infection. SUN1 limits the response to etoposide as measured by the levels of γH2AX, while SUN2 enhances the response. Strikingly, etoposide largely rescues the antiviral effect of SUN2 overexpression on HIV-1, while SUN1 is resistant to this effect. This result suggests that SUN1 and SUN2 may differ in the ways in which they establish interactions and functions within the nucleus, in line with previously reports showing non-redundant effects of SUN1 and SUN2 (Lei et al., 2009; Liu et al., 2007; Zhu et al., 2017)

Etoposide treatment also enhances the infection by HIV-1 by 2-fold in HeLa cells in the absence of SUN protein overexpression, while HIV-2 is largely unaffected. Stimulation of HIV-1 infection was also observed with bleomycin. Such a proviral effect of DNA damage has been previously observed in conditions of integrase inhibition (Ebina et al., 2012; Koyama et al., 2013). In contrast, it was previously reported that etoposide treatment inhibits HIV-1 infection in MDMs (Mlcochova et al., 2018). We speculate that this is explained by the presence of a SAMHD1-dependent block induced by etoposide in macrophages, but not in HeLa cells.

Similar to etoposide and bleomycin, ATR inhibition also enhances HIV-1 infection by 2-fold. The lack of a requirement for ATR in HIV infection is consistent with prior studies (Ariumi et al., 2005; Dehart et al., 2005). Interestingly, the effect of ATR inhibition requires the presence of the Vpr gene in HIV-1. As a virus-encoded gene, Vpr has been shown to induce an ATR-dependent G_2 arrest of the cell cycle (Zimmerman et al., 2006). Using purified and p24-normalized virus preparations, we made the unexpected observation that the Vpr-deficient virus is actually as infectious as the WT virus stimulated with ATR inhibition. In other words, in this asynchronous system of single-round infection of HeLa cells, the presence of the Vpr gene appears to provide a counter-intuitive 2-fold reduction in infectivity of the virus, which is alleviated by ATR inhibition. However, Vpr has been associated with an enhanced expression for the viral LTR during G_2 arrest (Goh et al., 1998). We speculate that in terms of viral replicative fitness, the reduction in single-round infectivity entailed by Vpr is cancelled out by this proviral effect of Vpr during G_2 arrest. Of note, both SUN1 and SUN2 overexpression inhibit HIV-1 infection irrespective of ATR inhibition. In contrast, etoposide rescues the antiviral effect of SUN2 on HIV-1, raising the possibility that ATR itself might play a role in the rescue of the SUN2 antiviral effect.

Multiple lines of evidence from our work indicate that the structure of the nuclear envelope impacts HIV infection. The ability of SR-KASH to partially rescue the antiviral effects of SUN proteins indicates that the LINC complex, which is located at the nuclear envelope, is involved. Despite the important morphological changes induced by SUN protein expression, we did not observe any change at the level of gene expression. This result suggests that SUN-mediated effects on the nucleus and HIV infection are post-transcriptional or that other changes in nucleic acid contents not assessed by our method are implicated. ATR is enriched at the nuclear envelope during the S phase and upon mechanical stretching, two processes that increase nuclear envelope stress (Kumar et al., 2014). ATR-deficient cells exhibit deformed nuclei, reminiscent of Lamin A/C depletion or SUN protein overexpression (Kidiyoor et al., 2020). Vpr overexpression was previously shown to induce herniations of the nuclear envelope associated with defects in the nuclear lamina (de Noronha et al., 2001). We also find that endogenous Lamin A/C has an antiviral effect, in agreement with a previous study (Sun et al., 2018).

We examined several effects of SUN protein overexpression and endogenous Lamin A/C on nuclear shape, deformability, NPC distribution and function, and chromatin dynamics. The effects on HIV-1 infection match the effects of the proteins on chromatin dynamics: decreased HIV-1 infection is associated with a decreased chromatin motility inside the nucleus and with decreased rotation of the nucleus relative to the cytoplasm. In contrast, HIV-2 infection is more susceptible to SUN2 than SUN1 and is not affected by Lamin A/C depletion. Overexpression of SUN2 deforms nuclei more than SUN1 but internal chromatin dynamics and nuclear rotation are less impacted. This strain specificity could be linked to a different dependency on host factors between HIV-1 and HIV-2 (Braaten and Luban, 2001). SUN and lamin proteins have been previously linked to chromatin mobility and nuclear rotation (Ji et al., 2007; Lottersberger et al., 2015; Oza et al., 2009; Ranade et al., 2019). Interestingly, nuclear rotation is required for optimal infection by another nuclear-invading virus, human cytomegalovirus (HCMV) (Procter et al., 2018). This rotation is required to promote spatial chromatin segregation that favors viral gene expression (Procter et al., 2018). We propose that HIV-1 infection requires nuclear rotation and chromatin movements for optimal integration and subsequent viral expression.

Our results highlight the interplay between HIV infection, structural proteins of the nuclear envelope, and the DNA damage response. Nuclear rotation and chromatin dynamics emerge as potentially important factors that control HIV infection. Future studies are required to address the underlying molecular mechanisms, which we anticipate will require the use of biophysical approaches. It will also be important to examine these mechanisms in the frame of the diversity of lentiviruses and their relevance for viral replication and innate immune sensing mechanisms in primary target cells.

STAR★METHODS

Detailed methods are provided in the online version of this paper and include the following:

- KEY RESOURCES TABLE
- RESOURCE AVAILABILITY
  - Lead contact
  - Materials availability
  - Data and code availability
- EXPERIMENTAL MODEL AND SUBJECT DETAILS
  - Cell lines and primary cultures
- METHOD DETAILS
  - Constructs
  - Virus production

- Cell transduction for protein overexpression or knockdown
- Cell infection
- DNA damage induction
- HIV DNA quantification
- Western blotting
- Live confocal imaging
- Confocal Immunofluorescence Imaging
- Fluorescence recovery after photobleaching
- Intracellular staining for flow cytometry
- Electron microscopy
- Micropipette aspiration microscopy
- Gene expression analysis by microarray

- QUANTIFICATION AND STATISTICAL ANALYSIS
- ADDITIONAL RESOURCES

SUPPLEMENTAL INFORMATION

Supplemental information can be found online at https://doi.org/10.1016/j.celrep.2021.109763.

ACKNOWLEDGMENTS

We thank V. Teixeira Rodrigues and J. Nikolic for assistance with primary macrophages; P. Benaroch for critically reading this manuscript; and M. Piel, N. De Silva, N. Jeremiah, V. Parissi, and F. Halary for discussions. We acknowledge the PICT-IBiSA imaging facility, member of the France-BioImaging national research infrastructure, supported by the CelTisPhyBio Labex (ANR-10-LBX-0038) part of the IDEX PSL (ANR-10-IDEX-0001-02 PSL), and Audrey Rapinat and David Gentien from the Genomics Platform at Institut Curie. This work was supported by Institut Curie, INSERM, and by grants from the Agence Nationale de la Recherche (ANR-10-IDEX-0001-02 PSL, ANR-11-LABX-0043, ANR-17-CE15-0025-01, ANR-19-CE15-0018-01, ANR-18-CE92-0022-01, and France-BioImaging ANR-10-INSB-04), the Agence Nationale de la Recherche sur le SIDA (ECTZ118797, ECTZ36691, ECTZ25472, and ECTZ71745), and Sidaction (VIH2016126002, 20-2-AEQ-12822-2, and 17-1-AAE-11097-2). A.B. was supported by fellowships from PSL University and Fondation pour la Recherche Médicale (grant no. 8250). P.M.D. was supported by fellowships from La Ligue contre le Cancer (REMX17751) and Fondation ARC (PDF20161205227).

AUTHOR CONTRIBUTIONS

A.B. performed experiments, analyzed data, and designed the study. A.W. contributed to some experiments. M.M. developed scripts for image analysis. P.M.D. performed the nuclear deformation assay. M.J. performed electron microscopy experiments. M.P. co-supervised A.W. X.L. assisted with the experimental setup and coordinated the study. N.M. designed and coordinated the study and wrote the first manuscript. All authors contributed to the text.

DECLARATION OF INTERESTS

The authors declare no competing interests.

Received: January 15, 2021
Revised: July 21, 2021
Accepted: September 3, 2021
Published: September 28, 2021

REFERENCES

Ariumi, Y., Turelli, P., Masutani, M., and Trono, D. (2005). DNA damage sensors ATM, ATR, DNA-PKcs, and PARP-1 are dispensable for human immunodeficiency virus type 1 integration. J. Virol. *79*, 2973–2978.

Bhargava, A., Lahaye, X., and Manel, N. (2018). Let me in: Control of HIV nuclear entry at the nuclear envelope. Cytokine Growth Factor Rev. *40*, 59–67.

Braaten, D., and Luban, J. (2001). Cyclophilin A regulates HIV-1 infectivity, as demonstrated by gene targeting in human T cells. EMBO J. *20*, 1300–1309.

Burke, B., and Stewart, C.L. (2013). The nuclear lamins: Flexibility in function. Nat. Rev. Mol. Cell Biol. *14*, 13–24.

Cerboni, S., Jeremiah, N., Gentili, M., Gehrmann, U., Conrad, C., Stolzenberg, M.C., Picard, C., Neven, B., Fischer, A., Amigorena, S., et al. (2017). Intrinsic antiproliferative activity of the innate sensor STING in T lymphocytes. J. Exp. Med. *214*, 1769–1785.

Davidson, P.M., Fedorchak, G.R., Mondésert-Deveraux, S., Bell, E.S., Isermann, P., Aubry, D., Allena, R., and Lammerding, J. (2019). High-throughput microfluidic micropipette aspiration device to probe time-scale dependent nuclear mechanics in intact cells. Lab Chip *19*, 3652–3663.

De Iaco, A., and Luban, J. (2014). Cyclophilin A promotes HIV-1 reverse transcription but its effect on transduction correlates best with its effect on nuclear entry of viral cDNA. Retrovirology *11*, 11.

de Noronha, C.M., Sherman, M.P., Lin, H.W., Cavrois, M.V., Moir, R.D., Goldman, R.D., and Greene, W.C. (2001). Dynamic disruptions in nuclear envelope architecture and integrity induced by HIV-1 Vpr. Science *294*, 1105–1108.

Dehart, J.L., Andersen, J.L., Zimmerman, E.S., Ardon, O., An, D.S., Blackett, J., Kim, B., and Planelles, V. (2005). The ataxia telangiectasia-mutated and Rad3-related protein is dispensable for retroviral integration. J. Virol. *79*, 1389–1396.

Dharan, A., Bachmann, N., Talley, S., Zwikelmaier, V., and Campbell, E.M. (2020). Nuclear pore blockade reveals that HIV-1 completes reverse transcription and uncoating in the nucleus. Nat. Microbiol. *5*, 1088–1095.

Donahue, D.A., Amraoui, S., di Nunzio, F., Kieffer, C., Porrot, F., Opp, S., Diaz-Griffero, F., Casartelli, N., and Schwartz, O. (2016). SUN2 overexpression deforms nuclear shape and inhibits HIV. J. Virol. *90*, 4199–4214.

Donahue, D.A., Porrot, F., Couespel, N., and Schwartz, O. (2017). SUN2 silencing impairs CD4 T cell proliferation and alters sensitivity to HIV-1 infection independently of cyclophilin A. J. Virol. *91*, e02303-16.

Ebina, H., Kanemura, Y., Suzuki, Y., Urata, K., Misawa, N., and Koyanagi, Y. (2012). Integrase-independent HIV-1 infection is augmented under conditions of DNA damage and produces a viral reservoir. Virology *427*, 44–50.

Foote, K.M., Nissink, J.W.M., McGuire, T., Turner, P., Guichard, S., Yates, J.W.T., Lau, A., Blades, K., Heathcote, D., Odedra, R., et al. (2018). Discovery and characterization of AZD6738, a potent inhibitor of ataxia telangiectasia mutated and Rad3 Related (ATR) kinase with application as an anticancer agent. J. Med. Chem. *61*, 9889–9907.

Goh, W.C., Rogel, M.E., Kinsey, C.M., Michael, S.F., Fultz, P.N., Nowak, M.A., Hahn, B.H., and Emerman, M. (1998). HIV-1 Vpr increases viral expression by manipulation of the cell cycle: A mechanism for selection of Vpr in vivo. Nat. Med. *4*, 65–71.

Gonzalo, S. (2014). DNA damage and lamins. In Cancer Biology and the Nuclear Envelope, E.C. Schirmer and J.I. de las Heras, eds. (Springer New York), pp. 377–399.

Ji, J.Y., Lee, R.T., Vergnes, L., Fong, L.G., Stewart, C.L., Reue, K., Young, S.G., Zhang, Q., Shanahan, C.M., and Lammerding, J. (2007). Cell nuclei spin in the absence of lamin B1. J. Biol. Chem. *282*, 20015–20026.

Kidiyoor, G.R., Li, Q., Bastianello, G., Bruhn, C., Giovannetti, I., Mohamood, A., Beznoussenko, G.V., Mironov, A., Raab, M., Piel, M., et al. (2020). ATR is essential for preservation of cell mechanics and nuclear integrity during interstitial migration. Nat. Commun. *11*, 4828.

Koyama, T., Sun, B., Tokunaga, K., Tatsumi, M., and Ishizaka, Y. (2013). DNA damage enhances integration of HIV-1 into macrophages by overcoming integrase inhibition. Retrovirology *10*, 21.

Kumar, A., Mazzanti, M., Mistrik, M., Kosar, M., Beznoussenko, G.V., Mironov, A.A., Garrè, M., Parazzoli, D., Shivashankar, G.V., Scita, G., et al. (2014). ATR mediates a checkpoint at the nuclear envelope in response to mechanical stress. Cell *158*, 633–646.

Lahaye, X., Satoh, T., Gentili, M., Cerboni, S., Conrad, C., Hurbain, I., El Marjou, A., Lacabaratz, C., Lelièvre, J.D., and Manel, N. (2013). The capsids of HIV-1 and HIV-2 determine immune detection of the viral cDNA by the innate sensor cGAS in dendritic cells. Immunity *39*, 1132–1142.

Lahaye, X., Satoh, T., Gentili, M., Cerboni, S., Silvin, A., Conrad, C., Ahmed-Belkacem, A., Rodriguez, E.C., Guichou, J.-F., Bosquet, N., et al. (2016). Nuclear envelope protein SUN2 promotes cyclophilin-A-dependent steps of HIV replication. Cell Rep. *15*, 879–892.

Lammerding, J., Schulze, P.C., Takahashi, T., Kozlov, S., Sullivan, T., Kamm, R.D., Stewart, C.L., and Lee, R.T. (2004). Lamin A/C deficiency causes defective nuclear mechanics and mechanotransduction. J. Clin. Invest. *113*, 370–378.

Lawrence, K.S., Tapley, E.C., Cruz, V.E., Li, Q., Aung, K., Hart, K.C., Schwartz, T.U., Starr, D.A., and Engebrecht, J. (2016). LINC complexes promote homologous recombination in part through inhibition of nonhomologous end joining. J. Cell Biol. *215*, 801–821.

Lei, K., Zhang, X., Ding, X., Guo, X., Chen, M., Zhu, B., Xu, T., Zhuang, Y., Xu, R., and Han, M. (2009). SUN1 and SUN2 play critical but partially redundant roles in anchoring nuclei in skeletal muscle cells in mice. Proc. Natl. Acad. Sci. USA *106*, 10207–10212.

Lei, K., Zhu, X., Xu, R., Shao, C., Xu, T., Zhuang, Y., and Han, M. (2012). Inner nuclear envelope proteins SUN1 and SUN2 play a prominent role in the DNA damage response. Curr. Biol. *22*, 1609–1615.

Liu, Q., Pante, N., Misteli, T., Elsagga, M., Crisp, M., Hodzic, D., Burke, B., and Roux, K.J. (2007). Functional association of Sun1 with nuclear pore complexes. J. Cell Biol. *178*, 785–798.

Lottersberger, F., Karssemeijer, R.A., Dimitrova, N., and de Lange, T. (2015). 53BP1 and the LINC complex promote microtubule-dependent DSB mobility and DNA repair. Cell *163*, 880–893.

Luo, X., Yang, W., and Gao, G. (2018). SUN1 regulates HIV-1 nuclear import in a manner dependent on the interaction between the viral capsid and cellular cyclophilin A. J. Virol. *92*, e00229-18.

Manel, N., Hogstad, B., Wang, Y., Levy, D.E., Unutmaz, D., and Littman, D.R. (2010). A cryptic sensor for HIV-1 activates antiviral innate immunity in dendritic cells. Nature *467*, 214–217.

Mangeot, P.E., Nègre, D., Dubois, B., Winter, A.J., Leissner, P., Mehtali, M., Kaiserlian, D., Cosset, F.L., and Darlix, J.L. (2000). Development of minimal lentivirus vectors derived from simian immunodeficiency virus (SIVmac251) and their use for gene transfer into human dendritic cells. J. Virol. *74*, 8307–8315.

Mlcochova, P., Caswell, S.J., Taylor, I.A., Towers, G.J., and Gupta, R.K. (2018). DNA damage induced by topoisomerase inhibitors activates SAMHD1 and blocks HIV-1 infection of macrophages. EMBO J. *37*, 50–62.

Oza, P., Jaspersen, S.L., Miele, A., Dekker, J., and Peterson, C.L. (2009). Mechanisms that regulate localization of a DNA double-strand break to the nuclear periphery. Genes Dev. *23*, 912–927.

Procter, D.J., Banerjee, A., Nukui, M., Kruse, K., Gaponenko, V., Murphy, E.A., Komarova, Y., and Walsh, D. (2018). The HCMV assembly compartment is a dynamic Golgi-derived MTOC that controls nuclear rotation and virus spread. Dev. Cell *45*, 83–100.e7.

Ranade, D., Pradhan, R., Jayakrishnan, M., Hegde, S., and Sengupta, K. (2019). Lamin A/C and Emerin depletion impacts chromatin organization and dynamics in the interphase nucleus. BMC Mol. Cell Biol. *20*, 11.

Rello-Varona, S., Gámez, A., Moreno, V., Stockert, J.C., Cristóbal, J., Pacheco, M., Cañete, M., Juarranz, A., and Villanueva, A. (2006). Metaphase arrest and cell death induced by etoposide on HeLa cells. Int. J. Biochem. Cell Biol. *38*, 2183–2195.

Roshal, M., Kim, B., Zhu, Y., Nghiem, P., and Planelles, V. (2003). Activation of the ATR-mediated DNA damage response by the HIV-1 viral protein R. J. Biol. Chem. *278*, 25879–25886.

Saini, M., and Potash, M.J. (2006). Novel activities of cyclophilin A and cyclosporin A during HIV-1 infection of primary lymphocytes and macrophages. J. Immunol. *177*, 443–449.

Schaller, T., Ocwieja, K.E., Rasaiyaah, J., Price, A.J., Brady, T.L., Roth, S.L., Hué, S., Fletcher, A.J., Lee, K., KewalRamani, V.N., et al. (2011). HIV-1 capsid-cyclophilin interactions determine nuclear import pathway, integration targeting and replication efficiency. PLoS Pathog. *7*, e1002439.

Schaller, T., Bulli, L., Pollpeter, D., Betancor, G., Kutzner, J., Apolonia, L., Herold, N., Burk, R., and Malim, M.H. (2017). Effects of inner nuclear membrane proteins SUN1/UNC-84A and SUN2/UNC-84B on the early steps of HIV-1 infection. J. Virol. *91*, e00463-17.

Schindelin, J., Arganda-Carreras, I., Frise, E., Kaynig, V., Longair, M., Pietzsch, T., Preibisch, S., Rueden, C., Saalfeld, S., Schmid, B., et al. (2012). Fiji: An open-source platform for biological-image analysis. Nat. Methods *9*, 676–682.

Schoggins, J.W., Wilson, S.J., Panis, M., Murphy, M.Y., Jones, C.T., Bieniasz, P., and Rice, C.M. (2011). A diverse range of gene products are effectors of the type I interferon antiviral response. Nature *472*, 481–485.

Silvin, A., Yu, C.I., Lahaye, X., Imperatore, F., Brault, J.B., Cardinaud, S., Becker, C., Kwan, W.H., Conrad, C., Maurin, M., et al. (2017). Constitutive resistance to viral infection in human $CD141^{+}$ dendritic cells. Sci. Immunol. *2*, eaai8071.

Singh, M., Hunt, C.R., Pandita, R.K., Kumar, R., Yang, C.-R., Horikoshi, N., Bachoo, R., Serag, S., Story, M.D., Shay, J.W., et al. (2013). Lamin A/C depletion enhances DNA damage-induced stalled replication fork arrest. Mol. Cell. Biol. *33*, 1210–1222.

Starr, T.K., Jameson, S.C., and Hogquist, K.A. (2003). Positive and negative selection of T cells. Annu. Rev. Immunol. *21*, 139–176.

Sun, W.-W., Jiao, S., Sun, L., Zhou, Z., Jin, X., and Wang, J.-H. (2018). SUN2 modulates HIV-1 infection and latency through association with lamin A/C to maintain the repressive chromatin. MBio. *9*, e02408–17.

Tseng, Q., Duchemin-Pelletier, E., Deshiere, A., Balland, M., Guillou, H., Filhol, O., and Théry, M. (2012). Spatial organization of the extracellular matrix regulates cell-cell junction positioning. Proc. Natl. Acad. Sci. USA *109*, 1506–1511.

Yamashita, M., and Engelman, A.N. (2017). Capsid-dependent host factors in HIV-1 infection. Trends Microbiol. *25*, 741–755.

Yamashita, M., Perez, O., Hope, T.J., and Emerman, M. (2007). Evidence for direct involvement of the capsid protein in HIV infection of nondividing cells. PLoS Pathog. *3*, 1502–1510.

Zhu, R., Antoku, S., and Gundersen, G.G. (2017). Centrifugal displacement of nuclei reveals multiple LINC complex mechanisms for homeostatic nuclear positioning. Curr. Biol. *27*, 3097–3110.e5.

Zimmerman, E.S., Sherman, M.P., Blackett, J.L., Neidleman, J.A., Kreis, C., Mundt, P., Williams, S.A., Warmerdam, M., Kahn, J., Hecht, F.M., et al. (2006). Human immunodeficiency virus type 1 Vpr induces DNA replication stress in vitro and in vivo. J. Virol. *80*, 10407–10418.

STAR★METHODS

KEY RESOURCES TABLE

REAGENT or RESOURCE	SOURCE	IDENTIFIER
Antibodies		
Actin (Clone C4)	Millipore	Cat# MAB1501, RRID: AB_2223041
Vinculin (Clone hVIN-1)	SIGMA	Cat# V9264, RRID: AB_10603627
SUN1 (EPR6554)	Abcam	Cat# ab124770 RRID:AB_10976056
SUN2	Atlas antibodies	Cat# HPA001209 RRID:AB_1080465
SUN2	Millipore	Cat# ABT272
Lamin A/C	Sigma	Cat# SAB4200236 RRID:AB_10743057
Lamin B2 clone LN43	Abcam	Cat #ab8983 RRID:AB_306912
NUP153	Sigma	Cat# HPA027896 RRID:AB_10611243
GFP Antibody Dylight 488 Conjugated Pre-Adsorbed (Polyclonal)	Rockland	Cat# 600-141-215 RRID: AB_1961516
HIV-1 p24 Clone KC57 – FITC	Beckman Coulter	Cat# 6604665 RRID:AB_1575987
H2AX p-S139 Clone N1-431	BD	Cat# 562377 RRID:AB_2737611
Mouse IgG1 κ isotype control Clone MOPC-21	BD	Cat# 554680 RRID:AB_395506
Rabbit-IgG (H+L) Alexa Fluor 546 conjugated	Invitrogen	Cat# A-11010 RRID:AB_2534077
Rabbit-IgG HRP-linked	Ozyme	Cat# 7074S RRID:AB_2099233
Mouse IgG HRP-linked	Ozyme	Cat# 7076S RRID:AB_330924
Bacterial and virus strains		
HIVGFP (NL4-3 strain)	Manel et al., 2010	Vif-, Vpr-, Vpu-, Env-, Nef-; GFP in Nef
HIVGFP N74D	Lahaye et al., 2016	Vif-, Vpr-, Vpu-, Env-, Nef-; GFP in Nef; CA mutation N74D
HIVGFP env-nef-	This study	Vif+, Vpr+, Vpu+, Env-, Nef-; GFP in Nef
HIVGFP env- nef- vpr-	This study	Vif+, Vpr-, Vpu+, Env-, Nef-; GFP in Nef
HIV-mTagBFP2 (NL4-3 strain)	This study	Vif-, Vpr-, Vpu-, Env-, Nef-; BFP in Nef
pLai ΔEnv GFP3	Yamashita et al., 2007	Vif+, Vpr+, Vpu+, Env-, Nef-; GFP
pTHRO.c/2626	NIH HIV Reagent Program ARP-11745	Full-length transmitter/founder HIV-1 clone
pCH058.c/2960	NIH HIV Reagent Program ARP-11856	Full-length transmitter/founder HIV-1 clone
pCH077.t/2627	NIH HIV Reagent Program ARP-11742	Full-length transmitter/founder HIV-1 clone
JR-CSF	Dan Littman lab, New York University	Full length HIV-1
YU-2	Dan Littman lab, New York University	Full length HIV-1
HIV-2 ROD9 ΔenvΔnef mTagBFP2+	This study	Vif+, Vpr+, Vpx+, Env-, Nef-; BFP in Nef
HIV-2 ROD9 ΔenvΔnef GFP	Manel et al., 2010	Vif+, Vpr+, Vpx+, Env-, Nef-; GFP in Nef
pJK7312As Δnef GFP+	Silvin et al., 2017	Vif+, Vpr+, Vpx+, Env+, Nef-; GFP in Nef
pSIV3+	Mangeot et al., 2000	/
Biological samples		
Human Healthy blood donors for primary PBMCs and MDMs	This manuscript	N/A
Human serum	Sigma	Cat# H4522
Chemicals, peptides, and recombinant proteins		
Human M-CSF	Miltenyi Biotec	Cat# 130-096-492
TransIT®-293 Transfection Reagent	Euromedex	Cat# MIR2706
Puromycin	Invivogen	Cat# ant-pr-1 CAS: 58-58-2
Protamine sulfate salt from salmon	SIGMA	Cat# P4020-1G CAS: 53597-25-4
Fetal bovine serum from Eurobio	Eurobio	Cat# CVFSVF0001

(*Continued on next page*)

Continued

REAGENT or RESOURCE	SOURCE	IDENTIFIER
Fetal bovine serum from GIBCO	Thermo Fisher Scientific	Cat# 10270-106
Fetal bovine serum from Corning	Thermo Fisher Scientific	Cat# 15377636
Penicillin-Streptomycin	Thermo Fisher Scientific	Cat# 15140122
Ficoll-Paque PLUS	Dutscher	Cat# 17-1440-03
Gentamicin (50mg/ml)	Thermo Fisher Scientific	Cat# 15750037
HEPES (1M)	Thermo Fisher Scientific	Cat# 15630080
DMEM, high glucose, GlutaMAX supplement	Thermo Fisher Scientific	Cat# 61965026
RPMI 1640 Medium, GlutaMAX supplement	Thermo Fisher Scientific	Cat# 61870010
cOmplete, EDTA-free, Protease inhibitor cocktails tablets	Roche	Cat# 11873580001
Azidothymidine	SIGMA	Cat# A2169; CAS: 30516-87-1; AZT
Nevirapine	SIGMA	Cat# SML0097; CAS: 129618-40-2; NVP
Cyclosporine A	Euromedex	Cat# S2286; CAS: 59865-13-3; CsA
Saponin from quillaja bark	Sigma Aldrich	S7900-100G
Goat serum	Sigma Aldrich	Cat# G9023-10ML
Fluoromount G with DAPI	eBioscience	Cat# 00-4959-52
Fluoromount G	eBioscience	Cat# 00-4958-02
SiR-DNA	Tebu-Bio	Cat# SC007
NucBlue DNA staining	Invitrogen	Cat# R37605
Etoposide	SIGMA	Cat# E1383-100MG CAS: 33419-42-0
Hydroxyurea	Sigma	Cat# H8627 CAS: 127-07-1
Bleomycin	Sigma	Cat# B8416 CAS: 9041-93-4
Q-VD-Oph	Selleckchem	Cat# S7311 CAS: 1135695-98-5
AZD6738	Selleckchem	Cat# S7693 CAS: 1352226-88-0
DMSO	VWR Chemicals	Cat# BDH1115 CAS: 67-68-5
Critical commercial assays		
Purelink HiPure Plasmid Midiprep Kit	Thermo Fisher Scientific	Cat# K210015
Nucleospin Gel and PCR Clean-Up kit	Macherey-Nagel	Cat# 740609.50
CD14 MicroBead human	Milteny Biotec	Cat# 130-050-201
LS columns	Milteny Biotec	Cat# 130-042-401
NucleoSpin RNA	Macherey-Nagel	Cat # 740955.50
NucleoSpin Tissue	Macherey-Nagel	Cat# 740952.50
LightCycler480 SYBR Green I Master	Roche	Cat# 4887352001
HIV-1 p24 ELISA Kit	Xpressbio	Cat# XB-1010
Foxp3 / Transcription Factor Staining Buffer Set	eBioscience	Cat# 00-5523-00
Deposited data		
Raw and analyzed data	This manuscript	NCBI GEO: GSE162019
Experimental models: Cell lines		
293FT	Thermo Fisher Scientific	Cat# R70007 RRID: CVCL_6911
HeLa	Laboratory of Dan Littman, New York University	N/A RRID: CVCL_0030
GHOST X4R5	NIH AIDS Reagent Program	Cat# 3942 RRID: CVCL_1E10
Oligonucleotides: See Table S1		
Recombinant DNA		
pCMV-VSVG	Manel et al., 2010	N/A
psPAX2	Manel et al., 2010	N/A
pTRIP-SFFV-tagBFP-2A	Cerboni et al., 2017	BFP
pTRIP-SFFV-TagRFP657-2A	This study	RFP657

(*Continued on next page*)

Continued

REAGENT or RESOURCE	SOURCE	IDENTIFIER
pTRIP-SFFV-EGFP	Lahaye et al., 2016	GFP
pTRIP-CMV-EGFP-2A		GFP
pTRIP-SFFV-tagBFP-2A-SUN1	This study (MGC cDNA cloneID: 40148817)	BFP
pTRIP-SFFV-tagBFP-2A-NtSUN2	This study	BFP
pTRIP-SFFV-tagBFP-2A-SUN1 Dharmacon (1-298)-ntSUN2 (220-717)	This study	BFP
pTRIP-SFFV-tagBFP-2A-NtSUN2 (1-219)-SUN1 Dharmacon (299-785)	This study	BFP
pTRIP-SFFV-TagRFP657-2A-SUN1 Dharmacon	This study (MGC cDNA cloneID: 40148817)	RFP657
pTRIP-SFFV-TagRFP657-2A-ntSUN2	This Study	RFP657
pTRIP-SFFV-EGFP-SR-KASH	This study	GFP
pLKO1puro-shLACZ	pLKO.1 clone ID TRCN0000072229	shRNA sequence: GCGATCGTAATCACCCGAGTG
pLKO.1-Puro-LMNA sh2	pLKO.1 clone ID TRCN0000061835	shRNA sequence: GAAGCAACTTCAGGATGAGAT
pLKO.1-Puro-LMNB2 sh5	pLKO.1 clone ID TRCN0000072422	shRNA sequence: CTACAAGTTCACGCCCAAGTA
Software and algorithms		
GraphPad Prism 7 and 8	GraphPad	https://www.graphpad.com/
Fiji	ImageJ	https://fiji.sc/
FlowJo	Tree Star	https://www.flowjo.com
Image Lab software – Version 5.2.1	BioRad	https://www.bio-rad.com/fr-fr/product/image-lab-software?ID=KRE6P5E8Z
LightCycler 480	Roche	https://lifescience.roche.com/en_fr/products/lightcycler14301-480-software-version-15.html
R	R Project	https://www.r-project.org
Bioconductor (packages listed in STAR methods)	Bioconductor	https://www.bioconductor.org

RESOURCE AVAILABILITY

Lead contact

Further information and requests for resources and reagents should be directed to and will be fulfilled by the lead contact, Nicolas Manel (nicolas.manel@curie.fr).

Materials availability

Plasmids generated in this study will be provided directly or through Addgene or similar service upon request.

Data and code availability

Gene expression data have been deposited at GEO and are publicly available as of the date of publication. The accession number is listed in the Key Resources Table. Microscopy data reported in this paper will be shared by lead contact upon request.

This paper does not report original code.

Any additional information required to reanalyze the data reported in this paper is available from the lead contact upon request.

EXPERIMENTAL MODEL AND SUBJECT DETAILS

Cell lines and primary cultures

GHOST (GHOST X4R5), 293FT and HeLa female cell lines were cultured in DMEM with Glutamax, 10% fetal bovine serum (FBS) (Corning), and penicillin-streptomycin (GIBCO). Human peripheral blood mononuclear cells (PBMCs) were isolated from buffy coats from normal human donors (approved by the Institut National de la Santé et de la Recherche Médicale ethics committee) using Ficoll-Paque PLUS (GE). $CD14^+$ cells were isolated by a positive selection with anti-human CD14 magnetic beads (Miltenyi) from PBMCs.

To obtain MDMs, $CD14^+$ cells were cultured in RPMI with Glutamax, 5% FBS (Eurobio), 5% human serum (Sigma), Penicillin-Streptomycin, Gentamicin (50 μg/ml, GIBCO) and HEPES (GIBCO) in the presence of recombinant human M-CSF (Miltenyi) at 50 ng/ml. Fresh media was added at day 5 or 6, and cells were treated/infected at day 9, after detachment via incubation with StemPro Accutase Cell Dissociation Reagent (GIBCO) for 30 minutes at 37°C. Drug treatments performed on cultured cells are listed in Key Resources Table.

METHOD DETAILS

Constructs

The plasmid constructs for lentiviral expression and HIV infection used in this study are listed in the Key Resources Table. pTRIP-SFFV-tagBFP-2A-SUN1 Dharmacon was generated by overlapping PCR cloning from commercially bought cDNA (MGC cDNA cloneID: 40148817) into pTRIP-SFFV-tagBFP-2A (Cerboni et al., 2017). pTRIP-SFFV-tagBFP-2A-ntSUN2 was generated by overlapping PCR mutagenesis from pLX304-SUN2 (Lahaye et al., 2016) into pTRIP-SFFV-tagBFP-2A with concomitant introduction of silent mutations that are not targeted by SUN2 shRNA 4 and 5 (respectively GAGCCTATTCAGACGTTTCACTTT to GAACCGATCCAAAC TTTCCATTTC and AAGAGGAAATCCAGCAACATGAAG to AAACGCAAGAGTTCTAATATGAAA). pTRIP-SFFV-tagBFP-2A-SUN1 Dharmacon (1-298)-ntSUN2 (220-717) and pTRIP-SFFV-tagBFP-2A-ntSUN2 (1-219)-SUN1 Dharmacon (299-785) were generated by overlapping PCR cloning from the full-length constructs. pTRIP-SFFV-tagRFP657-2A-SUN1 and pTRIP-SFFV-tagRFP657-2A-ntSUN2 were generated via restriction enzyme digestion from the tagBFP expressing vectors and ligation into pTRIP-SFFV-TagRFP657-2A backbone. HIV-GFP env-nef- was generated by PCR-mediated insertion of the Vpr+Vif+Vpu+ cassette from NL4-3 into HIV-GFP (Manel et al., 2010). HIV-GFP env-nef-vpr- was generated by overlapping PCR mutagenesis from HIV-GFP env-nef-, introducing a frameshift mutation within *vpr,* after the codon corresponding to amino-acid I63 (gaattc to gaaTTAAttc). HIV-mTagBFP2 and HIV-2 ROD9 ΔenvΔnef mTagBFP2+ were obtained via overlapping PCR mutagenesis, replacing GFP with the mTagBFP from pTRIP-SFFV-mTagBFP-2A.

Virus production

Viral particles were produced by transfection of 293FT cells in 6-well plates with 3 μg DNA and 8 μL TransIT-293 Transfection Reagent (Mirus Bio) per well. For VSV-G pseudotyped SIVmac virus-like particles (VLPs), 0.4 μg CMV-VSVG and 2.6 μg $pSIV3^+$ was used. For VSV-G pseudotyped HIV-1 and HIV-2 viruses used in the study, 0.4 μg CMV-VSVG and 2.6 μg HIV DNA was used. For overexpression or shRNA mediated knock-down, 0.4 μg CMV-VSVG, 1 μg psPAX2 and 1.6 μg of lentivector of interest were combined. One day after transfection, media was removed, cells were washed once, and 3 mL per well of RPMI medium with Glutamax, 10% FBS (GIBCO), PenStrep (GIBCO), 50 μg/ml Gentamicin (GIBCO) and 0.01 M HEPES (GIBCO) were added. Viral supernatants were harvested 1 day later, filtered using 0.45 μm pore filters, used fresh or aliquoted and frozen at −80°C. When required, the virus was purified and concentrated on a 20% sucrose cushion in phosphate buffered saline (PBS) in Ultra Clear Centrifuge tubes (Beckman Coulter), via ultracentrifugation at 4°C at 31,000 *x g* in a SW32Ti swinging bucket rotor (Beckman Coulter). Viral pellets were then resuspended in complete medium at a 100-fold concentration compared to crude. Viral titers were measured on GHOST cells (titration as previously described (Manel et al., 2010) or using HIV-1 p24 ELISA (XpressBio). ELISA absorbance acquisitions were acquired on a FLUOstar OPTIMA (BMG Labtech) and data were analyzed and exported to Excel with MARS Data Analysis Software (BMG Labtech).

Cell transduction for protein overexpression or knockdown

HeLa cells were counted and seeded in 6-well plates on the day prior to transduction. Purified virus was added at a 2:1 volume ratio on medium containing protamine at a final concentration of 1 μg/ml. $CD14^+$ monocytes were seeded in 10-cm dishes in the presence of 50 ng/ml M-CSF to induce differentiation into macrophages and transduced with purified SIVmac VLPs and lentiviruses carrying vector of interest, mixed at a 1:1 ratio. Human serum was added at day 1 post transduction. Transductions of monocytes was performed in the presence of protamine at a final concentration of 1 μg/ml. HeLa cells were washed once in PBS and passaged at 48 hours post transduction with or without 2 μg/ml of puromycin. For MDMs, medium was replaced at day 5-6 post transduction. Overexpression was assessed by quantification of fluorescent reporter signal via flow cytometry on a BD FACSVerse flow cytometer. Both overexpression and protein knock-down were confirmed by Western Blotting at day of experiment.

Cell infection

HeLa, GHOST and MDMs (day 8-9 post transduction) were seeded and infected in the presence of 1 μg/ml of protamine with serial dilutions of frozen viral stocks in a BSL-3 laboratory. For HIV-1 and HIV-2, viruses made with the plasmids HIVGFP (NL4-3 strain) and HIV-2 ROD9 ΔenvΔnef GFP (ROD strain), respectively, were used in most experiments, except noted otherwise. Virus was removed at 48 hours post-infection, cells were washed, harvested, stained for viability using Fixable Viability Dye eFluor 780 in PBS where required, fixed in 1% paraformaldehyde (PFA; Electron Microscopy Sciences) and analyzed for GFP, BFP or p24 positivity via flow cytometry on a BD FACSVerse flow cytometer. Viral titers were calculated based on seeded cell number and the percentages of infected cells, within the linear range of infection.

DNA damage induction

For chemical induction of DNA damage, HeLa cells were seeded in 12-well plates 24 hours prior to treatment and infection. The following day, cell medium was replaced with complete medium containing 1 μg/ml of protamine and different concentrations of either etoposide, hydroxyurea or bleomycin (Sigma). Corresponding concentrations of diluents DMSO or water were used as non-treated controls. Cells were infected immediately after treatment, as described above. Four hours later, drugs and viruses were removed and cells were washed once with PBS. 1mL of fresh medium per well was added and cells were put back in culture for 44 hours. In the case of etoposide treatment, medium was supplemented with 50 mM of Q-VD-Oph to allow cell survival. One control well per treatment condition was harvested at either 4 or 24 hours post treatment, for intranuclear γH2AX staining, as described.

For UV irradiation, HeLa cells were seeded in 12-well plates 24 hours prior to irradiation and infection. Media was replaced the following day to include 1 μg/ml of protamine and cells were UV irradiated at a 1 mJ/cm^2 setting for 2 s using UVILink *CL 508 Crosslinkers* from *UVITec*. Infection was performed immediately after irradiation and cells were left in culture for another 48 hours. One control well per irradiation condition was harvested at 4 hours post irradiation, for intranuclear γH2AX staining, as described.

HIV DNA quantification

HeLa cells and MDMs were infected as described, with the addition of infected wells treated with reverse transcriptase inhibitors as negative control. For this purpose, either 24 μM of AZT (Sigma) or 10 μM of NVP (Sigma) were used. After 24 hours, cells were washed in PBS and harvested. Total DNA was extracted from cell pellets using NucleoSpin Tissue (Macherey-Nagel) kit, as per manufacturer's protocol. Quantitative real-time PCR analysis was performed in a Roche LightCycler 480 with Roche 480 SYBR Green I master reagent in 20 mL final volume per well according to manufacturer specifications as previously described (Lahaye et al., 2013). Each sample was measured in triplicate for all primers. For beta-globin, primers were bglobin-f and bglobin-r. Cycling conditions were 1x 95°C for 5′; 35x 95°C for 10'', 65°C for 20'' (50°C for beta-globin) and 72°C for 30''. Relative concentrations of total DNA (Late RT), 2-LTR circles and integrated viral DNA were calculated relative to beta-globin using the ΔCt method. The primers used are listed in Table S1.

Western blotting

0.5 to 1 million cells were lysed in 100 μL of RIPA buffer (50 mM Tris HCl, 150 mM NaCl, 0.1% SDS, 0.5% DOC, 1% NP-40, Protease inhibitor (Roche; 1187358001)). Lysis was performed on ice for 30'. Lysates were cleared by centrifugation at 8000 g for 8 minutes at 4°C, 20 μl of Laemmli 6x (12% SDS, 30% Glycerol, 0.375 M Tris-HCl pH 6.8, 30% 2-mercaptoethanol, 1% bromophenol blue) was added and samples were boiled at 95°C for 15'. Cellular protein lysates were resolved on Criterion or 4% – 20% Bio-Rad precast SDS-PAGE gels and transferred to PVDF membranes (Bio-Rad). Membranes were saturated and proteins were blotted with antibodies in 5% non-fat dry milk, PBS 0.1% Tween buffer. ECL signal generated via Clarity Western ECL substrate (Bio-Rad) was recorded on the ChemiDoc-XRS or ChemiDoc Touch Bio-Rad Imager. Data were analyzed and quantified with the Image Lab software (Bio-Rad). The antibodies used in this study are listed in the Key Resources Table.

Live confocal imaging

For live imaging, HeLa cells were plated either in a glass bottom FluoroDish (World Precision Instruments) or in a glass-bottom Cellview Cell Culture Dish with 4 compartments (Greiner Bio-One), on the day prior to experiments. One hour before imaging, cells were incubated with either 1 μM of SiR-DNA (Tebu Bio) or 2 drops of NucBlue Live Ready Probes (Invitrogen), directly in the culture medium, at 37°C. Images of cells were acquired with a Leica DmI8 inverted microscope equipped with an SP8 confocal unit using a 20x dry objective (NA = 0.75, pixel size was fixed to 0.284 μm). Imaging was performed in an on-stage incubator chamber at 37°C, with 5% CO_2. An image per condition was taken every 2 or 6 minutes, depending on the experiment.

Image analysis was performed using Fiji software (Schindelin et al., 2012). For chromatin dynamics analysis, a homemade macro was first used to do segmentation of each nucleus on the Video and identify them using the 3D object counter. Particle Image Velocimetry (PIV) analysis was then performed on SiR-DNA staining using the PIV plug-in (Tseng et al., 2012). PIV is a basic optic flow analysis, that divides each image of a stack in small clusters of pixels (interrogation windows) and measures the displacement of each cluster between pairs of consecutive frames. The cross-correlation then generates a pattern of ''movements'' within the nucleus that are color-coded based on the amplitude of the vector corresponding to the displacement of each cluster. An in-house script was used to first align each individual nucleus, then measure and average SiR-DNA displacements over the ten first time points. Red shades indicate higher amplitudes of displacement while violets correspond to quasi-immobile clusters. For nuclear rotation analysis, a macro was used to measure rotation angles across the first 30 frames. Briefly, individual nuclei were first aligned using a translation transformation of the MultiStackReg plug-in (Brad Busse, Stanford), then they were aligned using the rotation transformation and the transformation was applied to a reference image containing 2 fixed points (one at the center and one on the edge) to measure the rotation. A threshold of 1 degree/minute was used to define rotating nuclei. The percentage of rotation time and the average velocity was then computed.

Confocal Immunofluorescence Imaging

For immunofluorescence, HeLa cells were grown overnight onto 12 mm glass coverslips (Thermo Scientific) placed in 6-well plates. For nuclear shape quantification, 1 μM of SiR-DNA was added in cell culture media and cells were incubated for 2 hours at 37°C. Cells

were then fixed with 4% PFA for 20 minutes at room temperature. Coverslips were washed multiple times with PBS and quenched with 0.1 M Glycine in PBS (Life Technologies) for 10 minutes at room temperature. For nuclear shape quantification, coverslips were washed multiple times in PBS, rinsed once in distilled water and were ready for mounting and imaging. For intracellular staining, coverslips were further blocked with PBS, 0.2% (w/v) bovine serum albumin (BSA) (Euromedex), 0.05% (w/v) Saponin from quillaja bark (SIGMA) for 30 minutes at room temperature. Cells were stained overnight with anti-NUP153 antibody at 2 μg/mL (1:50 dilution) or with Normal Rabbit IgG Isotype Control at corresponding concentration of the primary antibody, in PBS, 0.2% (w/v) BSA, 0.05% (w/v) Saponin + 10% goat serum (Sigma), at 4°C in a humidified chamber. The following day, cells were washed multiple times and incubated with the secondary antibody Alexa Fluor 546 goat anti-rabbit IgG (H+L) (Invitrogen; 1:200 dilution in PBS-BSA-Saponin) in the presence of 1 μM of SiR-DNA for 2 hours in the dark, at room temperature. Coverslips were washed multiple times in PBS-BSA-Saponin and finally rinsed once in distilled water. Coverslips for all experiments were mounted onto glass slides using Fluoromount G (eBioscience) mounting medium. The slides were finally dried at 37°C for 1h and stored at 4°C. Cells were imaged with a Leica DmI8 inverted microscope equipped with an SP8 confocal unit using an oil immersion 63x objective (NA = 1.4) for NUP-153 staining or an oil immersion 40x objective (N = 1.3) for nuclear shape measurement, with applied Type F Immersion Liquid (Leica).

Fluorescence recovery after photobleaching

Cells were seeded at 2.5 × 10^5 cells/dish in a glass bottom FuoroDish (World Precision Instruments) on the day prior to the experiment. Cells were imaged with a Leica DmI8 inverted microscope equipped with an SP8 confocal unit using a 20x dry objective (NA = 0.75). Imaging was performed in an on-stage incubator chamber at 37°C, with 5% CO_2. Two independent modules were used in a sequential manner: one for bleaching, one for imaging the signal recovery. During the application of the bleaching module, the 488 laser was focused at an intensity of 5% and with a gain of 0.1% on to an area within the nucleus of each cell at maximum zoom for 20 s. Immediately afterward, the first sequence was manually cancelled, the resolution was optimized, imaging area was restored to the whole cell for the second sequence. The laser power was set for optimal imaging level and images of the whole cell were acquired for 3 min circa at the rate of one image every 2.2 s.

Intracellular staining for flow cytometry

Cell surface staining was performed in PBS, 1% BSA (Euromedex), 1 mM EDTA (GIBCO), 0.01% NaN3 (AMRESCO) (FACS Buffer) at 4°C. Viability staining (Live-Dead) with Fixable Viability Dye eFluor 780 was performed in PBS at 4°C. Intracellular p24 staining was carried out as follows: 48 hours after infection, cells were extensively washed with PBS, harvested and fixed/stained using the BD Cytoperm/Cytofix kit, as per manufacturer's protocol, using the anti-HIV-1 core antibody clone KC57 coupled to FITC. Intracellular staining of γH2AX was performed using the FOXP3/Transcription Factor Staining Buffer Set (eBioscience) as per manufacturer's protocol. Cells were resuspended in FACS Buffer prior to final acquisition. All flow cytometry acquisitions were performed on the FACSVerse (BD) using the FACSSuite software (BD) and analyzed on FlowJo v10. The antibodies used are listed in the Key Resources Table.

Electron microscopy

Cells were seeded at 5 × 10^4 cells/well in a 24w plate onto sterile 12 mm glass coverslips (Thermo Scientific) and left to adhere overnight. The following morning, cells were washed in PBS and were fixed using 2% glutaraldehyde in 0.1 M cacodylate buffer, pH 7.4 for 1h, post fixed for 1h with 2% buffered osmium tetroxide, dehydrated in a graded series of ethanol solution, and then embedded in epoxy resin. Images were acquired with a digital 4k CCD camera Quemesa (EMSIS GmbH, Münster, Germany) mounted on a Tecnai Spirit transmission electron microscope (ThermoFisher, Eindhoven, the Netherlands) operated at 80kV.

Micropipette aspiration microscopy

Prior to harvest, HeLa cell lines were incubated with 1 μM SiR-DNA dye from Tebu Bio for 1h30 at 37°C in cell culture medium. Cells were washed, harvested, and resuspended at a concentration of 5x10^6 cells/mL in sterile 3% BSA in PBS-0.2% FBS. Cells were subjected to the experimental conditions as described previously (Davidson et al., 2019).

Gene expression analysis by microarray

We performed three independent experiments with control, SUN1 and SUN2 expressing cells. Total RNA was extracted from 10^6 HeLa cells using NucleoSpin RNA and adjusted to 50 ng/μL. A WT PLUS amplification and labeling protocol was conducted with 100 ng of total RNA. Samples passed the quality control with a high score. The Affymetrix analysis was performed by the NGS platform at Institut Curie using the Human Gene 2.0 ST chip. Human Gene 2.0ST array were scanned using a Genechip 7G scanner, according to the supplier's protocol. Micro-array analyses were processed with R using packages from Bioconductor. The quality control was performed using ArrayQualityMetrics package without detecting any outlier among the experiment. Data were normalized using the Robust Multi-Array Average algorithm from the Oligo package. Annotation of the probes was done using the hugene20 annotation data (chip hugene20sttranscriptcluster) from Bioconductor. Differential gene-expression analysis was performed with Limma.

QUANTIFICATION AND STATISTICAL ANALYSIS

Statistical analyses were performed in Prism 7 or 8 (GraphPad Software). The statistical tests used, as well as statistical parameters including the exact value of n, dispersion, and precision measures, are reported in the figures and figure legends. In the figures, significance is indicated as follows: *p < 0.05, **p < 0.01, ***p < 0.001; ****p < 0.0001; ns, not statistically significant.

ADDITIONAL RESOURCES

The graphical abstract was created with BioRender.com.

APPENDIX C: List of publications

- Bhargava A., Williart A., Maurin M., Davidson PA., Jouve M., Piel M., Lahaye X., Manel N. Inhibition of HIV infection by structural proteins of the inner nuclear membrane is associated with reduced chromatin dynamics. *Cell Reports*. 2021. doi: 10.1016/j.celrep.2021.109763

Contribution: I performed the image analysis to assess chromatin and nuclear dynamics.

- Nader GPF., Aguëra-Gonzalez S., Routet F., Gratia M., Maurin M., Cancila V., Cadart C., Palamidessi A.,Nalio Ramos R., San Roman M., Gentili M., Yamada A., Williart A., Lodillinsky C., Lagoutte E., Villard C., Viovy JL., Tripodo C., Galon J., Scita G., Manel N., Chavrier P., Piel M. Compromised nuclear envelope integrity drives TREX1-dependent DNA damage and tumor cell invasion. *Cell*. 2021. doi: 10.1016/j.cell.2021.08.035

Contribution: I performed an experiment to control the independency of NE ruptures from the cell cycle stage at 2 µm confinement in DCIS.

- Srivastava N., Nader GPF., Williart A., Rollin R., Cuvelier D., Lomakin A., Piel M. Nuclear fragility, blaming the blebs. *Current Opinion in Cell Biology.* 2021. doi: 10.1016/j.ceb.2021.01.007

Contribution: I participated to the text.

- Nader GPF., Williart A., Piel M. Nuclear deformations, from signaling to perturbation and damage. *Current Opinion in Cell Biology*. 2021. doi: 10.1016/j.ceb.2021.07.008

Contribution: I participated to the text.

- Zakharova VV., Magnitov MD., Del Maestro L., Ulianov SV., Glentis A., Uyanik B., Williart A., Karpukhina A., Demidov O., Joliot V., Vassetzky YS., Mège RM., Piel M., Razin SV,Ait-Si-Ali S. SETDB1 fuels the lung cancer phenotype by modulating epigenome, 3D genome organization and chromatin mechanical properties. *Nucleic Acids Research*. 2022. doi: 10.1093/nar/gkac234

Contribution: I performed the experiments to measure chromatin dynamics in WT and KO contexts.

- Venkova L., Singh Vishen A., Lembo S., Srivastava N., Duchamp B., Ruppel A., Williart A., Vassilopoulos S., Deslys A., Garcia Arcos JM, Diz-Muñoz A., Balland M., Joanny JF., Cuvelier D., Sens P., Piel M. A mechano-osmotic feedback couples cell volume to the rate of cell deformation. *Elife.* 2022. 10.7554/eLife.72381

Contribution: I performed an experiment to measure plasma membrane tension in osmotic shock.

- Alraies A., Rivera CA., Delgado MG., Sanséau D., Maurin M., Amadio R., Piperno GM., Dunsmore G., Yatim A., Lacerda Mariano L., Sáez PJ, Gratia M., Lamiable O., Moreau A., Williart A., Albaud B., Legoix B., Nakano H., Cook DN., Lawrence T., Manel N., Benvenuti F., Ginhoux F., Moreau HD.,

Nader GPF., Piel M., Lennon-Duménil AM. A Shape Sensing Mechanism driven by Arp2/3 and cPLA2 licenses Dendritic Cells for Migration to Lymph Nodes in Homeostasis. *Biorxiv*. 2022

Contribution: I performed the NE fluctuations experiment.

- Williart A., Popard H., Piel M. Ruptures mécaniques de l'enveloppe du noyau des cellules et cancer du sein. *médecine/sciences*. 2022. doi: 10.1051/medsci/2023056

Contribution: I wrote the main part of the text.

Résumé en français

INTRODUCTION

Le noyau est l'organite caractéristique du groupe des Eucaryotes. C'est le compartiment qui contient l'ADN génomique de la cellule. Bien qu'il forme un compartiment, il est en contact permanent avec le cytosol et le reste de la cellule.

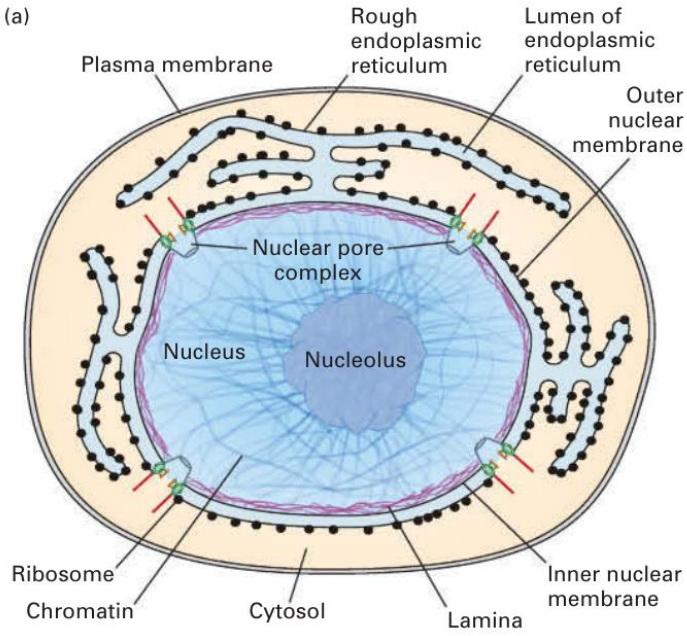

Figure 55 : Ultrastructure du noyau
(Lodish *et al.*, 2016)

I. Le noyau, un organite composé de multiples couches

Le noyau est délimité par un double membrane lipidique appelée enveloppe nucléaire. La composition des membranes nucléaires est restée longtemps indéterminée, en raison des difficultés techniques à obtenir des membranes pures. Elle diffère des autres membranes cellulaires par son plus haut taux de phosphatidylcholine et sa faible teneur en cholestérol et en sphingolipides (van Meer *et al.*, 2008; Bigay and Antonny, 2012). Il est intéressant de noter que, bien qu'elles soient en continuité, il semble que la

composition lipidique des membranes interne et externe soit différente. L'enveloppe apparaît également comme un compartiment dynamique du point de vue de sa composition lipidique, puisque différentes enzymes modifiant les lipides, telles que cPLA2 (Enyedi *et al.*, 2016), ou la lipine (Péterfy *et al.*, 2001).

L'enveloppe est perforée par des pores nucléaires, de larges complexes macromoléculaires qui contrôlent les échanges entre le cytosol et le nucléoplasme. Son architecture complexe comprend de multiples protéines transmembranaires au niveau des points de haute courbure à la jonction entre membranes interne et externe, ainsi que des protéines solubles en interaction avec elles, à la fois du côté cytosolique et du côté nucléaire. De récents travaux ont montré que son diamètre peut être modulé lors de chocs osmotiques ou de privation de nutriments chez la levure (Zimmerli *et al.*, 2021). Les échanges entre noyau et cytoplasme sont contrôlés par la capacité des molécules à transiter au cœur du pore. Les molécules de petite taille peuvent diffuser librement, tandis que les plus volumineuses requièrent l'interaction avec des protéines navettes via des séquences spécifiques. Ce contrôle assure la spécificité du contenu nucléoplasmique.

L'espace périnucléaire est en continuité avec la lumière du réticulum et est délimité par la membrane interne et la membrane externe. A ce titre, il constitue un probable réservoir de calcium, bien que très peu de canaux calciques soient caractérisés dans l'enveloppe nucléaire, à l'exception de quelques types cellulaires.

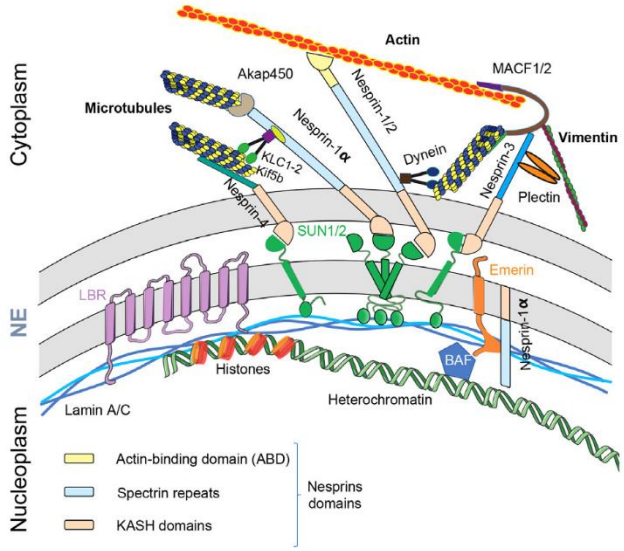

Figure 56 : Organisation du complexe LINC
(Janin and Gache, 2018)

La largeur de l'espace périnucléaire est maintenue par le complexe LINC, ancré dans les membranes interne via les protéines SUN, et externe via les nesprines. Les protéines SUN 1 et 2, organisés en trimères, sont liées covalamment aux nesprines par deux ponts disulfure. Du côté nucléaire, les protéines SUN interagissent avec la lamina, le réseau protéique sous-jacent à la membrane interne, et l'ADN. Du côté cytoplasmique, les nesprines interagissent avec le cytosquelette et, par ces interactions, sont reliées à la membrane plasmique. Ainsi, le complexe LINC assure la continuité mécanique entre le cytoplasme et le noyau (Maniotis *et al.*, 1997).

L'enveloppe nucléaire est soutenue par un réseau de filaments intermédiaires, les lamines. Il existe 3 gènes codant des lamines chez les Mammifères, *LMNB1*, codant la lamine B1, *LMNB2*, codant la lamine B2, et *LMNA*, qui peut, par épissage alternatif, donner naissance à la lamine A ou la lamine C, collectivement nommées lamine A/C. Les trois lamines possèdent des structures similaires, mais les différences de modifications post-traductionnelles résultent en un attachement direct des lamines B à la membrane interne, tandis que les lamines A et C ne sont pas directement liées à la membrane et peuvent être présentes sous forme soluble dans le nucléoplasme.

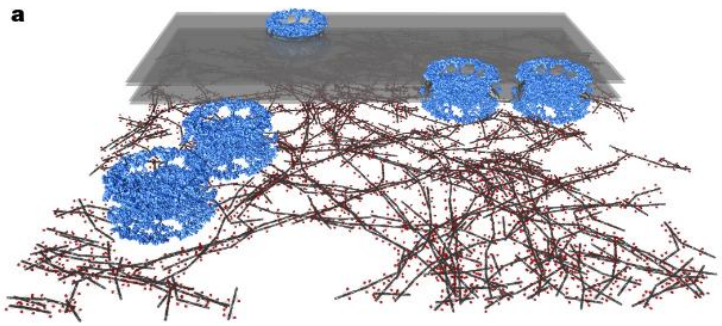

Figure 57 : Structure du réseau de lamines
*(*Xenopus laevis*) Lamines (domaine en bâtonnet en gris and domaine immunoglobuline en rouge), pores nucléaires (bleu), membranes internes et externe (gris transparent), reconstruction d'après un cryo-tomogramme (Turgay et al., 2017)*

Les lamines forment des filaments de 3.5 nm de diamètre et s'assemblent dans un réseau de 14 nm d'épaisseur (Turgay *et al.*, 2017) sous la membrane interne en deux réseaux concentriques (Shimi *et al.*, 2015). Le réseau de lamines B est en interaction directe avec la membrane, tandis que le réseau de lamines A/C se situe en-dessous du premier. Le turnover de la lamine est extrêmement lent, de plus de 180 min, et le réseau n'a pas de propriétés contractiles, contrairement au cortex d'actomyosine.

Le noyau est l'hôte de l'ADN génomique de la cellule. Celui-ci est composé de paires de chromosomes, des molécules linéaires à base de nucléotides, dont le squelette osidique est chargé négativement (Figure 58A). La structure en double brin de l'ADN repose sur des interactions faibles entre les bases azotées des nucléotides, proposées par Watson et Crick lorsque la structure de la double hélice fut mise en évidence.

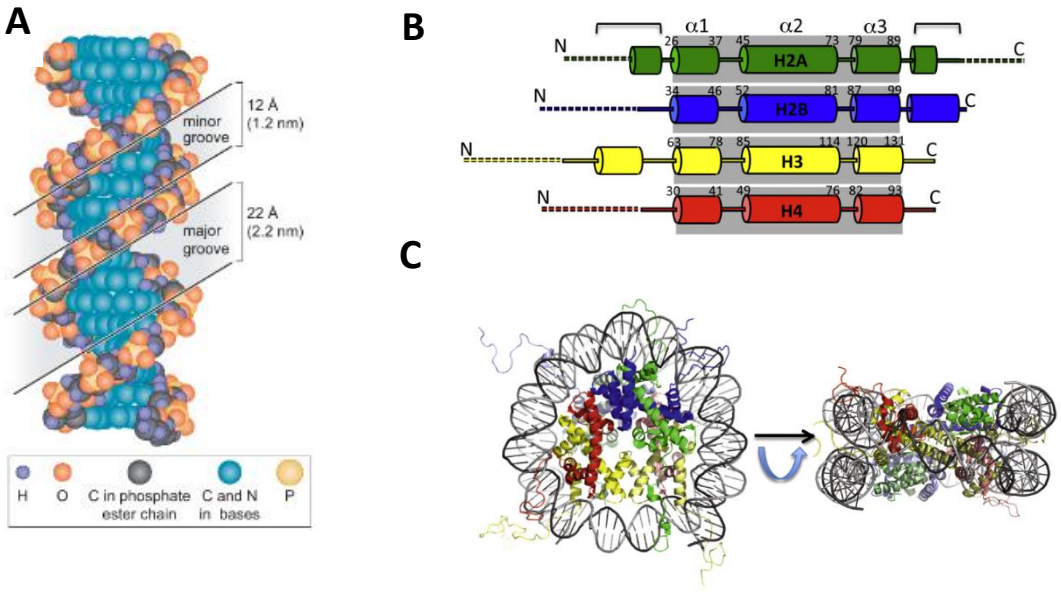

Figure 58 : Structure de l'unité de base de l'organisation de la chromatine, le nucléosome
A. Polymère linéaire d'ADN (Watson et al., 2014) B. Structure des histones du cœur C. Vues du dessus et latérale du nucléosome avec l'octamère d'histones et l'ADN enroulé (Cutter and Hayes, 2015)

On estime à environ 2 m la longueur d'ADN linéaire comprise dans un noyau mammifère, d'environ 10 µm de diamètre. Les interactions entre l'ADN et de multiples protéines, qui forment ensemble la chromatine, participent à la compaction et l'organisation 3D du génome.

L'ADN linéaire est enroulé autour d'un octamère protéique constitué de deux tétramères d'histones, appelé le nucléosome (Figure 58B et C). Les deux tétramères H2A/H2B/H3/H4 se superposent et forment le cœur du nucléosome. L'ADN interagit de manière essentiellement non-spécifique avec les histones (Luger *et al.*, 1997).

L'ADN comme les histones peuvent subir des déformations post-transcriptionnelles. Ainsi, l'ADN peut être méthylé au niveau de la cytidine, ce qui augmente l'affinité de l'ADN pour la queue des histones (Li *et al.*, 2022). Les histones, quant à elles, peuvent être modifiées de multiples manières, en particulier sur les résidus de lysine. L'organisation tridimensionnelle de la chromatine émerge principalement des modifications sur les queues des histones qui servent de plate-forme de recrutement pour d'autres protéines.

La chromatine est généralement divisée entre euchromatine, peu condensée et transcriptionnellement active, et hétérochromatine, constitutive ou facultative, dense et silencieuse. Ces états sont chacun associés à des marques caractéristiques. L'euchromatine est caractérisée par des acétylations de l'histone 3, qui permettent le recrutement de la machinerie de transcription (Vermeulen *et al.*, 2007). A l'opposé du spectre de condensation, on distingue l'hétérochromatine constitutive, dans des régions du génome généralement dépourvues de gènes et qui restent condensées et la chromatine facultative, dont le niveau de condensation est plus dynamique et peut être modulée par différents signaux. Ces types de chromatine sont associées à des modifications des histones caractéristiques, permettant le recrutement de différentes protéines, qui structurent la chromatine et organisent sa compaction.

La structure 3D de la chromatine, à l'échelle au-dessus du nucléosome, est assez peu connue. Les techniques de capture de conformation de chromosomes ont permis de mettre en évidence des interactions de moyenne et longue distance entre des régions distantes d'un même chromosome et entre chromosomes. Au sein d'un même chromosome, les cartes d'interaction suggèrent une structure en forme de boucles Les régions de même degré de condensation ont une plus forte probabilité d'interagir avec elles-mêmes, même à de longues « distances » chromosomiques.

La lamine et l'enveloppe participent également à l'organisation tridimensionnelle de la chromatine. En effet, de nombreuses protéines de la membrane interne, comme LAP2β, BAF ou l'émerine, interagissent directement avec l'ADN, de même que les lamines. Les régions associées à la lamina, dénommées LAD, sont généralement composés d'hétérochromatine et sont peu exprimées.

Le noyau est donc un organite à la structure complexe, dont les différents composants sont en interaction les uns avec les autres. Il forme un compartiment fortement différent du cytosol mais est physiquement intégré au reste de la cellule.

II. Fonctions de l'enveloppe nucléaire

L'enveloppe nucléaire constitue une barrière physique qui permet d'isoler l'ADN du cytoplasme et constitue un rempart supplémentaire entre le génome et l'environnement. Ainsi, le milieu extracellulaire contient des pathogènes susceptibles de nuire à l'intégrité du génome, tels que de nombreux virus. Si une partie des virus effectue son cycle dans le cytoplasme en ne détournant que la machinerie de synthèse protéique de l'hôte, d'autres ont besoin d'accéder au contenu nucléaire, voire de s'intégrer dans le génome de l'hôte pour compléter leur cycle. Nous discuterons dans la partie suivante des stratégies développées par de nombreux virus pour réussir à la contourner, mais il est intéressant de noter que de

nombreux virus requérant le contact avec le noyau n'ont d'autre méthode que d'attendre la dissolution de l'enveloppe associée à la mitose. D'autres ont développé des mécanismes permettant d'assurer leur passage par le pore nucléaire, soit en favorisant l'interaction avec certaines nucléoporines, soit en développant des séquences de type NLS dans leurs protéines de capside ou accessoires. Certains virus sont en partie assemblés dans le noyau et doivent, une fois assemblés, être capables d'en sortir. Certains induisent ainsi une voie de signalisation qui mime l'entrée en mitose et le désassemblage de l'enveloppe, tandis que d'autres remodèlent largement l'enveloppe en provoquant une fusion locale des membranes interne et externe. Ces profonds remodelages induits par les virus montrent le potentiel plastique de l'enveloppe nucléaire. Le cytoplasme lui-même contient également des enzymes dont l'activité peut être néfaste pour le génome. En effet, il comporte notamment des nucléases ou des senseurs d'ADN, au départ associées à l'immunité antivirale intrinsèque, qui peuvent causer des dommages à l'ADN (Nader *et al.*, 2021).

L'enveloppe et la lamina jouent un rôle de structure et participent à l'organisation tridimensionnelle du génome. Elles sont aussi actrices de différents processus liés à l'ADN. Des études ont montré que les LAD n'étaient pas simplement des domaines structurels mais aussi fonctionnels, et étaient étroitement corrélés au niveau d'expression des gènes. Les LAD sont relativement homogènes en termes de caractéristiques chromatiniennes et sont particulièrement enrichis en marques chromatiniennes d'extinction des gènes. Par ailleurs, l'insertion de rapporteurs dans les LAD induit une expression des gènes plus faible que dans d'autres régions du génome (Akhtar *et al.*, 2013). Ceci indique que la localisation au niveau de la périphérie semble être en partie instructive pour l'extinction de l'expression des gènes, soulignant un rôle fonctionnel de l'architecture de l'enveloppe. La périphérie joue également un rôle dans les processus de réparation de l'ADN. Chez la levure, les cassures double brin de l'ADN sont relocalisées au niveau des pores nucléaires lors de leur réparation. Le double KO SUN1 SUN2 induit également des difficultés de réparation (Lei *et al.*, 2012), suggérant que les protéines de la membrane interne peuvent être des acteurs importants dans ces phénomènes.

III. Dynamique de l'enveloppe nucléaire

Jusqu'à présent, nous avons évoqué les fonctions associées au noyau en considérant sa structure comme stable. Néanmoins, le noyau peut être profondément remodelé lors de différents processus biologiques.

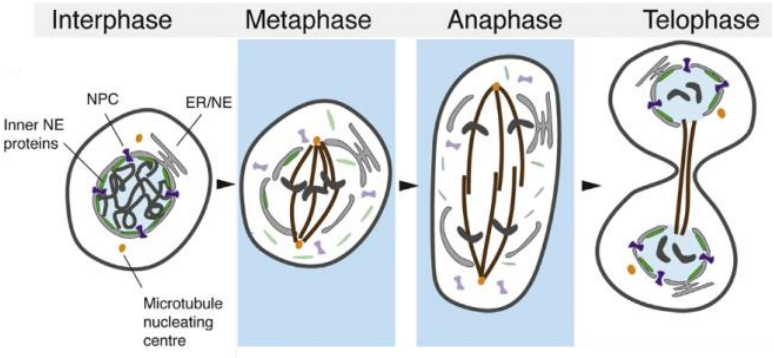

Figure 59 Dynamique de la structure nucléaire en mitose
Adapté de (Dey and Baum, 2021)

Ainsi, chez les eucaryotes effectuant une mitose dite « ouverte », comme les Mammifères, l'enveloppe nucléaire est complètement désassemblée et reformée à l'issue de la division. Le désassemblage de l'enveloppe nucléaire s'effectue sous le contrôle du complexe cycline B – Cdk1, qui phosphoryle certaines nucléoporines ainsi que le réseau de lamine A/C (Glavy *et al.*, 2007). Ainsi, les domaines solubles des pores nucléaires sont désassemblés, les filaments de lamines A et C se désagrègent et rompent leur association avec la membrane nucléaire interne, et l'enveloppe est présente dans le cytoplasme sous forme de composants solubles ou de vésicules. Durant la télophase, les protéines interagissant avec la chromatine et l'enveloppe sont recrutées sur les chromosomes. L'enveloppe nucléaire est ainsi réassemblée séquentiellement.

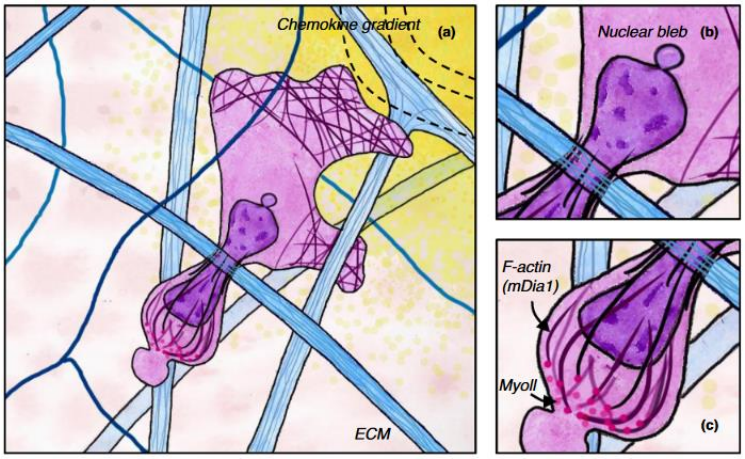

Figure 60 : Déformations du noyau lors de la migration confinée
(Vargas et al.*, 2017)*

Les interactions du noyau et de l'enveloppe avec le reste de la cellule sont également dynamiques. Lors des processus migratoires, et en fonction du mode de migration, les interactions avec le cytosquelette

peuvent être profondément remodelées. Ainsi, des fibres d'actine spécifiques, les lignes TAN, sont observées dans les cellules effectuant des migrations mésenchymateuses. Elles émanent des nesprines et forment des liens forts avec le cortex de la cellule. Le positionnement du noyau dans la cellule varie en fonction du type de migration et des interactions entre Lors de migration dans des environnements complexes, le noyau, qui est deux à dix fois plus rigide que le corps cellulaire, peut représenter un obstacle à la migration. Dans ces situations, il est fortement déformé, à la fois par l'environnement et par les fibres contractiles d'actomyosine qui exercent les forces nécessaires à la locomotion de la cellule (Figure 60).

IV. La mécanique et le noyau

Le noyau peut donc ainsi être soumis à des contraintes importantes, par l'environnement ou le cytosquelette. Ces déformations peuvent être perçues par la cellule et fonctionner comme signal initiant des voies de transduction ou des changements du comportement cellulaire.

Les capacités prolifératives des cellules ou leurs fonctions peuvent être altérées en fonction de leur environnement, de la rigidité de leur substrat ou de leur degré d'interaction avec d'autres cellules. Ces paramètres sont perçus par la cellule au niveau de la membrane plasmique, au moyen des points d'adhésion focale et des jonctions cellulaires. La voie Hippo a été identifiée comme élément déterminant de la réponse aux changements mécaniques de l'environnement. Lorsque les facteurs de transcription YAP et TAZ sont phosphorylés par LATS1/2, ils sont séquestrés dans le cytoplasme. Leur déphosphorylation entraîne leur relocalisation nucléaire et l'activation de voies pro-prolifératives. La voie YAP/TAZ est ainsi impliquée dans de nombreux cancers. Les signaux induisant l'activation de YAP/TAZ sont restés longtemps méconnus, jusqu'à ce que de multiples facteurs mécaniques soient identifiés : rigidité du substrat, contrainte de cisaillement, interactions cellule-cellule (Dupont *et al.*, 2011; Aragona *et al.*, 2013; Panciera *et al.*, 2017)…

Le noyau lui-même a également émergé comme étant capable de mécanosensation. Des travaux ont ainsi montré que la relocalisation nucléaire n'était pas simplement au changement du statut de phosphorylation, mais également à une augmentation de l'import actif de YAP/TAZ (Elosegui-Artola *et al.*, 2017; Andreu *et al.*, 2022). Celui-ci passerait par une dilatation des pores nucléaires (Zimmerli *et al.*, 2021) (Figure 61A). Différentes enzymes sont également recrutées au niveau de l'enveloppe nucléaire lors de déformations, soit par choc osmotique, soit par compression (Figure 61B). C'est ainsi le cas pour la lipase

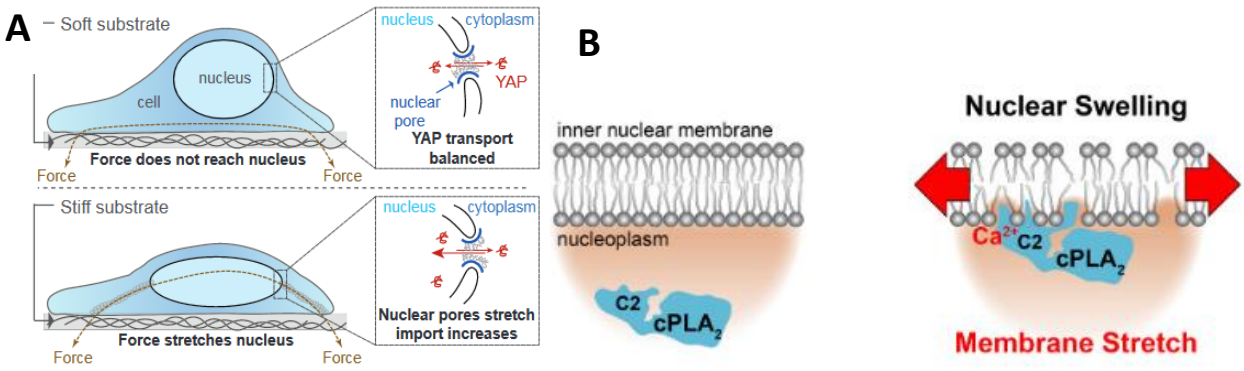

Figure 61 : Mécanosensation par le noyau

A. Augmentation de l'import nucléaire en présence de forces appliquées au noyau (Elosegui-Artola *et al.*, 2017)*) B. Recrutement de cPLA2 à l'enveloppe nucléaire lors de chocs hypoosmotiques* (Enyedi *et al.*, 2016)

cPLA2 (Enyedi *et al.*, 2016; Lomakin *et al.*, 2020; Venturini *et al.*, 2020) et la kinase ATM (Kumar *et al.*, 2014). Enfin, des déformations extrêmes du noyau peuvent conduire à des ruptures de l'enveloppe, qui causent des dommages à l'ADN en raison de la fuite de facteurs de réparation (Irianto *et al.*, 2017; Xia *et al.*, 2018) ou de contact avec des nucléases cytosoliques (Nader *et al.*, 2021). Ces dommages à l'ADN peuvent induire l'entrée en sénescence ou une transition épithélio-mésenchymateuse partielle en fonction des types cellulaires (Nader *et al.*, 2021), influençant donc le devenir cellulaire et tissulaire.

La contribution relative des différents composants aux propriétés mécaniques globales du noyau, qui déterminent sa déformabilité, a été étudiée. Des expériences d'étirement de cellules ont montré que les lamines de type B ne contribuent presque pas à la rigidité du noyau (Figure 62A), tandis que les lamines A et C en sont les principaux déterminants (Figure 62B).

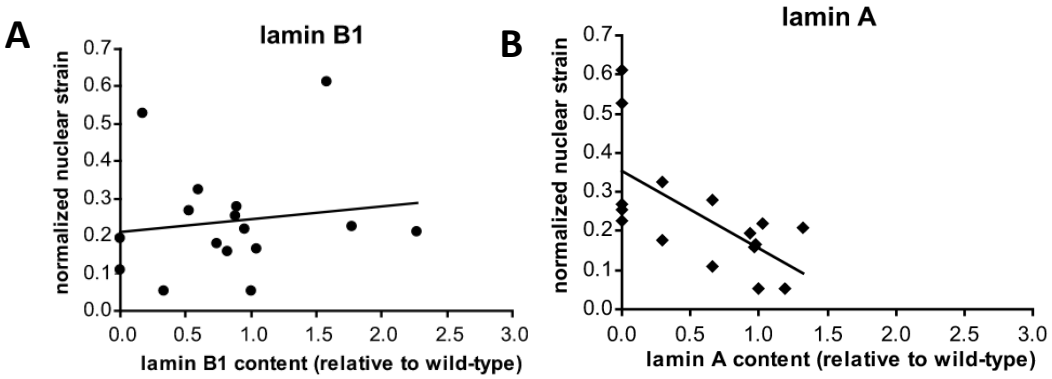

Figure 62 : Contribution des différentes lamines à la rigidité du noyau

(Lammerding et al.*, 2006)*

A. Déformation normalisée du noyau en fonction du niveau de lamine B1 B. Déformation normalisée du noyau en fonction du niveau de lamine A

La chromatine, bien que globalement plus molle que la lamina, participe également à la rigidité du noyau. Ceci a été montré dans des expériences d'aspiration par micropipette en modulant le niveau de compaction, soit en l'augmentant, conduisant à une rigidification du noyau (Figure 63A), soit en la digérant partiellement, induisant alors un ramollissement du noyau (Figure 63B).

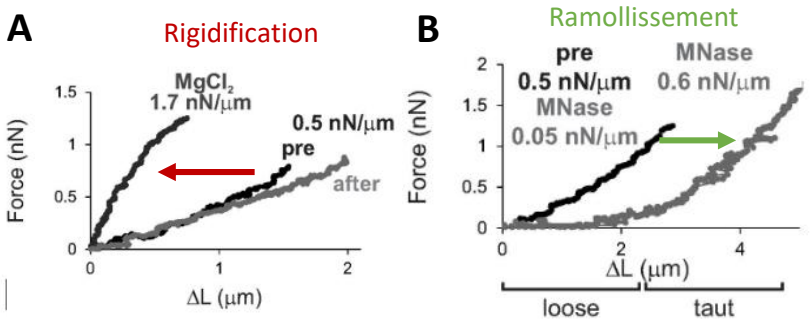

Figure 63 : Contribution de la chromatine à la mécanique du noyau
(Stephens et al.*, 2017)*
A. Augmentation de la condensation de la chromatine par traitement au $MgCl_2$ B. Réduction de la rigidité de la chromatine par digestion par micronucléase

Il est proposé que la chromatine contribue davantage à la réponse aux déformations locales, tandis que la lamina serait responsable de la réponse aux déformations de grandes amplitudes.

Ces deux composants, ainsi que l'enveloppe nucléaire elle-même, comme le suggère le recrutement d'enzymes au niveau de la membrane interne, pourraient être modifiés en réponse aux déformations, et servir ainsi de senseurs, en augmentant par exemple leur tension interne. Les déformations peuvent également impacter le volume des objets. Ceci a été montré pour la cellule, qui perd du volume pour différents niveaux de déformation (Venkova *et al.*, 2022), et observé pour le noyau (Rowat *et al.*, 2006). Une modification du volume entraîne un changement des équilibres chimiques, et pourrait également servir de signal.

L'objectif de ce travail de thèse est d'intégrer de manière quantitative les différents paramètres mécaniques en réponse aux déformations, afin de proposer un modèle global de réponse du noyau aux contraintes mécaniques.

MATERIEL ET METHODES

L'essentiel de ce travail a été réalisé dans des lignées cellulaires HeLa et MDA-MB-231 surexprimant un marqueur de l'enveloppe nucléaire, la protéine de la membrane interne LAP2b, fusionnée à la GFP (Figure 62).

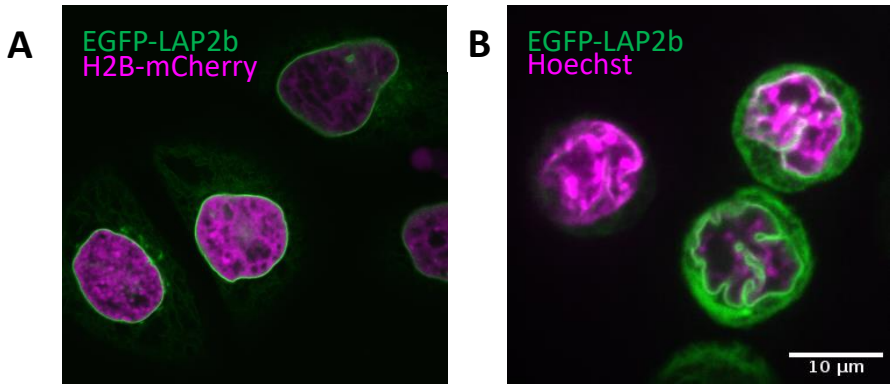

Figure 64 : Enveloppe nucléaire marquée par EGFP-LAP2b
A. HeLa étalées sur lamelle de verre B. HeLa adhérées sur poly-L-lysine

Les déformations ont été appliquées en utilisant des systèmes de confinement 2D reposant sur la fabrication de micropiliers en PDMS de hauteur contrôlée, allant de 2 à 20 µm (Figure 65).

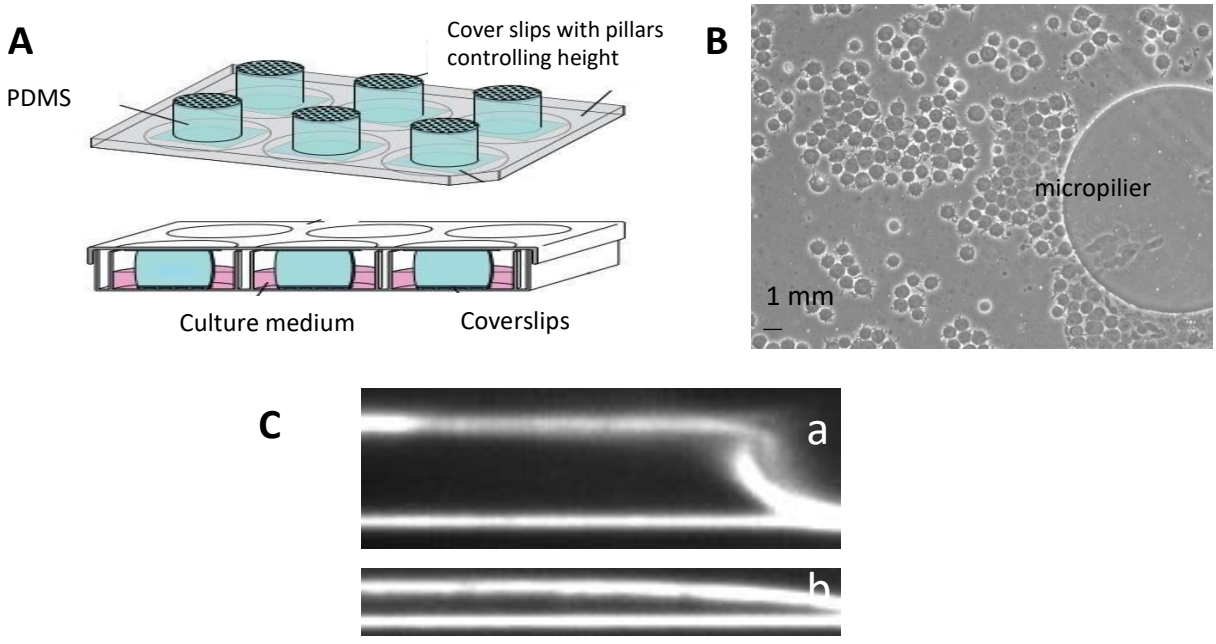

Figure 65 : Système de confinement 6 puits par micropiliers de PDMS
A. Système de confinement 6 puits en PDMS B. Vue en lumière transmise de cellules HeLa confinées à 3 µm C. Vue orthogonale de la chambre confinée (a. 10 µm, b. 3 µm)

RESULTATS

I. Caractéristiques des plis du noyau

Le point de départ de ce travail est l'observation de la grande diversité de formes des noyaux *in vivo*, en particulier dans l'exemple des embryons de souris. En fonction de l'environnement de la cellule, son noyau peut être lisse et régulier (Figure 66, cadre orange) dans les cellules de la couche superficielle de l'embryon, tandis que les cellules de la masse interne ont des noyaux plissés, aux formes plus irrégulières (Figure 66, cadre vert).

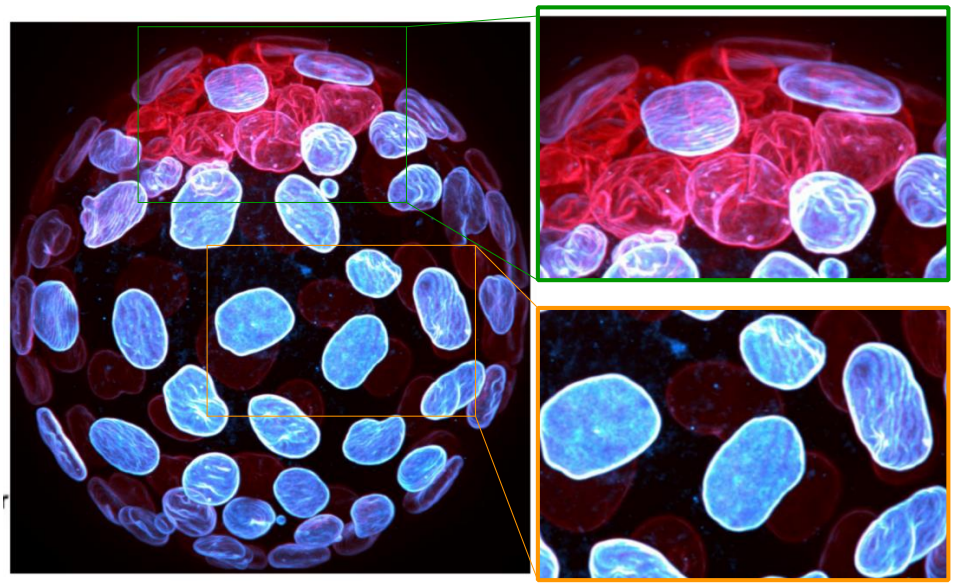

Figure 66 : Noyaux des cellules d'un embryon de souris
Bleu : lamine B1, rouge : lamine A/C

Ces différents niveaux de plis peuvent être reproduits *in vitro* en modulant les conditions d'étalement de la cellule : plus celle-ci s'étale, plus les plis s'ouvrent. Inversement, plus la cellule est ronde, plus le noyau est plissé. Les plis peuvent être ouverts par l'application d'un confinement vertical à des hauteurs de plus en plus faibles (Figure 67).

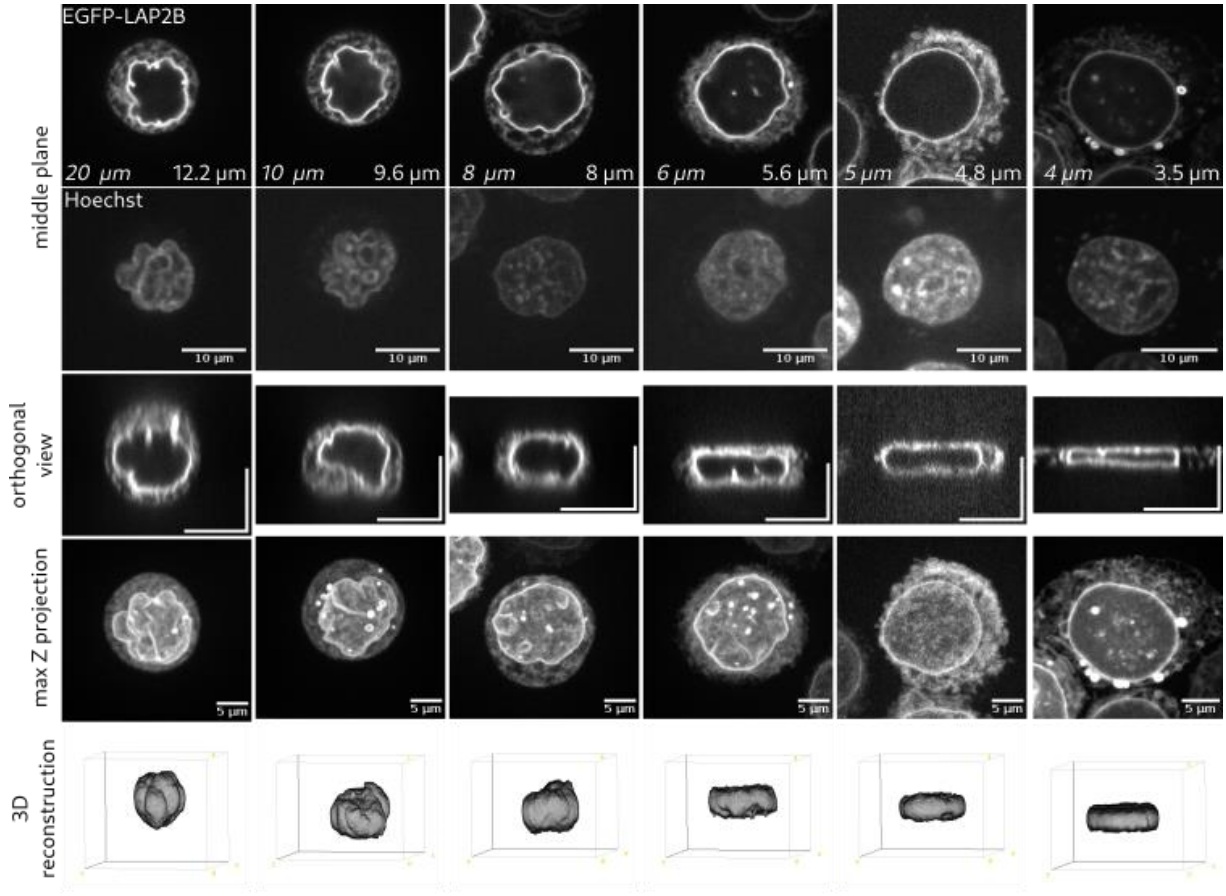

Figure 67 : Ouverture des plis du noyau par confinement
Italique : hauteur de confinement, droit : hauteur du noyau

Nous proposons différentes manières de mesurer le niveau de plis de l'enveloppe nucléaire. La première, le ratio EFC (Elliptic Fourier Coefficients), repose sur l'approximation du contour par des ellipses de Fourier successives. Le ratio EFC est défini comme $\frac{grand\ axe_1 + petit\ axe_1}{\sum_{i=2}^{25} grand\ axe_i + petit\ axe_i}$. Plus l'objet est lisse, plus le ratio EFC est grand. Conformément aux observations, le ratio EFC, initialement faible lorsque les cellules sont peu confinées, augmente avec le confinement et atteint un plateau en-dessous de 4 µm (Figure 68A et B, courbe verte). Nous avons également mesuré la courbure de Menger en chaque point du contour de chaque cellule et défini un score de courbure, qui mesure la proportion du contour avec de fortes valeurs de courbure locale (|courbure| > 0.1). Ce score, initialement autour de 18%, diminue avec le confinement et atteint un plateau en-dessous de 4 µm (Figure 68B, courbe bleue). De la même manière, nous avons mesuré en chaque point du contour de l'enveloppe la distance à l'enveloppe convexe et défini un score de profondeur, qui mesure la proportion du contour avec une profondeur supérieure à 2 pixels. Ce score a une valeur d'environ 30% lorsque les noyaux ne sont pas confinés, et diminue avec le confinement

(Figure 68B, courbe violette). Par trois mesures différentes, nous montrons donc que les plis du noyau sont ouverts par le confinement.

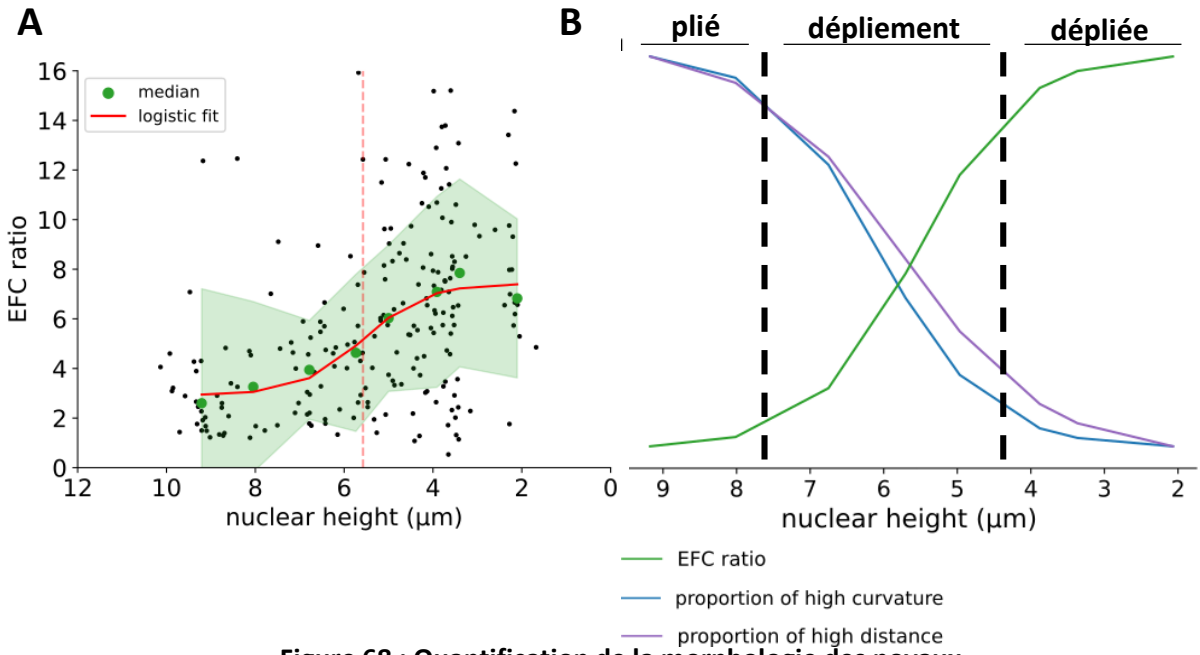

Figure 68 : Quantification de la morphologie des noyaux

A. Evolution du ratio EFC en fonction de la hauteur du noyau B. Evolution des trois paramètres morphométries en fonction de la hauteur

L'ouverture des plis par le confinement est réversible. En effet, en retirant le confinement après deux minutes d'application, nous observons que les plis se reforment, à des positions différentes des plis présents avant confinement (Figure 69). Ceci suggère une origine mécanique des plis, plutôt que l'existence de points d'ancrage spécifiques.

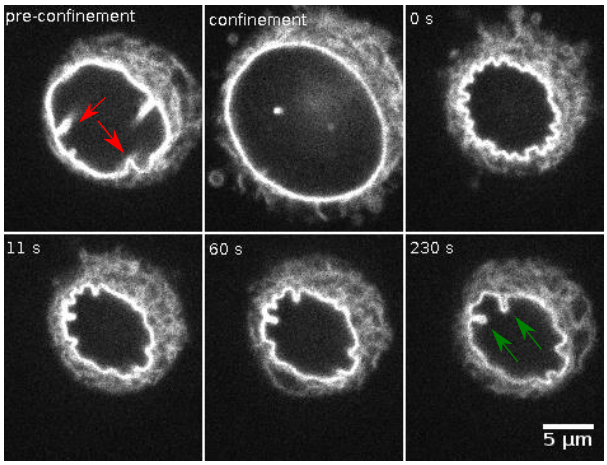

Figure 69 : Reformation des plis après déconfinement

(confinement 8 µm)

II. Proposition d'un modèle expliquant la formation de plis de l'enveloppe

Nous proposons un modèle, pour l'instant qualitatif, de représentation du noyau composé de deux matériaux purement élastiques, considérant un couche mince et rigide, la lamina, liée à une couche épaisse et plus molle, la chromatine. Le modèle suppose une longueur de repos de la lamina supérieure à celle de la chromatine, et on définit δ, la disparité de longueur de repos, tel que $\delta = \frac{L_L - L_C}{L_L}$.

Ce modèle définit un seuil de valeur de δ à partir duquel le flambage devient favorable, et où la disparité de longueur est accommodée par la déformation de l'ensemble plutôt que par la compression de la lamina (Figure 70). Le seuil de flambage δ_1^* se situe à 1% d'excès de surface, ce qui rend ce comportement extrêmement favorable.

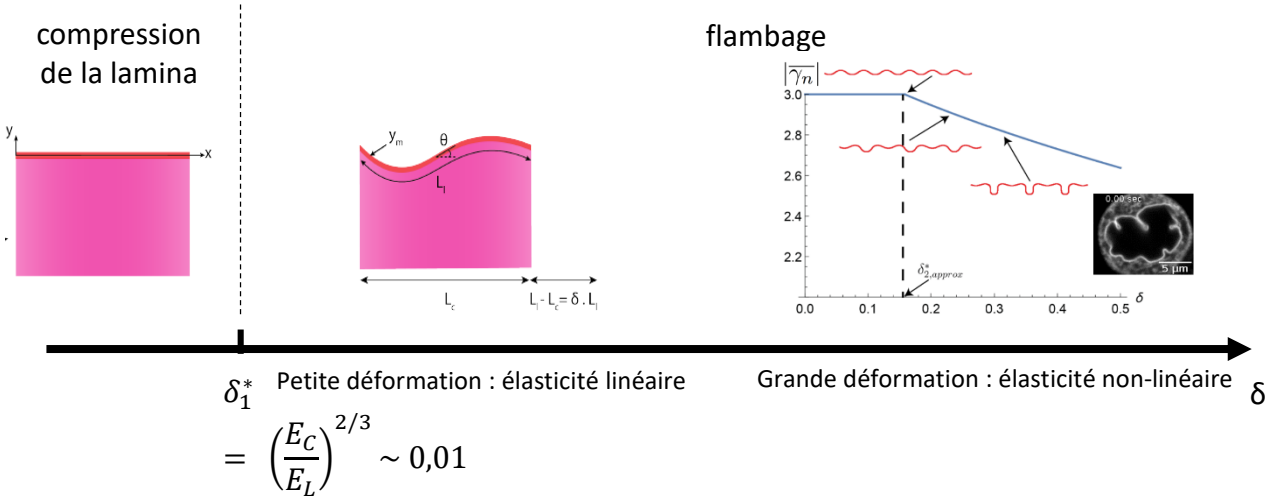

Figure 70 : Modèle du noyau prenant en compte la chromatine et la lamina
δ : disparité de longueur de repos entre chromatine et lamina, E_C et E_L : modules d'Young de la chromatine et de la lamina

On peut donc raisonnablement faire l'hypothèse que le régime rencontré par les cellules se situent loin du seuil de flambage, ce qui introduit une composante non-linéaire à la déformation. Les simulations de forme de l'enveloppe approchent alors la forme des plis observés dans les cellules non-confinées, avec une transition de plis régulièrement distribués pour une gamme de delta moyens vers une focalisation en certains points et un aplanissement autour pour des delta plus importants.

En prenant le temps après déconfinement comme proxy de variation de δ, on peut utiliser la dynamique de reformation des plis comme méthode pour approcher les différentes gammes de disparité de longueur de repos. Les formes de plis observées après déconfinement sont d'abord régulières, et certains plis s'approfondissent ensuite, tandis que d'autres portions de l'enveloppe s'aplanissent (Figure 69). Ce

comportement est perdu en absence de lamine A/C, associé à une lamina plus molle. Ces données soutiennent la proposition du modèle d'une contribution des propriétés mécaniques des composantes rigide et molle du noyau à la formation des plis.

III. La tension nucléaire répond aux déformations selon deux régimes

Le modèle que nous proposons prédit que tant que l'enveloppe possède des repliements, la tension dans la lamina demeure très faible. Nous montrons par une méthode qualitative de mesures de fluctuations de l'enveloppe qu'il existe effectivement un régime de déformation dans lequel les fluctuations de l'enveloppe sont relativement constantes, avant de diminuer en-dessous d'un seuil de hauteur situé à 6 µm (Figure 71A).

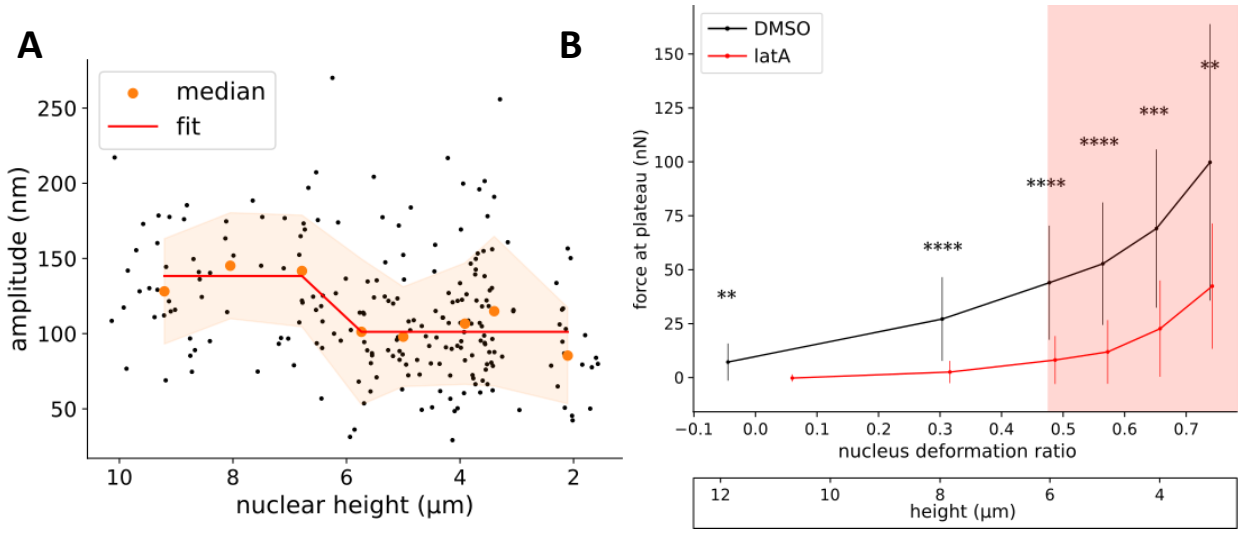

Figure 71 : Régime de déformation sans augmentation de la tension nucléaire

A. Amplitude des fluctuations de l'enveloppe nucléaire en fonction de la hauteur du noyau B. Force mesurée par AFM après relaxation à chaque palier de hauteur en présence (DMSO) ou absence d'actine (latrunculine A)

Ceci est confirmé par des mesures quantitatives de la réponse de force de la cellule par AFM. En présence du cytosquelette d'actine, la force développée par la cellule augmente dès que le noyau commence à être déformée. Néanmoins, le principal élément capable de développer des forces dans la cellule est le cytosquelette d'actomyosine. Lorsque celui-ci est dépolymérisé, seul le cytoplasme reste visible, et nous pouvons accéder à la réponse de force générée par le noyau. Celle-ci reste presque nulle pour une large gamme de hauteur et ne commence à augmenter qu'en-dessous de 6 µm (Figure 71B). Cette force

résiduelle est presque entièrement abolie en absence de lamine A/C, indiquant que la tension nucléaire semble principalement portée par cette composante de la lamina.

Ces résultats confirment l'existence d'une gamme de déformation du noyau pour lequel aucune augmentation de tension n'est détectée, conformément aux prédictions du modèle.

IV. Le volume nucléaire répond aux déformations selon deux régimes

Le modèle pompe-et-efflux enchâssé proposant un modèle physique des volumes du cytoplasme et du noyau prédit qu'un changement de tension dans l'interface noyau-cytosol affecte le volume nucléaire (Rollin *et al.*, 2023). Du fait de l'équilibre du potentiel chimique de l'eau, on peut écrire l'égalité suivante, avec ΔP la différence de pression hydrostatique et $\Delta\Pi$ la différence de pression osmotique entre les deux compartiments, $\Delta P = \Delta\Pi$. Tant que la tension dans l'interface est faible, ΔP, qui est proportionnel à la tension, est proche de 0. On peut donc obtenir une expression simple du volume nucléaire en fonction des quantités en osmolytes nucléaires et cytoplasmiques, ainsi que du volume du cytoplasme. Lorsque la tension augmente et n'est plus négligeable, $\Delta P > 0$, et de même, $\Delta\Pi > 0$. Cette pression intranucléaire prédite par le modèle, supérieure à celle du cytoplasme, devrait donc se traduire par une diminution du volume nucléaire.

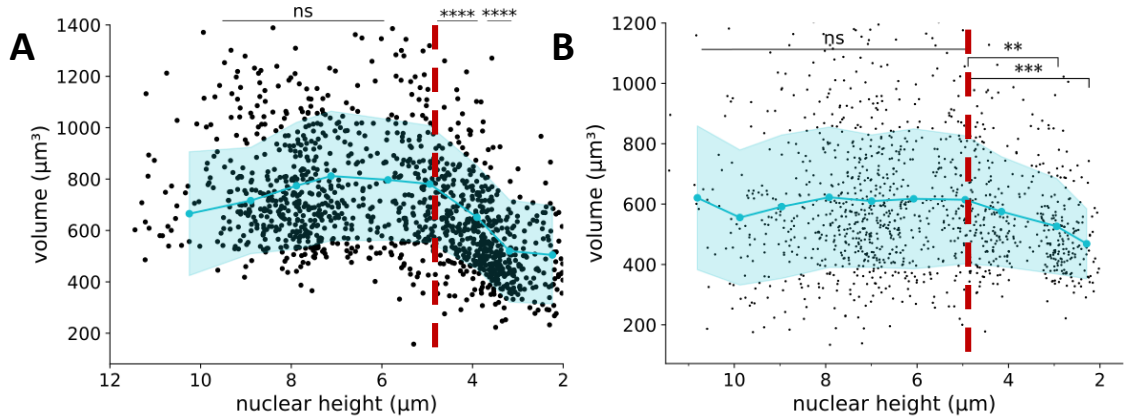

Figure 72 : Volume nucléaire en fonction de la hauteur

A. Volume nucléaire dans les cellules HeLa B. Volume nucléaire dans les cellules MDA-MB-231

Nous montrons dans deux lignées cellulaires différentes que le volume nucléaire demeure constant pour une large gamme de déformation, avant de diminuer de près de 40% dans les HeLa (Figure 72A) et de 20% dans les MDA-MB-231 (Figure 72B). L'intégration de ces mesures avec les mesures de force et de morphologie dans les cellules HeLa permettent de confirmer que le seuil de diminution du volume, autour de 5 µm, se situe au-delà du seuil d'augmentation de la lamina.

DISCUSSION

Dans ce travail, nous avons montré que les noyaux, loin d'être uniquement des objets sphériques lisses, peuvent prendre une grande variété de formes. In vivo, alors que l'enveloppe nucléaire est lisse et ovale dans les cellules de la couche plane à la surface de l'embryon, les noyaux de la masse interne peuvent présenter des plis profonds vers l'intérieur. Ceux-ci peuvent être ouverts par l'application de contraintes mécaniques, soit internes à la cellule via son étalement, soit de manière externe. Nous avons développé plusieurs quantifications de la morphologie des noyaux et de leur niveau de repliement. Les propriétés particulières des plis (réversibilité de leur ouverture, reformation en différentes positions) nous ont conduits à proposer un modèle expliquant leur origine du fait des propriétés mécaniques et géométriques de la lamina et de la chromatine. Nous proposons de considérer le noyau comme composé de deux couches élastiques : l'une, mince et rigide, la lamina, et la seconde, épaisse et molle, la chromatine, avec une longueur au repos de la lamina plus importante que celle de la chromatine. Le flambage de la lamina est favorisé dans ce modèle dès que le pourcentage d'excès de surface dépasse 1%. Ainsi, les plis émergent de non-linéarités dans la réponse élastique.

Ce modèle prédit que tant que l'enveloppe est plissée, la tension dans la lamina demeure très faible. Nous avons confirmé cette prédiction de manière d'abord qualitative, en mesurant les fluctuations de l'enveloppe nucléaire, et en montrant que les fluctuations demeurent stables jusqu'à une hauteur de 6 µm, en-dessous de laquelle elles diminuent brutalement. Nous avons ensuite utilisé la microscopie à force atomique avec un cantilever plat à large surface, permettant de déformer une cellule entière, afin de caractériser la réponse de force, et la tension, pour des confinements croissants. Nous avons montré que sur une gamme de déformation jusqu'à 6 µm, le noyau se déformait sans exercer de réponse de force, donc sans se tendre. En-dessous de cette hauteur, qui correspond dans les cellules HeLa à une déformation d'environ 55%, le noyau se tend. Cette tension est principalement supportée par la lamine A/C.

Une conséquence de cette tension est de modifier l'équilibre des forces à l'interface noyau/cytoplasme. D'après un modèle de pompe-et-efflux enchâssé des volumes nucléaire et cytoplasmique, tant que la tension dans l'interface noyau/cytoplasme reste faible, le volume du noyau est principalement déterminé par l'équilibre de pression osmotique. En revanche, lorsque la tension augmente, la différence de pression hydrostatique entre le noyau et le cytoplasme augmente. Ce modèle prédit donc qu'en cas de tension dans l'interface, le volume nucléaire devrait décroître. Nous avons mesuré le volume nucléaire à l'échelle

de la population et confirmé que, dans deux lignées cellulaires, le volume demeure constant pour une gamme de déformation allant jusqu'à 5 µm. En-dessous de ce seuil, le volume décroît de 20 à 40% selon la lignée. Ce résultat est également conservé à l'échelle de la cellule unique et en absence d'actine, indiquant que ce comportement ne dépend pas des forces exercées par le cytosquelette d'actomyosine sur le noyau.

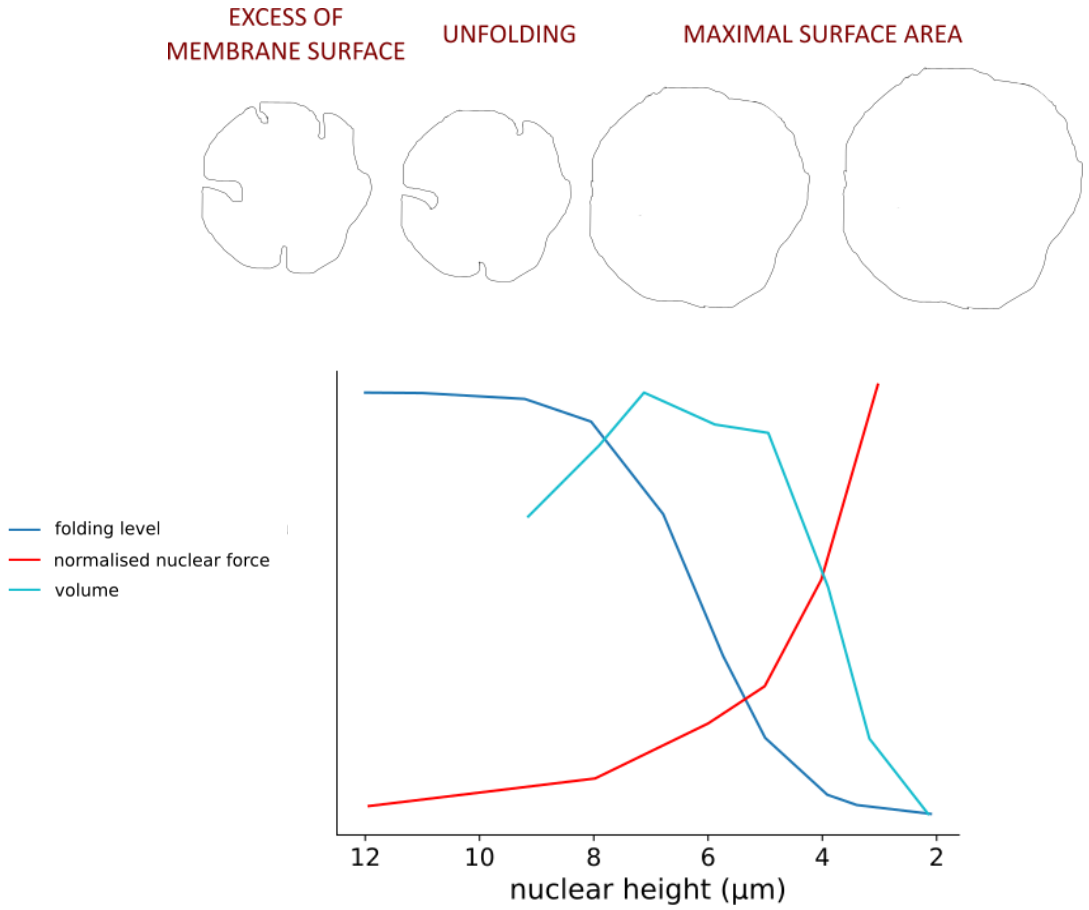

Figure 73 : Modèle de réponse du noyau aux déformations mécaniques

Nous proposons donc une intégration quantitative des paramètres de morphologie, tension et volume en du noyau en réponse aux déformations mécaniques (Figure 73). Nous proposons qu'il existe un excès de surface d'enveloppe nucléaire conduisant à la formation de plis, qui peuvent être ouverts par des contraintes mécaniques de l'environnement. Le régime de dépliement constitue un régime de déformation sans danger pour la cellule, où la tension du noyau demeure faible et le volume nucléaire constant, maintenant ainsi les concentrations des composants nucléaires à leur niveau homéostatique. Lorsque l'enveloppe est entièrement dépliée, le noyau se tend et son volume commence à diminuer du fait du changement de l'équilibre des forces au niveau de l'enveloppe.

Certaines questions restent ouvertes à l'issue de ce travail. D'un point de vue mécanistique, le rôle du cytosquelette, en particulier les microtubules, reste à explorer, notamment du fait de leur importance connue dans les changements de morphologie lors de la différenciation des cellules hématopoïétiques. Du point de vue des échelles considérées, le travail présenté dans cette thèse se concentre sur une échelle de temps intermédiaire, de l'ordre de la dizaine de minutes. Les réponses mécaniques à des échelles plus courtes (secondes) ou plus longues (heures) n'ont ainsi pas été explorées. Enfin, nous avons proposé des conséquences possibles de l'augmentation de la tension et de la diminution du volume mais ces directions n'ont pas été développées dans le présent travail. Nous proposons que la tension du noyau soit à l'origine des modifications du transport nucléo-cytoplasmique lorsque la cellule subit des contraintes. Nous supposons que la diminution du volume nucléaire s'accompagne d'augmentation de concentration des composants nucléaires, ce qui peut perturber les équilibres de séparation de phase liquide-liquide ou les réactions biochimiques. Enfin, nous proposons que l'augmentation de pression intranucléaire dans le régime de perte de volume soit à l'origine de la fragilité du noyau et des ruptures de l'enveloppe.

BIBLIOGRAPHY

Abaitua, F, Hollinshead, M, Bolstad, M, Crump, CM, and O'Hare, P (2012). A Nuclear Localization Signal in Herpesvirus Protein VP1-2 Is Essential for Infection via Capsid Routing to the Nuclear Pore. J Virol 86, 8998–9014.

Ahn, J-H, Cho, M-G, Sohn, S, and Lee, J-H (2019). Inhibition of PP2A activity by H2O2 during mitosis disrupts nuclear envelope reassembly and alters nuclear shape. Exp Mol Med 51, 1–18.

Akhtar, W, de Jong, J, Pindyurin, AV, Pagie, L, Meuleman, W, de Ridder, J, Berns, A, Wessels, LFA, van Lohuizen, M, and van Steensel, B (2013). Chromatin Position Effects Assayed by Thousands of Reporters Integrated in Parallel. Cell 154, 914–927.

Al Jord, A et al. (2022). Cytoplasmic forces functionally reorganize nuclear condensates in oocytes. Nat Commun 13, 5070.

Alberts, B, Johnson, A, Lewis, J, Morgan, D, Raff, M, Roberts, K, and Walter, P (2015). Molecular Biology of the Cell, Garland Science.

Almonacid, M et al. (2019). Active Fluctuations of the Nuclear Envelope Shape the Transcriptional Dynamics in Oocytes. Developmental Cell 51, 145-157.e10.

Alraies, Z et al. (2022). A Shape Sensing Mechanism driven by Arp2/3 and cPLA $_2$ licenses Dendritic Cells for Migration to Lymph Nodes in Homeostasis, Cell Biology.

Amendola, M, and Van Steensel, B (2015). Nuclear lamins are not required for lamina-associated domain organization in mouse embryonic stem cells. EMBO Reports 16, 610–617.

Andreu, I et al. (2022). Mechanical force application to the nucleus regulates nucleocytoplasmic transport. Nat Cell Biol 24, 896–905.

Aragona, M, Panciera, T, Manfrin, A, Giulitti, S, Michielin, F, Elvassore, N, Dupont, S, and Piccolo, S (2013). A Mechanical Checkpoint Controls Multicellular Growth through YAP/TAZ Regulation by Actin-Processing Factors. Cell 154, 1047–1059.

Arya, SB, Chen, S, Jordan-Javed, F, and Parent, CA (2022). Ceramide-rich microdomains facilitate nuclear envelope budding for non-conventional exosome formation. Nat Cell Biol 24, 1019–1028.

Assies, L et al. (2021). Flipper Probes for the Community. Chimia 75, 1004.

Aureille, J et al. (2019). Nuclear envelope deformation controls cell cycle progression in response to mechanical force. EMBO Reports, 11.

Azioune, A, Carpi, N, Tseng, Q, Théry, M, and Piel, M (2010). Protein Micropatterns. In: Methods in Cell Biology, Elsevier, 133–146.

Baarlink, C, Wang, H, and Grosse, R (2013). Nuclear Actin Network Assembly by Formins Regulates the SRF Coactivator MAL. Science 340, 864–867.

Bahmanyar, S, and Schlieker, C (2020). Lipid and protein dynamics that shape nuclear envelope identity. MBoC 31, 1315–1323.

Bakhoum, SF, Thompson, SL, Manning, AL, and Compton, DA (2009). Genome stability is ensured by temporal control of kinetochore–microtubule dynamics. Nat Cell Biol 11, 27–35.

Barbier, L, Sáez, PJ, Attia, R, Lennon-Duménil, A-M, Lavi, I, Piel, M, and Vargas, P (2019). Myosin II Activity Is Selectively Needed for Migration in Highly Confined Microenvironments in Mature Dendritic Cells. Front Immunol 10.

Barton, LJ, Soshnev, AA, and Geyer, PK (2015). Networking in the nucleus: a spotlight on LEM-domain proteins. Current Opinion in Cell Biology 34, 1–8.

Barzilai, S et al. (2017). Leukocytes Breach Endothelial Barriers by Insertion of Nuclear Lobes and Disassembly of Endothelial Actin Filaments. Cell Reports 18, 685–699.

Baum, B, and Baum, DA (2020). The merger that made us. BMC Biol 18, 72.

Beaudouin, J, Gerlich, D, Daigle, N, Eils, R, and Ellenberg, J (2002). Nuclear Envelope Breakdown Proceeds by Microtubule-Induced Tearing of the Lamina. Cell 108, 83–96.

Beck, M, and Hurt, E (2017). The nuclear pore complex: understanding its function through structural insight. Nat Rev Mol Cell Biol 18, 73–89.

Bell, ES et al. (2022). Low lamin A levels enhance confined cell migration and metastatic capacity in breast cancer. Oncogene 41, 4211–4230.

Benham-Pyle, BW, Pruitt, BL, and Nelson, WJ (2015). Mechanical strain induces E-cadherin–dependent Yap1 and β-catenin activation to drive cell cycle entry. Science 348, 1024–1027.

Bhargava, A, Lahaye, X, and Manel, N (2018). Let me in: Control of HIV nuclear entry at the nuclear envelope. Cytokine & Growth Factor Reviews 40, 59–67.

Bhargava, A, Williart, A, Maurin, M, Davidson, PM, Jouve, M, Piel, M, Lahaye, X, and Manel, N (2021). Inhibition of HIV infection by structural proteins of the inner nuclear membrane is associated with reduced chromatin dynamics. Cell Reports 36, 109763.

Biedzinski, S, Agsu, G, Vianay, B, Delord, M, Blanchoin, L, Larghero, J, Faivre, L, Théry, M, and Brunet, S (2020). Microtubules control nuclear shape and gene expression during early stages of hematopoietic differentiation. The EMBO Journal 39, e103957.

Bigay, J, and Antonny, B (2012). Curvature, Lipid Packing, and Electrostatics of Membrane Organelles: Defining Cellular Territories in Determining Specificity. Developmental Cell 23, 886–895.

Bley, CJ et al. (2022). Architecture of the cytoplasmic face of the nuclear pore. Science 376, eabm9129.

Booth, EA, Spagnol, ST, Alcoser, TA, and Dahl, KN (2015). Nuclear stiffening and chromatin softening with progerin expression leads to an attenuated nuclear response to force. Soft Matter 11, 6412–6418.

Boumendil, C, Hari, P, Olsen, KCF, Acosta, JC, and Bickmore, WA (2019). Nuclear pore density controls heterochromatin reorganization during senescence. Genes Dev 33, 144–149.

Brau, F, Vandeparre, H, Sabbah, A, Poulard, C, Boudaoud, A, and Damman, P (2011). Multiple-length-scale elastic instability mimics parametric resonance of nonlinear oscillators. Nature Phys 7, 56–60.

Briand, N, and Collas, P (2020). Lamina-associated domains: peripheral matters and internal affairs. Genome Biol 21, 85.

Brueckner, L, Zhao, PA, Van Schaik, T, Leemans, C, Sima, J, Peric-Hupkes, D, Gilbert, DM, and Van Steensel, B (2020). Local rewiring of genome–nuclear lamina interactions by transcription. The EMBO Journal 39, e103159.

Burke, B, and Stewart, CL (2002). Life at the edge: the nuclear envelope and human disease. Nat Rev Mol Cell Biol 3, 575–585.

Cadart, C, Monnier, S, Grilli, J, Sáez, PJ, Srivastava, N, Attia, R, Terriac, E, Baum, B, Cosentino-Lagomarsino, M, and Piel, M (2018). Size control in mammalian cells involves modulation of both growth rate and cell cycle duration. Nat Commun 9, 3275.

Calero-Cuenca, FJ, Janota, CS, and Gomes, ER (2018). Dealing with the nucleus during cell migration. Current Opinion in Cell Biology 50, 35–41.

Caridi, CP et al. (2018). Nuclear F-actin and myosins drive relocalization of heterochromatic breaks. Nature 559, 54–60.

Cassany, A, Ragues, J, Guan, T, Bégu, D, Wodrich, H, Kann, M, Nemerow, GR, and Gerace, L (2015). Nuclear Import of Adenovirus DNA Involves Direct Interaction of Hexon with an N-Terminal Domain of the Nucleoporin Nup214. J Virol 89, 1719–1730.

Cattin, CJ, Düggelin, M, Martinez-Martin, D, Gerber, C, Müller, DJ, and Stewart, MP (2015). Mechanical control of mitotic progression in single animal cells. Proc Natl Acad Sci USA 112, 11258–11263.

Cautain, B, Hill, R, De Pedro, N, and Link, W (2015). Components and regulation of nuclear transport processes. FEBS J 282, 445–462.

Champion, L, Pawar, S, Luithle, N, Ungricht, R, and Kutay, U (2019). Dissociation of membrane–chromatin contacts is required for proper chromosome segregation in mitosis. MBoC 30, 427–440.

Chang, L et al. (2022). Nuclear peripheral chromatin-lamin B1 interaction is required for global integrity of chromatin architecture and dynamics in human cells. Protein Cell 13, 258–280.

Chang, Y-C, Nalbant, P, Birkenfeld, J, Chang, Z-F, and Bokoch, GM (2008). GEF-H1 Couples Nocodazole-induced Microtubule Disassembly to Cell Contractility via RhoA. MBoC 19, 2147–2153.

Chen, N-Y et al. (2016). HIV-1 capsid is involved in post-nuclear entry steps. Retrovirology 13.

Chen, NY, Kim, P, Weston, TA, Edillo, L, Tu, Y, Fong, LG, and Young, SG (2018). Fibroblasts lacking nuclear lamins do not have nuclear blebs or protrusions but nevertheless have frequent nuclear membrane ruptures. Proc Natl Acad Sci USA 115, 10100–10105.

Chin, CR, Perreira, JM, Savidis, G, Portmann, JM, Aker, AM, Feeley, EM, Smith, MC, and Brass, AL (2015). Direct Visualization of HIV-1 Replication Intermediates Shows that Capsid and CPSF6 Modulate HIV-1 Intra-nuclear Invasion and Integration. Cell Reports 13, 1717–1731.

Chung, DKC, Chan, JNY, Strecker, J, Zhang, W, Ebrahimi-Ardebili, S, Lu, T, Abraham, KJ, Durocher, D, and Mekhail, K (2015). Perinuclear tethers license telomeric DSBs for a broad kinesin- and NPC-dependent DNA repair process. Nat Commun 6, 7742.

Colom, A, Derivery, E, Soleimanpour, S, Tomba, C, Molin, MD, Sakai, N, González-Gaitán, M, Matile, S, and Roux, A (2018). A fluorescent membrane tension probe. Nature Chem 10, 1118–1125.

Constantinescu, D, Gray, HL, Sammak, PJ, Schatten, GP, and Csoka, AB (2006). Lamin A/C Expression Is a Marker of Mouse and Human Embryonic Stem Cell Differentiation. Stem Cells 24, 177–185.

Cordenonsi, M et al. (2011). The Hippo Transducer TAZ Confers Cancer Stem Cell-Related Traits on Breast Cancer Cells. Cell 147, 759–772.

Cramer, LP (2010). Forming the cell rear first: breaking cell symmetry to trigger directed cell migration. Nat Cell Biol 12, 628–632.

Crisp, M, Liu, Q, Roux, K, Rattner, JB, Shanahan, C, Burke, B, Stahl, PD, and Hodzic, D (2006). Coupling of the nucleus and cytoplasm: role of the LINC complex. The Journal of Cell Biology 172, 41–53.

Cutter, AR, and Hayes, JJ (2015). A brief review of nucleosome structure. FEBS Letters 589, 2914–2922.

Dahl, KN (2004). The nuclear envelope lamina network has elasticity and a compressibility limit suggestive of a molecular shock absorber. Journal of Cell Science 117, 4779–4786.

Danielsson, BE, George Abraham, B, Mäntylä, E, Cabe, JI, Mayer, CR, Rekonen, A, Ek, F, Conway, DE, and Ihalainen, TO (2023). Nuclear lamina strain states revealed by intermolecular force biosensor. Nat Commun 14, 3867.

Davidson, PM, Denais, C, Bakshi, MC, and Lammerding, J (2014). Nuclear Deformability Constitutes a Rate-Limiting Step During Cell Migration in 3-D Environments. Cel Mol Bioeng 7, 293–306.

Dazzoni, R, Grélard, A, Morvan, E, Bouter, A, Applebee, CJ, Loquet, A, Larijani, B, and Dufourc, EJ (2020). The unprecedented membrane deformation of the human nuclear envelope, in a magnetic field, indicates formation of nuclear membrane invaginations. Sci Rep 10, 5147.

De Vos, WH et al. (2011). Repetitive disruptions of the nuclear envelope invoke temporary loss of cellular compartmentalization in laminopathies. Human Molecular Genetics 20, 4175–4186.

De Vries, AHB, Krenn, BE, Van Driel, R, Subramaniam, V, and Kanger, JS (2007). Direct Observation of Nanomechanical Properties of Chromatin in Living Cells. Nano Lett 7, 1424–1427.

Deacon, EM, Pettitt, TR, Webb, P, Cross, T, Chahal, H, Wakelam, MJO, and Lord, JM (2002). Generation of diacylglycerol molecular species through the cell cycle: a role for 1-stearoyl, 2-arachidonyl glycerol in the activation of nuclear protein kinase C-βII at G2/M. Journal of Cell Science 115, 983–989.

Dehingia, B, Milewska, M, Janowski, M, and Pękowska, A (2022). CTCF shapes chromatin structure and gene expression in health and disease. EMBO Reports 23, e55146.

Déjardin, T, Carollo, PS, Sipieter, F, Davidson, PM, Seiler, C, Cuvelier, D, Cadot, B, Sykes, C, Gomes, ER, and Borghi, N (2020). Nesprins are mechanotransducers that discriminate epithelial–mesenchymal transition programs. Journal of Cell Biology 219, e201908036.

Denais, CM, Gilbert, RM, Isermann, P, McGregor, AL, te Lindert, M, Weigelin, B, Davidson, PM, Friedl, P, Wolf, K, and Lammerding, J (2016). Nuclear envelope rupture and repair during cancer cell migration. Science 352, 353–358.

Dey, G, and Baum, B (2021). Nuclear envelope remodelling during mitosis. Current Opinion in Cell Biology 70, 67–74.

Dharan, A, Bachmann, N, Talley, S, Zwikelmaier, V, and Campbell, EM (2020). Nuclear pore blockade reveals that HIV-1 completes reverse transcription and uncoating in the nucleus. Nat Microbiol.

Di Nunzio, F et al. (2013). Nup153 and Nup98 bind the HIV-1 core and contribute to the early steps of HIV-1 replication. Virology 440, 8–18.

Donahue, DA, Amraoui, S, di Nunzio, F, Kieffer, C, Porrot, F, Opp, S, Diaz-Griffero, F, Casartelli, N, and Schwartz, O (2016). SUN2 Overexpression Deforms Nuclear Shape and Inhibits HIV. Journal of Virology 90, 4199–4214.

Donahue, DA, Porrot, F, Couespel, N, and Schwartz, O (2017). SUN2 Silencing Impairs CD4 T Cell Proliferation and Alters Sensitivity to HIV-1 Infection Independently of Cyclophilin A. Journal of Virology 91.

Dopie, J, Skarp, K-P, Kaisa Rajakylä, E, Tanhuanpää, K, and Vartiainen, MK (2012). Active maintenance of nuclear actin by importin 9 supports transcription. Proc Natl Acad Sci USA 109.

Drin, G, Casella, J-F, Gautier, R, Boehmer, T, Schwartz, TU, and Antonny, B (2007). A general amphipathic α-helical motif for sensing membrane curvature. Nat Struct Mol Biol 14, 138–146.

Drozdz, MM, Jiang, H, Pytowski, L, Grovenor, C, and Vaux, DJ (2017). Formation of a nucleoplasmic reticulum requires de novo assembly of nascent phospholipids and shows preferential incorporation of nascent lamins. Sci Rep 7, 7454.

Dultz, E, and Ellenberg, J (2010). Live imaging of single nuclear pores reveals unique assembly kinetics and mechanism in interphase. Journal of Cell Biology 191, 15–22.

Duong, NT, Morris, GE, Lam, LT, Zhang, Q, Sewry, CA, Shanahan, CM, and Holt, I (2014). Nesprins: Tissue-Specific Expression of Epsilon and Other Short Isoforms. PLoS ONE 9, e94380.

Dupont, S et al. (2011). Role of YAP/TAZ in mechanotransduction. Nature 474, 179–183.

Earle, AJ, Kirby, TJ, Fedorchak, GR, Isermann, P, Patel, J, Iruvanti, S, Moore, SA, Bonne, G, Wallrath, LL, and Lammerding, J (2020). Mutant lamins cause nuclear envelope rupture and DNA damage in skeletal muscle cells. Nat Mater 19, 464–473.

Ellenberg, J, Siggia, ED, Moreira, JE, Smith, CL, Presley, JF, Worman, HJ, and Lippincott-Schwartz, J (1997). Nuclear Membrane Dynamics and Reassembly in Living Cells: Targeting of an Inner Nuclear Membrane Protein in Interphase and Mitosis. Journal of Cell Biology 138, 1193–1206.

Elosegui-Artola, A et al. (2017). Force Triggers YAP Nuclear Entry by Regulating Transport across Nuclear Pores. Cell 171, 1397-1410.e14.

Enyedi, B, Jelcic, M, and Niethammer, P (2016). The Cell Nucleus Serves as a Mechanotransducer of Tissue Damage-Induced Inflammation. Cell 165, 12.

Evans, E, Heinrich, V, Ludwig, F, and Rawicz, W (2003). Dynamic Tension Spectroscopy and Strength of Biomembranes. Biophysical Journal 85, 2342–2350.

Fedorenko, OA, and Marchenko, SM (2014). Ion channels of the nuclear membrane of hippocampal neurons: NUCLEAR ION CHANNELS OF HIPPOCAMPAL NEURONS. Hippocampus 24, 869–876.

Ferrera, D, Canale, C, Marotta, R, Mazzaro, N, Gritti, M, Mazzanti, M, Capellari, S, Cortelli, P, and Gasparini, L (2014). Lamin B1 overexpression increases nuclear rigidity in autosomal dominant leukodystrophy fibroblasts. FASEB j 28, 3906–3918.

Finch, JT, and Klug, A (1976). Solenoidal model for superstructure in chromatin. Proc Natl Acad Sci USA 73, 1897–1901.

Fischer-Friedrich, E, Hyman, AA, Jülicher, F, Müller, DJ, and Helenius, J (2014). Quantification of surface tension and internal pressure generated by single mitotic cells. Sci Rep 4, 6213.

Franco-Obregón, A, Wang, H, and Clapham, DE (2000). Distinct Ion Channel Classes Are Expressed on the Outer Nuclear Envelope of T- and B-Lymphocyte Cell Lines. Biophysical Journal 79, 202–214.

Fritzsche, M, Lewalle, A, Duke, T, Kruse, K, and Charras, G (2013). Analysis of turnover dynamics of the submembranous actin cortex. MBoC 24, 757–767.

Funkhouser, CM, Sknepnek, R, Shimi, T, Goldman, AE, Goldman, RD, and Olvera De La Cruz, M (2013). Mechanical model of blebbing in nuclear lamin meshworks. Proc Natl Acad Sci USA 110, 3248–3253.

Furukawa, K, and Kondo, T (1998). Identification of the lamina-associated-polypeptide-2-binding domain of B-type lamin. Eur J Biochem 251, 729–733.

Ganem, NJ, Godinho, SA, and Pellman, D (2009). A mechanism linking extra centrosomes to chromosomal instability. Nature 460, 278–282.

Garner, MH (2002). Na,K-ATPase in the Nuclear Envelope Regulates Na+: K+ Gradients in Hepatocyte Nuclei. Journal of Membrane Biology 187, 97–115.

Gerace, L, and Blobel, G (1980). The nuclear envelope lamina is reversibly depolymerized during mitosis. Cell 19, 277–287.

Gibson, BA, Blaukopf, C, Lou, T, Chen, L, Doolittle, LK, Finkelstein, I, Narlikar, GJ, Gerlich, DW, and Rosen, MK (2023). In diverse conditions, intrinsic chromatin condensates have liquid-like material properties. Proc Natl Acad Sci USA 120, e2218085120.

Gibson, BA, Doolittle, LK, Schneider, MWG, Jensen, LE, Gamarra, N, Henry, L, Gerlich, DW, Redding, S, and Rosen, MK (2019). Organization of Chromatin by Intrinsic and Regulated Phase Separation. Cell 179, 470-484.e21.

Glavy, JS, Krutchinsky, AN, Cristea, IM, Berke, IC, Boehmer, T, Blobel, G, and Chait, BT (2007). Cell-cycle-dependent phosphorylation of the nuclear pore Nup107–160 subcomplex. Proc Natl Acad Sci USA 104, 3811–3816.

Gomes, ER, Jani, S, and Gundersen, GG (2005). Nuclear Movement Regulated by Cdc42, MRCK, Myosin, and Actin Flow Establishes MTOC Polarization in Migrating Cells. Cell 121, 451–463.

Gonzalez, Y, Saito, A, and Sazer, S (2012). Fission yeast Lem2 and Man1 perform fundamental functions of the animal cell nuclear lamina. Nucleus 3, 60–76.

Guilluy, C, Osborne, LD, Landeghem, LV, Sharek, L, Superfine, R, Garcia-Mata, R, and Burridge, K (2014). Isolated nuclei adapt to force and reveal a mechanotransduction pathway in the nucleus. 16, 16.

Gunn, AL, Yashchenko, AI, and Hatch, EM (2023). A high-content siRNA screen reveals new regulators of nuclear membrane stability, Cell Biology.

Haider, A et al. (2018). PCYT1A Regulates Phosphatidylcholine Homeostasis from the Inner Nuclear Membrane in Response to Membrane Stored Curvature Elastic Stress. Developmental Cell 45, 481-495.e8.

Halfmann, CT, Sears, RM, Katiyar, A, Busselman, BW, Aman, LK, Zhang, Q, O'Bryan, CS, Angelini, TE, Lele, TP, and Roux, KJ (2019). Repair of nuclear ruptures requires barrier-to-autointegration factor. The Journal of Cell Biology 218, 2136–2149.

Hampoelz, B, and Lecuit, T (2011). Nuclear mechanics in differentiation and development. Current Opinion in Cell Biology 23, 668–675.

Hansen, JC, Maeshima, K, and Hendzel, MJ (2021). The solid and liquid states of chromatin. Epigenetics & Chromatin 14, 50.

Hatch, EM, Fischer, AH, Deerinck, TJ, and Hetzer, MW (2013). Catastrophic Nuclear Envelope Collapse in Cancer Cell Micronuclei. Cell 154, 47–60.

Hatch, EM, and Hetzer, MW (2015). Linking Micronuclei to Chromosome Fragmentation. Cell 161, 1502–1504.

Hennig, T, and O'Hare, P (2015). Viruses and the nuclear envelope. Current Opinion in Cell Biology 34, 113–121.

Herman, AB et al. (2021). Reduction of lamin B receptor levels by miR-340-5p disrupts chromatin, promotes cell senescence and enhances senolysis. Nucleic Acids Research 49, 7389–7405.

Hieda, M (2017). Implications for Diverse Functions of the LINC Complexes Based on the Structure. Cells 6, 3.

Hirano, Y, Hizume, K, Kimura, H, Takeyasu, K, Haraguchi, T, and Hiraoka, Y (2012). Lamin B Receptor Recognizes Specific Modifications of Histone H4 in Heterochromatin Formation. Journal of Biological Chemistry 287, 42654–42663.

Höger, T, Zatloukal, K, Waizenegger, I, and Krohne, G (1990). Characterization of a second highly conserved B-type lamin present in cells previously thought to contain only a single B-type lamin. Chromosoma, 379–390.

Hwang, S, Williams, JF, Kneissig, M, Lioudyno, M, Rivera, I, Helguera, P, Busciglio, J, Storchova, Z, King, MC, and Torres, EM (2019). Suppressing Aneuploidy-Associated Phenotypes Improves the Fitness of Trisomy 21 Cells. Cell Reports 29, 2473-2488.e5.

Irianto, J et al. (2017). DNA Damage Follows Repair Factor Depletion and Portends Genome Variation in Cancer Cells after Pore Migration. Current Biology 27, 210–223.

Jacquemyn, J, Cascalho, A, and Goodchild, RE (2017). The ins and outs of endoplasmic reticulum-controlled lipid biosynthesis. EMBO Reports 18, 1905–1921.

Jacquemyn, J, Foroozandeh, J, Vints, K, Swerts, J, Verstreken, P, Gounko, NV, Gallego, SF, and Goodchild, R (2021). Torsin and NEP1R1-CTDNEP1 phosphatase affect interphase nuclear pore complex insertion by lipid-dependent and lipid-independent mechanisms. The EMBO Journal 40, e106914.

Jahed, Z, Vu, UT, Fadavi, D, Ke, H, Rathish, A, Kim, SCJ, Feng, W, and Mofrad, MRK (2018). A molecular model for LINC complex regulation: activation of SUN2 for KASH binding. Molecular Biology of the Cell 29, 2012–2023.

Janin, A, and Gache, V (2018). Nesprins and Lamins in Health and Diseases of Cardiac and Skeletal Muscles. Front Physiol 9, 1277.

Janssen, A, Marcelot, A, Breusegem, S, Legrand, P, Zinn-Justin, S, and Larrieu, D (2022). The BAF A12T mutation disrupts lamin A/C interaction, impairing robust repair of nuclear envelope ruptures in Nestor–Guillermo progeria syndrome cells. Nucleic Acids Research 50, 9260–9278.

Jeong, S, Ahn, J, Jo, I, Kang, S-M, Park, B-J, Cho, H-S, Kim, Y-H, and Ha, N-C (2022). Cyclin-dependent kinase 1 depolymerizes nuclear lamin filaments by disrupting the head-to-tail interaction of the lamin central rod domain. Journal of Biological Chemistry 298, 102256.

Jones, PA, and Liang, G (2009). Rethinking how DNA methylation patterns are maintained. Nat Rev Genet 10, 805–811.

Kanellos, G et al. (2015). ADF and Cofilin1 Control Actin Stress Fibers, Nuclear Integrity, and Cell Survival. Cell Reports 13, 1949–1964.

Katta, SS, Smoyer, CJ, and Jaspersen, SL (2014). Destination: inner nuclear membrane. Trends in Cell Biology 24, 221–229.

Keizer, VIP et al. (2022). Live-cell micromanipulation of a genomic locus reveals interphase chromatin mechanics.

Kidiyoor, GR et al. (2020). ATR is essential for preservation of cell mechanics and nuclear integrity during interstitial migration. Nat Commun 11, 4828.

Kim, M, Kim, M, Lee, S, Kuninaka, S, Saya, H, Lee, H, Lee, S, and Lim, D-S (2013). cAMP/PKA signalling reinforces the LATS–YAP pathway to fully suppress YAP in response to actin cytoskeletal changes. EMBO J 32, 1543–1555.

Kind, J, Pagie, L, Ortabozkoyun, H, Boyle, S, de Vries, SS, Janssen, H, Amendola, M, Nolen, LD, Bickmore, WA, and van Steensel, B (2013). Single-Cell Dynamics of Genome-Nuclear Lamina Interactions. Cell 153, 178–192.

King, MC, Lusk, C, and Blobel, G (2006). Karyopherin-mediated import of integral inner nuclear membrane proteins. Nature 442, 1003–1007.

Kinugasa, Y et al. (2019). Very-long-chain fatty acid elongase Elo2 rescues lethal defects associated with loss of the nuclear barrier function. Journal of Cell Science, jcs.229021.

Klupp, BG, Granzow, H, and Fuchs, W Vesicle formation from the nuclear membrane is induced by coexpression of two conserved herpesvirus proteins.

Korfali, N et al. (2012). The nuclear envelope proteome differs notably between tissues. Nucleus 3, 552–564.

Krupina, K, Goginashvili, A, and Cleveland, DW (2021). Causes and consequences of micronuclei. Current Opinion in Cell Biology 70, 91–99.

Kumar, A et al. (2014). ATR Mediates a Checkpoint at the Nuclear Envelope in Response to Mechanical Stress. Cell 158, 633–646.

LaFave, MC, Varshney, GK, Gildea, DE, Wolfsberg, TG, Baxevanis, AD, and Burgess, SM (2014). MLV integration site selection is driven by strong enhancers and active promoters. Nucleic Acids Research 42, 4257–4269.

Lafontaine, DLJ, Riback, JA, Bascetin, R, and Brangwynne, CP (2021). The nucleolus as a multiphase liquid condensate. Nat Rev Mol Cell Biol 22, 165–182.

Lahaye, X et al. (2016). Nuclear Envelope Protein SUN2 Promotes Cyclophilin-A-Dependent Steps of HIV Replication. Cell Reports 15, 879–892.

Lammerding, J, Fong, LG, Ji, JY, Reue, K, Stewart, CL, Young, SG, and Lee, RT (2006). Lamins A and C but Not Lamin B1 Regulate Nuclear Mechanics. J Biol Chem 281, 25768–25780.

Lammerding, J, Hsiao, J, Schulze, PC, Kozlov, S, Stewart, CL, and Lee, RT (2005). Abnormal nuclear shape and impaired mechanotransduction in emerin-deficient cells. Journal of Cell Biology 170, 781–791.

Lammerding, J, Schulze, PC, Takahashi, T, Kozlov, S, Sullivan, T, Kamm, RD, Stewart, CL, and Lee, RT (2004). Lamin A/C deficiency causes defective nuclear mechanics and mechanotransduction. J Clin Invest 113, 370–378.

Larson, AG, Elnatan, D, Keenen, MM, Trnka, MJ, Johnston, JB, Burlingame, AL, Agard, DA, Redding, S, and Narlikar, GJ (2017). Liquid droplet formation by HP1α suggests a role for phase separation in heterochromatin. Nature 547, 236–240.

Le Berre, M, Aubertin, J, and Piel, M (2012). Fine control of nuclear confinement identifies a threshold deformation leading to lamina rupture and induction of specific genes. Integrative Biology 4, 1406.

Le Berre, M, Zlotek-Zlotkiewicz, E, Bonazzi, D, Lautenschlaeger, F, and Piel, M (2014). Methods for Two-Dimensional Cell Confinement. In: Methods in Cell Biology, Elsevier, 213–229.

Ledeen, RW, and Wu, G (2007). Sodium-Calcium Exchangers in the Nucleus: An Unexpected Locus and an Unusual Regulatory Mechanism. Annals of the New York Academy of Sciences 1099, 494–506.

Lee, C-P, and Chen, M-R (2021). Conquering the Nuclear Envelope Barriers by EBV Lytic Replication. Viruses 13, 702.

Lei, K, Zhu, X, Xu, R, Shao, C, Xu, T, Zhuang, Y, and Han, M (2012). Inner Nuclear Envelope Proteins SUN1 and SUN2 Play a Prominent Role in the DNA Damage Response. Current Biology 22, 1609–1615.

Levental, KR et al. (2009). Matrix Crosslinking Forces Tumor Progression by Enhancing Integrin Signaling. Cell 139, 891–906.

Levine, MS, and Holland, AJ (2018). The impact of mitotic errors on cell proliferation and tumorigenesis. Genes Dev 32, 620–638.

Li, C, Goryaynov, A, and Yang, W (2016). The selective permeability barrier in the nuclear pore complex. Nucleus 7, 430–446.

Li, S, Peng, Y, Landsman, D, and Panchenko, AR (2022). DNA methylation cues in nucleosome geometry, stability and unwrapping. Nucleic Acids Research 50, 1864–1874.

Li, T, Huang, T, Du, M, Chen, X, Du, F, Ren, J, and Chen, ZJ (2021). Phosphorylation and chromatin tethering prevent cGAS activation during mitosis. Science 371, eabc5386.

Lieberman-Aiden, E et al. (2009). Comprehensive Mapping of Long-Range Interactions Reveals Folding Principles of the Human Genome. Science 326, 289–293.

Lin, F, and Worman, HJ (1993). Structural organization of the human gene encoding nuclear lamin A and nuclear lamin C. Journal of Biological Chemistry 268, 16321–16326.

Lionetti, MC, Bonfanti, S, Fumagalli, MR, Budrikis, Z, Font-Clos, F, Costantini, G, Chepizhko, O, Zapperi, S, and La Porta, CAM (2020). Chromatin and Cytoskeletal Tethering Determine Nuclear Morphology in Progerin-Expressing Cells. Biophysical Journal 118, 2319–2332.

Liu, B et al. (2005). Genomic instability in laminopathy-based premature aging. Nat Med 11, 780–785.

Liu, Q, Pante, N, Misteli, T, Elsagga, M, Crisp, M, Hodzic, D, Burke, B, and Roux, KJ (2007). Functional association of Sun1 with nuclear pore complexes. The Journal of Cell Biology 178, 785–798.

Lodish, H, Berk, A, Kaiser, CA, Krieger, M, Bretscher, A, Ploegh, H, Amon, A, and Martin, KC (2016). Molecular Cell Biology, w.h. freeman.

Lomakin, AJ et al. (2020). The nucleus acts as a ruler tailoring cell responses to spatial constraints. Science 370, eaba2894.

Lu, L, Ladinsky, MS, and Kirchhausen, T (2011). Formation of the postmitotic nuclear envelope from extended ER cisternae precedes nuclear pore assembly. Journal of Cell Biology 194, 425–440.

Luger, K, Mäder, Armin W, Richmond, Robin K, Sargent, David F, and Richmond, Timothy J (1997). Crystal structure of the nucleosome core particle at 2.8 A˚ resolution. Nature 389.

Luo, X, Yang, W, and Gao, G (2018). SUN1 Regulates HIV-1 Nuclear Import in a Manner Dependent on the Interaction between the Viral Capsid and Cellular Cyclophilin A. Journal of Virology 92, e00229-18.

Luxton, GWG, Gomes, ER, Folker, ES, Vintinner, E, and Gundersen, GG (2010). Linear Arrays of Nuclear Envelope Proteins Harness Retrograde Actin Flow for Nuclear Movement. Science 329, 956–959.

Maciejowski, J, Li, Y, Bosco, N, Campbell, PJ, and de Lange, T (2015). Chromothripsis and Kataegis Induced by Telomere Crisis. Cell 163, 1641–1654.

Malhas, A, Goulbourne, C, and Vaux, DJ (2011). The nucleoplasmic reticulum: form and function. Trends in Cell Biology 21, 362–373.

Maniotis, AJ, Chen, CS, and Ingber, DE (1997). Demonstration of mechanical connections between integrins, cytoskeletal filaments, and nucleoplasm that stabilize nuclear structure. Proceedings of the National Academy of Sciences 94, 849–854.

Marciniak, M, Gilbert, A, Loncaric, F, Fernandes, JF, Bijnens, B, Sitges, M, King, A, Crispi, F, and Lamata, P (2021). Septal curvature as a robust and reproducible marker for basal septal hypertrophy. Journal of Hypertension 39, 1421–1428.

Marschall, M, Feichtinger, S, and Milbradt, J (2011). Regulatory Roles of Protein Kinases in Cytomegalovirus Replication. In: Advances in Virus Research, Elsevier, 69–101.

McMahon, HT, and Boucrot, E (2015). Membrane curvature at a glance. Journal of Cell Science 128, 1065–1070.

van Meer, G, Voelker, DR, and Feigenson, GW (2008). Membrane lipids: where they are and how they behave. Nat Rev Mol Cell Biol 9, 112–124.

Mehl, JL, Earle, A, Lammerding, J, Mhlanga, M, Vogel, V, and Jain, N (2022). Blockage of lamin-A/C loss diminishes the pro-inflammatory macrophage response. IScience 25, 105528.

Mellad, JA, Warren, DT, and Shanahan, CM (2011). Nesprins LINC the nucleus and cytoskeleton. Current Opinion in Cell Biology 23, 47–54.

Mettenleiter, TC (2016). Breaching the Barrier—The Nuclear Envelope in Virus Infection. Journal of Molecular Biology 428, 1949–1961.

Millán-Zambrano, G, Burton, A, Bannister, AJ, and Schneider, R (2022). Histone post-translational modifications — cause and consequence of genome function. Nat Rev Genet 23, 563–580.

Moir, RD, Yoon, M, Khuon, S, and Goldman, RD (2000). Nuclear Lamins A and B1: Different Pathways of Assembly during Nuclear Envelope Formation in Living Cells. The Journal of Cell Biology 151.

Moreau, HD et al. (2019). Macropinocytosis Overcomes Directional Bias in Dendritic Cells Due to Hydraulic Resistance and Facilitates Space Exploration. Developmental Cell 49, 171-188.e5.

Murphy, SP, Simmons, CR, and Bass, HW (2010). Structure and expression of the maize (Zea maysL.) SUN-domain protein gene family: evidence for the existence of two divergent classes of SUN proteins in plants. BMC Plant Biol 10, 269.

Nader, GP de F et al. (2021). Compromised nuclear envelope integrity drives TREX1-dependent DNA damage and tumor cell invasion. Cell 184, 5230-5246.e22.

Naetar, N, Ferraioli, S, and Foisner, R (2017). Lamins in the nuclear interior − life outside the lamina. Journal of Cell Science 130, 2087–2096.

Nakajima, H et al. (2017). Flow-Dependent Endothelial YAP Regulation Contributes to Vessel Maintenance. Developmental Cell 40, 523-536.e6.

Nava, MM et al. (2020). Heterochromatin-Driven Nuclear Softening Protects the Genome against Mechanical Stress-Induced Damage. Cell 181, 800-817.e22.

Nmezi, B et al. (2019). Concentric organization of A- and B-type lamins predicts their distinct roles in the spatial organization and stability of the nuclear lamina. Proc Natl Acad Sci USA 116, 4307–4315.

Nozaki, T et al. (2017). Dynamic Organization of Chromatin Domains Revealed by Super-Resolution Live-Cell Imaging. Molecular Cell 67, 282-293.e7.

Ohba, T, Schirmer, EC, Nishimoto, T, and Gerace, L (2004). Energy- and temperature-dependent transport of integral proteins to the inner nuclear membrane via the nuclear pore. Journal of Cell Biology 167, 1051–1062.

Oza, P, Jaspersen, SL, Miele, A, Dekker, J, and Peterson, CL (2009). Mechanisms that regulate localization of a DNA double-strand break to the nuclear periphery. Genes Dev 23, 912–927.

Pajerowski, JD, Dahl, KN, Zhong, FL, Sammak, PJ, and Discher, DE (2007). Physical plasticity of the nucleus in stem cell differentiation. Proc Natl Acad Sci USA 104, 15619–15624.

Panciera, T, Azzolin, L, Cordenonsi, M, and Piccolo, S (2017). Mechanobiology of YAP and TAZ in physiology and disease. Nat Rev Mol Cell Biol 18, 758–770.

Paquin, KL, and Howlett, NG (2018). Understanding the Histone DNA Repair Code: H4K20me2 Makes Its Mark. Molecular Cancer Research 16, 1335–1345.

Parry, DAD, Conway, JF, and Steinert, PM (1986). Structural studies on lamin. Similarities and differences between lamin and intermediate-filament proteins. Biochemical Journal 238, 305–308.

Patteson, AE, Vahabikashi, A, Pogoda, K, Adam, SA, Mandal, K, Kittisopikul, M, Sivagurunathan, S, Goldman, A, Goldman, RD, and Janmey, PA (2019). Vimentin protects cells against nuclear rupture and DNA damage during migration. Journal of Cell Biology 218, 4079–4092.

Peng, K, Muranyi, W, Glass, B, Laketa, V, Yant, SR, Tsai, L, Cihlar, T, Müller, B, and Kräusslich, H-G (2014). Quantitative microscopy of functional HIV post-entry complexes reveals association of replication with the viral capsid. ELife 3.

Pennacchio, FA et al. (2022). Force-biased nuclear import sets nuclear-cytoplasmic volumetric coupling by osmosis, Cell Biology.

Percipalle, P (2013). Co-transcriptional nuclear actin dynamics. Nucleus 4, 43–52.

Peter, M, Nakagawa, J, Dorée, M, Labbé, JC, and Nigg, EA (1990). Identification of major nucleolar proteins as candidate mitotic substrates of cdc2 kinase. Cell 60, 791–801.

Péterfy, M, Phan, J, Xu, P, and Reue, K (2001). Lipodystrophy in the fld mouse results from mutation of a new gene encoding a nuclear protein, lipin. Nat Genet 27, 121–124.

Peterson, TR et al. (2011). mTOR Complex 1 Regulates Lipin 1 Localization to Control the SREBP Pathway. Cell 146, 408–420.

Pfeifer, CR, Tobin, MP, Cho, S, Vashisth, M, Dooling, LJ, Vazquez, LL, Ricci-De Lucca, EG, Simon, KT, and Discher, DE (2022). Gaussian curvature dilutes the nuclear lamina, favoring nuclear rupture, especially at high strain rate. Nucleus 13, 130–144.

Plessner, M, Melak, M, Chinchilla, P, Baarlink, C, and Grosse, R (2015). Nuclear F-actin Formation and Reorganization upon Cell Spreading. J Biol Chem 290, 11209–11216.

Pocaterra, A, Romani, P, and Dupont, S (2020). YAP/TAZ functions and their regulation at a glance. Journal of Cell Science 133, jcs230425.

Pocivavsek, L, Dellsy, R, Kern, A, Johnson, S, Lin, B, Lee, KYC, and Cerda, E (2008). Stress and Fold Localization in Thin Elastic Membranes. Science 320, 912–916.

Polioudaki, H, Kourmouli, N, Drosou, V, Bakou, A, Theodoropoulos, PA, Singh, PB, Giannakouros, T, and Georgatos, SD (2001). Histones H3/H4 form a tight complex with the inner nuclear membrane protein LBR and heterochromatin protein 1. EMBO Reports 2, 920–925.

Porwal, M et al. (2013). Parvoviruses Cause Nuclear Envelope Breakdown by Activating Key Enzymes of Mitosis. PLoS Pathog 9, e1003671.

Prentice-Mott, HV, Chang, C-H, Mahadevan, L, Mitchison, TJ, Irimia, D, and Shah, JV (2013). Biased migration of confined neutrophil-like cells in asymmetric hydraulic environments. Proc Natl Acad Sci USA 110, 21006–21011.

Raab, M et al. (2016). ESCRT III repairs nuclear envelope ruptures during cell migration to limit DNA damage and cell death. Science 352, 359–362.

Renkawitz, J et al. (2019). Nuclear positioning facilitates amoeboid migration along the path of least resistance. Nature 568, 546–550.

Richmond, TJ, Finch, JT, Rushton, B, Rhodes, D, and Klug, A (1984). Structure of the Ilucleosome core particle at 7 A resolution.

Röber, R, Gieseler, R, Peters, J, Weber, K, and Osborn, M (1990a). Induction of nuclear lamins A/C in macrophages in in vitro cultures of rat bone marrow precursor cells and human blood monocytes, and in macrophages elicited in vivo by thioglycollate stimulation J H Peters, K Weber, M Osborn. Experimental Cell Research, 185–194.

Röber, R-A, Sauter, A, Weber, K, and Osborn, M (1990b). Cells of the cellular immune and hemopoietic system of the mouse lack lamins A/C: distinction *Versus* other somatic cells. Journal of Cell Science 95, 587–598.

Rollin, R (2021). Physical principles of size and density regulation in the cell and the cell nucleus., PhD thesis.

Rollin, R, Joanny, J-F, and Sens, P (2023). Physical basis of the cell size scaling laws. ELife 12, e82490.

Romanauska, A, and Köhler, A (2018). The Inner Nuclear Membrane Is a Metabolically Active Territory that Generates Nuclear Lipid Droplets. Cell 174, 700-715.e18.

Roux, KJ, Crisp, ML, Liu, Q, Kim, D, Kozlov, S, Stewart, CL, and Burke, B (2009). Nesprin 4 is an outer nuclear membrane protein that can induce kinesin-mediated cell polarization. Proc Natl Acad Sci USA 106, 2194–2199.

Rowat, AC, Jaalouk, DE, Zwerger, M, Ung, WL, Eydelnant, IA, Olins, DE, Olins, AL, Herrmann, H, Weitz, DA, and Lammerding, J (2013). Nuclear Envelope Composition Determines the Ability of Neutrophil-type Cells to Passage through Micron-scale Constrictions. Journal of Biological Chemistry 288, 8610–8618.

Rowat, AC, Lammerding, J, and Ipsen, JH (2006). Mechanical Properties of the Cell Nucleus and the Effect of Emerin Deficiency. Biophysical Journal 91, 4649–4664.

Rusiñol, AE, and Sinensky, MS (2006). Farnesylated lamins, progeroid syndromes and farnesyl transferase inhibitors. Journal of Cell Science 119, 3265–3272.

Samwer, M, Schneider, MWG, Hoefler, R, Schmalhorst, PS, Jude, JG, Zuber, J, and Gerlich, DW (2017). DNA Cross-Bridging Shapes a Single Nucleus from a Set of Mitotic Chromosomes. Cell 170, 956-972.e23.

Sapra, KT, Qin, Z, Dubrovsky-Gaupp, A, Aebi, U, Müller, DJ, Buehler, MJ, and Medalia, O (2020). Nonlinear mechanics of lamin filaments and the meshwork topology build an emergent nuclear lamina. Nat Commun 11, 6205.

Schaller, T, Bulli, L, Pollpeter, D, Betancor, G, Kutzner, J, Apolonia, L, Herold, N, Burk, R, and Malim, MH (2017). Effects of Inner Nuclear Membrane Proteins SUN1/UNC-84A and SUN2/UNC-84B on the Early Steps of HIV-1 Infection. Journal of Virology 91.

Schatten, G, Maul, GG, Schatten, H, Chaly, N, Simerly, C, Balczon, R, and Brown, DL (1985). Nuclear lamins and peripheral nuclear antigens during fertilization and embryogenesis in mice and sea urchins. Proc Natl Acad Sci USA 82, 4727–4731.

Schirmer, EC, and Gerace, L (2005). The nuclear membrane proteome: extending the envelope. Trends in Biochemical Sciences 30, 551–558.

Schrank, BR, Aparicio, T, Li, Y, Chang, W, Chait, BT, Gundersen, GG, Gottesman, ME, and Gautier, J (2018). Nuclear ARP2/3 drives DNA break clustering for homology-directed repair. Nature 559, 61–66.

Schreiner, SM, Koo, PK, Zhao, Y, Mochrie, SGJ, and King, MC (2015). The tethering of chromatin to the nuclear envelope supports nuclear mechanics. Nat Commun 6, 7159.

Shah, P, Hobson, CM, Cheng, S, Colville, MJ, Paszek, MJ, Superfine, R, and Lammerding, J (2021). Nuclear Deformation Causes DNA Damage by Increasing Replication Stress. Current Biology 31, 753-765.e6.

Shimi, T et al. (2008). The A- and B-type nuclear lamin networks: microdomains involved in chromatin organization and transcription. Genes & Development 22, 3409–3421.

Shimi, T, Kittisopikul, M, Tran, J, Goldman, AE, Adam, SA, Zheng, Y, Jaqaman, K, and Goldman, RD (2015). Structural organization of nuclear lamins A, C, B1, and B2 revealed by superresolution microscopy. MBoC 26, 4075–4086.

Sieprath, T et al. (2015). Sustained accumulation of prelamin A and depletion of lamin A/C both cause oxidative stress and mitochondrial dysfunction but induce different cell fates. Nucleus 6, 236–246.

Solovei, I et al. (2013). LBR and Lamin A/C Sequentially Tether Peripheral Heterochromatin and Inversely Regulate Differentiation. Cell 152, 584–598.

Sołtysik, K, Ohsaki, Y, Tatematsu, T, Cheng, J, Maeda, A, Morita, S, and Fujimoto, T (2021). Nuclear lipid droplets form in the inner nuclear membrane in a seipin-independent manner. Journal of Cell Biology 220, e202005026.

Sosa, BA, Rothballer, A, Kutay, U, and Schwartz, TU (2012). LINC Complexes Form by Binding of Three KASH Peptides to Domain Interfaces of Trimeric SUN Proteins. Cell 149, 1035–1047.

Starr, DA (2007). Communication between the cytoskeleton and the nuclear envelope to position the nucleus. Mol BioSyst 3, 583.

Stephens, AD, Banigan, EJ, Adam, SA, Goldman, RD, and Marko, JF (2017). Chromatin and lamin A determine two different mechanical response regimes of the cell nucleus. MBoC 28, 1984–1996.

Stephens, AD, Liu, PZ, Banigan, EJ, Almassalha, LM, Backman, V, Adam, SA, Goldman, RD, and Marko, JF (2018). Chromatin histone modifications and rigidity affect nuclear morphology independent of lamins. MBoC 29, 220–233.

Strickfaden, H, Tolsma, TO, Sharma, A, Underhill, DA, Hansen, JC, and Hendzel, MJ (2020). Condensed Chromatin Behaves like a Solid on the Mesoscale In Vitro and in Living Cells. Cell 183, 1772-1784.e13.

Sun, Z, Guo, SS, and Fässler, R (2016). Integrin-mediated mechanotransduction. Journal of Cell Biology 215, 445–456.

Swift, J et al. (2013). Nuclear Lamin-A Scales with Tissue Stiffness and Enhances Matrix-Directed Differentiation. Science 341, 1240104–1240104.

Takaki, T et al. (2017). Actomyosin drives cancer cell nuclear dysmorphia and threatens genome stability. Nat Commun 8, 16013.

Tamashunas, AC et al. (2020). High-throughput gene screen reveals modulators of nuclear shape. MBoC 31, 1392–1402.

Tenga, R, and Medalia, O (2020). Structure and unique mechanical aspects of nuclear lamin filaments. Current Opinion in Structural Biology 64, 152–159.

Terry, LJ, and Wente, SR (2009). Flexible Gates: Dynamic Topologies and Functions for FG Nucleoporins in Nucleocytoplasmic Transport. Eukaryot Cell 8, 1814–1827.

Thevenaz, P, Ruttimann, UE, and Unser, M (1998). A pyramid approach to subpixel registration based on intensity. IEEE Trans on Image Process 7, 27–41.

Thiam, H-R et al. (2016). Perinuclear Arp2/3-driven actin polymerization enables nuclear deformation to facilitate cell migration through complex environments. Nature Communications, 14.

Tsai, P-L, Zhao, C, Turner, E, and Schlieker, C (2016). The Lamin B receptor is essential for cholesterol synthesis and perturbed by disease-causing mutations. ELife 5, e16011.

Tsuchiya, Y, Hase, A, Ogawa, M, Yorifuji, H, and Arahata, K (2001). Distinct regions specify the nuclear membrane targeting of emerin, the responsible protein for Emery-Dreifuss muscular dystrophy: Emery-Dreifuss muscular dystrophy. European Journal of Biochemistry 259, 859–865.

Turgay, Y, Eibauer, M, Goldman, AE, Shimi, T, Khayat, M, Ben-Harush, K, Dubrovsky-Gaupp, A, Sapra, KT, Goldman, RD, and Medalia, O (2017). The molecular architecture of lamins in somatic cells. Nature 543, 261–264.

Turgay, Y, Ungricht, R, Rothballer, A, Kiss, A, Csucs, G, Horvath, P, and Kutay, U (2010). A classical NLS and the SUN domain contribute to the targeting of SUN2 to the inner nuclear membrane. EMBO J 29, 2262–2275.

Vaidžiulytė, K, Macé, A-S, Battistella, A, Beng, W, Schauer, K, and Coppey, M (2022). Persistent cell migration emerges from a coupling between protrusion dynamics and polarized trafficking. ELife 11, e69229.

Van Schaik, T, Vos, M, Peric-Hupkes, D, Hn Celie, P, and Van Steensel, B (2020). Cell cycle dynamics of lamina-associated DNA. EMBO Reports 21, e50636.

Van Steensel, B, and Belmont, AS (2017). Lamina-Associated Domains: Links with Chromosome Architecture, Heterochromatin, and Gene Repression. Cell 169, 780–791.

Vargas, JD, Hatch, EM, Anderson, DJ, and Hetzer, MW (2012). Transient nuclear envelope rupturing during interphase in human cancer cells. Nucleus 3, 88–100.

Vargas, P et al. (2016). Innate control of actin nucleation determines two distinct migration behaviours in dendritic cells. Nat Cell Biol 18, 43–53.

Vargas, P, Barbier, L, Sáez, PJ, and Piel, M (2017). Mechanisms for fast cell migration in complex environments. Current Opinion in Cell Biology 48, 72–78.

Venkova, L et al. (2022). A mechano-osmotic feedback couples cell volume to the rate of cell deformation. ELife 11, e72381.

Venturini, V et al. (2020). The nucleus measures shape changes for cellular proprioception to control dynamic cell behavior. Science 370, eaba2644.

Vermeulen, M, Mulder, KW, Denissov, S, Pijnappel, WWMP, Van Schaik, FMA, Varier, RA, Baltissen, MPA, Stunnenberg, HG, Mann, M, and Timmers, HThM (2007). Selective Anchoring of TFIID to Nucleosomes by Trimethylation of Histone H3 Lysine 4. Cell 131, 58–69.

Vietri, M et al. (2020). Unrestrained ESCRT-III drives micronuclear catastrophe and chromosome fragmentation. Nat Cell Biol 22, 856–867.

Wada, K-I, Itoga, K, Okano, T, Yonemura, S, and Sasaki, H (2011). Hippo pathway regulation by cell morphology and stress fibers. Development 138, 3907–3914.

Wang, L et al. (2019). Histone Modifications Regulate Chromatin Compartmentalization by Contributing to a Phase Separation Mechanism. Molecular Cell 76, 646-659.e6.

Wang, N, Tytell, JD, and Ingber, DE (2009). Mechanotransduction at a distance: mechanically coupling the extracellular matrix with the nucleus. Nat Rev Mol Cell Biol 10, 75–82.

Watson, JD, Baker, TA, Bell, SP, Gann, A, Levine, M, and Losick, R (2014). Molecular Biology of the Gene.

Weigelin, B, Bakker, G-J, and Friedl, P (2012). Intravital third harmonic generation microscopy of collective melanoma cell invasion: Principles of interface guidance and microvesicle dynamics. IntraVital 1, 32–43.

Wilhelmsen, K, Litjens, SHM, Kuikman, I, Tshimbalanga, N, Janssen, H, Van Den Bout, I, Raymond, K, and Sonnenberg, A (2005). Nesprin-3, a novel outer nuclear membrane protein, associates with the cytoskeletal linker protein plectin. Journal of Cell Biology 171, 799–810.

Wolf, K, te Lindert, M, Krause, M, Alexander, S, te Riet, J, Willis, AL, Hoffman, RM, Figdor, CG, Weiss, SJ, and Friedl, P (2013). Physical limits of cell migration: Control by ECM space and nuclear deformation and tuning by proteolysis and traction force. Journal of Cell Biology 201, 1069–1084.

Woodcock, CL, Frado, LL, and Rattner, JB (1984). The higher-order structure of chromatin: evidence for a helical ribbon arrangement. Journal of Cell Biology 99, 42–52.

Wu, J, Lewis, AH, and Grandl, J (2017). Touch, Tension, and Transduction – The Function and Regulation of Piezo Ion Channels. Trends in Biochemical Sciences 42, 57–71.

Xia, Y et al. (2018). Nuclear rupture at sites of high curvature compromises retention of DNA repair factors. Journal of Cell Biology 217, 3796–3808.

Yang, SH, Jung, H-J, Coffinier, C, Fong, LG, and Young, SG (2011). Are B-type lamins essential in all mammalian cells? Nucleus 2, 562–569.

Zhang, Q (2001). Nesprins, a novel family of nuclear envelope proteins. Journal of Cell Science.

Zhu, R, Antoku, S, and Gundersen, GG (2017). Centrifugal Displacement of Nuclei Reveals Multiple LINC Complex Mechanisms for Homeostatic Nuclear Positioning. Current Biology 27, 3097-3110.e5.

Zidovska, A (2020). Chromatin: Liquid or Solid? Cell 183, 1737–1739.

Zierhut, C, Yamaguchi, N, Paredes, M, Luo, J-D, Carroll, T, and Funabiki, H (2019). The Cytoplasmic DNA Sensor cGAS Promotes Mitotic Cell Death. Cell 178, 302-315.e23.

Zila, V et al. (2021). Cone-shaped HIV-1 capsids are transported through intact nuclear pores. Cell 184, 1032-1046.e18.

Zimmerli, CE et al. (2021). Nuclear pores dilate and constrict in cellulo. Science 374, eabd9776.

ABSTRACTS

université PARIS-SACLAY

ÉCOLE DOCTORALE
Structure et dynamique des systèmes vivants (SDSV)

Titre : Enveloppe nucléaire et réponse du noyau aux déformations mécaniques

Mots clés : noyau, enveloppe nucléaire, biophysique, VIH

Résumé : Le noyau, qui abrite le génome des cellules eucaryotes, est l'organite le plus volumineux et le plus rigide de la cellule. Il est délimité par une double membrane percée de pores, l'enveloppe nucléaire, elle-même soutenue par la lamina, un réseau de filaments intermédiaires, les lamines. L'enveloppe, la lamina et la chromatine sont connectées par un réseau d'interaction protéines-protéines et protéines-ADN, qui, grâce au complexe du Linker entre Nucléosquelette et Cytosquelette, sont en continuité mécanique avec le cytoplasme et la membrane plasmique. La capacité de la cellule à percevoir les signaux mécaniques de son environnement au niveau de la membrane plasmique est bien connue. Le noyau lui-même a émergé comme un composant mécano-sensible, par son interaction avec la membrane plasmique et par sa propre capacité à percevoir les déformations. Cependant, la compréhension physique du noyau et de ses propriétés mécaniques en réponse aux déformations reste incomplète. Dans ce travail, nous avons utilisé différentes approches pour déformer le noyau (microscopie à force atomique, confineur micro-fabriqué) et comprendre comment l'enveloppe nucléaire et la lamina déterminent la réponse du noyau aux contraintes mécaniques, en nous concentrant sur une échelle de temps de l'ordre de plusieurs minutes. Nous avons montré que les noyaux peuvent adopter différentes formes in vivo et in vitro. En particulier, en l'absence de contrainte, l'enveloppe nucléaire développe des plis et invaginations, qui peuvent s'ouvrir réversiblement lorsque les noyaux sont déformés. Nous proposons un modèle d'instabilité mécanique reposant sur les différences de rigidité et de surface de l'ensemble enveloppe-lamina et de la chromatine pour expliquer la formation, la réversibilité et la forme de ces repliements. Ce modèle prédit que tant que l'enveloppe possède des plis, sa tension reste proche de zéro, ce qui propose un régime de déformation sans tension. Nous montrons cette prédiction par une méthode d'imagerie dynamique mesurant les fluctuations de l'enveloppe, ainsi que par une mesure quantitative des forces exercées par le noyau par microscopie à force atomique. Nous avons ainsi mis en évidence l'existence de deux régimes de déformation : un régime sans tension, jusqu'à une hauteur seuil de 6 µm, en-dessous de laquelle la lamina se tend. Associés à ces deux régimes de tension, nous avons montré que le noyau répond en deux régimes de volume lorsque la déformation s'effectue sans tension, le volume nucléaire reste quasi-constant, tandis que lorsque le noyau est tendu, le volume du noyau diminue. Nous proposons que le premier régime permettent aux noyaux d'avoir une gamme de déformation sans risque pour leur intégrité, tandis que le second puisse être à la fois un signal perçu par la cellule et participer aux phénomènes de rupture d'enveloppe et de dommages à l'ADN observés dans les noyaux sous contrainte.

université PARIS-SACLAY

ÉCOLE DOCTORALE
Structure et dynamique des systèmes vivants (SDSV)

Title : Nuclear envelope and nuclear response to mechanical deformation

Keywords: nucleus, nuclear envelope, biophysics, HIV

Abstract: The nucleus is home to the genome in eukaryotic cells. It is the largest and stiffest organelle in the cell and is delimited by a double membrane pierce by nuclear pores, the nuclear envelope, supported the lamina, a meshwork of intermediate filaments called the lamins. The envelope, the lamina and the chromatin are connected by multiple protein-protein and protein-DNA interactions. They ensure a mechanical continuity with the cytoplasm and the plasma membrane through the Linker of Nucleoskeleton and Cytoskeleton complex. The cells' ability to sense the mechanical cues from the environment has long been known. The nucleus itself has emerged as a mechano-sensitive organelle, both in interaction with the plasma membrane and on its own. However, the physical understanding of the nucleus and its mechanical propertis in response to deformations remains incomplete. In this work, we used several approaches to impose deformations to the nucleus (atomic force microscopy, microfabricated confiner) and understand how the nuclear envelope and the lamina determine the nuclear response to mechanical constraints. We focused on time scales of several minutes. We showed that nuclei can harbor several shapes in vivo and in vitro. In particular, nuclei in absence of constraints display folds and invaginations, which can be reversibly opened up by deformation.
We propose the model of a mechanical instability to explain the formation, shape and reversibility of the folds. It is based on the differences in rigidity and surface between the lamina-envelope layers and the chromatin. The model predicts that as long as the nuclear envelope is folded, its tension should remain close to zero, which proposes a deformation regime without tension. We have demonstrated this prediction by an imaging technique measuring nuclear envelope fluctuations, as well as by quantitative force measurements with atomic force microscopy. We have thus shown that there are two regimes of deformation: the first one, without tension, until a threshold height of 6 µm, and a second one, below the threshold, where the lamina becomes tensed. We have additionally shown that a two-regime response in volume is associated to the regimes in tension. As long as the tension remains low, the nuclear volume remains nearly constant. Once it is tensed, the nuclear volume starts to decrease. We propose that the first regime represent a safe range of deformation where the nucleus can adapt to constraints without altering its properties. We make the hypothesis that the second regime can constitute a signal perceived by the cell, and participate to the phenomena of nuclear envelope ruptures and DNA damage observed in deformed nuclei.